

Nonstationary Impedance Measurements in Forced and Natural Dynamic Conditions using Dynamic Multi-Frequency Analysis

Vom Fachbereich Produktionstechnik
der
UNIVERSITÄT BREMEN

zur Erlangung des Grades
Doktor-Ingenieur
genehmigte

Dissertation
von
M.Sc. Dominique Koster

Gutachter:
Prof. Fabio La Mantia
Prof. Monica Santamaria (Universität Palermo)

Tag der mündlichen Prüfung: 22. Oktober 2019

Erklärung

Ich erkläre hiermit an Eides statt, dass ich die vorliegende Dissertation

1. ohne unerlaubte fremde Hilfe angefertigt habe,
2. keine anderen als die von mir angegebenen Quellen und Hilfsmittel benutzt habe und
3. die den benutzten Werken wörtlich oder inhaltlich entnommenen Stellen als solche kenntlich gemacht habe.

Bremen, den 13.05.2019

.....

Dominique Koster

Acknowledgements

There's a number of people that played a decisive role for the completion of this project, who should be mentioned herein.

First, I would like to thank my supervisor, Professor Fabio La Mantia, who always provided me with encouragement and guidance. Due to his competence and scientific experience, I have gained valuable insight into the field of electrochemistry.

Moreover, I'm extremely grateful to Professor Monica Santamaria, who accepted to be the second reviewer of my dissertation.

I would also like to acknowledge my committee members, Professor Lucio Colombi Ciacchi, Dr. Ingo Bardenhagen, Collins Erinmwmingbovo, and Sascha Stallmann.

Furthermore, I would like to thank all my colleagues from the group of Energy Storage and Energy Conversion Systems, whom I had great pleasure working with.

Many thanks should also go to Professor Katharina Krischer, for the nice collaboration and for hosting me in her group of Chemical Physics beyond Equilibrium at Technical University of Munich.

Some people, who are particularly important to me and who deserve special mention are:

Giorgia, for our 'three little pig-trips' and all the fun time.

Ghoncheh, who accompanied me on this way – our Medoo sessions made what seemed to be unbearable bearable.

Nico – who would have thought that conferences could be that much fun? Thanks for your help and for cheering me up, when I felt down, and

Elena, for sharing the passion for coffee, cinnamon rolls, and dogs with me.

Finally, I would like to express my deepest thanks to my parents, Monika and Michael Koster, for their unconditional love and support and, of course, to my brother Michael, for his hugs, punches, smiles, uncountable MÄDN and Kniffel sessions, and simply for being my best friend.

Kurzfassung

Die vorliegende Arbeit beschäftigt sich mit der Charakterisierung elektrochemischer Systeme mit Hilfe von dynamischer Impedanzspektroskopie. Elektrochemische Reaktionen erfolgen durch das Zusammenspiel verschiedener Prozesse, die auf unterschiedlichen Zeitskalen ablaufen. Um einen Einblick in die Kinetik einer heterogenen Elektronentransferreaktion gewinnen zu können, ist die gleichzeitige Erfassung der Zeitkonstanten, der ihr zugrunde liegenden Prozesse wünschenswert. Elektrochemische Impedanzspektroskopie (EIS) basiert auf der stufenweisen Potentialablenkung eines Systems mit Sinuswellen unterschiedlicher Frequenzen. Die resultierende Stromantwort lässt Rückschlüsse auf den Mechanismus einer Reaktion zu. Mit Hilfe von EIS können zahlreiche Elektrodenprozesse gleichzeitig untersucht werden. Diese Methode setzt die Stationarität des betrachteten Systems während der gesamten Messdauer voraus. Für eine große Anzahl elektrochemischer Systeme ist die Einstellung eines stabilen stationären Zustandes jedoch nicht möglich oder nur von kurzer Dauer, da das System während der Untersuchung irreversible Änderungen erfährt. Die Dynamische Multifrequenzanalyse (DMFA) verwendet eine Multisinusfunktion, die zur gleichzeitigen Anregung verschiedener Frequenzanteile dient und so die Möglichkeit zur Durchführung von Impedanzmessungen unter nicht-stationären Bedingungen bietet.

Im Rahmen dieser Arbeit wird DMFA zur Untersuchung des dynamischen Impedanzverhaltens unterschiedlicher elektrochemischer Systeme herangezogen. Am Beispiel eines einfachen Redox-Prozesses werden grundlegende Prinzipien zur Durchführung und Analyse dynamischer Impedanzmessungen erläutert. Es wird gezeigt, dass die Auswertung der Spektren mittels komplexer nichtlinearer Regression eine physikalische Interpretation der Messergebnisse zulässt. Basierend darauf werden unterschiedliche Stadien der kathodischen Wasserstoffentwicklungsreaktion (HER) untersucht. Durch die Kombination von quasi-zyklischer Voltammetrie mit der Multifrequenzanregung wird das zu untersuchende System in einen dynamischen Zustand überführt. Auf diese Weise kann ein Zusammenhang zwischen den unterschiedlichen Reaktionsstadien dieses Prozesses hergestellt werden. Die zeitliche Entwicklung der physikalischen Variablen erlaubt neue Einblicke in die Reaktionskinetik der HER. Weiterhin wird DMFA zur Betrachtung, der im Zusammenhang mit der elektrochemischen Oxidation von p-dotiertem Silizium auftretenden Stromschwingungen eingesetzt. Die Analyse des Systems im dynamischen Gleichgewichtszustand bildet die Grundlage für die Charakterisierung spontan auftretender Schwingungszustände, deren Schwingungsdynamik mit Hilfe dynamischer Impedanzmessungen systematisch untersucht wird.

Abstract

This thesis is concerned with the characterization of electrochemical systems by means of dynamic impedance spectroscopy. Electron transfer reactions across electrified interfaces involve a variety of processes, occurring at different time scales. A detailed understanding of the reaction kinetics requires the investigation of the system over a wide range of frequencies in order to capture all time constants related to the different underlying processes. In electrochemical impedance spectroscopy (EIS) a small-amplitude sinusoidal potential perturbation is imposed on the system by successively changing the frequency of the sinusoidal wave. The system's response to the perturbation signal provides an insight into the mechanism governing the reaction. EIS is a powerful tool that allows for the investigation of a variety of electrode processes in a single measurement. This method requires the stationarity of the system throughout the acquisition time of one full impedance spectrum. However, in many electrochemical systems a stable steady-state cannot be established, since the system undergoes irreversible changes during the measurement. Dynamic multi-frequency analysis (DMFA) uses a multi-sine waveform to apply all frequencies to the system simultaneously, thus allowing for the acquisition of impedance spectra in dynamic conditions.

Here, DMFA is employed for the investigation of the nonstationary impedance behavior of different electrochemical systems, exhibiting either forced or natural reaction dynamics. Fundamental principles of data recording and analysis are examined by application of DMFA to a simple redox process. It is demonstrated that the temporal evolution of physical variables can be extracted from data analysis using suitable electrical equivalent circuits (EECs). Based on these results, different stages of the hydrogen evolution reaction (HER) are examined by means of DMFA. To do so, the system is subjected to forced dynamic conditions by combining *quasi-dc* voltammetry and multi-sine impedance spectroscopy, thus providing a concatenated picture of the overall process. The investigation of the temporal evolution of the kinetic variables gives new insight into the mechanism of the HER. Finally, DMFA is employed for the examination of self-sustained current oscillations during the anodic electrodisolution of p-type silicon in fluoride containing electrolytes. The analysis of the system in dynamic equilibrium conditions provides the foundation for the investigation of the electrodisolution process in the oscillatory regime. DMFA allows for the characterization of different types of current oscillations in terms of their oscillatory reaction dynamics.

Contents

1. Dynamic Impedance Spectroscopy	1
2. Theoretical Background	7
2.1. Fundamentals of Electrochemistry	7
2.1.1. Electrochemical Systems	7
2.1.2. The Electric Double Layer	8
2.1.3. Heterogeneous Charge Transfer Reactions	10
2.2. Convolution and Transfer Functions in Linear Systems Theory	11
2.3. Electrochemical Impedance Spectroscopy	15
2.3.1. Complex Impedance as a Transfer Function	15
2.3.2. Application of Impedance Spectroscopy to Investigate Kinetic Parameters	19
2.4. The Concept of DMFA	25
2.4.1. The Dynamic Impedance Expression	25
2.4.2. Linearization of Nonstationary Systems	28
2.4.3. Frequency Dependence of Physical Variables in Dynamic Conditions	29
2.4.4. Data Fitting of Dynamic Impedance Spectra	32
3. Dynamic Impedance Spectroscopy using DMFA	35
3.1. Perturbation Signals in DMFA	35
3.1.1. The Quasi-Triangular Potential Perturbation	35
3.1.2. Design of the Multi-Sine Signal	37
3.2. Multi-Sine DC-Voltammetry	41
3.2.1. Determination of the Filter Bandwidth	41
3.2.2. Impact of the Multi-Sine Intensity on the Linearity of the System	50
3.2.3. Impedance Analysis using Equivalent Circuits	54
3.2.4. Effect of the Electrode Dimension on the Reaction Kinetics	58
4. Studies on the Kinetics of the HER	71
4.1. Movement Towards an Environmentally Friendly Energy Economy	71
4.1.1. A Hydrogen Economy	72
4.1.2. Generation of Molecular Hydrogen by Electrolysis	73
4.1.3. The Cathodic Hydrogen Evolution Reaction	76
4.1.4. Kinetics of the HER	78
4.2. Dynamic Impedance Studies on the HER by means of DMFA	82
4.2.1. Voltammetric Characterization of the System	82
4.2.2. Impedance Spectroscopy in Forced Dynamic Conditions	85
4.2.3. The Electro-Sorption Reaction	87
4.2.4. The Hydrogen Evolution Region	95
4.3. Effect of Perchlorates on the HER Kinetics	100

5. Reaction Dynamics of the Oscillatory Electrodeposition of p-Type Silicon	107
5.1. Nonlinear Dynamics	107
5.1.1. Oscillatory Dynamics	108
5.1.2. Bifurcation Theory	109
5.1.3. The Silicon Electrodeposition Reaction in Fluoride Containing Media .	110
5.2. The Anodic Electrodeposition of p-Type Si in Quasi-Stationary Conditions .	112
5.2.1. Voltammetric Characterization of the Si Electrodeposition Reaction .	112
5.2.2. Impedance Studies in the Regime of Negative Differential Resistance .	113
5.3. Reaction Dynamics in the Oscillatory Regime	116
5.3.1. Low-Amplitude Oscillations	119
5.3.2. Shoulder Oscillations	124
5.3.3. High-Amplitude Oscillations	129
6. Conclusion and Outlook	135
7. Experimental	139
7.1. Dynamic Impedance Measurements	139
7.1.1. Instrumental Set-Up	139
7.1.2. Cell Set-Up	140
7.1.3. Perturbation Signals	142
7.1.4. Data Acquisition	143
7.1.5. Data Processing	143
7.1.6. Fitting of Dynamic Impedance Spectra	145
7.2. Materials and Instruments	147
7.3. Experimental Protocols	149
7.3.1. Fabrication of Micro- and Multibarrel Electrodes	149
7.3.2. Measurements on the Reaction Dynamics of a Redox Couple	152
7.3.3. Measurements on the Reaction Dynamics of the HER	153
7.3.4. Measurements on the Anodic Electro-Dissolution of p-Type Si	154
7.4. Conductivity and Mobility	157
Appendix	159
A. Complex Impedance Expression	159
B. Comparison of EIS and DMFA	161
C. Multi-Sine Amplitude at Micro- and Multibarrel Electrodes	163
D. Dynamic Impedance Spectra in the Adsorption Region	165
E. Effect of the Rotation Speed on the Dynamic Impedance Response	167
References	169
Publications	181

Nomenclature

Latin notation

A	surface area of a disk electrode
A	amplitude of the fundamental harmonics in the multi-sine signal
a	activity
bw	bandwidth of the quadrature filter function
bw_{dc}	bandwidth of quasi-triangular wave
C	capacitance
c	concentration
c_{ox}	concentration of oxidized species
c_{red}	concentration of reduced species
D	diffusion coefficient
d	distance between fundamental frequencies in the multi-sine signal
d_i	inner Helmholtz plane
d_o	outer Helmholtz plane
E	potential of an electrode versus a reference
E_{eq}	equilibrium potential
F	Faraday constant
f_b	base frequency of the multi-sine signal
f_c	characteristic frequency
f_{dc}	fundamental frequency of the quasi-triangular wave
f_{osc}	fundamental frequency of the natural oscillation
f_{sa}	sampling frequency
g	quadrature filter function
H	complex transfer function
h	response to the Dirac delta function
I	Fourier transform of the current
i	current
Δi	amplitude of current response in static conditions
I_{abs}	absolute current signal in Fourier space
i_{ac}	ac current contribution
Δi_{ac}	amplitude of current signal in dynamic conditions
i_{dc}	dc current contribution
i_{dl}	charging current
i_F	faradaic current
i_l	limiting current
i_p	peak current
i_{ss}	steady-state current
i_0	exchange current
J	flux of species
j	current density
j	imaginary number
L	inductance

n	phase angle of constant phase element
Q	constant phase element
q	electric charge
R	resistance
R	ideal gas constant
r	disk electrode radius
T	total duration of the experiment
T	absolute temperature
t	time
t	transport number
U	Fourier transform of the voltage
u	voltage
Δu	amplitude of single-frequency potential perturbation
u	mobility
U_{abs}	absolute voltage signal in Fourier space
u_{ac}	<i>ac</i> voltage contribution
Δu_{ac}	amplitude of the multi-sine signal
u_{dc}	<i>dc</i> voltage contribution
Δu_{dc}	amplitude of the quasi-triangular wave
W	weight factor in dynamic conditions
w	weight factor in static conditions
w	window function
Y	complex admittance
Z	complex impedance
z	charge number
\overline{Z}	complex conjugate of Z
Z_{Im}	imaginary impedance component
Z_{Re}	real impedance component
Z_W	Warburg impedance

Greek notation

α	symmetry coefficient
Δ	time interval
δ	diffusion layer thickness
δ	Dirac delta function
δ_{Δ}	unit impulse function
ε_0	vacuum permittivity
η	overpotential
κ	ionic conductivity
κ	dielectric constant
λ_i	ion molar conductivity
λ°	molar conductivity
μ	chemical potential
$\tilde{\mu}$	electrochemical potential
ν	scan rate
σ	Warburg coefficient
σ	standard deviation
τ	time constant
Φ	electric potential
ϕ	phase angle
φ	electrochemical phase
χ^2	sum of squares in regression analysis
ω	angular frequency

Abbreviations

<i>ac</i>	alternating current
AFM	atomic force microscopy
CE	counter electrode
CNLS	complex nonlinear least-squares
CPE	constant phase element
CV	cyclic voltammogram
<i>dc</i>	direct current
DFT	discrete Fourier transform
DMFA	dynamic multi-frequency analysis
EEC	electrical equivalent circuit
EIS	electrochemical impedance spectroscopy
FFT	fast Fourier transform
FT	Fourier transform
HER	hydrogen evolution reaction
HOR	hydrogen oxidation reaction
ID	inner diameter
iFT	inverse Fourier transform
IHP	inner Helmholtz plane
LTI	linear time-invariant
NLS	nonlinear least-squares
OD	outer diameter
OHP	outer Helmholtz plane
OPD	over-potential deposition
p.a.	pro analysi
PDEIS	potentiodynamic electrochemical impedance spectroscopy
PMMA	polymethylmethacrylate
pwt	proportional weighting
RDE	rotating disk electrode
RE	reference electrode
RHE	reversible hydrogen electrode
RT	room temperature
SHE	standard hydrogen electrode
STFT	short time Fourier transform
TEM	transmission electron microscopy
UPD	under-potential deposition
uwt	unity weighting
WE	working electrode

1. Dynamic Impedance Spectroscopy

Electrochemical techniques aim to provide an accurate kinetic and mechanistic characterization of electrode processes. Cyclic voltammetry and electrochemical impedance spectroscopy (EIS) are the most popular methods for the investigation of electrochemical systems, as they yield valuable insights into the thermodynamic and kinetic properties that govern the overall reaction sequence. The instrumentation and software needed to perform cyclic voltammetry and EIS are implemented in any commercially available potentiostat. Cyclic voltammetry enables the study of electron transfer reactions across electrified interfaces by recording the current response of a working electrode (WE) to a triangular potential perturbation. In contrast, EIS imposes a small-amplitude sinusoidal potential perturbation on the system by successively changing the frequency of the sinusoidal wave, where the impedance is given by the complex ratio of the Fourier transform (FT) of the potential and the FT of the current response. EIS represents a powerful method, as it can be applied for the examination of a variety of electrode processes, including charge transfer and accumulation at the electrified interface, transport phenomena as well as adsorption and intercalation reactions (Chan et al., 2015). A detailed understanding of reaction mechanisms, however, requires the investigation of a system over a wide potential and frequency range in order to capture all time constants related to the different underlying processes (Sacci and Harrington, 2014). Figure 1.1 gives an overview of the most common electrode processes and the time-scales at which they occur.

In direct current (*dc*) voltammetry the frequency dependent information can be obtained from variations in scan rate of the cyclic voltammogram (CV). While the faradaic current has a square root dependence on the applied scan rate, the charging current increases proportionally to it, thus, the signal-to-noise ratio substantially decreases at very high scan rates (Guo, 2015). Moreover, for an accurate description of the reaction kinetics by means of cyclic voltammetry, the system needs to be in an identical state over the whole series of individual measurements (Bond and coworkers, 1977). In the case of EIS stability, linearity, and causality of the system under investigation are required (Darowicki, 2003). Although a common characteristic of electrochemical systems is their nonlinear behavior, quasi-linear conditions may be attained by using small-amplitude perturbation signals (Orazem, 2017). Most electrochemical systems are substantially unstable, such that the state of the electrode undergoes irreversible changes throughout the experiment (Stoynov, 1993). Under these conditions, the concept of EIS in its usual interpretation fails. The restriction of EIS to stationary systems can be attributed to the difficulty of collecting multi-dimensional impedance data arrays (Ragoisha, 2004). The

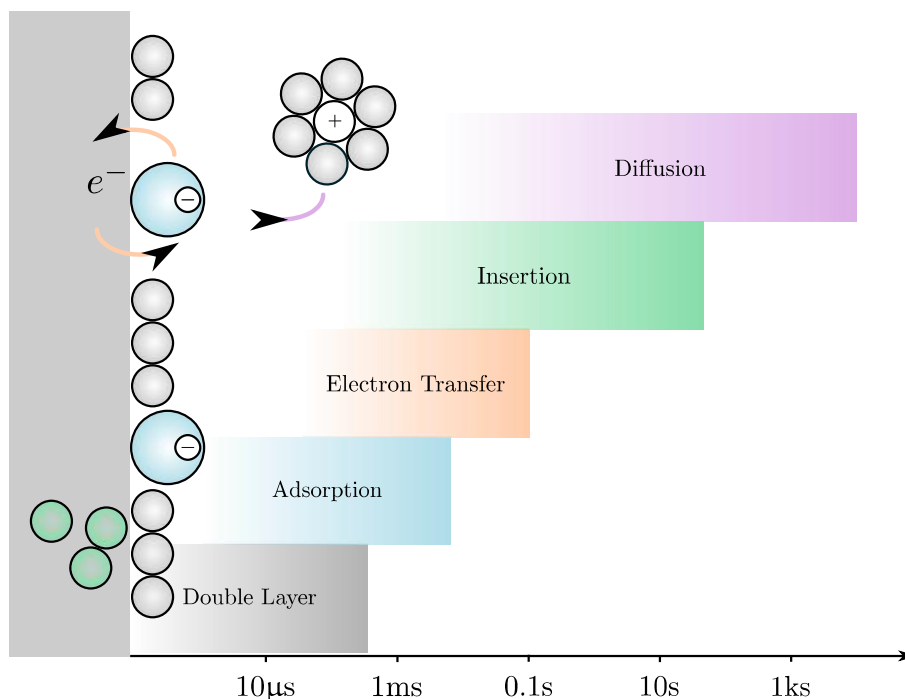


Figure 1.1.: Time scales of different electrode processes.

impedance, however, is physically meaningful in both stationary and nonstationary conditions (Ragoisha, 2005). To enable the investigation of time-varying phenomena, the major objective lies in the acquisition of dynamic impedance spectra.

The concept of alternating current (*ac*) voltammetry was developed to overcome the restrictions associated with *dc* voltammetry and EIS. This method is based on the acquisition of a set of CVs superimposed by a single-frequency sinusoidal perturbation, where the frequency of the small-amplitude *ac* signal is changed from one voltammogram to the next, while the scan rate is kept constant. Harrington (1993) discussed how to reconstruct dynamic impedance spectra from a series of *ac* voltammograms. Although *ac* voltammetry enables the examination of an electrochemical system in its dynamic state and does not require static conditions, the behavior of the system must be reproducible over the whole set of recorded cycles, a restriction that can hardly be satisfied when using solid electrodes. However, the concept of *ac* voltammetry is not restricted to single-frequency perturbations but allows for the application of multi-sine waves. This property has laid the foundation for the development of nonstationary impedance techniques, where the first attempt of measuring dynamic impedance spectra goes back to Bond and coworkers (1977), who performed data acquisition by a fast Fourier transform (FFT) approach.

Since the early 1970s, admittance measurements were carried out by applying Laplace and Fourier transforms to calculate the frequency domain equivalent of the system's current response to an *ac* potential perturbation from time domain signals. Smith and coworkers (1976) developed powerful instrumentation, data acquisition and processing strategies based on a digital FFT approach that allowed for the measurement of impedance spectra at constant potentials

with high speed and accuracy. Creason and Smith (1972) demonstrated that the application of random and pseudo-random white noise as perturbation waveforms yielded reliable impedance spectra when converting the rapidly changing time domain data arrays into the frequency domain by means of FFT. Although pseudo-random white noise provided better impedance results than the broadband random white-noise signal, it was found that the nonlinear contributions of the conventional pseudo-white noise lead to distortions in the impedance spectra (Creason et al., 1972). In order to minimize the effects of nonlinearity, a modified perturbation signal with a randomized phase distribution was created, composed of a set of odd harmonics of the pseudo-white noise signal's fundamental harmonic. In doing so, it was possible to record high quality impedance spectra at a particular *dc* potential. In later studies, Creason and coworkers (1973) investigated the effect of different perturbation signals on the efficiency of impedance measurements on the chromicyanide system at dropping mercury electrodes. The measurements were performed using complex periodic signals, almost periodic signals, aperiodic transients, and bandwidth limited white noise. The studies revealed that a complex periodic waveform being composed of odd harmonics of a fundamental frequency yields the best impedance results.

While the FFT approaches discussed above were restricted to measurements at constant *dc* potentials, the pioneering work of Bond and coworkers (1977) dealt with the superposition of a triangular potential sweep with a multi-sinusoidal signal. The time domain potential and current data arrays were divided into smaller fractions by applying a rectangular window function, where each segment was transformed into Fourier space by means of FFT to calculate the impedance at different potentials of the triangular scan. This method allowed for the extraction of both *dc* and *ac* responses in a single measurement. In doing so, the state of the electrode did not change throughout the acquisition of impedance data at different frequencies. In order to reach high-frequency perturbations, short data sampling times had to be applied. Therefore, the measurements required demanding software and hardware development in order to handle the large data sets and to accomplish the mathematical transformations. According to Ragoisha (2005), the low intensity of the multi-sine input combined with the temporal variation of the system's properties lead to a non-uniformity in the system's output, where the poor resolution of the frequency spectra resulted in erroneous impedance data. The higher the degree of nonlinearity of the system and the lower the frequency under investigation the more dominant unwanted interferences became. Therefore, Stoynov (1985) presented a numerical four-dimensional FT algorithm to correct the error related to the time-delay associated with nonstationary systems. Although the concept of nonstationary impedance spectroscopy offered some unique features, the need of expensive instrumentation made further development of this technique unfeasible at that time. However, with the development of computer technology and the availability of highly efficient FT algorithms, significant progress was made in this field. The vast majority of research contributions that deals with the concept of dynamic impedance spectroscopy is concerned with the acquisition of a set of single impedance spectra collected at different points within a certain potential range. In this case, the small-amplitude perturbation frequencies are imposed either

successively or simultaneously. This method provides a means for the investigation of the electrode reaction at different times and at different stages, however, the different measurements are not connected. Popkirov (1996) used a two-cell set-up to perform in-situ impedance measurements during current relaxation processes after a potential step experiment by applying a small-amplitude multi-sine perturbation to one of the cells. In doing so, the impedance spectra were recorded successively at different times after the potential step. The measurement set-up allowed for the subtraction of the current contributions related to the relaxation process when two identical cells were used that were held at the same conditions before and throughout the measurement. Although this method allowed for the correction of nonlinear distortions, it required perfect synchronization of both cells at any time. Another approach was presented by Ragoisha (2004), who introduced the concept of potentiodynamic electrochemical impedance spectroscopy (PDEIS). Here, each potential step of a staircase potential ramp was perturbed by a set of consecutively applied single frequencies. This method allowed for the real-time analysis of the current response signal, however, the system was subject to the same restrictions as in classic EIS. Twenty years after Bond and coworkers (1977) had published their pioneering work on dynamic impedance spectroscopy, Hazi (1997) designed an FT microcomputer-based set-up for the acquisition of nonstationary impedance spectra, where a *dc* potential step function was superimposed by a multi-sinusoidal waveform. FT measurements enabled the calculation of impedance data over the full range of frequencies and potentials. This approach allowed for the measurement of dynamic impedance spectra with the same efficiency as reported by Bond, and at the same time, the FT instrumentation was optimized with respect to cost and size.

Darowicki (2000) developed a similar method based on coupling of pseudo-white noise and short time Fourier transform (STFT) that enabled instantaneous acquisition of dynamic impedance spectra while linearly changing electrode potential. The time-dependent current response was decomposed by applying a Gaussian window. The fraction of the signal that was cut out by the window function was then transformed into Fourier space. In the same way, the perturbation signal was decomposed into a package of elementary voltage signals, where the impedance was extracted from the ratio of the elementary voltage and current signals. In doing so, it was possible to recover a time-dependent series of impedance spectra. The validity of the concept was verified by investigations of a simulated nonstationary model electric-system and has later been applied for the study of stress corrosion cracking behavior of stainless steel (Darowicki, 2003). Sacci and Harrington (2014) discussed a similar approach. In this case, the accuracy of FT was increased by subtracting the *dc* potential before carrying out the transformation of the voltage signal. Due to the fact that it was impossible to deduce the current response without the *ac* contribution, the above described strategy could not be applied for the current signal. Therefore, a base-line correction method was introduced that highly increased the accuracy of the FT. Moreover, it was pointed out how to determine the lowest valid frequency at a given sweep rate, which was found to be a function of rate constants.

Recently, Battistel (2016) introduced a new approach for measuring dynamic impedance spectra by means of dynamic multi-frequency analysis (DMFA), which was applied to simulated systems. The concept of DMFA is based on the superposition of a quasi-triangular waveform and a multi-sine signal, where a quadrature filter function of finite bandwidth is applied to extract the temporal variation of the current response signals in Fourier space. The below Figure 1.2 shows a schematic representation of the principle of DMFA. Although data processing is performed in the Fourier domain, the time-dependence of the system can be recovered using inverse Fourier transform (iFT).

In contrast to the FFT-EIS technique developed by Bond and coworkers (1977), which is limited by the poor bandwidth of the window function, DMFA allows for the recovery of low-frequency impedance data with high precision (Battistel and La Mantia, 2019). This technique gives access to dynamic impedance spectra covering a wide range of frequencies and potentials in a single measurement. As stated by Battistel (2016), DMFA offers the possibility of data fitting by means of conventional electrical equivalent circuits (EECs). Due to its dynamic nature, DMFA gives insight into the temporal development of kinetic parameters, which is a prerequisite for a detailed understanding and the optimization of electrode processes. Despite the unique features that are offered by this technique, it has to be noted that the quality of the dynamic impedance spectra is significantly affected by the experimental settings, which are strongly dependent on the type of system under investigation.

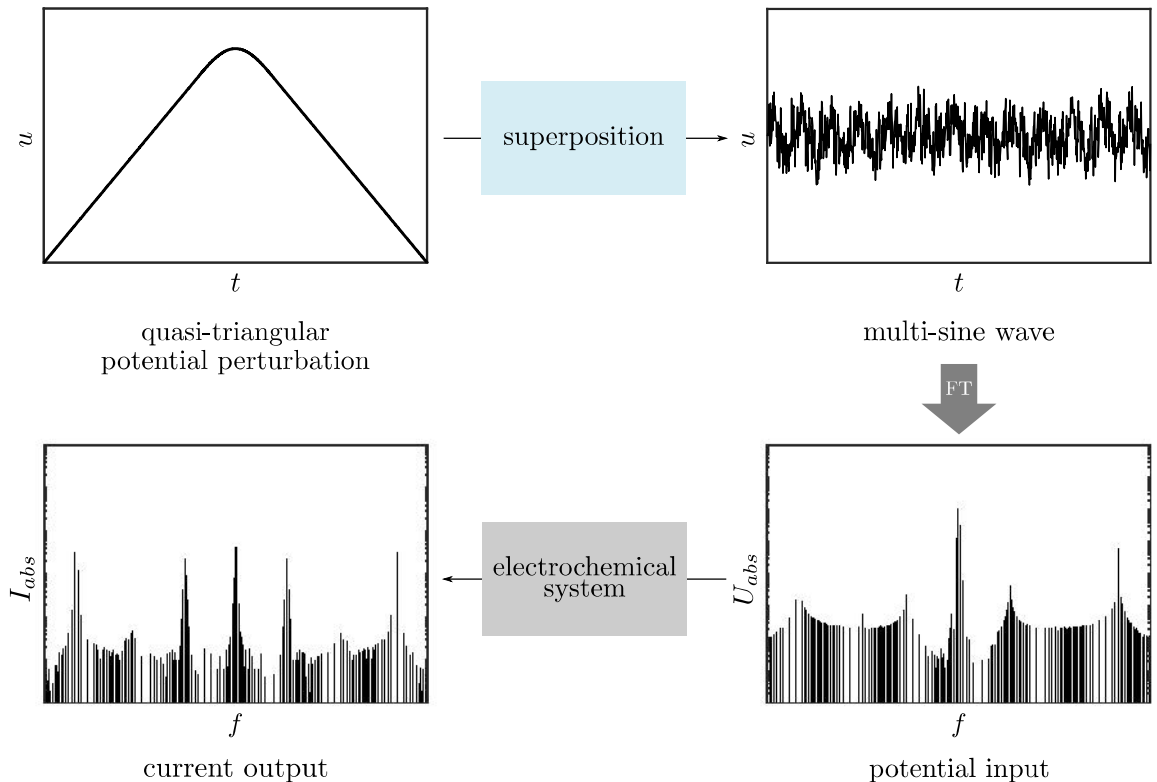


Figure 1.2.: Schematic representation of the concept of DMFA.

The present work aims to demonstrate that DMFA can be employed for the investigation of nonstationary electrochemical processes, exhibiting either forced or natural reaction dynamics. The major objective lies in the acquisition of reliable dynamic impedance spectra in real-world conditions, which can be analyzed by means of suitable EECs that allow for a physical interpretation of the data. It is desired to observe the temporal evolution of the kinetic variables governing the reaction under investigation in order to obtain a concatenated picture of the overall process. The aim is to gain new insight into the reaction dynamics of two fundamentally different processes, namely the cathodic hydrogen evolution reaction (HER) and the anodic electrodisolution of p-type silicon. Below, the outline of this thesis is given.

The starting point is the development of the theoretical framework of DMFA, addressed in Chapter 2. Based on the linear time-invariant (LTI) systems theory, the complex impedance expression is derived in terms of a transfer function. Subsequently, a dynamic impedance expression is defined, which provides the foundation of the experimental results presented and discussed in Chapters 3 to 5.

The successive Chapter 3 is concerned with the principles of data recording and analysis by means of DMFA. First, the perturbation signals employed in DMFA are introduced. Next, the method is applied to a simple redox process in order to demonstrate the feasibility of reliable dynamic impedance spectra acquisition. In particular, it is investigated how to determine the bandwidth of the quadrature filter to obtain accurate dynamic impedance spectra. Moreover, the impact of the multi-sine amplitude on the linearity of the system is studied. After that, an outline of how to analyze experimental data using EECs is provided.

In the subsequent Chapter 4 DMFA is employed to examine the reaction kinetics of different stages of the HER at polycrystalline Pt electrodes. The first part of the Chapter gives a comprehensive introduction into the topic. In the second part, dynamic impedance studies are presented. Here, the system is subjected to forced dynamic conditions in order to avoid bubble nucleation on the electrode surface. This allows for the investigation of the physical processes governing the HER in a potential range, which cannot be accessed using conventional EIS.

The following Chapter 5 deals with the investigation of self-sustained current oscillations observed during the anodic electrodisolution of p-type silicon in fluoride containing electrolytes. First, fundamental concepts of the theory of nonlinear dynamics are introduced. Using DMFA, the reaction is studied in dynamic equilibrium conditions. Subsequently, the system is investigated in the oscillatory regime. In the presence of a serial resistance different types of current oscillations emerge, which are analyzed by means of DMFA in order to develop a framework for identifying the origin of the oscillatory instabilities causing these phenomena.

Next, Chapter 6 provides concluding remarks and gives an outlook for future examinations. The experimental procedures employed in this work are presented in the final Chapter 7.

2. Theoretical Background

This Chapter provides a number of concepts and theories based on which the framework of DMFA is developed. Section 2.1 introduces the fundamentals of electrochemistry in as much detail as needed to follow the discussions in subsequent Chapters of this thesis. Section 2.2 deals with the theory of LTI systems that allows for the derivation of the complex impedance expression in terms of a transfer function, which is addressed in Section 2.3. Later on, the concept of DMFA is outlined in Section 2.4, which builds the foundation of the dynamic impedance studies presented in this work.

2.1. Fundamentals of Electrochemistry

Kinetic studies on electrochemical systems focus on the investigation of interfacial charge transfer dynamics. This Section introduces the double layer theory that is commonly employed to describe the electric field across the electrode/electrolyte interface. The structure of the double layer influences the kinetics of faradaic charge transfer reactions, where the overpotential is the driving force of the electrode reaction.

2.1.1. Electrochemical Systems

Electrochemistry is concerned with charge transfer reactions that occur across the boundary between an electronic and an ionic conductor (Bockris, 1998). In electrochemical systems electrodes are referred to as electronic conductors, e.g. metals, alloys, or semiconductors that enable passage of electrons, whereas electrolytes are to be understood as ionic conductors, in which ions are the mobile species (Newman, 2004). Although one is most often interested in the reaction occurring at one isolated boundary, single interfaces cannot be experimentally investigated. Thus, the most general electrochemical cell must be composed of at least three different phases, namely two electrodes separated by an electrolyte, which are connected via an external circuit (Newman, 2004). The electrode at which the half-reaction of interest takes place is termed WE, while the second electrode refers to as counter electrode (CE). Whenever two or more phases are in contact, there is an exchange in species that can be transported between them until equilibrium conditions are attained (Newman, 2004). The below Figure 2.1 shows the Galvani representation of the above described electrochemical cell, where the phases

β and β' refer to the two electrodes, and phase ε corresponds to the electrolytic solution. α and α' represent the metal wires that connect the electrodes to the external circuit. The phase boundaries between the different phases are indicated by vertical lines. The cell is said to be in equilibrium if a certain thermodynamic property of each phase is in equilibrium with that of its neighbouring phases, thus being referred to as e.g. thermal or mechanical equilibrium. In order to attain a chemical equilibrium, the chemical potential μ of those species that are present in both adjacent phases must be identical (Orazem, 2017), such that

$$\mu_i^\varphi = \mu_i^{\varphi'},$$

with

$$\mu_i^\varphi = \mu_{i,0}^\varphi RT \ln a_i,$$

where μ_i^φ is the chemical potential of species i in phase φ , $\mu_{i,0}^\varphi$ corresponds to its chemical potential in standard conditions, R is the universal gas constant, T is the absolute temperature, and a_i is the activity of the species. While neutral species are characterized by their chemical potential, charged species must be described in terms of their electrochemical potential, which is defined as

$$\tilde{\mu}_i^\varphi = \mu_i^\varphi + z_i F \phi_i^\varphi, \quad (2.1)$$

where z_i is the charge number of the ion, F is the Faraday constant, and ϕ_i^φ is the electric potential of species i in phase φ . The first term on the right-hand side of (2.1) represents the chemical state of the species, while the second term refers to its electric state. Both quantities the chemical and the electrochemical potential are affected by temperature, pressure, and composition of the electrolyte, with the electrochemical potential also being influenced by electric field forces (Newman, 2004).

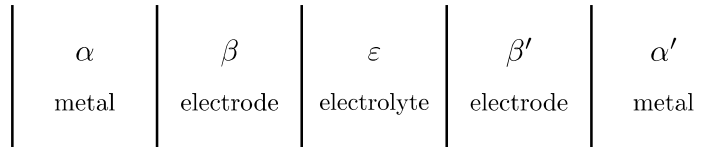


Figure 2.1.: Galvani representation of an electrochemical cell composed of two electrodes separated by an electrolyte solution.

2.1.2. The Electric Double Layer

When a solid electrode is in contact with an electrolyte solution, the accumulation of charged particles on either side of the interface causes the generation of an electric field across the phase

boundary. When there is no charge on the electrode itself, this behavior is due to the tendency of certain species in solution to locate in the vicinity of the solid electrode (Newman, 2004). In addition to that, an electric field across the electrode/electrolyte interface forms when the electrode is charged. The charge on the WE can be varied by an external power supply that is included into the circuit. As a two electrode set-up does not enable the measurement of the potential of a single electrode, the use of a reference electrode (RE) becomes necessary to control the potential of the WE. The RE needs to fulfil the properties of having a known potential and approaching ideal nonpolarizability (Bard, 2001). Under these conditions, it is possible to precisely monitor the potential difference between the WE and the RE while current is passing between the WE and the CE. When the potential of the WE deviates from its equilibrium potential, the excess charge on the electrode that is located in a thin layer at the interfacial region causes the attraction of ions on the solution side of the interface. This results in the flow of a charging current, which is defined as

$$i_{dl} = \frac{dq}{dt} = C_{dl} \frac{du}{dt}, \quad \text{with} \quad C_{dl} = \frac{dq}{du},$$

where C_{dl} is the double layer capacitance, q corresponds to the electric charge, u is the applied voltage, and t is time. Due to their dipole character, neutral water molecules tend to orient themselves at the phase boundary and participate in the formation of the so-called electric double layer, which is schematically represented in Figure (2.2). At the solution side of the interface the location d_i of the electric centers of specifically adsorbed ions and solvent molecules forms the inner Helmholtz plane (IHP). Solvated ions can only approach the electrode surface to a certain distance d_o . The positions of the centers of these ions constitute the outer Helmholtz plane (OHP) (Bard, 2001). The region next to the OHP is called the diffuse layer. Due to the in-

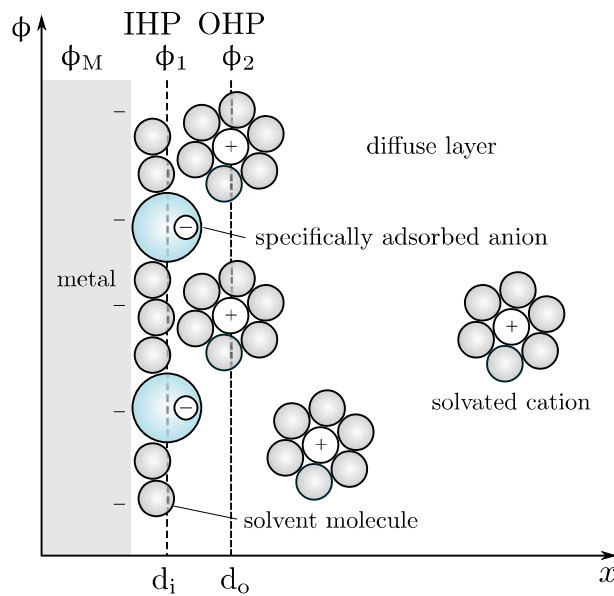


Figure 2.2.: Schematic representation of the electric double layer, adapted from Bard (2001).

fluence of the electric field, solvated ions and solvent molecules in the diffuse layer are partially oriented. In contrast, the bulk solution is not affected by electric field forces. According to the principle of electroneutrality, the charge of the particles in solution must be equal in value and opposite in sign with respect to that on the metal side, as described by

$$q_M + q_1 + q_2 = 0,$$

where q_M is the charge of the metal, q_1 refers to the charge within the area between the electrode surface and d_o , and q_2 is the charge of the diffuse layer, including the OHP.

2.1.3. Heterogeneous Charge Transfer Reactions

In the presence of electroactive species the overpotential η acts as the driving force for electrochemical reactions to take place and determines the amount of current that is flowing through the cell. It represents the deviation of the working electrode's potential E from its equilibrium value E_{eq} , such that

$$\eta = E - E_{eq}.$$

The resulting current flow that is composed of a faradaic and a nonfaradaic current contribution is defined as

$$i = i_{dl} + i_F,$$

where i_{dl} is related to the current that flows due to double layer charging and i_F can be attributed to the current flow due to the charge transfer reaction. η is usually comprised of a sum of overpotentials related to different phenomena. In total, there are four types of overpotentials that may contribute to η , such that

$$\eta = \eta_s + \eta_{ct} + \eta_{mt} + \eta_x,$$

where η_s is attributed to the overpotential due to the ohmic drop in the electrolyte, η_{ct} represents the overpotential related to the transfer of charged species across the interface, and η_{mt} can be interpreted as the activation energy barrier that must be surmounted in order to drive mass transport of reactive species to the electrode surface. The term η_x may be used to describe different specific phenomena, e.g. chemical reactions, adsorption and desorption processes, or electrodeposition reactions (La Mantia, 2009). The mechanism of a charge transfer reaction may be described in terms of the Butler-Volmer equation, which is based on the activated complex theory and provides a relation between the faradaic current and the charge transfer

overpotential

$$i_F = i_0 \left[\exp\left(\frac{\alpha n}{RT} \eta_{ct}\right) - \exp\left(\frac{-(1-\alpha)n}{RT} \eta_{ct}\right) \right],$$

where i_0 is the exchange current, α denotes the symmetry coefficient, and n is the number of electrons involved in the reaction. Due to the fact that the Butler-Volmer relation omits any variations in concentration of the electroactive species, the current-overpotential equation is frequently used. The latter specifically considers changes in concentration, such that

$$i_F = i_0 \left[\frac{c_{red}(x=0)}{c_{red}(x=\infty)} \exp\left(\frac{\alpha n}{RT} \eta\right) - \frac{c_{ox}(x=0)}{c_{ox}(x=\infty)} \exp\left(\frac{-(1-\alpha)n}{RT} \eta\right) \right].$$

Here, $c_{red}(x=0)$ and $c_{ox}(x=0)$ are the concentrations of the reduced and oxidized species at the electrode surface, respectively. $c_{red}(x=\infty)$ and $c_{ox}(x=\infty)$ correspond to their bulk concentrations. In this case, η includes a mass-transfer contribution and is thus composed of η_{ct} and η_{mt} . The exchange current is directly proportional to the standard rate constant k^0 , which may be understood as a measure of the kinetic facility of a redox couple, where the parameters are linked through the relationship (Bard, 2001)

$$i_0 = F A k^0 c_{ox}(x=\infty)^{1-\alpha} c_{red}(x=\infty)^\alpha,$$

with A being the surface area of the electrode.

A faradaic reaction can be described in terms of a series of resistances related to the different overpotentials. Ohm's law describes the linear current/potential relationship across an ideal resistor

$$u(t) = R i(t). \quad (2.2)$$

Here, R refers to the resistance, which is the fundamental property of a resistor. The structure of the double layer significantly affects the charge transfer kinetics of a faradaic reaction, as it behaves like a capacitor that is in parallel with the electrode reactions. Therefore, the current that flows between the WE and the CE can either contribute to the charge transfer reaction or participate in the charging of the double-layer (Newman, 2004).

2.2. Convolution and Transfer Functions in Linear Systems Theory

The fundamental task in electrochemistry is the characterization of a system with unknown properties. Commonly, this task is accomplished by investigating the system's response to a certain perturbation signal. EIS has widely been applied for the identification of mechanisms

of electrochemical reactions, where the desired information is commonly extracted from a system's response to a small-amplitude sinusoidal potential perturbation. While EIS is exclusively restricted to the investigation of stationary systems, this thesis aims to provide an accurate and detailed characterization of the reaction kinetics of electrochemical systems in nonstationary conditions. The fundamental question is how to relate the input and output signals in order to obtain valuable information on the reaction kinetics. Although heterogeneous charge transfer reactions across electrified interfaces are highly nonlinear, here, the linear systems theory is introduced, as it builds the foundation of EIS and plays a vital role for the development of the concept of DMFA. These methods make use of the fact that almost any electrochemical system behaves linearly within a certain potential window or when subject to other specific restrictions. The power of these techniques arises from the fact that linear systems exhibit some unique properties that make them particularly amenable to analysis. This Chapter provides the essential mathematical tools needed to analyze LTI systems, also of particular importance for the analysis of dynamic impedance spectra. The theories developed in this Section are restricted to time-invariant systems, i.e. to systems that give the same response to a specific input signal at any time, where a time delay in the time dependent input causes the same time shift in the time dependent system's response.

As stated by Oppenheim and Willsky (1983), linear systems obey the superposition principle, which is based on the properties of additivity and scaling, given by

$$\begin{aligned} x_1(t) + x_2(t) &\longrightarrow y_1(t) + y_2(t) && \text{and} \\ ax_1(t) &\longrightarrow ay_1(t), \end{aligned}$$

with a being a complex constant. The combination of both properties yields the following statement

$$ax_1(t) + bx_2(t) \longrightarrow ay_1(t) + by_2(t),$$

where a and b are complex constants. The superposition principle states that the response of a system to a linear combination of weighted signals may be expressed as the weighted sum of the responses to each signal.

One of the most remarkable characteristics of LTI systems is that any kind of input signal can be represented as a set of shifted impulse signals. In this case, the system's response can be derived from linear combinations of responses obtained from these basic signals. This property allows for the analysis of LTI systems by means of convolution integrals. Convolution integrals can be expressed in terms of unit impulse and unit step functions, which present basic signals from which other signals can be constructed. In what follows, the convolution integral is derived according to the approach reported by Hardt (2004).

The Dirac delta (impulse) function is of fundamental importance for the analysis of LTI systems and can be defined as

$$\delta(t) = \begin{cases} 0 & t \neq 0 \\ \text{undefined} & t = 0 \end{cases},$$

where the area under the function must be equal to unity, such that

$$\int_{-\infty}^{\infty} \delta(t) dt = 1.$$

With the above definitions, the impulse function can be understood as a short pulse at $t = 0$ that has infinite height. Under the assumption that the impulse signal does not occur instantaneously but evolves over a certain time interval Δ , the unit impulse function $\delta_{\Delta}(t)$ is defined as

$$\delta_{\Delta}(t) = \begin{cases} \frac{1}{\Delta} & \text{if } 0 < t \leq \Delta \\ 0 & \text{otherwise.} \end{cases}$$

The unit impulse function is graphically represented in Figure 2.3. In the limit $\Delta \rightarrow 0$, i.e. if the duration of the pulse becomes infinitesimally small $\delta_{\Delta}(t) = \delta(t)$. Under these conditions, the area of the unit impulse is located at $t = 0$. A continuous arbitrary function $f(t)$ may be approximated by a staircase function composed of a series of piecewise constant fragments of duration Δ , according to

$$f_{\Delta}(t) = f(n\Delta) \quad \text{for} \quad n\Delta \leq t < (n+1)\Delta,$$

where $f_{\Delta}(t) = f(t)$ when $\Delta \rightarrow 0$. $f_{\Delta}(t)$ can be represented as a sum of scaled pulses of fixed

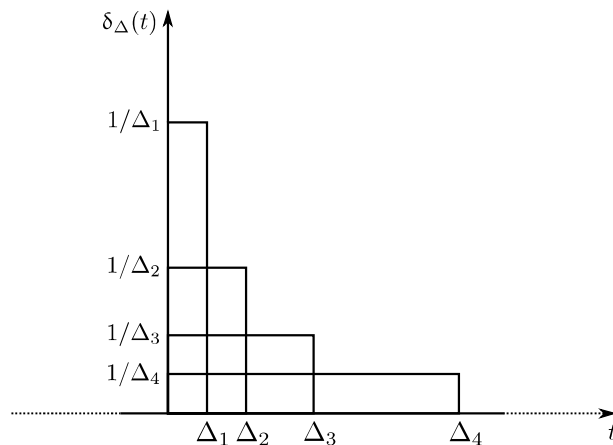


Figure 2.3.: Graphical representation of the unit impulse function, adapted from Hardt (2004).

duration Δ and varying amplitudes $f(n\Delta)$, such that

$$f_{\Delta}(t) = \sum_{n=-\infty}^{\infty} p_n(t),$$

with

$$p_n(t) = \begin{cases} f(n\Delta) & \text{if } n\Delta \leq t < (n+1)\Delta \\ 0 & \text{otherwise.} \end{cases}$$

Each pulse $p_n(t)$ can be expressed as a function of shifted unit impulses, according to

$$p_n(t) = f(n\Delta)\delta_{\Delta}(t - n\Delta)\Delta.$$

The short time delay can be attributed to the limited resolution of the measuring apparatus (Riley, 2004). The staircase function $f_{\Delta}(t)$ can thus be rewritten as

$$f_{\Delta}(t) = \sum_{n=-\infty}^{\infty} f(n\Delta)\delta_{\Delta}(t - n\Delta)\Delta.$$

Following the concept of linearity, the response $y_n(t)$ of an LTI system to $f_{\Delta}(t)$ can be deduced by superposition of the weighted and shifted responses $h_{\Delta}(k)$ to each of the scaled and shifted unit impulses $\delta_{\Delta}(t)$, which can be expressed as

$$y_{\Delta}(t) = \sum_{n=-\infty}^{\infty} f(n\Delta)h_{\Delta}(t - n\Delta)\Delta.$$

Under the assumption that each pulse is located in one point ($\Delta \rightarrow 0$) and when changing the variables according to $n\Delta = \tau$ and $\Delta = d\tau$, the response of an LTI system to an arbitrary function may be approximated by the integral of impulse responses, such that

$$y(t) = \int_{-\infty}^{\infty} f(\tau)h(t - \tau) d\tau, \quad (2.3)$$

where $h(t)$ is the response to the Dirac delta function. Equation (2.3) is frequently represented as

$$y(t) = f(t) * h(t).$$

The sign $(*)$ indicates convolution. According to the convolution theorem, which is defined as follows

$$Y(\omega) = \text{FT}[f(t) * h(t)](\omega) = F(\omega) H(\omega), \quad (2.4)$$

convolution integrals may be expressed as simple algebraic equations in Fourier space. In this case, FT denotes Fourier transform and $H(\omega)$ represents a complex transfer function (Stone and Goldbart, 2009).

2.3. Electrochemical Impedance Spectroscopy

EIS is based on the LTI systems theory and aims to extract information from a system's response to a sinusoidal input perturbation, where the condition of linearity is satisfied by keeping the amplitude of the *ac* signal sufficiently low. The term impedance was first defined by Heaviside, who laid the mathematical foundation of EIS by introducing the concept of operational calculus in the late 19th century (Macdonald, 2006). The work of Heaviside was concerned with the development of transmission line models for a transatlantic cable, however, the theory of transfer functions is valid for a large variety of different systems (Orazem, 2017). Nernst (1894) was the first to perform impedance measurements on electrochemical systems, where the electrical bridge developed by Wheatstone (1843) built the experimental apparatus for the determination of the dielectric constants of different electrolytes. One of the milestones in the history of EIS was the development of an impedance expression for diffusional fluxes of electroactive species by Warburg (1899). Nowadays, EIS is the guiding technique for the identification of mechanisms of electrochemical reactions and corrosion processes, as it provides a vast amount of information on the properties of electrochemical interfaces and on transport phenomena (Macdonald, 2006), (Bandarenka, 2013).

2.3.1. Complex Impedance as a Transfer Function

As outlined in Section 2.2, the response of an LTI system to an input signal can be readily computed according to the principle of superposition. In this case, the relationship between input and output signals is expressed in terms of convolution integrals. According to (2.4), the operation of convolution in the time domain corresponds to ordinary multiplication in Fourier space. This property provides a means for the representation of complex integro-differential equations as simple algebraic equations when converting the signals from the time domain into the frequency domain by applying FT. Under these conditions, the complex impedance expression can be derived in terms of a transfer function.

The current response of a linear system is linked to the voltage input signal through a convolution integral, such that

$$i(t) = \int_{-\infty}^{\infty} u(\tau) h(t - \tau) d\tau. \quad (2.5)$$

Transformation of the time signal into Fourier space yields an expression of the form

$$I(\omega) = U(\omega) Y(\omega).$$

Here, $I(\omega)$ and $U(\omega)$ represent the FTs of the current and voltage, respectively, and the transfer function $Y(\omega)$ refers to the complex admittance. Instead, when measuring the voltage response to a current perturbation, the transfer function becomes an impedance $Z(\omega)$. Impedance and admittance are inversely related, according to $Z(\omega) = \frac{1}{Y(\omega)}$. Although the vast majority of experiments corresponds to admittance measurements, in most cases only the impedance is considered (Orazem, 2017). The stationary impedance expression is defined as

$$Z(\omega) = \frac{\text{FT}[u(t)](\omega)}{\text{FT}[i(t)](\omega)} = \frac{U(\omega)}{I(\omega)}. \quad (2.6)$$

When a linear electrochemical system is subjected to a small-amplitude *ac* perturbation of the form

$$u(t) = u_{dc} + |\Delta u| \sin(\omega t + \phi_u), \quad (2.7)$$

where u_{dc} is the time-invariant potential contribution, $|\Delta u|$ represents the amplitude of the *ac* component, and ϕ_u is the phase angle of the function, the current response is also purely sinusoidal and oscillates at the same frequency as the input signal but is scaled in magnitude and shifted in phase, such that

$$i(t) = i_{dc} + |\Delta i| \sin(\omega t + \phi_i). \quad (2.8)$$

Here, i_{dc} denotes the steady-state current signal, $|\Delta i|$ is the amplitude of the current response, and ϕ_i is the phase angle of the current oscillation. In order to derive the impedance expression related to the current response to a small sinusoidal potential perturbation, equations (2.7) and (2.8) must be translated into the Fourier domain by means of FT. According to Chan et al. (2015), FT of a function $x(t)$ is given by

$$\text{FT}[x(t)](\omega) = \int_0^T x(t) e^{-j\omega t} dt. \quad (2.9)$$

Relation (2.9) is commonly defined in the limits of $-\infty$ and ∞ . However, due to the boundedness of a data set, it is more accurately defined here between 0 and T , where T represents the total duration of the measurement. Trigonometric identities can be expressed in terms of complex exponentials, which allow for a simplified mathematical treatment. With the Euler relationship

$$e^{jy} = \cos y + j \sin y \quad (2.10)$$

equation (2.7) may be written as

$$u(t) = u_{dc} + \frac{|\Delta u|}{2j} (e^{j(\omega t + \phi_u)} - e^{-j(\omega t + \phi_u)}) .$$

Using $\frac{|\Delta u|}{2j} = \tilde{u}_{ac}$, the FT of the single-frequency sinusoidal potential perturbation yields

$$\text{FT}[u(t)](\omega) = U(\omega) = \tilde{u}_{ac} e^{j\phi_u} T. \quad (2.11)$$

The dc term u_{dc} has no time dependence and refers to the zero frequency component. In a similar way, the FT of (2.8) is given by

$$\text{FT}[i(t)](\omega) = I(\omega) = \tilde{i}_{ac} e^{j\phi_i} T, \quad (2.12)$$

with $\tilde{i}_{ac} = \frac{|\Delta i|}{2j}$. From (2.6) it follows that the impedance expression is defined as the complex ratio between (2.11) and (2.12), following

$$Z(\omega) = \frac{U(\omega)}{I(\omega)} = \frac{\tilde{u}_{ac}}{\tilde{i}_{ac}} e^{j(\phi_u - \phi_i)}. \quad (2.13)$$

Here, $\frac{\tilde{u}_{ac}}{\tilde{i}_{ac}}$ and $\phi = (\phi_u - \phi_i)$ are the magnitude and phase of the impedance, respectively. Equation (2.13) considers only positive values of ω . Instead, when performing the FT on the negative side of the frequency axis, inserting $-\omega$ in the exponential of (2.9), the impedance is given by

$$Z(-\omega) = \frac{U(\omega)}{I(\omega)} = \frac{\tilde{u}_{ac}}{\tilde{i}_{ac}} e^{-j(\phi_u - \phi_i)} = \overline{Z}(\omega), \quad (2.14)$$

where $\overline{Z}(\omega)$ is the complex conjugate of (2.13). As shown in the complex plane diagram in Figure 2.4, the complex conjugate of the impedance can be understood as its reflection about the real axis (Orazem, 2017). The full derivations of (2.13) and (2.14) can be found in Appendix A.

Due to its complex nature, the impedance may be expressed as

$$Z = Z_{\text{Re}} + j Z_{\text{Im}},$$

where Z_{Re} and Z_{Im} refer to the real and the imaginary part of the impedance, respectively.

When relating the impedance expression to electrochemical systems, the real part can be figured as the resistance to motion of charged species, while the imaginary contribution may be interpreted as the difficulty for charged species to be separated in the system (Chan et al., 2015). The magnitude of the impedance is defined as

$$|Z(\omega)| = \sqrt{Z_{\text{Re}}(\omega)^2 + Z_{\text{Im}}(\omega)^2},$$

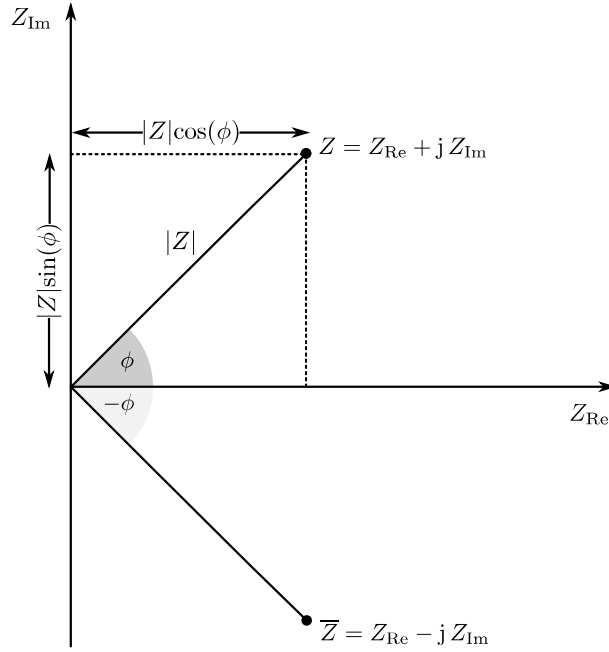


Figure 2.4.: Complex plane diagram, adapted from Orazem (2017).

and the phase angle ϕ is given by

$$\phi(\omega) = \tan^{-1} \left(\frac{Z_{\text{Im}}(\omega)}{Z_{\text{Re}}(\omega)} \right).$$

$Z_{\text{Re}}(\omega)$ and $Z_{\text{Im}}(\omega)$ can alternatively be written as

$$Z_{\text{Re}}(\omega) = |Z(\omega)| \cos(\phi(\omega)) \quad \text{and} \quad Z_{\text{Im}}(\omega) = |Z(\omega)| \sin(\phi(\omega)),$$

respectively. Impedance data can be graphically represented in the form of Nyquist plots, where the negative imaginary impedance contribution is plotted against the real part of the impedance, see Figure 2.5. Each point in the spectrum corresponds to an impedance value measured at a certain frequency. The Nyquist representation requires that both of the axis are plotted in equal scales. Due to the fact that Nyquist plots do not give any explicit information about the frequency domain, Bode plots are frequently employed. In this case, the modulus and the phase of the impedance are represented as a function of frequency (Chan et al., 2015). In this thesis the Nyquist representation is favored over the Bode representation, as its shape allows for a straightforward interpretation of the data. Since the focus of this work lies on the investigation of the temporal development of impedance data, an alternative 3-D representation of impedance spectra is employed in Chapter 5, where impedance is given as a function of time, illustrated using Nyquist plots.

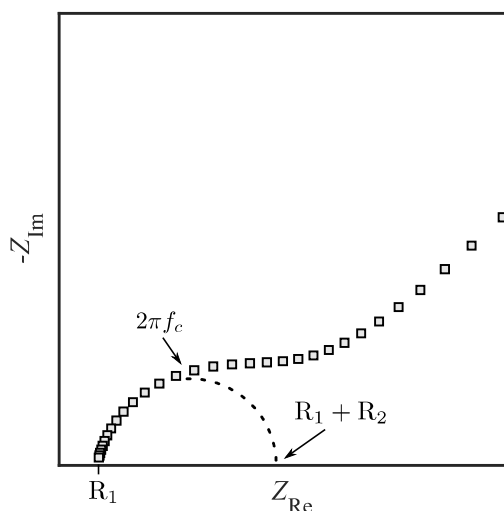


Figure 2.5.: Nyquist representation of impedance data.

2.3.2. Application of Impedance Spectroscopy to Investigate Kinetic Parameters

EIS is applied to obtain insight into electrode processes to gain information about the kinetic variables that govern the underlying reaction mechanisms. This Section provides the essential tools needed to develop models based on EECs. The focus lies on the construction of EECs from passive elements, including the derivation of the corresponding impedance expressions. It is discussed how to fit such a model to experimental impedance data by complex nonlinear least-squares (CNLS) techniques with the aim of extracting kinetic variables from experimental data and relating these quantities to physical processes. In what follows, the subject of mathematical regression is discussed on a level that is sufficient to understand the concept of data fitting that was performed in this thesis. For further details on this topic the reader is referred to the references provided in this Section and to textbooks dedicated to statistics.

Electrical Circuits

The most outstanding feature of EIS is that it enables modeling of electrode processes, where electrical analogues arranged in the form of EECs serve as approximations to analytical models based on physical parameters (Bockris, 2000). EECs can be constructed from resistors, capacitors, and inductors, which are referred to as passive elements, see Figure 2.6. According to Orazem (2017), a passive circuit element is a component that does not generate current or potential. As already discussed in Section 2.1.1, the relationship between current and potential for an ideal resistor is given by Ohm's law (2.2), stating that in this ideal case, the potential difference across the resistor is proportional to the current flowing through it. In an inductor,

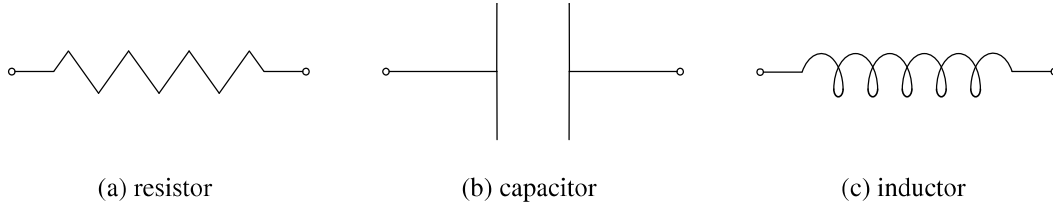


Figure 2.6.: Passive elements, adapted from Orazem (2017).

current and voltage are related as follows

$$u(t) = L \frac{di(t)}{dt}, \quad (2.15)$$

where L corresponds to the inductance, whereas the corresponding relationship for a capacitor is given by

$$i(t) = C \frac{du(t)}{dt}, \quad (2.16)$$

with C being the capacitance. As discussed in Section 2.3.1, if a sinusoidal voltage perturbation (2.7) is applied to a passive element, the corresponding current response (2.8) is again a pure sinusoidal wave, oscillating at the same frequency and being shifted in phase with respect to the voltage input. Therefore, with (2.7) the current/potential relationship across an ideal resistor can be redefined as

$$u_{dc} + |\Delta u| \sin(\omega t + \phi_u) = R (i_{dc} + |\Delta i| \sin(\omega t + \phi_i)). \quad (2.17)$$

Using the Euler relation, given by (2.10), equation (2.17) can be written as

$$u_{dc} + \tilde{u}_{ac} (e^{j(\omega t + \phi_u)} - e^{-j(\omega t + \phi_u)}) = R (i_{dc} + \tilde{i}_{ac} (e^{j(\omega t + \phi_i)} - e^{-j(\omega t + \phi_i)})). \quad (2.18)$$

When applying the FT to both sides of equation (2.18), it follows that

$$\int_0^T \tilde{u}_{ac} (e^{j(\omega t + \phi_u)} - e^{-j(\omega t + \phi_u)}) e^{-j\omega t} dt = R \int_0^T \tilde{i}_{ac} (e^{j(\omega t + \phi_i)} - e^{-j(\omega t + \phi_i)}) e^{-j\omega t} dt.$$

With definition (2.6), the impedance of a resistor equals the resistance R , having only a real contribution, such that

$$Z_R = \frac{\text{FT}[u(t)](\omega)}{\text{FT}[i(t)](\omega)} = \frac{U(\omega)}{I(\omega)} = R.$$

Accordingly, equation (2.15) may be alternatively represented as

$$\tilde{u}_{ac} (e^{j(\omega t + \phi_u)} - e^{-j(\omega t + \phi_u)}) = j\omega L \tilde{i}_{ac} (e^{j(\omega t + \phi_i)} - e^{-j(\omega t + \phi_i)}), \quad (2.19)$$

where FT of (2.19) yields the expression

$$\int_0^T \tilde{u}_{ac} (e^{j(\omega t + \phi_u)} - e^{-j(\omega t + \phi_u)}) e^{-j\omega t} dt = j\omega L \int_0^T \tilde{i}_{ac} (e^{j(\omega t + \phi_i)} - e^{-j(\omega t + \phi_i)}) e^{-j\omega t} dt.$$

Hence, the frequency dependent impedance expression for an inductor is given by

$$Z_L = j\omega L.$$

Following this procedure, the current and voltage relationship across a capacitor (2.16) can be redefined as

$$\tilde{i}_{ac} (e^{j(\omega t + \phi_i)} - e^{-j(\omega t + \phi_i)}) = j\omega C \tilde{u}_{ac} (e^{j(\omega t + \phi_u)} - e^{-j(\omega t + \phi_u)}). \quad (2.20)$$

In this case, the transformation of (2.20) into the Fourier domain results in expression

$$\int_0^T \tilde{i}_{ac} (e^{j(\omega t + \phi_i)} - e^{-j(\omega t + \phi_i)}) e^{-j\omega t} dt = j\omega C \int_0^T \tilde{u}_{ac} (e^{j(\omega t + \phi_u)} - e^{-j(\omega t + \phi_u)}) e^{-j\omega t} dt.$$

Therefore, the impedance for a capacitor may be expressed as

$$Z_C = \frac{1}{j\omega C}.$$

As EECs are constructed from series and/or parallel arrangements of electrical analogues, it is crucial to clarify how to obtain the impedance response of a full EEC from the above derived impedance expressions for single passive elements. According to Orazem (2017), passive elements have to be combined in series if the current flowing through each of them is the same and if the potential difference over all the elements equals the sum of potential differences across the single elements.

Consequently, the impedance response for a series combination of two electrochemical analogues is defined as the sum

$$Z = Z_1 + Z_2,$$

as illustrated in Figure 2.7a. Instead, if the potential difference across single dipoles is identical, and the overall current is given by the sum of the currents flowing through each element, passive elements must be arranged in parallel, see Figure 2.7b. In parallel combinations of electrical analogues the total impedance is equal to

$$Z = \left(\frac{1}{Z_1} + \frac{1}{Z_2} \right)^{-1}.$$

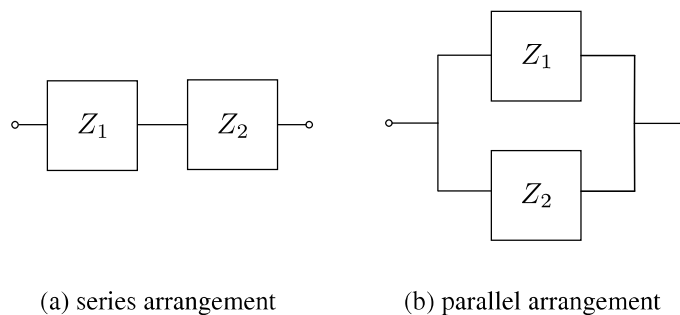


Figure 2.7.: Series and parallel arrangement of circuit components, adapted from Orazem (2017).

These fundamental relationships offer the possibility to derive impedance expressions even for complex EECs, containing nested circuit elements. Here, the question of interest is how to relate the physical processes that govern an electrochemical reaction to passive circuit elements. The general processes controlling the speed of a fast one-electron transfer reaction are the rate of the electron transfer reaction, mass transport of the electroactive species to the electrode surface as well as the resistance of the electrolyte R_s . Throughout his studies on the kinetics of rapid electrode reactions, Randles (1947) found that an electrode system governed by these three fundamental processes can be considered electrically equivalent to the circuit presented in Figure 2.8, in which R_s is related to the Ohmic drop in the electrolyte, and C_{dl} represents the double layer capacitance, which can be attributed to the accumulation of charged species at the electrode/electrolyte interface due to an electric field, as described in Section 2.1. R_{ct} is referred to as the charge transfer resistance, describing the electrokinetic limitation of the electron transfer reaction. The parameter Z_W represents the Warburg impedance, which is related to the limitation imposed by the diffusion of the reactive species to the electrode surface (Warburg, 1899). The Warburg impedance is usually described in terms of its Warburg coefficient σ . Most electrochemical processes are way more complex, and the phenomena that govern the system are no longer sufficiently described by means of the Randles circuit. However, this electrical analogue serves as a fundamental circuit model and enables the derivation of a relation between EECs and systems involving more complex physical processes, e.g. oxide layer formation or adsorption phenomena.

In an EEC the parallel arrangement of a resistive and an imaginary contribution simulates the current response due to a relaxation process, given by

$$\tau = (2\pi f_c)^{-1} = RC, \quad (2.21)$$

where τ is called the time constant and f_c represents the characteristic frequency of the process. Data fitting of the impedance expression related to the model circuit to experimental data allows for the extraction of the different physical variables and gives insight into the reaction kinetics.

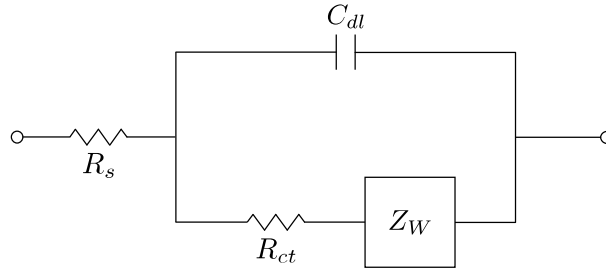


Figure 2.8.: Randles circuit, adapted from Battistel (2014).

In what follows, the concept of CNLS regression is described, a technique that is commonly applied to fit impedance spectra. The fitting routine of nonstationary impedance spectra is based on an extended concept of that method, addressed in Section 2.4.4.

Complex Nonlinear Regression

The nonlinear least-squares (NLS) regression technique aims to fit a model function to a set of experimental values by minimizing a function of the general form

$$\chi^2 = \sum_i w_i (y_i - y(x_i, \mathbf{P}))^2. \quad (2.22)$$

In (2.22) y_i represents the measured data point as a function of the variable i to which the regression of the model function y is performed. The latter does not only depend on the variable x_i but also on a set of parameters \mathbf{P} , related to the physical properties of the process. The right hand side of (2.22) is called the objective function, where the expression $(y_i - y(x_i, \mathbf{P}))^2$ is the residual of the objective function. The minimization procedure follows an iterative approach. Here, a specific algorithm is applied to identify the vector of parameters \mathbf{P} for which the objective function converges to a minimum by systematically changing a set of initially estimated input parameters. The χ^2 statistic is applied to evaluate the probability that a certain number of random normally distributed variables of unit variance has a sum of squares greater than χ^2 . The parameter w is referred to as the weight factor. Macdonald (1987) introduced different weighting possibilities. Ideally, w represents the standard deviation σ . Standard deviations can be experimentally assessed by performing multiple repetitions of the measurement under investigation. Since this method is usually not applicable, weight factors can also be chosen according to the difference in magnitude of the measured values. If the collected data are similar in magnitude, a unity weighting (uwt) can be applied, imposing the same error to all the data points. Instead, if the recorded values differ by several orders of magnitude, it is more appropriate to correlate the weight factor to the dimension of the data, thus assigning an

individual weighting to each data point. This weighting property is referred to as proportional weighting (pwt).

Due to the complex character of impedance values, regression of models to experimentally obtained impedance spectra needs to follow a specific algorithm and is usually performed by CNLS regression techniques. CNLS was first introduced by Sheppard (1970) and originates from the previously developed NLS regression techniques, where the main advantage of CNLS over NLS is that it enables simultaneous fitting of both real and imaginary components of a model function to a set of experimental data. This is particularly useful, since an independent fit of the two impedance components leads to uncorrelated parameters that might be considerably different. Later, Macdonald (1977) implemented the concept of weighted CNLS, which considers the frequency dependence of the impedance and includes an estimation for the variance of the data. According to Orazem (2017), in EIS the weighted CNLS regression procedure is performed by minimizing the following equation

$$\chi_k^2 = \sum_{m=1}^{N_f} \left(\frac{\left(Z_{\text{Re},k}(\omega_m) - \hat{Z}_{\text{Re},k}(\omega_m, \mathbf{P}_k) \right)^2}{V_{\text{Re},m}} + \frac{\left(Z_{\text{Im}}(\omega_m) - \hat{Z}_{\text{Im}}(\omega_m, \mathbf{P}_k) \right)^2}{V_{\text{Im},m}} \right), \quad (2.23)$$

where N_f denotes the number of frequencies applied throughout the experiment, $Z_{\text{Re}}(\omega_m)$ and $Z_{\text{Im}}(\omega_m)$ represent the frequency dependent real and imaginary components of the measured impedance, respectively, while $\hat{Z}_{\text{Re},k}(\omega_m, \mathbf{P}_k)$ and $\hat{Z}_{\text{Im},k}(\omega_m, \mathbf{P}_k)$ are the corresponding model components. The above equation is applied to fit single impedance spectra, where the index k is a constant. The individual weighting factors are given in terms of the estimated variances of the stochastic errors of the real and the imaginary components of the m th value, indicated by $V_{\text{Re},m}$ and $V_{\text{Im},m}$. Due to the fact that the variance terms of the real and imaginary units of the impedance differ, (2.23) assumes that there is no correlation between errors in the real and imaginary components at a frequency ω_m . In fact, from a physical point of view, the error influencing the real and imaginary component of the impedance must be identical. Impedance spectra are commonly recorded at various frequencies, covering several decades. Due to the frequency dependence of the impedance, the corresponding impedance values might differ strongly in magnitude. Thus, in order to fit impedance spectra, pwt is usually employed, which applies an individual weight factor on each data point and (2.23) can be rewritten as

$$\chi_k^2 = \sum_{m=1}^{N_f} \left(\frac{\left(Z_{\text{Re},k}(\omega_m) - \hat{Z}_{\text{Re},k}(\omega_m, \mathbf{P}_k) \right)^2 + \left(Z_{\text{Im},k}(\omega_m) - \hat{Z}_{\text{Im},k}(\omega_m, \mathbf{P}_k) \right)^2}{N_f \left((Z_{\text{Re},k}(\omega_m))^2 + (Z_{\text{Im},k}(\omega_m))^2 \right)} \right), \quad (2.24)$$

where the weighting of the real and the imaginary component of the impedance is identical for a given frequency ω_m .

2.4. The Concept of DMFA

Although EIS is a very powerful technique, its application is exclusively restricted to the investigation of stationary systems and does not give any information about the temporal development of the reaction parameters. It is important to recognize that the impedance expression (2.6) that was derived in Section 2.3.1 is only defined in the steady-state and has no basis in time dependent systems. This thesis aims to provide an accurate and detailed characterization of the reaction kinetics of electrochemical systems in nonstationary conditions. Therefore, the concept of DMFA is introduced here, which combines multi-sine impedance spectroscopy and quasi-*dc* voltammetry. This method enables the observation of the temporal development of the reaction parameters and gives access to impedance values for a large range of frequencies at different potentials in a single measurement. This is particularly useful when investigating unstable systems, where successive impedance measurements may result in a misleading data interpretation due to the degradation of the electroactive substance. Moreover, DMFA allows for the investigation of complex reaction mechanisms, e.g. inner sphere reactions. Similar to EIS, DMFA is based on the linear systems theory, which has a well developed framework and allows for the extraction of the usual impedance parameters (Battistel, 2016). The concepts developed in this Section are mainly based on the discussion published in Koster (2017) and Battistel and La Mantia (2019).

2.4.1. The Dynamic Impedance Expression

As outlined in Section 2.3.1, the concept of complex impedance has originally been derived for linear, time-invariant systems. The mathematical impedance expression for stationary systems is defined in terms of (2.6). In this case, the time-dependence of the current and potential data arrays is removed by transformation of the time-domain signals into frequency spectra by means of FT. In contrast, the theory of DMFA is based on a redefined, time-dependent impedance expression of the form

$$Z'(\omega) = \frac{\text{iFT}[U(\omega) g(\omega' - \omega, \text{bw})](t)}{\text{iFT}[I(\omega) g(\omega' - \omega, \text{bw})](t)}. \quad (2.25)$$

Here, g represents a quadrature filter function that decomposes the spectra in Fourier space, where the time dependence is recovered by applying the iFT to the filtered data. In (2.25) ω and bw represent the central frequency and the bandwidth of the filter, respectively. At first glance, the above equation looks considerably different from the stationary impedance expression, however, in what follows it is demonstrated that (2.25) coincides with (2.6) when the bandwidth of the filter tends towards zero. Under these conditions, $\frac{g}{\text{bw}}$ takes the form of a

nascent Dirac delta function, such that

$$\lim_{bw \rightarrow 0} \frac{g(\omega' - \omega, bw)}{bw} = \delta(\omega' - \omega). \quad (2.26)$$

According to Riley (2004), the fundamental property of the Dirac delta function is given by

$$\int_{-\infty}^{\infty} f(t) \delta(t - a) dt = f(a).$$

With the above relations

$$\int_{-\infty}^{\infty} \lim_{bw \rightarrow 0} \frac{g(\omega' - \omega, bw)}{bw} k(\omega') d\omega' = \int_{-\infty}^{\infty} \delta(\omega' - \omega) k(\omega') d\omega' = k(\omega) \quad (2.27)$$

holds. The iFT of a function $X(\omega')$ is generally defined as

$$\text{iFT}[X(\omega')](t) = \int_{-\infty}^{\infty} X(\omega') e^{j\omega' t} d\omega'. \quad (2.28)$$

Therefore, the numerator of equation (2.25) can be expressed as

$$\text{iFT}[U(\omega') g(\omega' - \omega, bw)](t) = \int_{-\infty}^{\infty} U(\omega') g(\omega' - \omega, bw) e^{j\omega' t} d\omega'. \quad (2.29)$$

Using (2.26) and (2.27), (2.29) can be written as

$$\int_{-\infty}^{\infty} U(\omega') \delta(\omega' - \omega) e^{j\omega' t} d\omega' = U(\omega) e^{j\omega t} \quad (2.30)$$

in the limit $bw \rightarrow 0$, where (2.29) was divided by bw . A similar expression can be derived for the denominator of (2.25), such that

$$\int_{-\infty}^{\infty} I(\omega') \delta(\omega' - \omega) e^{j\omega' t} d\omega' = I(\omega) e^{j\omega t}. \quad (2.31)$$

Finally, plugging (2.30) and (2.31) into (2.25) gives the following equation

$$Z'(\omega) = \lim_{bw \rightarrow 0} \frac{\text{iFT}[U(\omega) g(\omega' - \omega, bw)](t) bw}{\text{iFT}[I(\omega) g(\omega' - \omega, bw)](t) bw} = \frac{U(\omega) e^{j\omega t}}{I(\omega) e^{j\omega t}} = \frac{U(\omega)}{I(\omega)},$$

which is equivalent to the stationary impedance expression (2.6) that was derived in Section 2.3.1.

The uniqueness of DMFA is attributable to the fact that the data are filtered in Fourier space. In contrast, as known from Chapter 1, dynamic impedance techniques reported in literature are commonly based on an STFT approach, where a window function is applied to the signals in the time domain. The corresponding fraction of the decomposed data arrays is then transformed into the frequency domain by means of FT. Under these conditions, the dynamic impedance

may be expressed as

$$Z'(\omega', t) = \frac{\text{STFT}[u(t)](\omega', t)}{\text{STFT}[i(t)](\omega', t)}.$$

The application of STFT to a function $u(t)$ is defined as

$$\text{STFT}[u](\omega', t) = \int_{t' - \frac{\Delta t'}{2}}^{t' + \frac{\Delta t'}{2}} u(t) w(t - t') e^{-j\omega' t} dt, \quad (2.32)$$

where w is the window function and t corresponds to the instant of time at the center of the window. Equation (2.32) can be understood as the convolution of $u(t)$ and the window function. Due to the fact that the expression becomes zero when the lower limit of integration is smaller than $t' - \frac{\Delta t'}{2}$ or when the upper limit of integration is larger than $t' + \frac{\Delta t'}{2}$, respectively, it is possible to rewrite (2.32) by means of FT, such that

$$\text{STFT}[u](\omega', t) = \int_{-\infty}^{\infty} u(t) w(t - t') e^{-j\omega' t} dt = \text{FT}[u(t) w(t - t')](\omega'). \quad (2.33)$$

In this case, integration is performed from $-\infty$ to ∞ . With relations $\text{FT}[x(t)y(t)] = X(\omega) * Y(\omega)$ and $\text{FT}[x(t - t')](\omega') = X(\omega') e^{-j\omega' t}$, where the latter is referred to as the time-shifting property of the FT (Riley, 2004), (2.33) can be expressed as

$$\text{STFT}[u](\omega', t) = U(\omega') * W(\omega') e^{-j\omega' t}. \quad (2.34)$$

With $x(t) * y(t) = \int_{-\infty}^{\infty} x(t')y(t - t') dt'$, the right-hand side of (2.34) may be written as

$$U(\omega') * W(\omega') e^{-j\omega' t} = \int_{-\infty}^{\infty} U(\omega) (W(\omega' - \omega) e^{-j(\omega' - \omega)t} d\omega,$$

which can equivalently be expressed as

$$U(\omega') * W(\omega') e^{-j\omega' t} = e^{-j\omega' t} \int_{-\infty}^{\infty} U(\omega) W(\omega' - \omega) e^{j\omega t} d\omega. \quad (2.35)$$

With (2.35) and the definition of the iFT, given by (2.28), it follows that (2.34) can be redefined as

$$\text{STFT}[u](\omega', t) = e^{-j\omega' t} \text{iFT}[U(\omega) W(\omega' - \omega)](t).$$

Similarly, the current signal is given as

$$\text{STFT}[i](\omega', t) = e^{-j\omega' t} \text{iFT}[I(\omega) W(\omega' - \omega)](t).$$

Therefore, it can be concluded that the impedance expression derived from STFT is equivalent to the dynamic impedance expression when the FT of the window function equals the filter function, such that

$$Z'(\omega) = \frac{\text{iFT}[U(\omega) W(\omega' - \omega)](t)}{\text{iFT}[I(\omega) W(\omega' - \omega)](t)} = \frac{\text{iFT}[U(\omega) g(\omega' - \omega)](t)}{\text{iFT}[I(\omega) g(\omega' - \omega)](t)}.$$

2.4.2. Linearization of Nonstationary Systems

In Section 2.2, the LTI systems theory was introduced, which builds the basis for classic EIS measurements. The LTI systems theory exploits the fact that any electrochemical system behaves linearly to a certain extent when it is subject to specific restrictions. In EIS the condition of linearity is usually achieved by applying an *ac* perturbation of sufficiently low amplitude. Under these conditions, the input/output relationship may be expressed by means of a convolution integral, as given by (2.5). Actually, (2.5) represents the linearized response of a nonlinear time-invariant system to a voltage perturbation. The input/output relationship of nonlinear systems is commonly derived from Volterra series expansion, which can be defined as

$$i(t) = \sum_{n=1}^{\infty} \int_{-\infty}^{\infty} \left[\frac{y_n(\tau_1, \dots, \tau_n)}{n!} \prod_{i=1}^n u(t - \tau_i) d\tau_i \right], \quad (2.36)$$

where $\frac{y_n(\tau_1, \dots, \tau_n)}{n!}$ is referred to the n th order Volterra kernel. Equation (2.36) differs from (2.5) in that it takes into account the nonlinear response of the system. The Volterra series approach can also be employed in dynamic conditions, where u is expressed in terms of its *dc* and *ac* contributions, such that

$$i(t) = \sum_{n=1}^{\infty} \int_{-\infty}^{\infty} \left[\frac{y_n(\tau_1, \dots, \tau_n)}{n!} \prod_{i=1}^n (u_{dc}(t - \tau_i) + u_{ac}(t - \tau_i)) d\tau_i \right]. \quad (2.37)$$

In DMFA u_{dc} corresponds to the triangular potential scan and u_{ac} refers to the multi-sine perturbation. When applying Newton's binomial theorem, (2.37) can be rewritten as

$$i(t) = \sum_k \int_{-\infty}^{\infty} \left[\frac{y_k(\tau_1, \dots, \tau_k)}{k!} + \sum_{n=k+1}^{\infty} \int_{-\infty}^{\infty} \frac{y_n(\tau_1, \dots, \tau_n)}{(n-k)!k!} \prod_{i=k+1}^n u_{dc}(t - \tau_i) d\tau_i \right] \prod_{i=1}^k u_{ac}(t - \tau_i) d\tau_i.$$

Expansion of this expression up to the second order yields

$$\begin{aligned}
 i(t) = & \sum_{n=1}^{\infty} \int_{-\infty}^{\infty} \frac{y_n(\tau_1, \dots, \tau_k)}{n!} \prod_{i=1}^n u_{dc}(t - \tau_i) d\tau_i \\
 & + \int_{-\infty}^{\infty} \left[y_1(\tau_1) + \sum_{n=2}^{\infty} \int_{-\infty}^{\infty} \frac{y_n(\tau_1, \dots, \tau_n)}{(n-1)!} \prod_{i=2}^n u_{dc}(t - \tau_i) d\tau_i \right] u_{ac}(t - \tau_1) d\tau_1 \\
 & + \int_{-\infty}^{\infty} \left[\frac{y_2(\tau_2)}{2} + \sum_{n=3}^{\infty} \int_{-\infty}^{\infty} \frac{y_n(\tau_1, \dots, \tau_n)}{(n-2)!2!} \prod_{i=3}^n u_{dc}(t - \tau_i) d\tau_i \right] \prod_{i=1}^2 u_{ac}(t - \tau_i) d\tau_i,
 \end{aligned}$$

where the first term on the right-hand side refers to the *dc* current, while the second and third terms correspond to the linear and the nonlinear *ac* current contribution, respectively. Thus, under the assumption that the amplitude of the multi-sine signal is small with respect to the *dc* component, the current response can be approximated by its first order term, given by

$$i_{ac}(t) = \int_{-\infty}^{\infty} \left[y_1(\tau_1) + \sum_{n=2}^{\infty} \int_{-\infty}^{\infty} \frac{y_n(\tau_1, \dots, \tau_n)}{(n-1)!} \prod_{i=2}^n u_{dc}(t - \tau_i) d\tau_i \right] u_{ac}(t - \tau_1) d\tau_1,$$

which can be understood as the convolution integral of linear time-variant systems. DMFA uses the above current/potential relationship, where the restriction to linearity allows for straightforward data analysis just like in ordinary EIS. Section 3.2.2 discusses how to correctly determine the multi-sine amplitude in order to satisfy the condition of linearity by investigating the effect of nonlinear current contributions on the dynamic impedance spectra.

2.4.3. Frequency Dependence of Physical Variables in Dynamic Conditions

In DMFA dynamic impedance measurements are usually carried out by superposition of a quasi-triangular waveform with a multi-sinusoidal signal. Based on (2.7), describing the potential perturbation signal in classic EIS, an expression defining the total voltage perturbation in dynamic conditions was derived, given by

$$u(t) = u_{dc}(t) + \sum_m [\Delta u_{ac,m} (e^{j(\omega_m t + \phi_{u,m})} - e^{-j(\omega_m t + \phi_{u,m})})]. \quad (2.38)$$

Here, $u_{dc}(t)$ refers to the quasi-triangular potential input, while the second term on the right-hand side represents the multi-sinusoidal potential perturbation. $\Delta u_{ac,m}$ corresponds to the amplitude of the signal at the m th fundamental frequency. Just like the voltage input, the current response can be divided into its *dc* and *ac* contributions and may be expressed as follows

$$i(t) = i_{dc}(t) + \sum_m [\Delta i_{ac,m}(t) (e^{j(\omega_m t + \phi_{i,m}(t))} - e^{-j(\omega_m t + \phi_{i,m}(t))})].$$

It has to be noted that also the *ac* contribution has an apparent time-dependence, where $\Delta i_{ac,m}(t)$ represents the time-variant amplitude of the current response signals, which appear as skirts centered on the respective fundamental frequency, addressed in Section 3.2. As pointed out in Section 2.3.2, in EIS data fitting allows for the extraction of the physical variables that reflect the kinetic properties of the system under investigation. These quantities respond to a dynamic input signal in a similar way as the current response. Let \mathbf{x} be a vector of time-dependent physical variables, then the response of the vector to (2.38) can be expressed as

$$\mathbf{x}(t) = \mathbf{x}_{dc}(t) + \sum_m [\Delta \mathbf{x}_{ac,m}(t) (e^{j(\omega_m t + \phi_{\mathbf{x},m}(t))} - e^{-j(\omega_m t + \phi_{\mathbf{x},m}(t))})],$$

with $\mathbf{x}_{dc} = \mathbf{x}_{dc}(t)$ and

$$\mathbf{x}_{ac} = \sum_m [\Delta \mathbf{x}_{ac,m}(t) (e^{j(\omega_m t + \phi_{\mathbf{x},m}(t))} - e^{-j(\omega_m t + \phi_{\mathbf{x},m}(t))})].$$

In the most general way, a system may be described by the following set of equations

$$\boldsymbol{\tau}(\mathbf{x}, u) \dot{\mathbf{x}} = \mathbf{F}(\mathbf{x}, u) \quad (2.39)$$

$$i = i(\mathbf{x}, \dot{\mathbf{x}}, u, \dot{u}), \quad (2.40)$$

where $\boldsymbol{\tau}$ is a matrix of time constants and \mathbf{F} represents a vector of constitutive equations that relates the variables in \mathbf{x} with the potential. Let $\boldsymbol{\tau}$ be a diagonal matrix of the form

$$\boldsymbol{\tau} = \begin{bmatrix} \tau(\mathbf{x}, u) & 0 & \cdots & 0 \\ 0 & \tau(\mathbf{x}, u) & \cdots & 0 \\ \vdots & \vdots & \ddots & \vdots \\ 0 & 0 & \cdots & \tau(\mathbf{x}, u) \end{bmatrix},$$

then the system can be linearized by means of Taylor expansion about *dc*, where the left-hand side of (2.39) is approximated by the product of the first order Taylor series of $\tau(\mathbf{x}, u)$ and $\dot{\mathbf{x}}$, while the function $\mathbf{F}(\mathbf{x}, u)$ on the right-hand side of (2.39) is replaced by the linear term of its Taylor series, such that

$$\left[\boldsymbol{\tau}_{dc} + \frac{\partial \boldsymbol{\tau}}{\partial \mathbf{x}} \bigg|_{dc} \mathbf{x}_{ac} + \frac{\partial \boldsymbol{\tau}}{\partial u} \bigg|_{dc} u_{ac} \right] \dot{\mathbf{x}} = \mathbf{F}_{dc} + \frac{\partial \mathbf{F}}{\partial \mathbf{x}} \bigg|_{dc} \mathbf{x}_{ac} + \frac{\partial \mathbf{F}}{\partial u} \bigg|_{dc} u_{ac}, \quad (2.41)$$

where $u_{dc} = u_{dc}(t)$ and

$$u_{ac} = \sum_m [\Delta u_{ac,m} (e^{j(\omega_m t + \phi_{u,m})} - e^{-j(\omega_m t + \phi_{u,m})})].$$

With $\dot{\mathbf{x}} = \dot{\mathbf{x}}_{dc} + \dot{\mathbf{x}}_{ac}$, multiplication of the two terms on the left-hand side of (2.41) yields

$$\tau_{dc} \dot{\mathbf{x}}_{dc} + \tau_{dc} \dot{\mathbf{x}}_{ac} + \left. \frac{\partial \tau}{\partial \mathbf{x}} \right|_{dc} \dot{\mathbf{x}}_{dc} \mathbf{x}_{ac} + \left. \frac{\partial \tau}{\partial u} \right|_{dc} \dot{\mathbf{x}}_{dc} u_{ac} = \mathbf{F}_{dc} + \left. \frac{\partial \mathbf{F}}{\partial \mathbf{x}} \right|_{dc} \mathbf{x}_{ac} + \left. \frac{\partial \mathbf{F}}{\partial u} \right|_{dc} u_{ac}, \quad (2.42)$$

where the products of two ac terms were discarded as they are second order effects. In the same way, the first order Taylor approximation of (2.40) about dc is given by

$$i = i_{dc} + \left. \frac{\partial i}{\partial \mathbf{x}} \right|_{dc} \mathbf{x}_{ac} + \left. \frac{\partial i}{\partial \dot{\mathbf{x}}} \right|_{dc} \dot{\mathbf{x}}_{ac} + \left. \frac{\partial i}{\partial u} \right|_{dc} u_{ac} + \left. \frac{\partial i}{\partial \dot{u}} \right|_{dc} \dot{u}_{ac}. \quad (2.43)$$

With

$$\dot{\mathbf{x}}_{dc} = \frac{\partial \mathbf{x}_{dc}}{\partial t}$$

and

$$\begin{aligned} \dot{\mathbf{x}}_{ac} = & \sum_m \left(j\omega_m + \frac{\partial \phi_{\mathbf{x},m}}{\partial t} \right) \Delta \mathbf{x}_{ac,m}(t) \left(e^{j(\omega_m t + \phi_{\mathbf{x},m}(t))} + e^{-j(\omega_m t + \phi_{\mathbf{x},m}(t))} \right) \\ & + \sum_m \frac{\partial \Delta \mathbf{x}_{ac}}{\partial t} \left(e^{j(\omega_m t + \phi_{\mathbf{x},m}(t))} - e^{-j(\omega_m t + \phi_{\mathbf{x},m}(t))} \right), \end{aligned}$$

equations (2.42) and (2.43) may be rewritten as

$$\begin{aligned} & \tau_{dc} \frac{\partial \mathbf{x}_{dc}}{\partial t} + \left. \frac{\partial \tau}{\partial \mathbf{x}} \right|_{dc} \frac{\partial \mathbf{x}_{dc}}{\partial t} \mathbf{x}_{ac} + \left. \frac{\partial \tau}{\partial u} \right|_{dc} \frac{\partial \mathbf{x}_{dc}}{\partial t} u_{ac} \\ & + \tau_{dc} \sum_m \left(j\omega_m + \frac{\partial \phi_{\mathbf{x},m}}{\partial t} \right) \Delta \mathbf{x}_{ac,m}(t) \left(e^{j(\omega_m t + \phi_{\mathbf{x},m}(t))} + e^{-j(\omega_m t + \phi_{\mathbf{x},m}(t))} \right) \\ & + \tau_{dc} \sum_m \frac{\partial \Delta \mathbf{x}_{ac}}{\partial t} \left(e^{j(\omega_m t + \phi_{\mathbf{x},m}(t))} - e^{-j(\omega_m t + \phi_{\mathbf{x},m}(t))} \right) = \mathbf{F}_{dc} + \left. \frac{\partial \mathbf{F}}{\partial \mathbf{x}} \right|_{dc} \mathbf{x}_{ac} + \left. \frac{\partial \mathbf{F}}{\partial u} \right|_{dc} u_{ac} \end{aligned} \quad (2.44)$$

and

$$\begin{aligned} i = & i_{dc} + \left. \frac{\partial i}{\partial \mathbf{x}} \right|_{dc} \mathbf{x}_{ac} \\ & + \left. \frac{\partial i}{\partial \dot{\mathbf{x}}} \right|_{dc} \sum_m \left(j\omega_m + \frac{\partial \phi_{\mathbf{x},m}}{\partial t} \right) \Delta \mathbf{x}_{ac,m}(t) \left(e^{j(\omega_m t + \phi_{\mathbf{x},m}(t))} + e^{-j(\omega_m t + \phi_{\mathbf{x},m}(t))} \right) \\ & + \left. \frac{\partial i}{\partial \dot{\mathbf{x}}} \right|_{dc} \sum_m \frac{\partial \Delta \mathbf{x}_{ac}}{\partial t} \left(e^{j(\omega_m t + \phi_{\mathbf{x},m}(t))} - e^{-j(\omega_m t + \phi_{\mathbf{x},m}(t))} \right) + \left. \frac{\partial i}{\partial u} \right|_{dc} u_{ac} + \left. \frac{\partial i}{\partial \dot{u}} \right|_{dc} \dot{u}_{ac}, \end{aligned} \quad (2.45)$$

respectively. When the impedance is recorded in stationary conditions, as done in EIS, all time derivatives become zero. Under these conditions, (2.44) can be expressed as

$$\tau_{dc} \sum_m \left(j\omega_m + \frac{\partial \phi_{\mathbf{x},m}}{\partial t} \right) \Delta \mathbf{x}_{ac,m}(t) \left(e^{j(\omega_m t + \phi_{\mathbf{x},m}(t))} + e^{-j(\omega_m t + \phi_{\mathbf{x},m}(t))} \right) = \mathbf{F}_{dc} + \left. \frac{\partial \mathbf{F}}{\partial \mathbf{x}} \right|_{dc} \mathbf{x}_{ac} + \left. \frac{\partial \mathbf{F}}{\partial u} \right|_{dc} u_{ac},$$

whereas (2.45) does not change significantly. Equal relations hold in dynamic conditions, provided that the *dc* component changes very slowly compared with the *ac* component, so that all time derivatives tend towards zero. In this case, the physical variables show the same frequency dependence as observed for stationary systems. Since the circuit parameters are strongly linked to the physico-electrochemical quantities of the system, the above property allows for data fitting of dynamic impedance spectra by means of classic EECs.

2.4.4. Data Fitting of Dynamic Impedance Spectra

The fundamental concepts of CNLS regression techniques have already been discussed in Section 2.3.2, where (2.24) applies for weighted data fitting of a single impedance spectrum. In DMFA a single experiment gives access to a large number of impedance spectra at different potentials. Thus, in order to obtain a concatenated picture of the result, it is desired to fit various spectra simultaneously. Based on the fact that dynamic impedance spectra may be fitted to classic EECs, as discussed in the previous Section, Battistel (2016) introduced a modified expression of (2.24), given by

$$\chi_l^2 = \sum_{k=1}^N \sum_{m=1}^{N_f} \left(\frac{\left(Z_{\text{Re},k}(\omega_m) - \hat{Z}_{\text{Re},k}(\omega_m, \mathbf{P}_k) \right)^2 + \left(Z_{\text{Im},k}(\omega_m) - \hat{Z}_{\text{Im},k}(\omega_m, \mathbf{P}_k) \right)^2}{N \times N_f \left((Z_{\text{Re},k}(\omega_m))^2 + (Z_{\text{Im},k}(\omega_m))^2 \right)} \right). \quad (2.46)$$

Equation (2.46) allows for data fitting of a whole set of impedance spectra, where N is the number of impedance spectra to be fitted. The above expression differs from (2.24) in that it takes into account the correlation of the fitting parameters between the impedance spectra over the whole range of potentials. In addition to that, a smoothing factor was added to the regression procedure in order to prevent that a parameter P_n undergoes drastical changes from one potential to the other. The smoothing factor is expressed in terms of the second derivative of the parameter with respect to the time at which the impedance spectrum was recorded. Thus, the minimization of the smoothing term results in minimizing the curvature of the function, leading to a less abrupt variation of the respective parameter P_n with time. The regression term

for dynamic impedance spectra was therefore defined as

$$\chi_T^2 = \chi_l^2 + \sum_{n=1}^{N_p} W_n^2 \sum_{k=1}^N \left(\frac{\delta^2 P_{n,k}}{\delta t_k^2} \bigg|_{t_k} \right)^2, \quad (2.47)$$

with N_p being the number of parameters to be identified and W_n corresponding to a weight factor that allows to control the degree of variation of the single parameters. When W_n is set to infinite, the parameter under investigation is kept constant. In contrast, when W_n is set to 0, the parameter can freely develop.

3. Dynamic Impedance Spectroscopy using DMFA

In Section 2.4 the theoretical framework of DMFA was presented, a method that combines multi-sine impedance spectroscopy and quasi-*dc* voltammetry. This Chapter deals with the application of DMFA to a simple redox process, where the system is subjected to forced dynamic conditions. To start with, the perturbation signals used in DMFA are introduced. Here, the focus is on the generation of the multi-sine waveform, which builds the basis for this new technique. Later, the interaction between different experimental parameters is studied with respect to the reliability of the dynamic impedance spectra acquisition. The relation between the fundamental frequencies of the multi-sine signal and the quasi-triangular potential perturbation has an enormous impact on the performance of DMFA. In this context, the influence of the choice of quadrature filter bandwidth on the quality of dynamic impedance spectra is examined. Next, it is studied in which way the intensity of the multi-sine signal affects the linearity of the system. Based on these results, it is shown how to analyze dynamic impedance spectra by means of EECs in order to extract reliable kinetic variables. Finally, the influence of the electrode dimension on the reaction kinetics is investigated. Parts of the results presented in this Chapter were published in Koster (2017).

3.1. Perturbation Signals in DMFA

The performance of accurate nonstationary impedance measurements requires that the system is exposed to the same dynamic conditions throughout the acquisition time of one full impedance spectrum (Battistel, 2016). DMFA uses a multi-sine wave that simultaneously injects all the frequencies into the system to meet the above condition, where dynamic impedance spectra are acquired while superimposing this multi-sine signal on a quasi-triangular waveform.

3.1.1. The Quasi-Triangular Potential Perturbation

The below Figure 3.1 shows the comparison between the quasi-triangular wave used in DMFA and the classic triangular shape that is commonly applied in *dc* voltammetry. It must be emphasized that the two voltammetric curves only differ in that the quasi-triangular wave changes more smoothly at the reversal points. Although there is only a slight difference between the two waveforms in the time domain, their signals considerably differ in Fourier space. Periodic

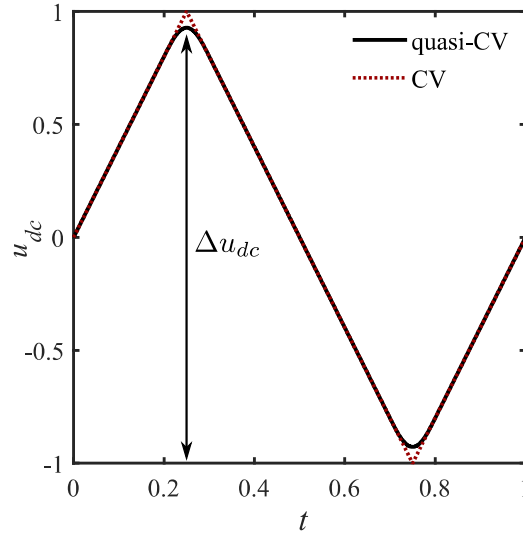


Figure 3.1.: Comparison of the quasi-triangular waveform used in DMFA and the classic triangular shape commonly applied in dc voltammetry.

signals can be represented as sums of trigonometric functions by means of Fourier series. Thus, FT of the two waveforms presented in Figure 3.1 leads to Fourier spectra containing peaks at the fundamental frequency f_{dc} and at the higher harmonic frequencies of the respective waveform, which form a skirt about the fundamental dc component, see Figure 3.2. The spectra reveal that the intensity of the higher harmonic signals of the quasi-triangular wave is much lower and drops faster as compared to that of the harmonics related to the classic triangular wave. This is due to the fact that Fourier series approximation of the latter requires a higher number of harmonic signals of significant amplitude in order to converge to the original function. To avoid unwanted interferences, the lowest frequency contained in the multi-sine wave must be located in a frequency range where the intensity of the higher harmonics of the (quasi-)triangular wave is negligibly small. Thus, the shape of the dc signal determines the smallest fundamental frequency of the multi-sinusoidal waveform. In DMFA the use of the quasi-triangular waveform is favored over the classic triangular wave, as it allows for the application of high scan rates while using low frequencies in the multi-sine signal. The fundamental frequency f_{dc} of the quasi-triangular waveform may be determined as follows

$$f_{dc} = \frac{\nu}{2 \Delta u_{dc}}, \quad (3.1)$$

where ν corresponds to the scan rate of the quasi-CV, and Δu_{dc} refers to its amplitude, as indicated in Figure 3.1.

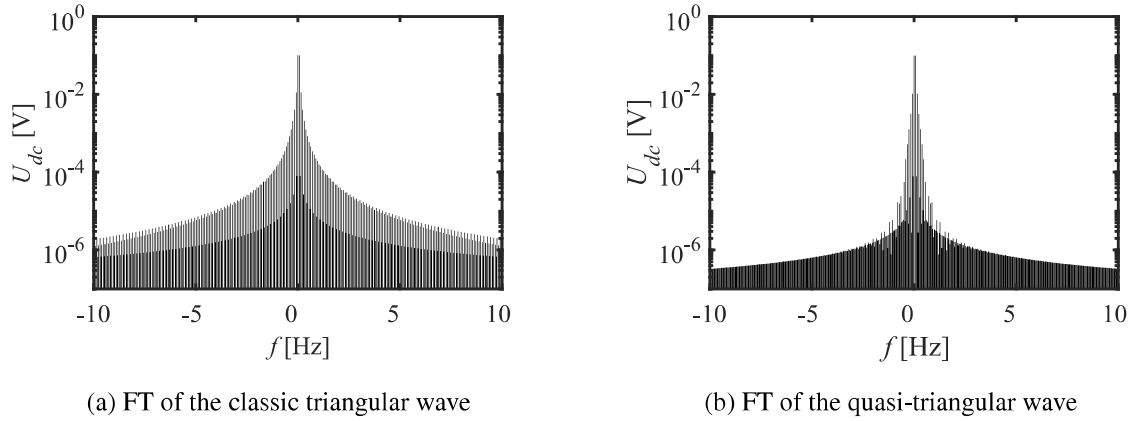


Figure 3.2.: Comparison of the classic triangular and the quasi-triangular potential perturbation in Fourier space.

3.1.2. Design of the Multi-Sine Signal

The design of the multi-sine wave plays a fundamental role in DMFA, as the shape of the signal drastically influences the accuracy and quality of the dynamic impedance spectra. Multi-sine signals are generally composed of a sum of well-chosen sine waves that oscillate at integer multiples of a common base frequency f_b . In order to capture all significant time constants of the process under investigation, the sinusoidal signals must be distributed over a broad range of frequencies. Any real-world electrochemical system behaves nonlinearly to a certain extent, meaning that the current response to a sinusoidal potential perturbation is not a pure sinusoidal oscillation but contains higher harmonics of the fundamental wave (Battistel, 2013). When a nonlinear system is perturbed with more than one sinusoidal wave, the interaction of the different signals results in intermodulation bands. The response of a nonlinear system to a double-frequency input, given by a lower frequency f_1 and a higher frequency f_2 , shows peaks at the fundamental input frequencies and their higher harmonics. Moreover, the intermodulation between the two fundamental input waves generates additional signals that are located at $f_2 - f_1$ and $f_1 + f_2$, respectively (Battistel, 2014).

While the signals related to the nonlinearity of the system cause unwanted distortions, DMFA uses the intermodulations between the higher harmonics of the quasi-CV and the fundamental frequencies of the multi-sine signal to extract the dynamic information of the system. Thus, the presence of both desired and unwanted interferences has to be considered when designing multi-sine signals for DMFA applications. The fundamental frequencies contained in the multi-sine wave must be selected in such a way that they do not coincide with higher order harmonics and intermodulation bands of other fundamental frequencies. In addition to that, the spacing between the selected fundamental frequencies must be large enough in order to guarantee that there is no overlap between the frequency skirts that stem from the intermodulations of the fundamental harmonics and the dc component.

Based on the above requirements, an algorithm was developed that allows for an appropriate choice of multi-sine signals. In order to cover a broad spectrum of frequencies, the fundamental harmonics of the multi-sine signal are chosen based on a proportionality factor m_k that relates the fundamental frequency values f_k to the base frequency f_b , such that

$$m_k = \frac{f_k}{f_b}, \quad (3.2)$$

where the m_k values follow a quasi-logarithmic distribution. Relation (3.2) states that every frequency f_k must be different from any other fundamental frequency. Additionally, the different fundamental harmonics need to be separated by a distance larger than d , following

$$|m_k - m_l| > d.$$

Moreover, every frequency must be located at a distance greater than d from the sum or the difference of two other frequencies, such that

$$|m_k - m_l \pm m_n| > d, \quad (3.3)$$

where l may be equal to n when using the negative sign in front of m_n . In this case, (3.3) defines the minimum allowed distance between a fundamental frequency and the second harmonic of another fundamental frequency. Otherwise, (3.3) represents the minimum allowed distance between a fundamental harmonic and the intermodulation bands generated by two different fundamental frequencies. Whenever one of the above constraints is not satisfied, the interfering frequency is excluded from the multi-sine waveform and a new value is introduced and validated. This algorithm enabled the generation of multi-sine signals containing up to 51 frequencies covering a maximum of 5 decades with $d = 1$. The parameter d plays a crucial role in the design of multi-sine waves, as it determines the maximum number of possible frequencies. Moreover, it controls the ratio between f_b and the fundamental frequency of the dc component. In Section 3.2.1 it is discussed how the parameter d affects the choice of the filter bandwidth.

When sinusoidal signals are summed up, the amplitude of the resulting signal may be significantly increased. The subsequent Figure 3.3 provides a simple illustration of this phenomenon. The intensity of a signal composed of a sum of sine waves of equal amplitudes, oscillating at different frequencies, is increased with respect to the amplitude of the single signals. The more sinusoids are summed up the stronger is this behavior, which is referred to as crest. In the measurements presented in this work, a slight phase shift is applied to all frequencies contained in the multi-sine signal. In doing so, the maxima of the sinusoids do not superimpose, thus leading to less intense peaks and a reduced crest behavior. In this way, the power injected into the system is intensified.

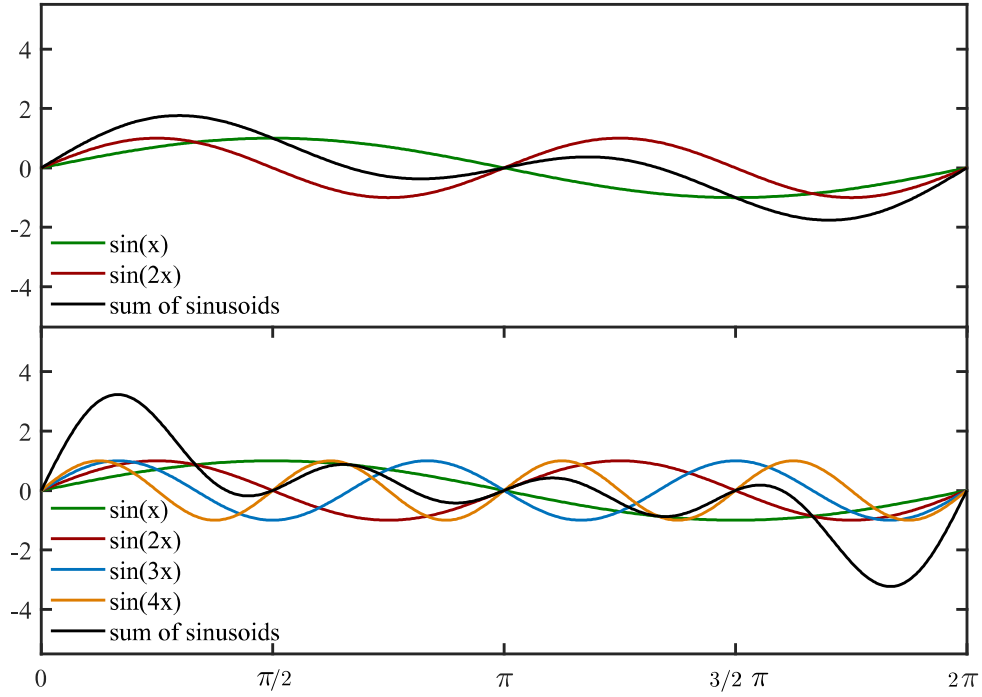


Figure 3.3.: Summation of sine waves of different frequencies.

Moreover, in order to improve the signal-to-noise ratio, the intensity of the peaks in the low-frequency region is amplified by defining the amplitude of each fundamental harmonic as follows

$$A_k = A_0 \left(1 + \frac{70 \text{ Hz}^{0.5}}{\sqrt{f_k}} \right), \quad (3.4)$$

where A_0 represents the initial amplitude of the signal.

The effect of shifting and scaling of the fundamental frequencies is investigated on a real-world multi-sine waveform that was constructed following the algorithm outlined above, where the signal containing 45 frequencies with $d = 7$ is examined in the time domain.

The multi-sine signal generated by simple summation of the different sinusoids contained in the spectrum is illustrated in Figure 3.4a. Under these conditions, the intensity of the signal is rather high and shows strong variations over time. In contrast, when a phase correction is applied to each fundamental frequency, the intensity of the signal is more homogeneous, as shown in Figure 3.4b. However, the total amplitude of the waveform is still high. In order to obtain quasi-linear conditions, the amplitude of the multi-sine perturbation must be sufficiently low. The overall intensity of the signal can be strongly reduced upon optimization of the amplitude according to (3.4), but the different values still vary along the time axis when no phase shift is applied, see Figure 3.4c.

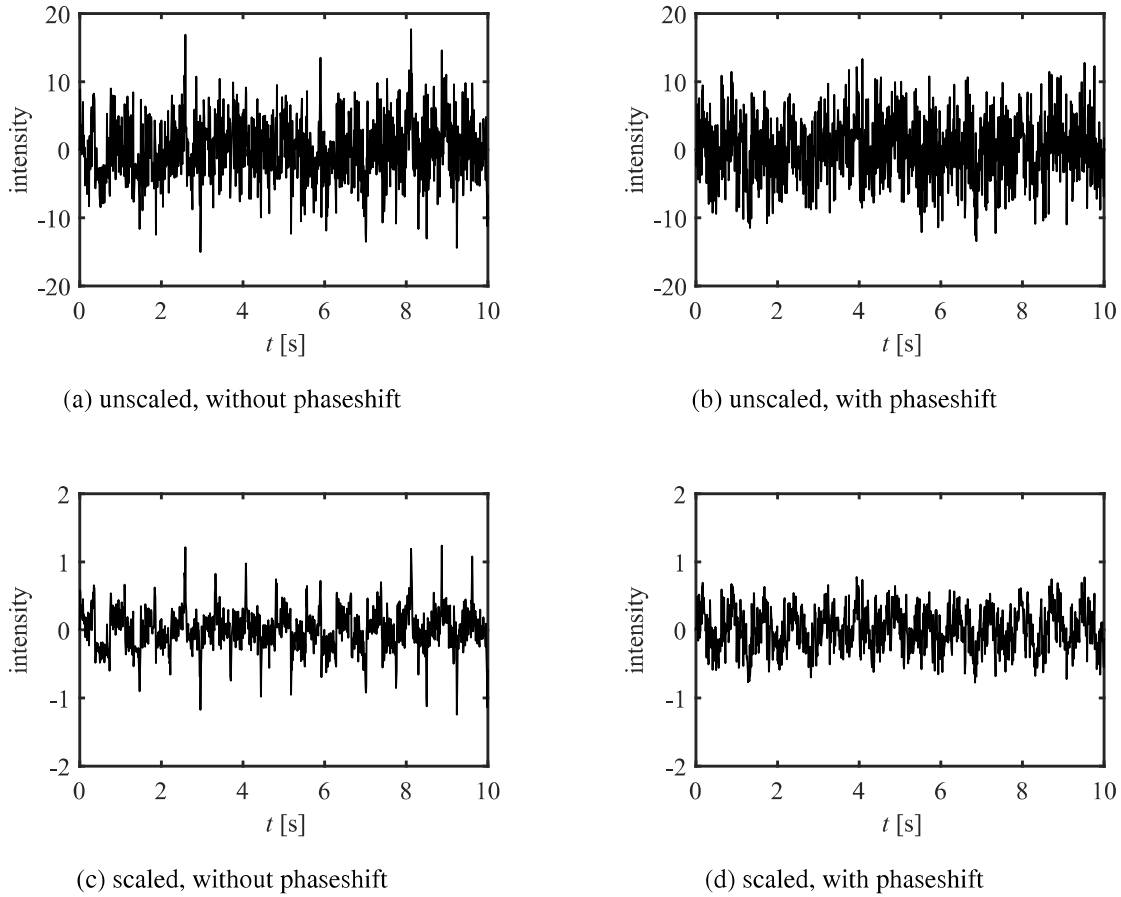


Figure 3.4.: Effect of scaling and shifting for a multi-sine signal containing 45 frequencies.

Therefore, the multi-sine signal has to be optimized with respect to both amplitude and phase in order to obtain a homogeneous, small-amplitude waveform, as presented in Figure 3.4d. It has to be noted that the intensities of the multi-sine wave presented here are dimensionless. In order to obtain the amplitude of the signal in Volts it must be amplified by a certain voltage Δu_{ac} .

The waveform shown in Figure 3.4d can equivalently be represented by the amplitude and phase spectra depicted in Figure 3.5. Due to the fact that the amplitude spectrum does not provide any information about the phasing of the fundamental harmonics contained in the multi-sine wave, both plots are required for a correct description of the signal in Fourier space.

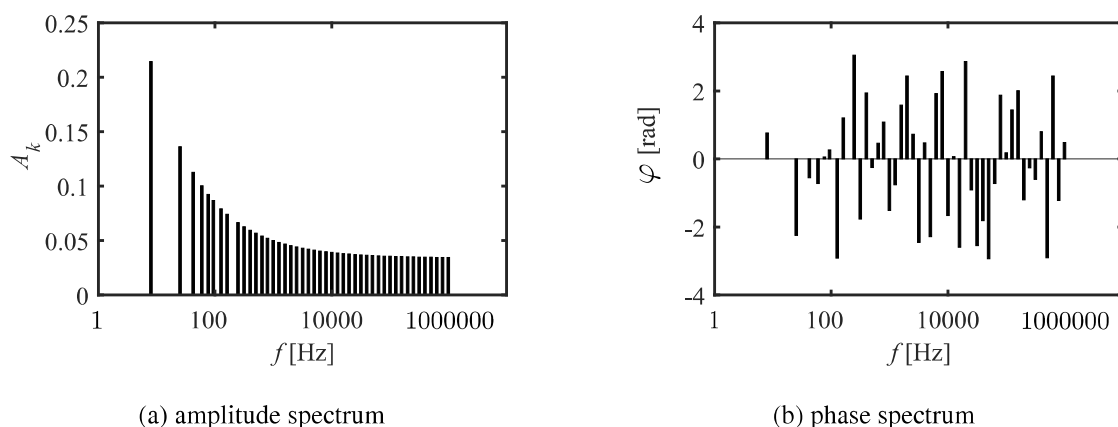


Figure 3.5.: Amplitude and phase spectra of a multi-sine signal containing 45 frequencies with $d = 7$.

3.2. Multi-Sine DC-Voltammetry

The fundamental frequencies of the quasi-triangular waveform and the multi-sine signal are strongly related. In order to acquire reliable dynamic impedance spectra, it is of crucial importance that the time scale of the multi-sine wave does not coincide with that of the quasi-triangular potential perturbation. Instead, the time scale of the multi-sine wave should be about ten times smaller than that of the quasi-CV (Battistel, 2016). In Fourier space the time scale corresponds to the bandwidth of the signal, i.e. to the frequency range that is covered by the signal. The larger the time scale of a signal the smaller is its bandwidth in frequency space.

DMFA measurements were carried out on the $\text{K}_3[\text{Fe}(\text{CN})_6]/\text{K}_4[\text{Fe}(\text{CN})_6]$ redox couple at Pt disk electrodes in order to study the interactions between the perturbation signals that were introduced in Section 3.1. In particular, it was investigated how the bandwidth of the quadrature filter function and the amplitude of the multi-sine signal affect the accuracy of the dynamic impedance spectra. Later, it is demonstrated how to analyze dynamic impedance spectra by means of EECs.

3.2.1. Determination of the Filter Bandwidth

DMFA measurements were performed at a $250 \mu\text{m}$ Pt-WE in a solution of 10 mM $\text{K}_3[\text{Fe}(\text{CN})_6]$ in 0.5 M KF. The below Figure 3.6 shows the total voltage perturbation due to the superposition of the quasi-CV and the multi-sine signal presented in Figure 3.5 and its corresponding current response. The potential was symmetrically changed about a constant dc value of 0.46 V vs. standard hydrogen electrode (SHE), where the amplitude Δu_{dc} of the quasi-triangular wave was set to 500 mV. The potential was scanned at a rate of $\nu = 50 \text{ mV s}^{-1}$, thus, according to (3.1), f_{dc} was equal to 0.05 Hz. In order to satisfy the condition that the time scales of the two

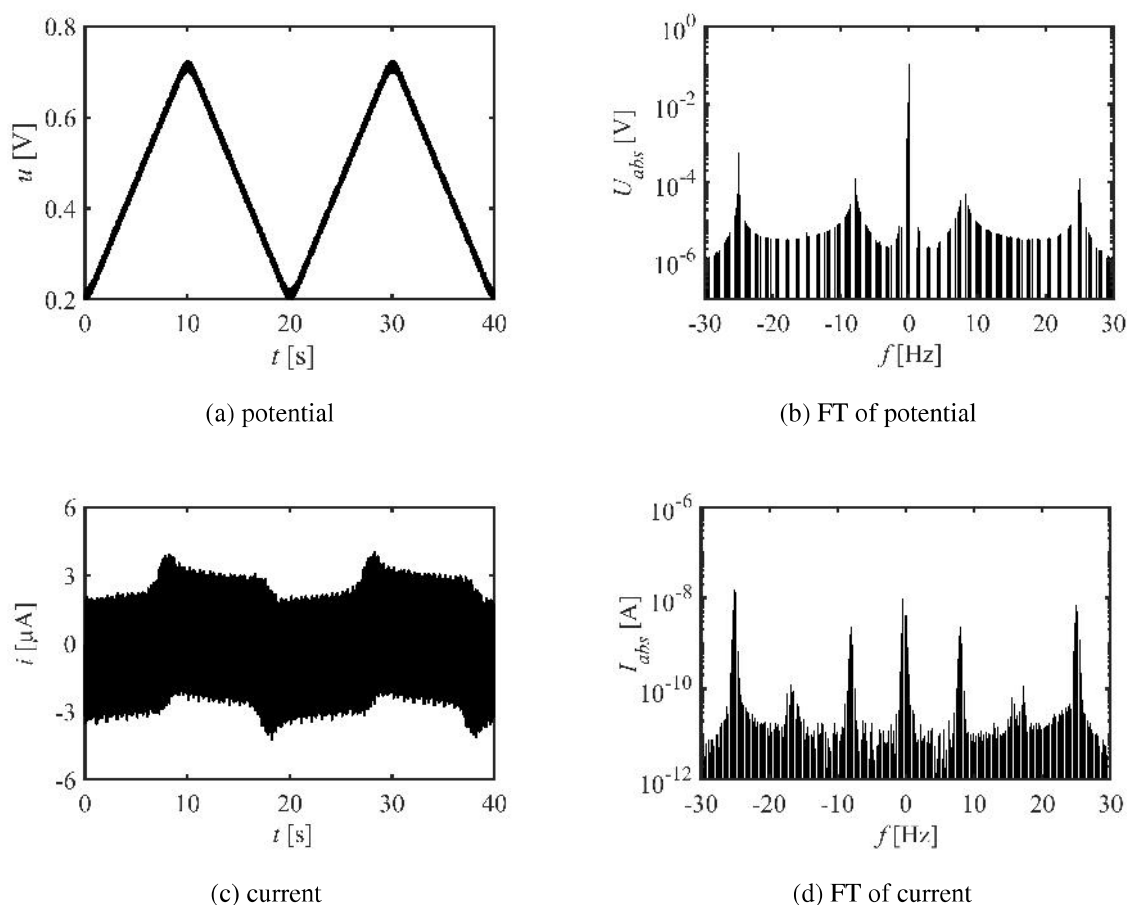


Figure 3.6.: Potential perturbation and current response recorded in 10 mM $K_3[Fe(CN)_6]$ in 0.5 M KF at a 250 μ m Pt electrode for a multi-sine signal in the time and in the Fourier domain. In Fourier space, only a small fraction of the overall spectrum is displayed. $\Delta u_{dc} = 500$ mV, $f_{dc} = 0.05$ Hz, $\Delta u_{ac} = 10$ mV, $f_b = 1$ Hz, $d = 7$.

perturbation signals do not overlap, the fundamental frequency f_b of the multi-sine wave was set to 1 Hz, thus allowing for the extraction of one full impedance spectrum at each point of the quasi-triangular scan. The multi-sine signal was amplified by a voltage Δu_{ac} of 10 mV.

In the time domain, the intensity of the multi-sine wave is very low with respect to the amplitude of the quasi-triangular voltage perturbation, see Figure 3.6a. In Fourier space, however, the signals related to the first two fundamental harmonics contained in the multi-sine wave have a good signal-to-noise ratio and appear at frequencies of 8 Hz and 25 Hz, respectively, as illustrated in Figure 3.6b. Spectral leakage was reduced by choosing a measurement time frame that contains an integer number of periods of the triangular wave and multi-sine oscillations, according to the procedure described in Section 7.1.4. In the time domain, the current response of the redox couple to the total potential perturbation appears as a broad band and does not allow for a direct interpretation of the signal, see Figure 3.6c. In contrast, transformation of the data array into Fourier space reveals some well defined features, where Figure 3.7 shows an enlarged section of Figure 3.6d. Here, the bandwidth of the quasi-triangular wave bw_{dc} , containing f_{dc} and

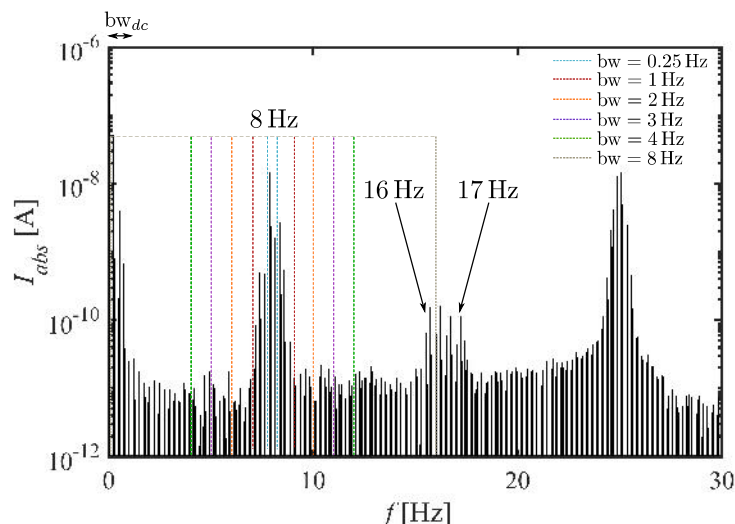


Figure 3.7.: FT of the current response signal in the low-frequency range. The dashed lines indicate the partial current signals extracted for different values of bw .

$\Delta u_{dc} = 500$ mV, $f_{dc} = 0.05$ Hz, $\Delta u_{ac} = 10$ mV, $f_b = 1$ Hz, $d = 7$.

its higher order harmonics, covers the frequency range between 0 Hz and 1 Hz. The first two fundamental harmonics of the multi-sine signal oscillate at frequencies of 8 Hz and 25 Hz, respectively. The skirts around these signals are due to intermodulations between the fundamental frequencies of the multi-sine wave and the harmonics of the quasi-CV and can thus be attributed to the time-variation of the system's response to the fundamental input signals. Furthermore, the spectrum contains the second order harmonic of the 8 Hz signal that partially overlaps with the signal related to the intermodulation of the first two fundamental harmonics, appearing at a frequency of 17 Hz.

As discussed in Section 2.4, DMFA uses a quadrature filter with a certain bandwidth bw in order to separate the partial voltage and current signals about each fundamental harmonic. The choice of bandwidth significantly affects the calculated impedance values. The following Figure 3.8 shows the dynamic impedance spectra extracted from the data arrays presented in Figure 3.6, where the bandwidth of the filter is varied in a range between 0.25 Hz and 8 Hz. The spectra presented here were recorded at the intermediate potential on the cathodic branch of the quasi-CV (0.46 V vs. SHE) and at potentials of -0.06 V and $+0.06$ V with respect to that point. It is obvious from Figure 3.7 that the filter discards a large fraction of the skirt centered on the fundamental harmonic when its bandwidth is set to 0.25 Hz. Although the bandwidth is too narrow to fully capture the temporal evolution of the current response, the quality of the spectra is reasonable, see Figure 3.8a. However, the loss of information is particularly apparent in the quasi-CV, where the initial shape of the quasi-triangular wave cannot be fully reconstructed, as the filter truncates all higher harmonics of the signal oscillating at frequencies $> bw$. When the bandwidth is set to a value of 1 Hz, the shape of the quasi-CV recollected from the current response to the overall voltage perturbation is exactly identical to that of the voltammogram

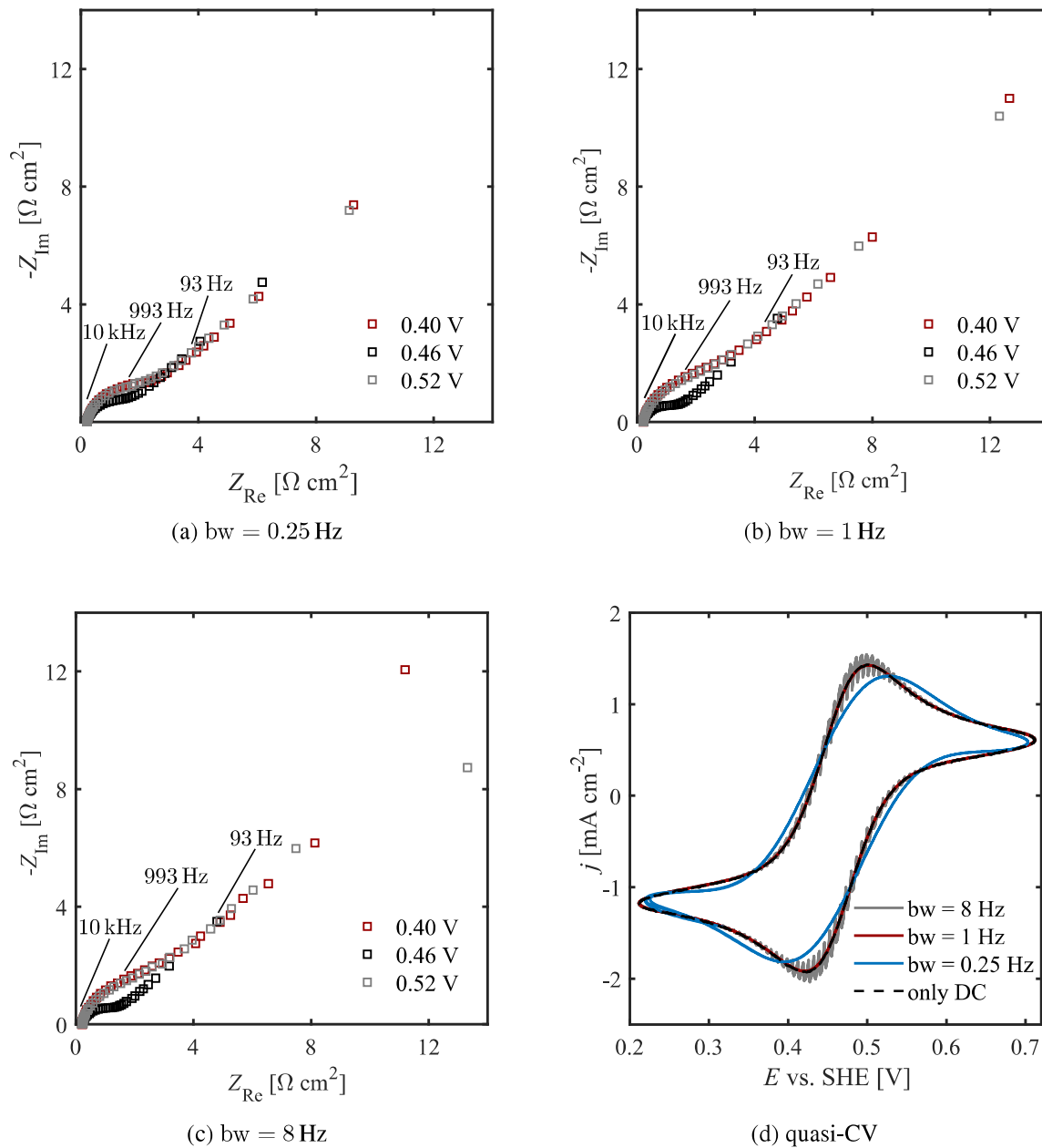
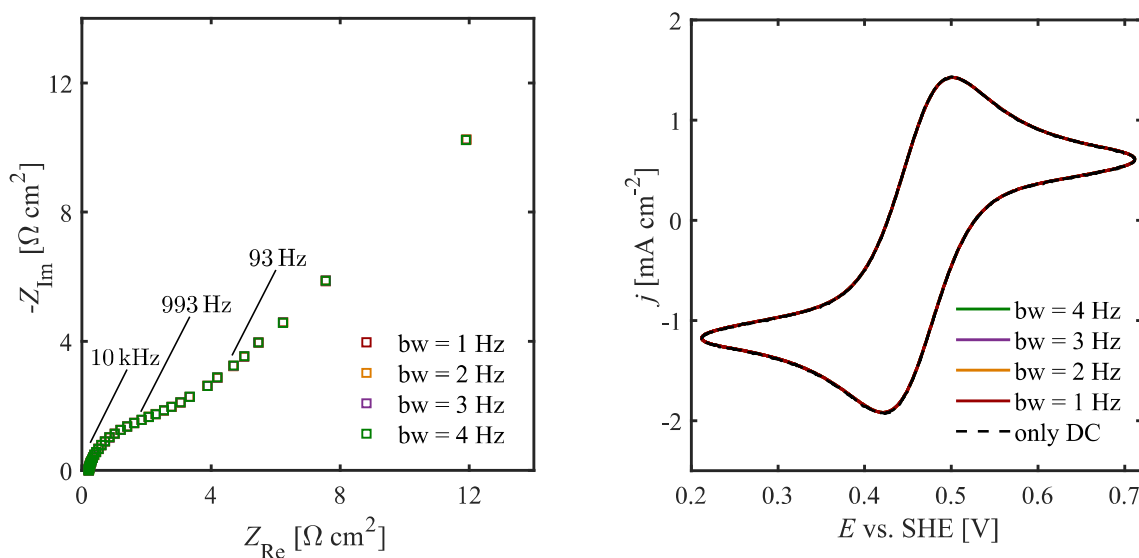


Figure 3.8.: Comparison of dynamic impedance spectra and quasi-CVs recorded in 10 mM $\text{K}_3[\text{Fe}(\text{CN})_6]$ in 0.5 M KF at a $250 \mu\text{m}$ Pt electrode using different values of bw . $\Delta u_{dc} = 500 \text{ mV}$, $f_{dc} = 0.05 \text{ Hz}$, $\Delta u_{ac} = 10 \text{ mV}$, $f_b = 1 \text{ Hz}$, $d = 7$.

recorded without the multi-sine perturbation. Under these conditions, the quality of the dynamic impedance spectra is very good, as can be seen in Figure 3.8b. In particular, the features related to the spectrum recorded at 0.46 V vs. SHE are more pronounced as compared to those presented in the equivalent spectrum in Figure 3.8a. Finally, the effect of another extreme case is investigated by applying a bandwidth of 8 Hz, so that the filter incorporates an excessively broad range of frequencies. Due to the large distance between the fundamental harmonics, the partial current and voltage signals do not contain unwanted perturbations, and therefore the quality of the impedance spectra is still high, see Figure 3.8c. Only the impedance values extracted for



(a) dynamic impedance spectra recorded at a potential of 400 mV vs. SHE

(b) recollected quasi-CVs

Figure 3.9.: Comparison of dynamic impedance spectra recorded in 10 mM $\text{K}_3[\text{Fe}(\text{CN})_6]$ in 0.5 M KF at a 250 μm Pt electrode and recollected quasi-CVs for different values of bw ranging from 1 Hz to 4 Hz. $\Delta u_{dc} = 500 \text{ mV}$, $f_{dc} = 0.05 \text{ Hz}$, $\Delta u_{ac} = 10 \text{ mV}$, $f_b = 1 \text{ Hz}$, $d = 7$.

the lowest frequency contained in the multi-sine wave are highly distorted, as the filter about the 8 Hz harmonic incorporates the signals related to the quasi-triangular waveform, as illustrated in Figure 3.7. In the same way, the first fundamental frequency of the multi-sinusoid is included in the reconstruction of the quasi-CV, thus resulting in a very noisy voltammogram, see Figure 3.8d.

After having studied the effects of an extremely small and large bandwidth on the dynamic impedance response, the bandwidth is varied in a range between 1 Hz and 4 Hz where no distortion due to incorporation of unwanted signals is expected. It seems that the spectra recorded at potentials outside the intermediate potential are more sensitive to perturbations. Therefore, the system was investigated at a potential of 0.4 V vs. SHE on the cathodic branch of the scan in order to detect even smallest distortions. Irrespective of the choice of bandwidth, the dynamic impedance spectra are of consistently high quality over the whole range of frequencies, and the original shape of the quasi-CV can perfectly be reconstructed, as illustrated in the above Figure 3.9. Therefore, it is concluded that the large spacing between the fundamental harmonics in the multi-sine waveform enables the extraction of reliable impedance spectra for a variety of different filter bandwidths. Due to the fact that a wrong choice of bandwidth does not necessarily result in noisy impedance spectra, it is of crucial importance to investigate the input and output signals in Fourier space to assure that the filter detects the temporal evolution of the system without incorporation of unwanted perturbation signals. In addition to that, the shape of the reconstructed quasi-CV provides valuable information about the validity of the bandwidth.

After having investigated the effect of filter bandwidth on the quality of the dynamic impedance spectra when applying a multi-sinusoidal perturbation with $d = 7$, a multi-sine signal with $d = 1$ was designed. In this case, the smaller spacing between the single frequencies allows for the incorporation of a larger number of fundamental harmonics into the waveform. The multi-sine signal containing 51 frequencies may be described by means of the amplitude and phase spectra presented in Figure 3.10. The new waveform was tested under the same experimental conditions as the multi-sine signal with $d = 7$, where Figure 3.11 shows the voltage and current signals in time and in Fourier space, respectively. In the time domain, the input and output signals that are obtained from superposition of the quasi-triangular wave with the new multi-sinusoid do not considerably differ from the spectra shown in Figure 3.6. In contrast, in Fourier space the perturbation signal given in Figure 3.11b shows twice as many fundamental harmonics in the low-frequency region as compared to that presented in Figure 3.6b. The current response contains peaks at the fundamental input frequencies as well as a variety of perturbation signals related to intermodulations and higher order harmonics, see Figure 3.11d.

Again, it is investigated in which way different values of filter bandwidth affect the dynamic impedance response. The subsequent Figure 3.12 shows the dynamic impedance spectra that were extracted using bandwidths ranging from 1 Hz to 4 Hz. Similar to the results depicted in Figure 3.8b, high quality impedance spectra are obtained when the bandwidth is set to 1 Hz, see Figure 3.12a. Under these conditions, the filter incorporates the full skirt centered on the fundamental harmonics, while unwanted perturbation signals are excluded, as illustrated in Figure 3.13. In contrast, when the bandwidth is extended to 2 Hz, the filter additionally captures signals related to the nonlinear response of the system, thus lowering the quality of the impedance spectra, see Figure 3.12b. The larger the bandwidth of the filter, the more significant become distortions in the spectra due to the incorporation of unwanted higher order harmonics, neighbouring signals, or intermodulations of fundamental harmonics. The Nyquist plots

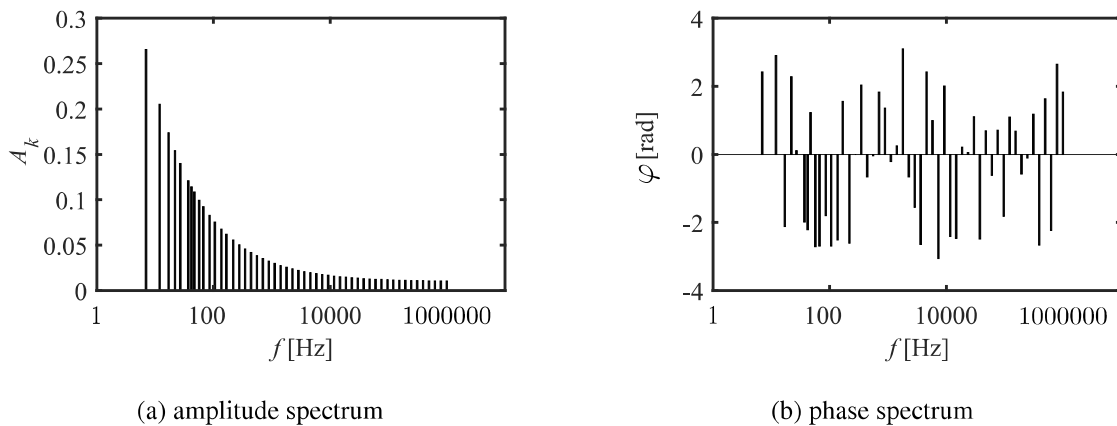


Figure 3.10.: Amplitude and phase spectra of a multi-sine signal containing 51 frequencies with $d = 1$.

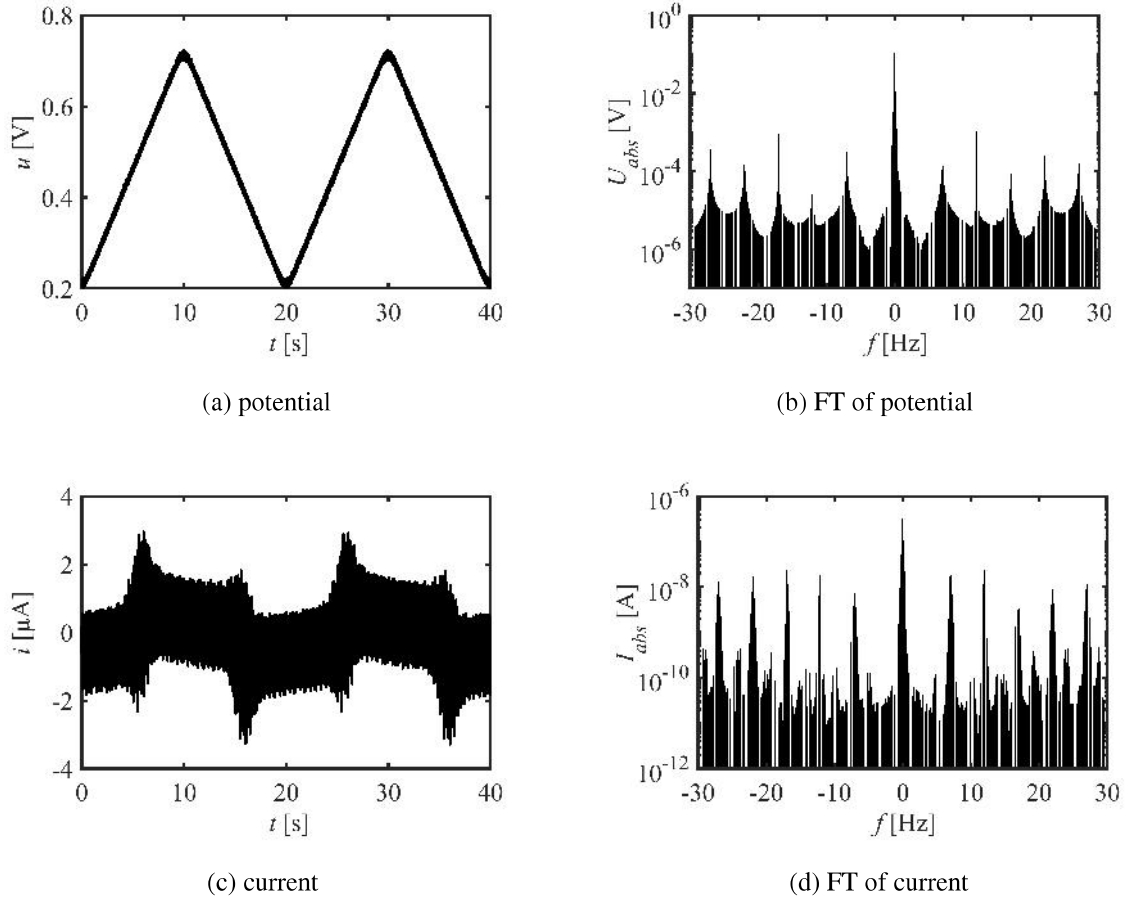


Figure 3.11.: Potential perturbation and current response recorded in 10 mM $\text{K}_3[\text{Fe}(\text{CN})_6]$ in 0.5 M KF at a $250\ \mu\text{m}$ Pt electrode for a multi-sine signal in the time and in the Fourier domain. In Fourier space, only a small fraction of the overall spectrum is displayed. $\Delta u_{dc} = 500\ \text{mV}$, $f_{dc} = 0.05\ \text{Hz}$, $\Delta u_{ac} = 10\ \text{mV}$, $f_b = 1\ \text{Hz}$, $d = 1$.

shown in Figure 3.14a reveal that this effect is particularly apparent in the low-frequency region where the distance between the fundamental harmonics contained in the multi-sine signal is small. Nevertheless, all bandwidths allow for an adequate reconstruction of the quasi-triangular wave. In this case, a bandwidth of 1 Hz is large enough to include all higher harmonics of the quasi-CV, whereas a bandwidth of 4 Hz is still sufficiently narrow to reject unwanted signals, see Figure 3.13. Therefore, the shape of the quasi-CV can successfully be rebuild when using bandwidths ranging from 1 Hz to 4 Hz, as shown in Figure 3.14b.

While the multi-sinusoid with $d = 7$ enables the extraction of reliable impedance spectra for all bandwidths between 1 Hz to 4 Hz, the choice of appropriate bandwidths is strongly restricted when applying the multi-sine waveform with $d = 1$. It is important to recognize that the actual distance between the fundamental frequencies in the multi-sine wave is not only controlled by the parameter d but also by the base frequency f_b of the signal.

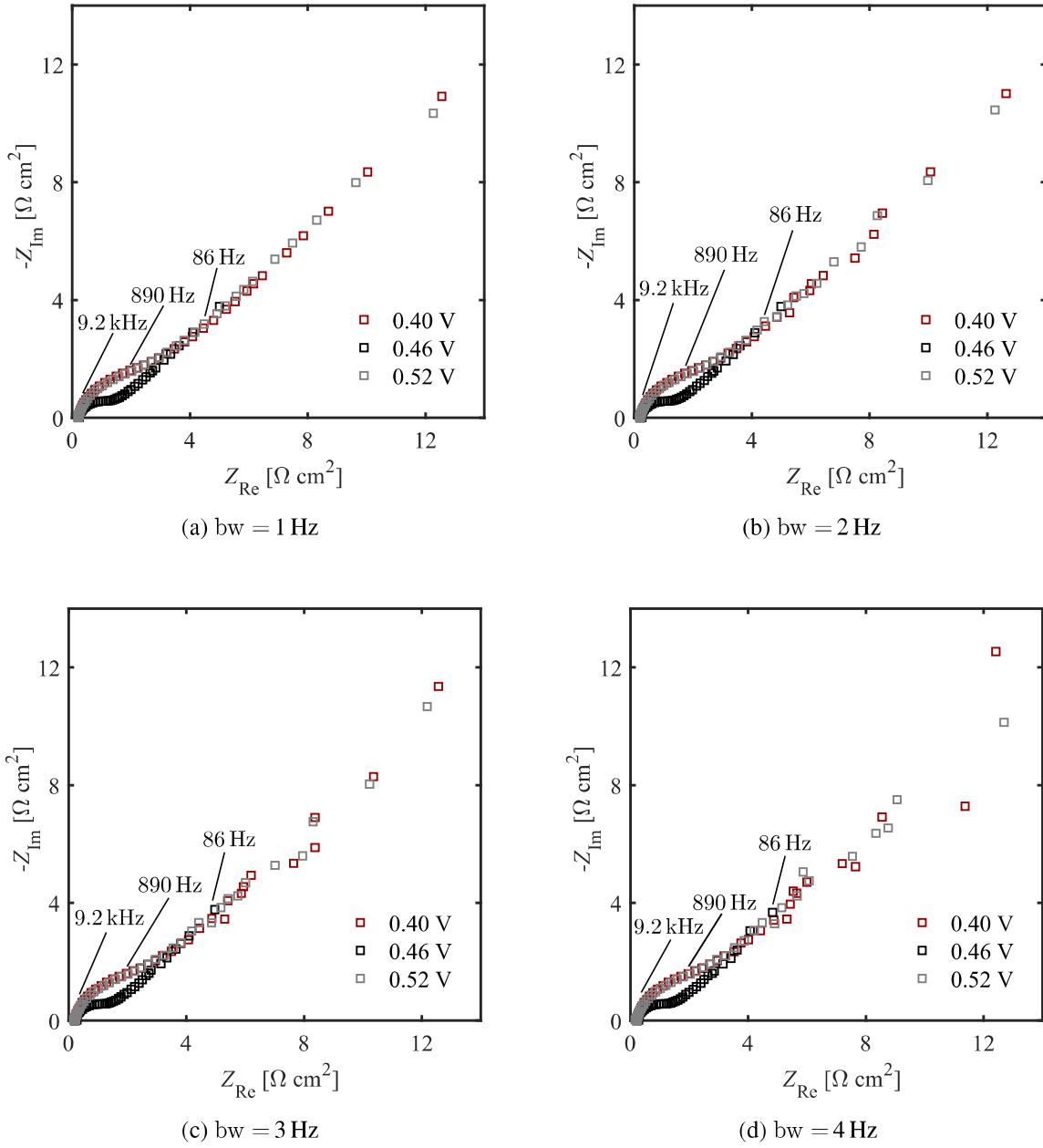


Figure 3.12.: Comparison of dynamic impedance spectra recorded in 10 mM $\text{K}_3[\text{Fe}(\text{CN})_6]$ in 0.5 M KF at a $250 \mu\text{m}$ Pt electrode using different values of bw . $\Delta u_{dc} = 500 \text{ mV}$, $f_{dc} = 0.05 \text{ Hz}$, $\Delta u_{ac} = 10 \text{ mV}$, $f_b = 1 \text{ Hz}$, $d = 1$.

Based on the above results, a generalized expression was formulated that enables the determination of the maximum possible filter bandwidth, such that

$$bw = f_b \left(\frac{d+1}{2} \right), \quad (3.5)$$

where bw has the unit of Hertz. In contrast, the minimum value of bw can be deduced from the bandwidth of the dc component. Thus, according to (3.5), the bandwidth of the filter may range from 1 Hz to 4 Hz when the waveform is designed with $d = 7$, assuming that bw_{dc} and f_b

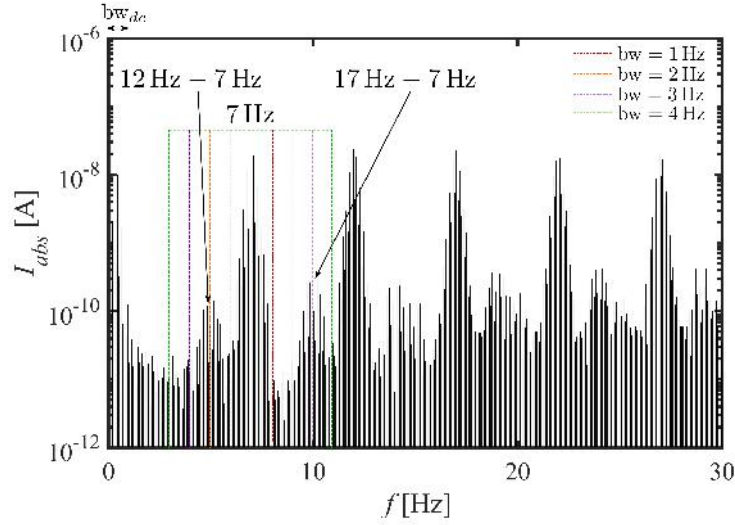


Figure 3.13.: FT of the current response signal in the low-frequency range. The dashed lines indicate the partial current signals extracted for different values of bw.

$\Delta u_{dc} = 500$ mV, $f_{dc} = 0.05$ Hz, $\Delta u_{ac} = 10$ mV, $f_b = 1$ Hz, $d = 1$.

are equal to 1 Hz. In contrast, when $d = 1$, the bandwidth is exclusively restricted to a value of 1 Hz. A proper choice of filter bandwidth is crucial for the acquisition of accurate impedance spectra in nonstationary conditions.

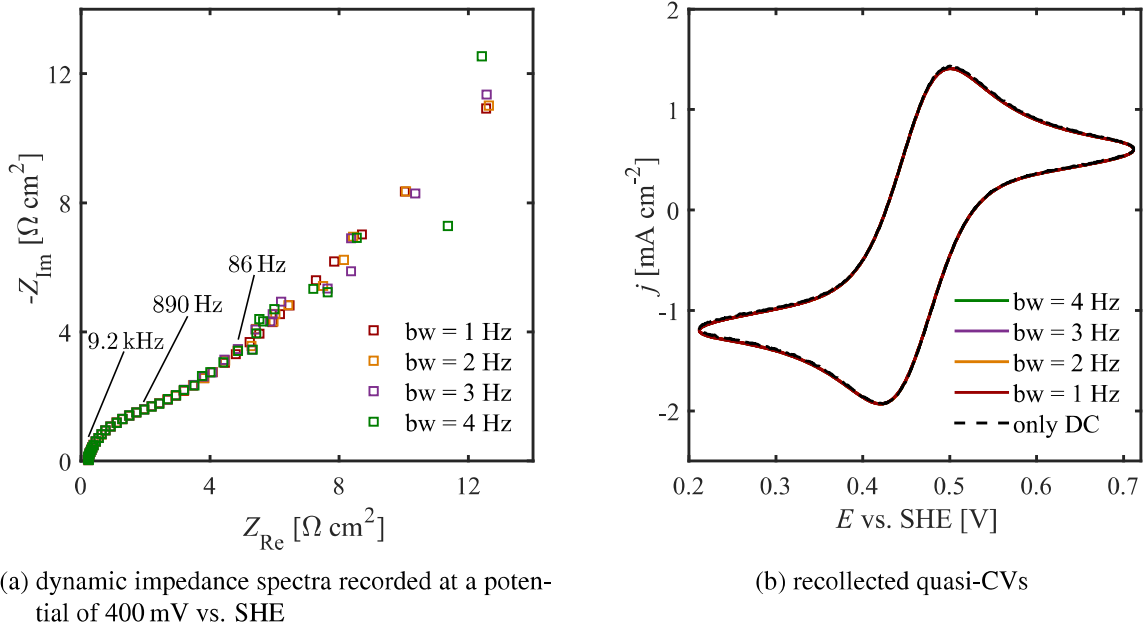


Figure 3.14.: Comparison of dynamic impedance spectra recorded in 10 mM $K_3[Fe(CN)_6]$ in 0.5 M KF at a 250 μ m Pt electrode and recollected quasi-CVs for different values of bw ranging from 1 Hz to 4 Hz. $\Delta u_{dc} = 500$ mV, $f_{dc} = 0.05$ Hz, $\Delta u_{ac} = 10$ mV, $f_b = 1$ Hz, $d = 1$.

Due to the fact that a larger distance between the fundamental harmonics allows for a more flexible choice of filter bandwidth, the measurements presented in the following Sections of this Chapter are performed with the multi-sine signal with $d = 7$, which is less sensitive to distortions and allows for the application of faster scan rates.

3.2.2. Impact of the Multi-Sine Intensity on the Linearity of the System

After having investigated how to correctly determine the bandwidth of the filter function, it is studied next in which way the intensity Δu_{ac} of the multi-sine signal affects the noise level of the output signals. To do so, Δu_{ac} is varied between 10 mV and 50 mV, where the corresponding voltage and current signals are investigated in Fourier space, illustrated in Figure 3.15. Since the background noise level of the spectra is not known exactly, a quantitative analysis of the signal-to-noise ratio cannot be performed. However, due to the nonlinearity of the system, it is possible to study the effect of the noise introduced by the nonlinear current response on the quality of the impedance spectra. The voltage spectra contain the signals corresponding to the quasi-triangular waveform as well as the peaks related to the first two fundamental frequencies of the multi-sine signal. In contrast, the current spectra do not only show the system's response to the first two fundamental signals but also contain the nonlinear second and third order harmonics related to the lowest multi-sine frequency. The intensity of the different peaks increases with increasing multi-sine amplitude. While the noise level of the first fundamental harmonic is influenced by the third order harmonic signal, the second order harmonic affects the zeroth harmonic. Here, the zeroth harmonic refers to the *dc* component of the signal. The current signals related to the first fundamental frequency and its second order harmonic are clearly visible in the spectra. In contrast, the intensity of the third order harmonic is negligibly small. Therefore, the change in current intensity of the first order harmonic signals upon variation of the multi-sine amplitude is examined with respect to the change in intensity of their second order harmonics. When the current intensity of a harmonic signal is proportionally related to the amplitude of the multi-sine input, such that

$$I_{abs} = b \Delta u_{ac}^p, \quad (3.6)$$

then

$$\log I_{abs} = \log b + p \log \Delta u_{ac}, \quad (3.7)$$

where b is a constant and p represents the slope of the function that reflects the order of proportionality (LeVeque, 2007). The absolute current signals I_{abs} related to the first order harmonic of the lowest frequency contained in the multi-sine signal, recorded at different values of Δu_{ac} , are shown in the below Table 3.1. Here, I_{abs} corresponds to the amplitude of the central peak of the signal. Equation (3.7) is derived from a first degree polynomial fit to the logarithmically

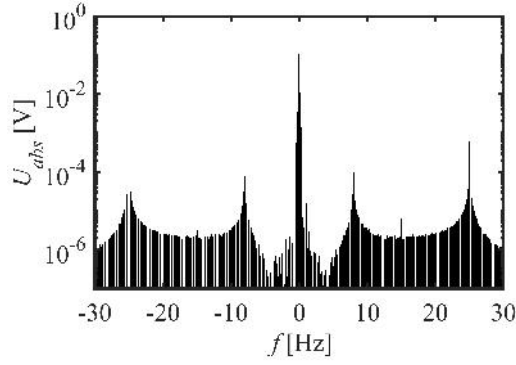
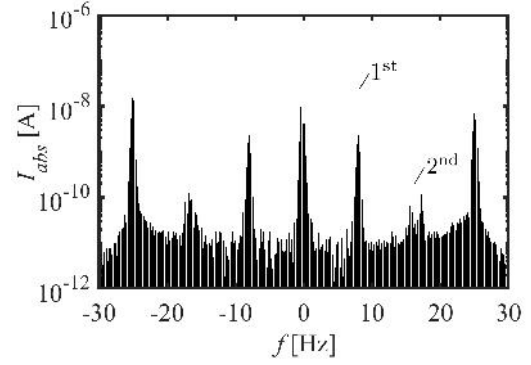
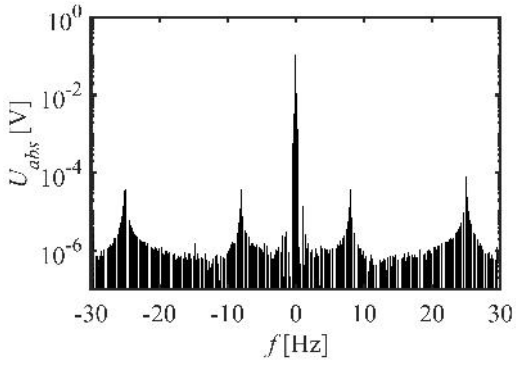
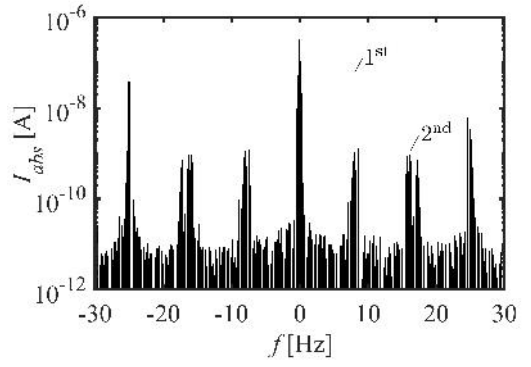
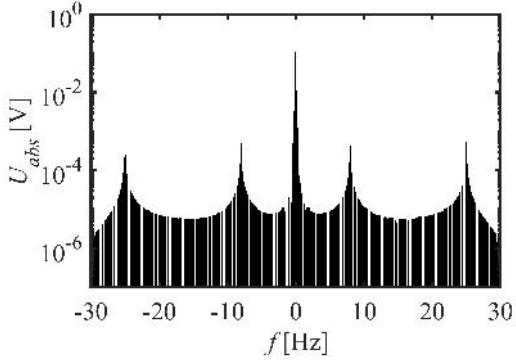
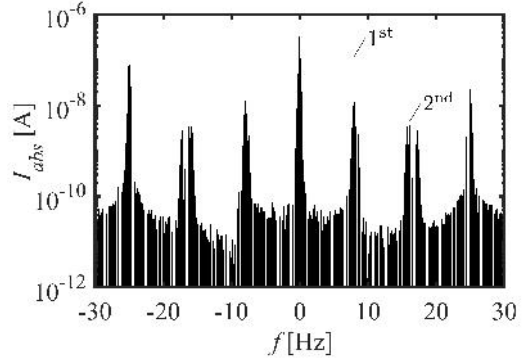
(a) FT of potential, $\Delta u_{ac} = 10$ mV(b) FT of current, $\Delta u_{ac} = 10$ mV(c) FT of potential, $\Delta u_{ac} = 25$ mV(d) FT of current, $\Delta u_{ac} = 25$ mV(e) FT of potential, $\Delta u_{ac} = 50$ mV(f) FT of current, $\Delta u_{ac} = 50$ mV

Figure 3.15.: Potential perturbation and current response recorded in 10 mM $\text{K}_3[\text{Fe}(\text{CN})_6]$ in 0.5 M KF at a $250\text{ }\mu\text{m}$ Pt electrode for a multi-sine signal in the low-frequency range. The measurements were performed at different multi-sine amplitudes. $\Delta u_{dc} = 500$ mV, $f_{dc} = 0.05$ Hz, $f_b = 1$ Hz, $d = 7$.

plotted data pairs. The experimental data and the corresponding fitted function are graphically represented in Figure 3.16a. The slope p takes a value of 0.99, thus, according to (3.6), the intensity of the first order harmonic signal is directly proportional to the amplitude of the multi-sine wave.

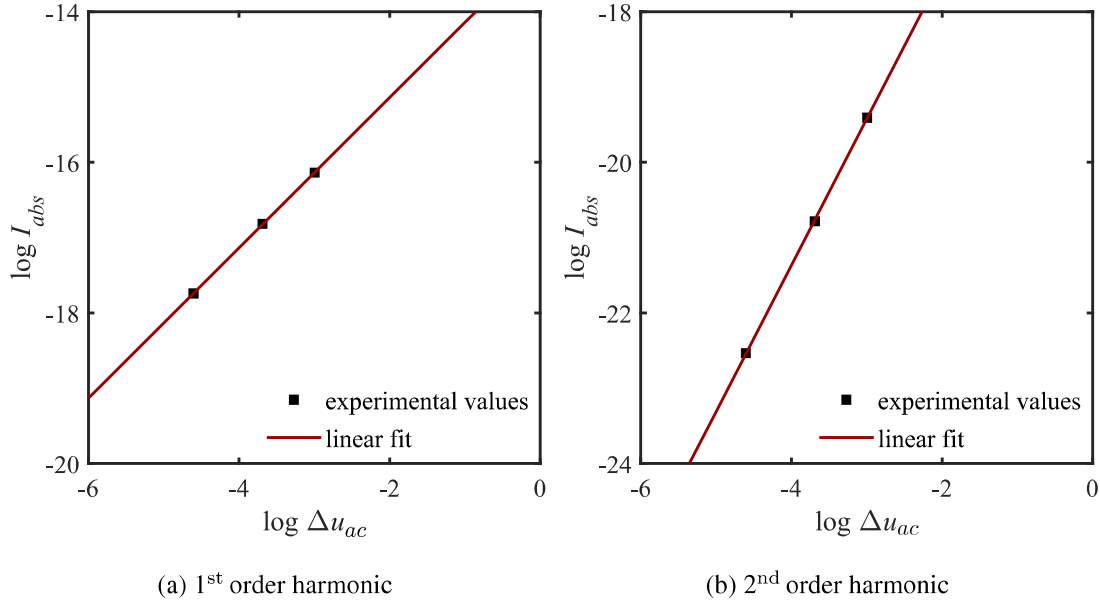


Figure 3.16.: Intensities of first order and second order harmonic signals related to the lowest frequency contained in the multi-sine signal at different values of Δu_{ac} .

In a similar way, the second order current response can be investigated. The corresponding current values are given in Table 3.2. Again, the first degree polynomial equation is obtained from linear data interpolation. In this case, p is equal to 1.94, thus revealing that the second order harmonic signals increase quadratically with Δu_{ac} , see Figure 3.16b.

Table 3.1.: Intensity of the first order harmonic current signal at different multi-sine amplitudes. The value I_{abs} refers to the amplitude of the peak located in the center of the signal.

Δu_{ac} [mV]	$\log \Delta u_{ac}$	I_{abs} [A]	$\log I_{abs}$
10	-2.00	1.97×10^{-8}	-7.71
25	-1.60	4.97×10^{-8}	-7.30
50	-1.30	9.80×10^{-8}	-7.01

Table 3.2.: Intensity of the second order harmonic current signal at different multi-sine amplitudes. The value I_{abs} refers to the amplitude of the peak located in the center of the signal.

Δu_{ac} [mV]	$\log \Delta u_{ac}$	I_{abs} [A]	$\log I_{abs}$
10	-2.00	1.64×10^{-10}	-9.79
25	-1.60	9.42×10^{-10}	-9.03
50	-1.30	3.73×10^{-9}	-8.43

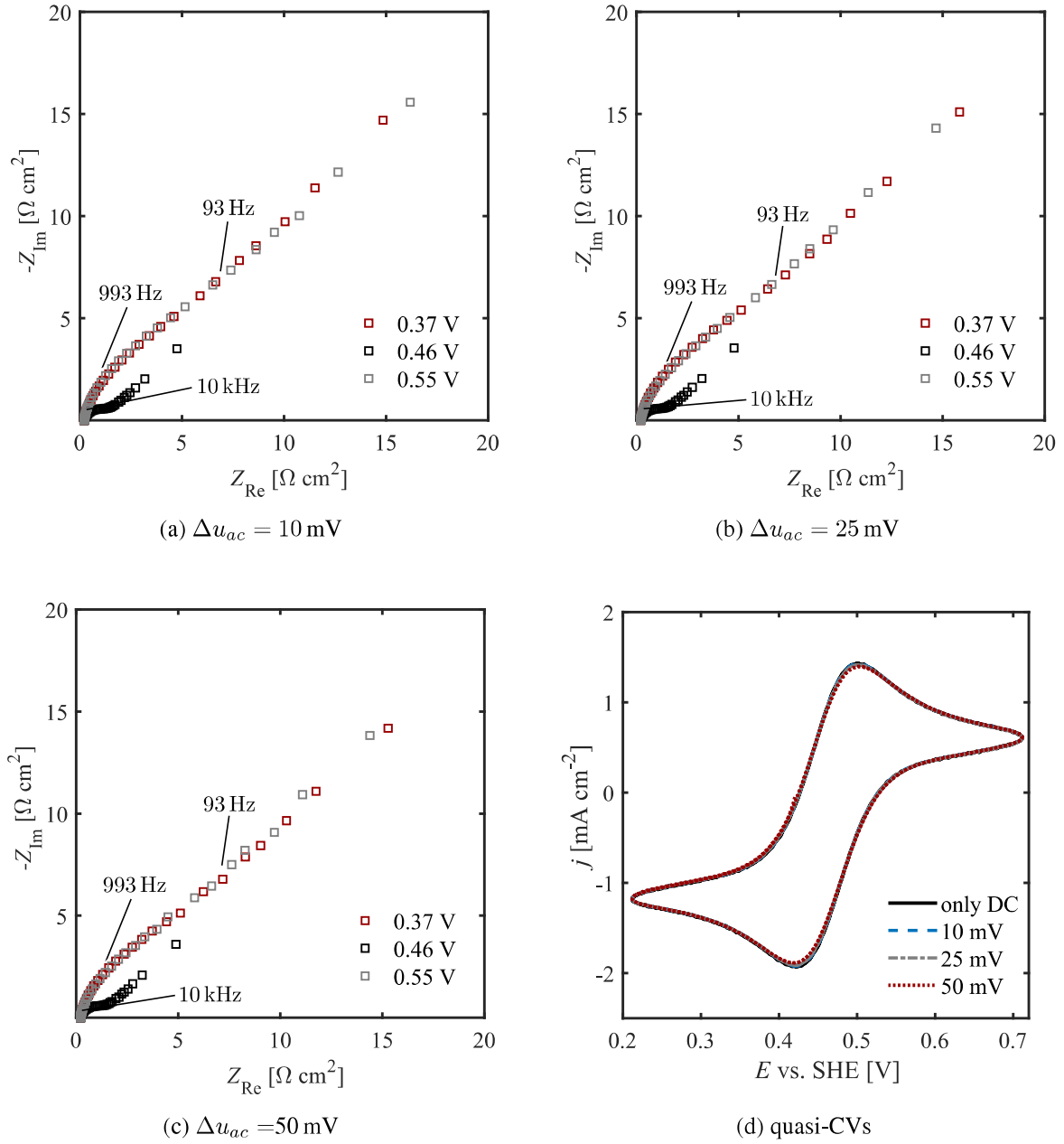


Figure 3.17.: Comparison of dynamic impedance spectra recorded in 10 mM $\text{K}_3[\text{Fe}(\text{CN})_6]$ in 0.5 M KF at a $250 \mu\text{m}$ Pt electrode using different values of multi-sine amplitude Δu_{ac} and corresponding quasi-CVs. $\Delta u_{dc} = 500 \text{ mV}$, $f_{dc} = 0.05 \text{ Hz}$, $f_b = 1 \text{ Hz}$, $d = 7$, $\text{bw} = 2 \text{ Hz}$.

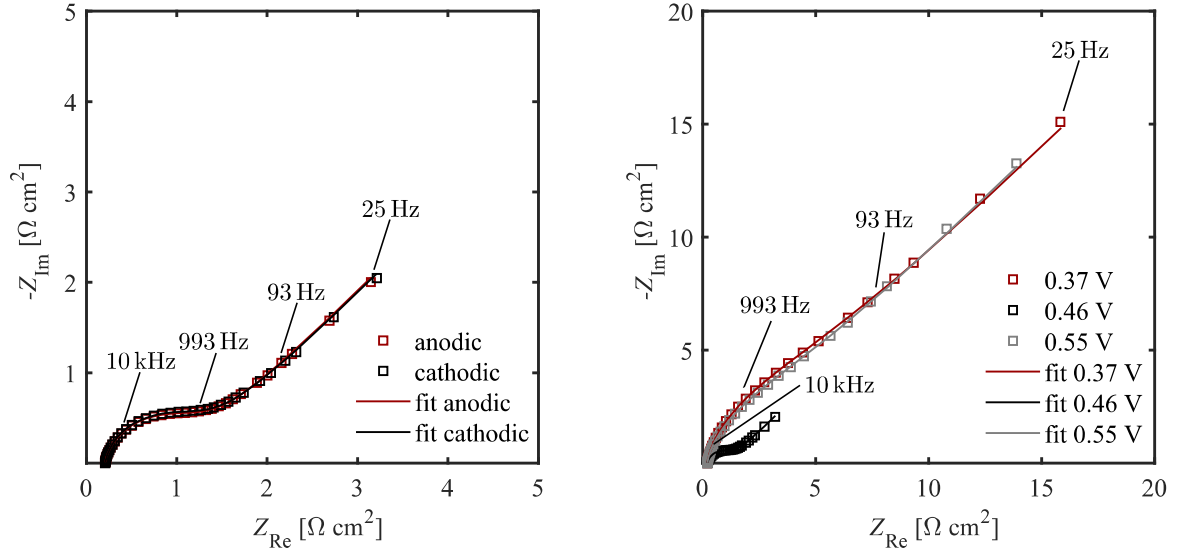
The above Figure 3.17 shows the dynamic impedance spectra extracted from the different data sets presented in Figure 3.15, where the bandwidth of the filter was set to a value of 2 Hz ($2 \times f_b$). The variation in multi-sine amplitude in a range between 10 mV and 50 mV does not lead to significant changes in the impedance spectra. As pointed out earlier in this Section, the second order harmonic introduces noise at the fundamental frequency of the quasi-triangular wave. As the nonlinear current contribution increases quadratically with the multi-sine amplitude, while the intensity of the fundamental harmonics only increases linearly, it is expected

that an increase in multi-sine amplitude causes severe distortions in the quasi-triangular waveform. However, Figure 3.17d shows that the intensity of the non-linear current component does not considerably affect the shape of the quasi-CV. Moreover, third order harmonic signals are negligibly small with respect to the fundamental harmonic signals. Therefore, it is concluded that the system can be considered quasi-linear when varying the multi-sine intensity in a range between 10 mV and 50 mV. It has to be noted that these values might considerably differ depending on the multi-sine signal and the system under investigation. In general, it can be stated that the condition of quasi-linearity holds as long as second and third order harmonics do not introduce distortions in the fundamental harmonics of the quasi-CV and the multi-sine wave, respectively, where second order current signals can be discarded by proper choice of filter bandwidth, as described in Section 3.2.1.

3.2.3. Impedance Analysis using Equivalent Circuits

The previous Sections of this Chapter dealt with a qualitative approach for the determination of appropriate parameter settings for the acquisition of reliable dynamic impedance spectra by means of DMFA. Based on these results, DMFA is applied in order to study the reaction kinetics of the system under investigation, where the dynamic impedance spectra recorded with $\Delta u_{ac} = 25$ mV, presented in Figure 3.17b, are studied in more detail. At a potential of 460 mV vs. SHE the spectra exhibit the typical shape of a fast charge transfer reaction, showing a high-frequency loop followed by a straight line forming an angle of 45° with the real axis. The spectra recorded on the anodic and cathodic branch of the scan are almost identical, see Figure 3.18a. While the semicircle in the high-frequency range can be attributed to an electron transfer process, the straight line in the low-frequency region is related to a diffusion impedance.

As already discussed in Section 2.3.2, dynamic impedance spectra may be interpreted using EECs, where the physical processes governing the reaction are related to passive circuit elements. To do so, data fitting was performed on the spectra presented in Figure 3.17b. CNLS regression was carried out using the algorithm developed in Section 2.4.4. The dynamic impedance spectra were fitted to the EEC presented in Figure 3.19. The spectra recorded on the anodic and cathodic branch of the quasi-CV were fitted separately in a potential range between 0.3 V and 0.6 V vs. SHE. The circuit can be understood as a modified version of the Randles circuit. The classic Randles circuit, introduced in Section 2.3.2, was found to serve as a suitable electrical analogue for the redox reaction of the $K_3[Fe(CN)_6]/K_4[Fe(CN)_6]$ couple when investigating simulated data (Battistel, 2016). In real-world conditions, the non-uniform disk current density distribution requires the use of a constant phase element (CPE) instead of an ideal capacitor. The CPE is composed of Q_{dl} and its corresponding phase angle n_{dl} from which an effective capacitance C_{dl} is calculated using (7.3). In addition to that, the parameter R_w is arranged in



(a) dynamic impedance spectra recorded at a potential of 460 mV vs. SHE

(b) experimental and fitted spectra at different potentials

Figure 3.18.: Experimental and fitted dynamic impedance spectra recorded in 10 mM $\text{K}_3[\text{Fe}(\text{CN})_6]$ in 0.5 M KF at a 250 μm Pt electrode. $\Delta u_{dc} = 500 \text{ mV}$, $f_{dc} = 0.05 \text{ Hz}$, $\Delta u_{ac} = 25 \text{ mV}$, $f_b = 1 \text{ Hz}$, $d = 7$, $\text{bw} = 2 \text{ Hz}$.

parallel with the Warburg element. R_w is used as a mathematical correction term in order to describe the slightly different diffusion behavior observed in dynamic conditions. Since the parameter R_w does not have any physical meaning, it is not addressed in the following discussion. As illustrated in Figure 3.18, the fitted spectra match the experimental results very well. Moreover, the χ^2 values of 1.78×10^{-4} and 1.81×10^{-4} obtained for the anodic and cathodic scan direction, respectively, reveal that the quality of the fitting is very high. In Figure 3.20 the extracted kinetic variables are represented as a function of potential, where the values are given per unit surface area. During the fitting procedure the smoothing coefficient was set to 0.1 for C_{dl} , R_{ct} , and σ_{ct} . Thus, the variables were allowed to change almost freely along the potential axis. In contrast, it was assumed that R_s is not affected by variations in potential. The solution

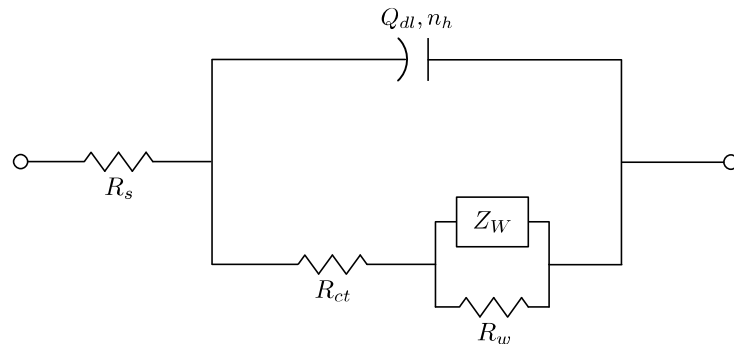


Figure 3.19.: Modified Randles circuit.

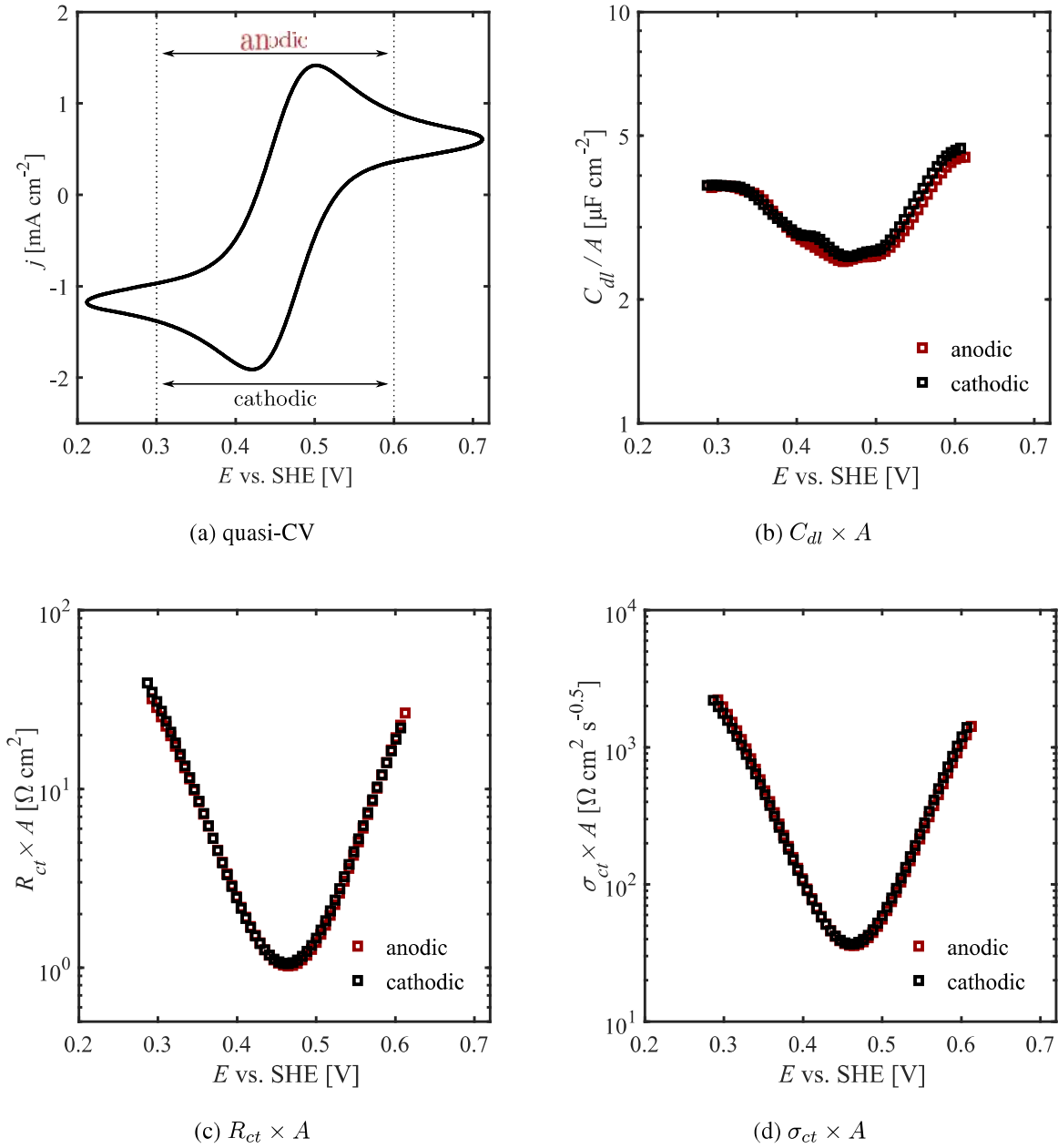


Figure 3.20.: Temporal evolution of fitting parameters extracted from data fitting of the dynamic impedance spectra recorded at a 250 μm electrode with the EEC presented in Figure 3.19.

resistance can be predicted using Newman's formula, which is defined as

$$R_s = \frac{1}{4\kappa r}, \quad (3.8)$$

where κ is the ionic conductivity and r is the radius of the disk electrode (Orazem, 2017). The calculated value of $0.22 \Omega \text{ cm}^2$ is in good agreement with the solution resistance extracted from data fitting, taking a value of $0.21 \Omega \text{ cm}^2$ for both directions of the scan. The variable n_{dl} varies in a range between 0.88 and 0.90, indicating that the behavior of the CPE is similar to that

of a pure capacitor. The variation of the different quantities along the potential axis is almost independent of the direction of the scan, where the small deviations can be attributed to the dynamic nature of the measurement, which lead to a slight difference in concentration ratio between oxidized and reduced species. Although the values extracted for C_{dl} are slightly lower than the values reported in literature (Gabrielli, 2006), they are still in a reasonable range. In this case, the deviation from literature values may be due to a difference in Pt surface properties.

As expected, the charge transfer resistance reaches a minimum value of $1.1 \Omega \text{ cm}^2$ at the intermediate point of the quasi-CV, thus indicating that at this potential the reaction rate is at a maximum, as this parameter is directly linked to the standard rate constant through the relationship

$$k^0 = \frac{RT}{n^2 F^2} \frac{1}{R_{ct} c_i(x = \infty)},$$

where $c_i(x = \infty)$ corresponds to the bulk concentration of the reactive species (Gabrielli, 2006). The R_{ct} value significantly increases up to $39.2 \Omega \text{ cm}^2$ when the potential is swept towards the extrema of the quasi-CV. The Warburg coefficient σ_{ct} follows the same trend, having a minimum at the standard potential of the redox couple. In order to determine the rate-limiting process of the redox reaction, a diffusion resistance R_d was calculated by multiplication of the Warburg coefficient with the square-root of the time constant of diffusion τ_d , such that

$$R_d = \sigma_{ct} \sqrt{\tau_d}, \quad (3.9)$$

where

$$\tau_d = \frac{r^2}{D_i}. \quad (3.10)$$

Here, D_i represents the diffusion coefficient of the reactive species. Due to the excess concentration of supporting electrolyte, only the diffusion coefficient of the reactive $[\text{Fe}(\text{CN})_6]^{3-}$ ion is considered. It has to be noted that this value serves as an approximate value, as the concentration ratio of the $[\text{Fe}(\text{CN})_6]^{3-}/[\text{Fe}(\text{CN})_6]^{4-}$ couple continuously changes throughout the scan. As the diffusion coefficients of the oxidized and the reduced species are very similar, this value represents a reasonable approximation to the actual coefficient, see Table 7.4. According to (3.10), the time constant of diffusion is equal to 17.4 s, thus resulting in $R_d \times A$ values ranging from $0.15 \text{ k}\Omega \text{ cm}^2$ at the intermediate potential to $9.18 \text{ k}\Omega \text{ cm}^2$ at potentials close to the reversal points of the quasi-CV. Due to the fact that $R_d \times A$ is much higher than the values obtained for $R_s \times A$ and $R_{ct} \times A$, it is concluded that mass transport is the rate-limiting step of the redox reaction.

3.2.4. Effect of the Electrode Dimension on the Reaction Kinetics

As shown in the previous Section, mass transport of electro-active species to the electrode surface significantly affects the electron transfer rate across the electrode/electrolyte interface. Microelectrodes exhibit some outstanding features that allow for kinetic studies of fast electrode reactions. The main characteristic of microelectrodes is that they are smaller in at least one of their dimensions than the diffusion layer thickness that develops in the time scale of the experiment (Bard, 2001). Typically, the dimension of a microelectrode is in the order of tens of micrometers or less (Stulik et al., 2000). This property leads to a quasi-hemispherical diffusion profile at microdisk electrodes. Due to the enhanced diffusion field, the efficiency of mass transport is significantly increased with respect to that observed at disk macroelectrodes, where planar diffusion dominates (Fleischmann, 1991), see Figure 3.21. Due to their unique properties, DMFA was performed at Pt disk microelectrodes having a diameter of 25 μm in order to study the effect of the electrode dimension on the reaction kinetics. In particular, it was investigated if microelectrodes may be employed for the acquisition of reliable dynamic impedance spectra by means of DMFA.

Fick's first law can be employed to describe the flux of a species as a function of position and time, see e.g Bard (2001), such that

$$J_i(x, t) = -D_i \frac{\partial c_i(x, t)}{\partial x}, \quad (3.11)$$

where J_i is the flux of the species i , D_i is the diffusion coefficient of the substance, and x is the distance to the electrode surface. In (3.11), $c_i(x = 0)$ refers to the surface concentration of the species, whereas $c_i(x = \infty)$ corresponds to its bulk concentration. At $t = 0$, $c_i(x = 0)$ equals $c_i(x = \infty)$. In contrast, for $t > 0$, $c_i(x = 0) < c_i(x = \infty)$ (Buchberger, 1998). The partial derivative $\frac{\partial c_i(x, t)}{\partial x}$ represents the concentration gradient that forms due to the depletion of electro-active species, which extends from the electrode surface to the location x . This region is referred to as the diffusion layer. The current flow is proportional to the flux and can be

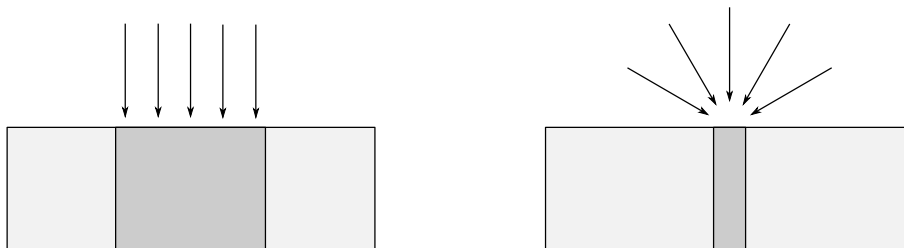


Figure 3.21.: Planar diffusion profile at disk macroelectrodes (left) and quasi-hemispherical diffusion at microdisk electrodes (right).

expressed as

$$i(x, t) = -nFA D_i \frac{\partial c_i(x, t)}{\partial x}, \quad (3.12)$$

where A is the area of the electrode. Equations (3.11) and (3.12) are limited to steady-state conditions. Under the assumption that the concentration gradient changes linearly within the diffusion layer, (3.12) can be rewritten as

$$i(x, t) = -nFA D_i \frac{c_i(x = \infty) - c_i(x = 0)}{\delta}. \quad (3.13)$$

Here, δ corresponds to the thickness of the diffusion layer (Buchberger, 1998). When applying a potential at which the electroactive species reacts so fast that its surface concentration $c_i(x = 0)$ is zero, (3.13) becomes

$$i(x, t) = -nFA D_i \frac{c_i(x = \infty)}{\delta}.$$

In nonstationary conditions δ is not constant but increases with increasing electrolysis time due to the ongoing depletion of reactive substances in the vicinity of the electrode surface, following

$$\delta = \sqrt{\pi D_i t}. \quad (3.14)$$

With (3.14), the diffusion limited current at disk macroelectrodes is defined as

$$i_l = -\frac{nFA D_i c_i(x = \infty)}{\sqrt{\pi D_i t}}. \quad (3.15)$$

Equation (3.15) is referred to as the Cottrell equation (Bard, 2001).

In contrast, microdisk electrodes can be characterized by their steady-state current, which is given by

$$i_{ss} = -\frac{nFA D_i c_i(x = \infty)}{\sqrt{\pi D_i t}} - \frac{4nFA D_i c_i(x = \infty)}{\pi r}, \quad (3.16)$$

where r is the radius of the electrode (Bard, 2001). From (3.16) it follows that i_{ss} is composed of a time-dependent and a time-independent term, where the current reaches a steady-state value when $\sqrt{\pi D_i t} \gg r$. Under these conditions, the first term on the right-hand side of (3.16) can be omitted and the time-independent term dominates. Steady-state conditions can be readily achieved at disk-microelectrodes, as the diffusion layer thickness only has to grow to the dimension of the disk (Bard, 2001). However, when $\sqrt{\pi D_i t} \ll r$, i.e. at very short times, the time-independent term becomes negligibly small and (3.16) takes the form of the Cottrell equation.

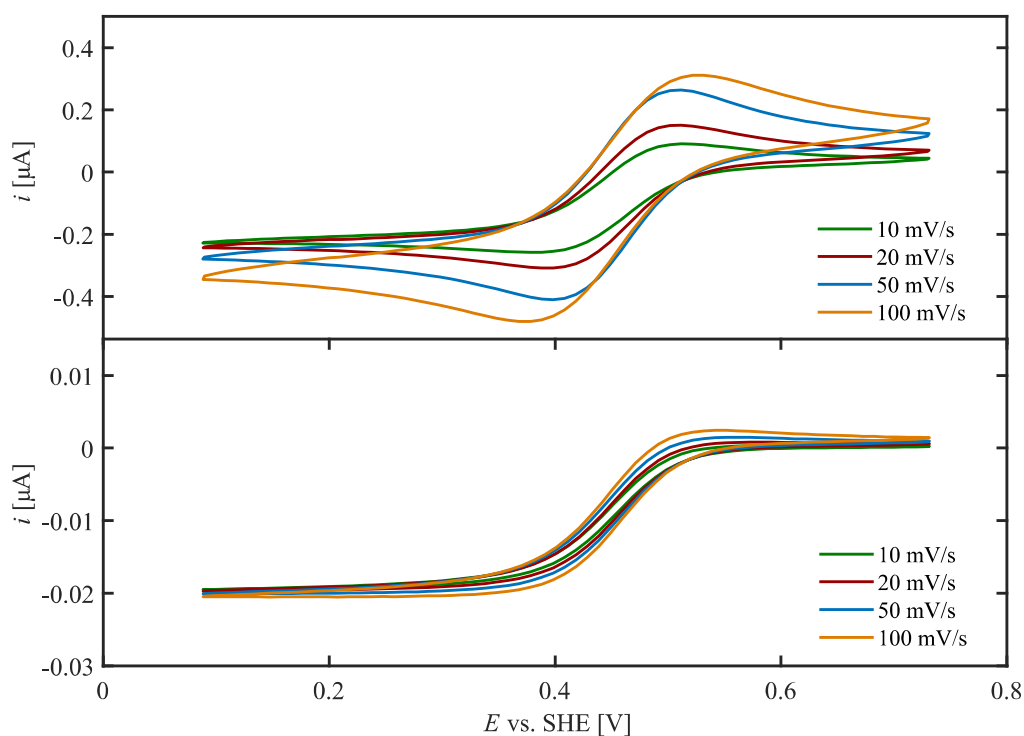


Figure 3.22.: Comparison of CVs recorded in 5 mM $K_3[Fe(CN)_6]$ in 0.5 M KF at a 250 μm (top) and at a 25 μm (bottom) Pt electrode. The measurements were performed at different scan rates ranging from 10 to 100 $mV s^{-1}$.

The above Figure 3.22 compares the voltammetric behavior of Pt macro- and microelectrodes at different scan rates. The measurements were carried out in 5 mM $K_3[Fe(CN)_6]$ in 0.5 M KF. The top Figure shows the CVs recorded at a 250 μm Pt electrode. In agreement with the above discussions, the peak-shaped voltammograms exhibit the characteristic features of a diffusion limited reaction at a stationary disk macroelectrode. Under these conditions, the peak current follows the scan rate dependence predicted by the Randles-Sevcik equation, which is given by

$$i_p = 0.4463 \sqrt{\left(\frac{F^3}{RT}\right) n^{\frac{3}{2}} A c_i \sqrt{D_i \nu}}. \quad (3.17)$$

Figure 3.23 provides a comparison of the measured peak currents and those calculated from (3.17). Here, the logarithmic i_p values are plotted as a function of the logarithm of the scan rate. Both data sets were fitted using linear data interpolation, where a slope of 0.55 and 0.50 was obtained for the fitted functions of the experimental and the calculated values, respectively, thus revealing that the peak current shows the square root dependence that is predicted by (3.17).

In contrast, the CVs recorded at a 25 μm Pt electrode do not exhibit the peak shape that is observed at macroelectrodes. Instead, the current attains steady-state values of about 20 nA that are almost independent of the scan rate. The values are in good agreement with the cal-

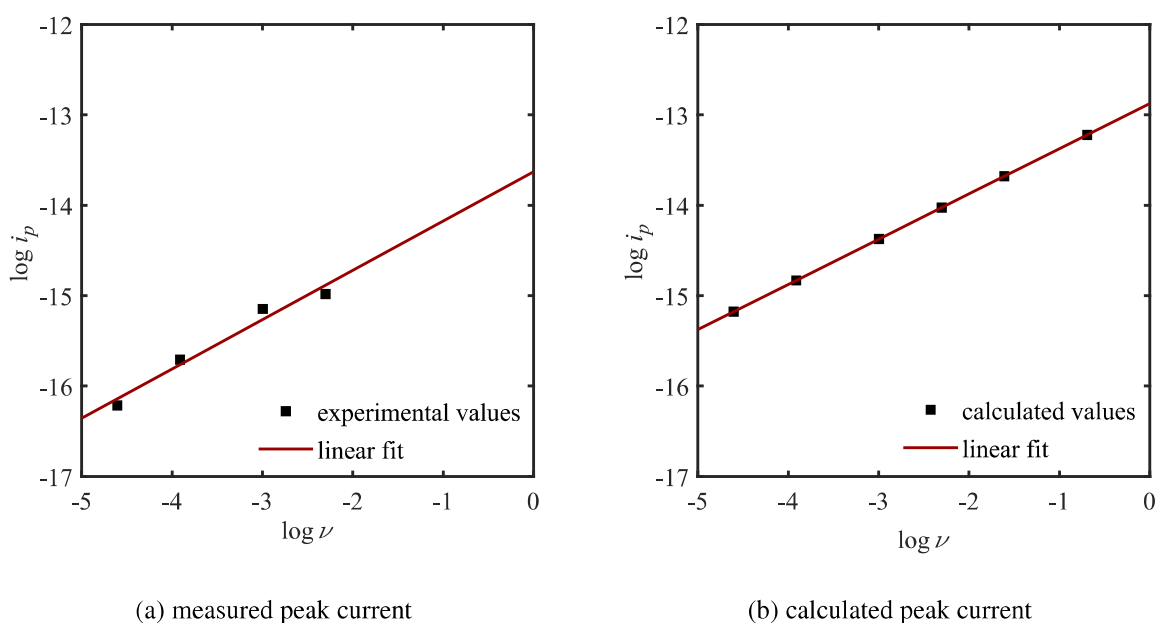


Figure 3.23.: Measured and calculated peak currents for the redox process at a 250 μm electrode at different scan rates.

culated value of 21.6 nA. The latter is obtained from (3.16), where the time-dependent term is neglected. These values indicate that the microscopic and the geometric electrode area are practically identical. The CVs confirm that a quasi-hemispherical diffusion profile is established on the electrode.

Although there is no direct dependence of the scan rate on the steady-state current recorded at microelectrodes, an accurate determination of a steady-state current is only possible if

$$\nu \ll \frac{RTD_i}{nFr^2} \quad (3.18)$$

holds (Bard, 2001). Equation (3.18) reveals that the steady-state response recorded at a 25 μm electrode under the conditions outlined above is constant unless the scan rate exceeds values of 147 mV s^{-1} . Otherwise, the time-dependent term of (3.16) governs the reaction and mass transport limitations can no longer be neglected, as shown in Figure 3.24.

Reaction Dynamics at Microelectrodes

In order to investigate the effect of the electrode dimension on the reaction kinetics, dynamic impedance spectra were recorded at the 25 μm electrode in 10 mM solution of $\text{K}_3[\text{Fe}(\text{CN})_6]$ in 0.5 M KF, using the same experimental settings that were employed throughout the acquisition of the dynamic impedance response at macroelectrodes. In contrast to the measurements presented in Section 3.2.3, the amplitude of the multi-sine signal was changed to a value of $u_{ac} = 50 \text{ mV}$, thus resulting in an enhanced signal-to-noise ratio. Under these conditions, the

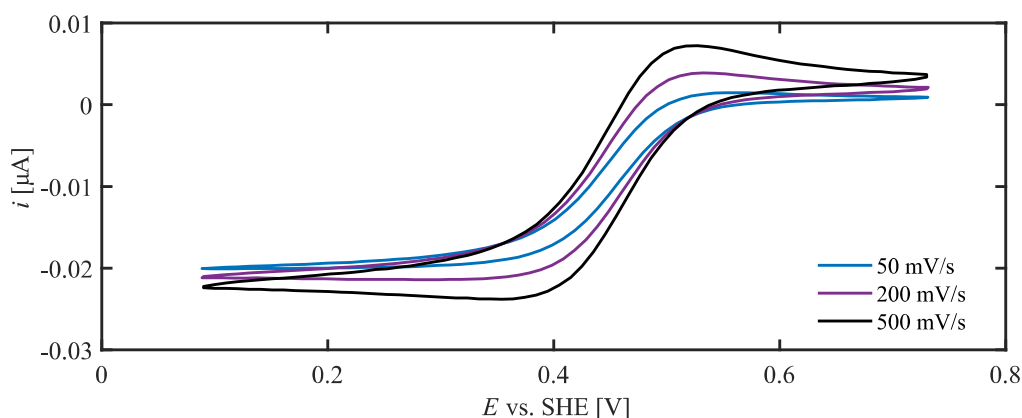


Figure 3.24.: Comparison of CVs recorded in 5 mM $\text{K}_3[\text{Fe}(\text{CN})_6]$ in 0.5 M KF at a 25 μm Pt electrode. The measurements were performed at different scan rates ranging from 50 to 500 mV s^{-1} .

system can be considered quasi-linear, since the intensity of the nonlinear signals is sufficiently small, as demonstrated in Appendix C.

The low-frequency impedance response of disk microelectrodes considerably differs from that observed at planar macroelectrodes (Fleischmann, 1991). At sufficiently low frequencies the imaginary part of the impedance recorded at microelectrodes tends towards zero, thus indicating the steady-state of diffusion, as observed in the CVs presented in Figure 3.22. This type of finite diffusion behavior can no longer be fitted by means of a classic Warburg element and must be captured using more complex differential equations (Fleischmann, 1991). However, when recording the impedance within a range of frequencies where steady-state diffusion behavior has not yet been established, the low-frequency region of the impedance spectrum resembles that observed for semi-infinite diffusion, as schematically depicted in Figure 3.25. The characteristic frequency f_d related to the diffusion process can be deduced from the diffusion coefficient and the radius of the WE, such that

$$f_d = \frac{D_i}{r^2}. \quad (3.19)$$

According to (3.19), f_d quadratically increases with decreasing radius of the electrode. For the redox system investigated here, the diffusion process may be observed at a characteristic frequency of 0.05 Hz when employing a 250 μm disk WE. In contrast, when using a microelectrode of 25 μm diameter, the value is shifted to 5 Hz.

The below Figure 3.26 shows the dynamic impedance spectra recorded at the 25 μm electrode at different potentials throughout the anodic and cathodic sweep. The spectra exhibit similar features as those recorded at macroelectrodes, where the imaginary part of the impedance increases with decreasing frequencies. This behavior is in good agreement with the above dis-

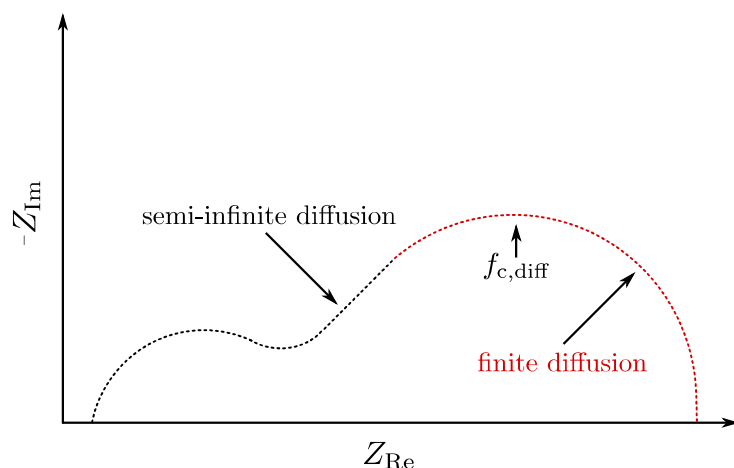


Figure 3.25.: Schematic representation of semi-infinite and finite-diffusion.

cussion, since the lowest frequency of 25 Hz exceeds the characteristic frequency of diffusion, indicating that the time-scale of the low-frequency perturbation is so small that a steady-state has not yet been reached. Therefore, the spectra can be fitted using the modified Randles circuit presented in Figure 3.19, containing the classic Warburg element. Although the slope of the impedance curve in the low-frequency region is not as steep as that observed in Figure 3.18, the quality of the fitting is very good. The χ^2 values obtained for the anodic and cathodic direction of the scan are equal to 5.52×10^{-5} and 5.69×10^{-5} , respectively, thus corresponding to an error of less than 0.8%.

The potential variation of the different kinetic variables that were extracted from the dynamic impedance spectra recorded at microelectrodes is illustrated in Figure 3.27. When calculated per unit surface area, all variables are in the same order of magnitude and follow the same trend as those observed at macroelectrodes. As demonstrated in Table 3.3, the values of $R_{ct} \times A$ and $\sigma_{ct} \times A$ that were extracted at the standard potential of the scan are very similar to those obtained at the 250 μm electrode. This behavior is not surprising, as the electron transfer kinetics in the intermediate potential region, and thus $R_{ct} \times A$, should not be affected by the dimension of the electrode. Also $\sigma_{ct} \times A$ should not change, as it only depends on the diffusion coefficient and on the concentration of reactive species at the electrode surface, which are the same on macro- and microelectrodes when defined per unit surface area. Due to the fact that the potential regions close to the reversal points of the quasi-CV are more affected by the diffusion profile,

Table 3.3.: Charge transfer resistance and Warburg coefficient per unit surface area extracted from data fitting at 0.46 V vs. SHE for different electrode geometries.

electrode geometry	surface area [cm^2]	$R_{ct} \times A$ [$\Omega \text{ cm}^2$]	$\sigma_{ct} \times A$ [$\Omega \text{ cm}^2 \text{ s}^{-0.5}$]
250 μm disk	4.91×10^{-4}	1.1	36.7
25 μm disk	4.91×10^{-6}	1.7	35.1

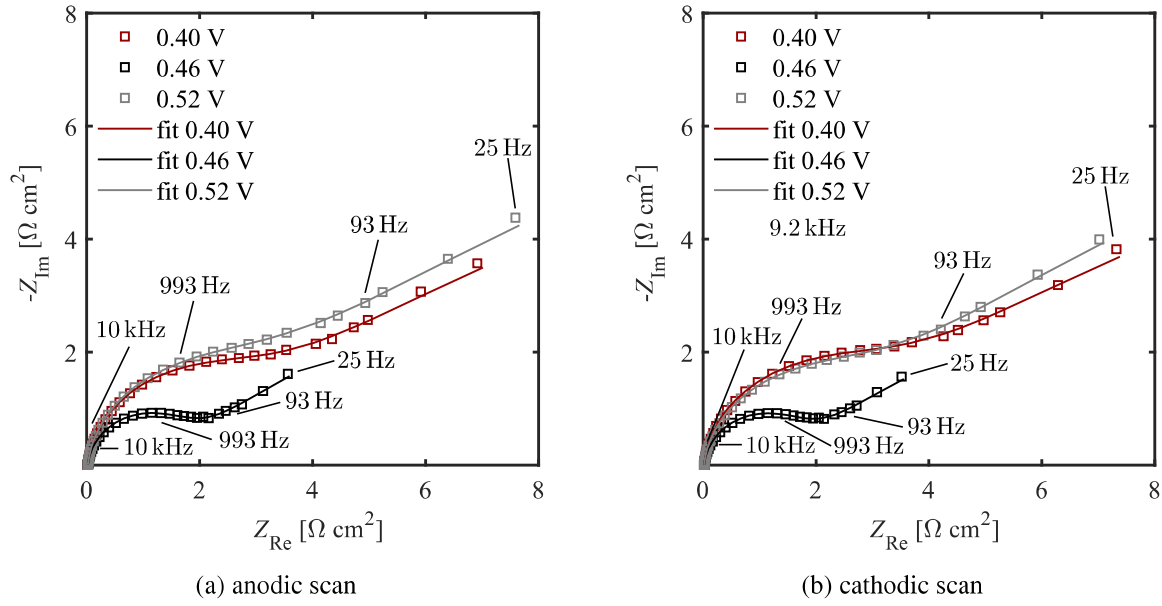


Figure 3.26.: Experimental and fitted dynamic impedance spectra recorded in 10 mM $K_3[Fe(CN)_6]$ in 0.5 M KF at a 25 μm Pt electrode. $\Delta u_{dc} = 500$ mV, $f_{dc} = 0.05$ Hz, $\Delta u_{ac} = 50$ mV, $f_b = 1$ Hz, $d = 7$, bw = 2Hz.

the different quantities are compared at a potential of 0.55 V vs. SHE in order to detect possible changes in electron transfer and diffusion behavior. However, even at this point in potential, the variables are not significantly affected by the size of the electrode and have similar values per unit surface area, as reported in Table 3.4. In contrast, the diffusion resistance calculated from (3.9), decreases proportionally to the size of the electrode, where the values are listed in Table 3.5. Although the diffusion resistance calculated for microelectrodes is significantly smaller than that observed at macroelectrodes, it still exceeds the values of R_s ($0.22 \Omega \text{ cm}^2$) and R_{ct} and thus remains the rate-limiting parameter.

Table 3.4.: Charge transfer resistance and Warburg coefficient per unit surface area extracted from data fitting at 0.55 V vs. SHE for different electrode geometries.

electrode geometry	surface area [cm^2]	$R_{ct} \times A$ [$\Omega \text{ cm}^2$]	$\sigma_{ct} \times A$ [$\Omega \text{ cm}^2 \text{ s}^{-0.5}$]
250 μm disk	4.91×10^{-4}	5.3	281.4
25 μm disk	4.91×10^{-6}	5.3	298.5

Table 3.5.: Diffusion resistance per unit surface area calculated from (3.9) for different electrode geometries.

electrode geometry	surface area [cm^2]	$R_{d(0.46 \text{ V})} \times A$ [$\Omega \text{ cm}^2$]	$R_{d(0.55 \text{ V})} \times A$ [$\text{k}\Omega \text{ cm}^2$]
250 μm disk	4.91×10^{-4}	153.4	1.17
25 μm disk	4.91×10^{-6}	14.9	0.15

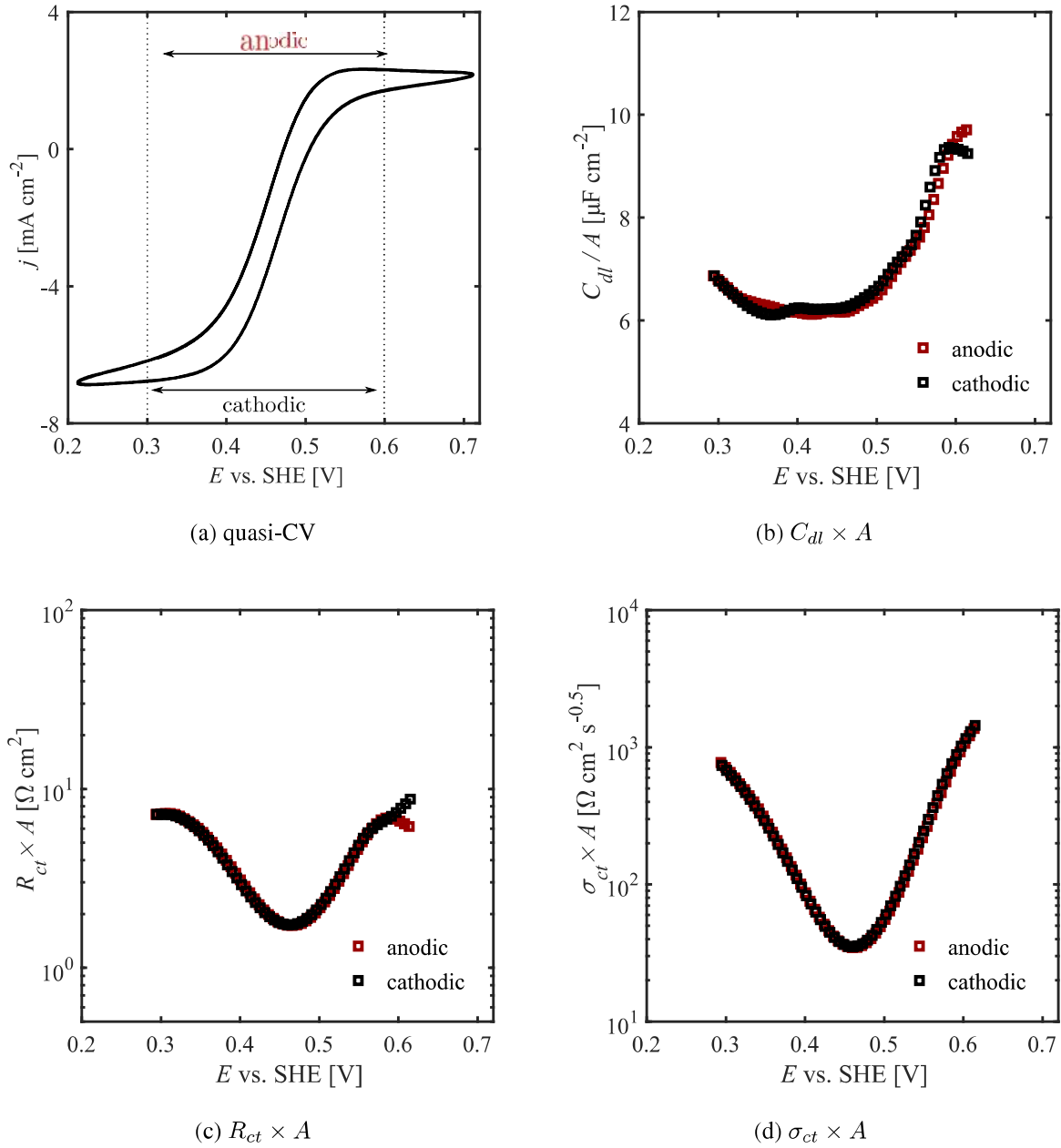


Figure 3.27.: Temporal evolution of fitting parameters extracted from data fitting of the dynamic impedance spectra recorded at a 25 μm electrode with the EEC presented in Figure 3.19.

Although the use of microelectrodes may be particularly useful in some conditions, e.g. when higher scan rates are required or when measuring in solutions of low conductivity, it has to be noted that the absolute resistance values are significantly increased when using microelectrodes. According to (3.8), the solution resistance proportionally increases with decreasing size of the electrode. Under the conditions specified above, the electrolyte resistance is about 400 Ω when employing a disk electrode of 250 μm diameter. In contrast, the value increases to approximately 4 kΩ when using an electrode of 25 μm diameter. This raise in electrolyte resistance may cause high-frequency artefacts, addressed in Chapter 4.

Reaction Dynamics at Multibarrel Electrodes

Multibarrel electrodes, being composed of a bundle of individual microelectrodes, represent an attractive alternative to single electrodes, as they exhibit microelectrode characteristics without suffering from the disadvantages outlined above. Therefore, multibarrel electrodes were produced according to the procedure outlined in Section 7.3.1. Each bundle was composed of a set of six individual Pt electrodes, each having a diameter of 25 μm . Therefore, the geometric area of the electrode was equal to $2.95 \times 10^{-5} \text{cm}^2$. The electrode was characterized by means of cyclic voltammetry in 10 mM solution of $\text{K}_3[\text{Fe}(\text{CN})_6]$ in 0.5 M KF, see Figure 3.28. Initially, the single electrodes were tested separately in order to check their functionality. Subsequently, the contact wires of the single electrodes were connected to form a bundle and another CV was recorded. When applying a scan rate of 50 mV s^{-1} , the CVs recorded for the individual electrodes are almost identical, exhibiting the peakless shape typically observed at microelectrodes, having steady-state current values ranging from 33.47 nA to 36.75 nA. The measured currents are slightly lower than the theoretically expected value of 43.2 nA, thus revealing that the radius of each single electrode is about 10 μm . The subtle deviation is attributed to the fabrication process of the electrodes, where melting of the Pt wires in the glass capillary may cause small changes in surface area. The steady-state current response of the multibarrel electrode is equal to the sum of the single steady-state current values. This behavior reveals that the distance between the individual electrodes is large, meaning that the electrodes do not interfere with each other (Stulik et al., 2000). Although the current values recorded at the multibarrel electrode are six times larger than those measured at single microelectrodes, the shape of the CV still exhibits microelectrode features.

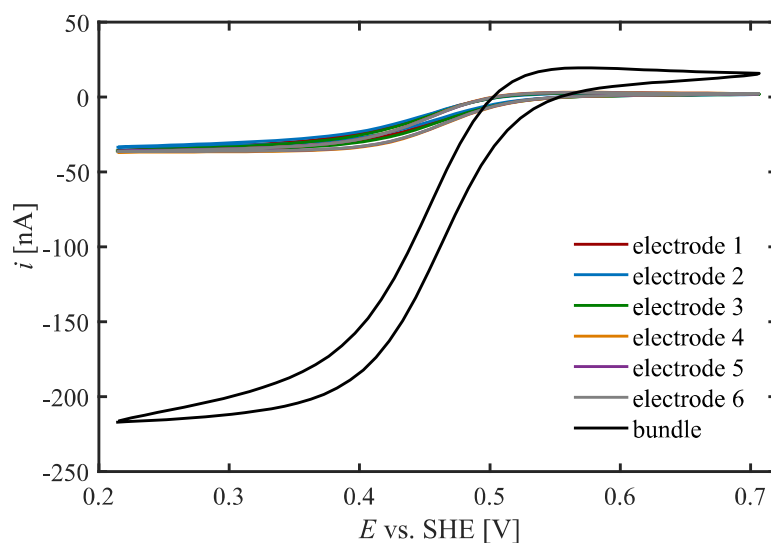


Figure 3.28.: CVs recorded with individual microelectrodes and the multibarrel electrode in 10 mM $\text{K}_3[\text{Fe}(\text{CN})_6]$ in 0.5 M KF at a scan rate of 50 mV s^{-1} .

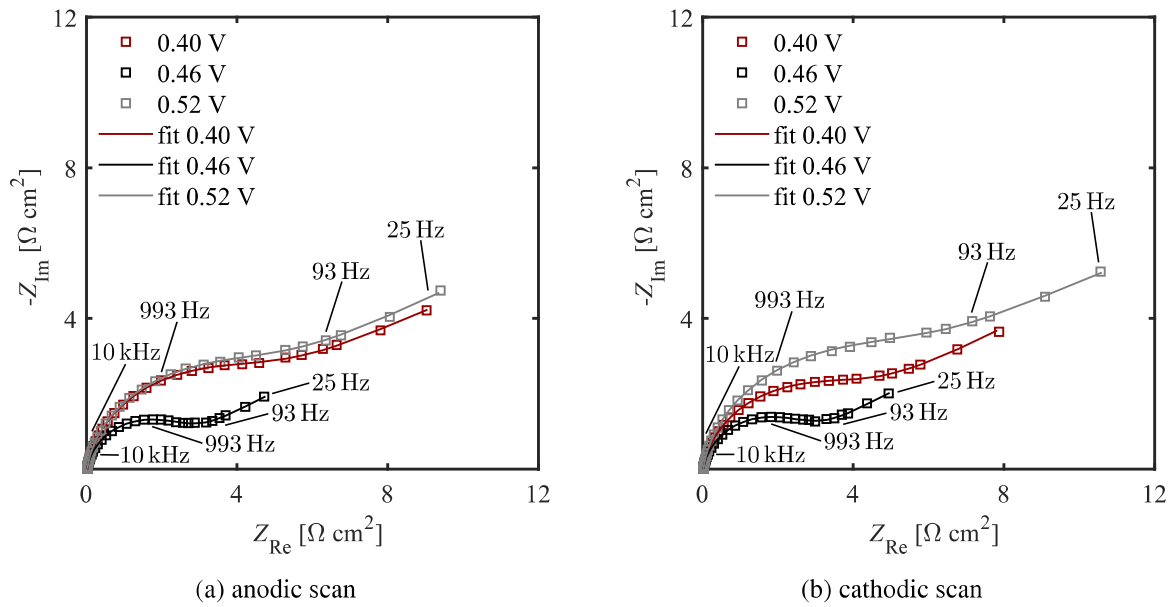


Figure 3.29.: Experimental and fitted dynamic impedance spectra recorded in 10 mM $\text{K}_3[\text{Fe}(\text{CN})_6]$ in 0.5 M KF at a multibarrel electrode. $\Delta u_{dc} = 500$ mV, $f_{dc} = 0.05$ Hz, $\Delta u_{ac} = 50$ mV, $f_b = 1$ Hz, $d = 7$, $\text{bw} = 2$ Hz.

DMFA was performed at a multibarrel electrode, using the same experimental conditions as applied for microelectrodes, in order to study if the variation of the reaction parameters extracted for the redox process follows the behavior observed at macro- and microelectrodes. The above Figure 3.29 shows the Nyquist plots of the dynamic impedance spectra recorded at different potentials throughout the anodic and cathodic sweep and their corresponding fitted spectra. As expected, the shape of the spectra resembles that observed at single microelectrodes, exhibiting semi-infinite diffusion behavior in the frequency range under investigation.

Due to the fact that the individual microelectrode surfaces do not interfere with each other, the characteristic frequency of diffusion f_d is identical to that observed at single microelectrodes. Therefore, data fitting could be performed with the EEC presented in Figure 3.19. Also in this case, the fitting quality is very good ($\chi^2 = 5.43 \times 10^{-5}$), yielding the kinetic variables given in Figure 3.30. The temporal behavior of the values per unit surface area is governed by the same features as observed for macro- and microelectrodes. As established in the previous studies, the

Table 3.6.: Charge transfer resistance and Warburg coefficient per unit surface area extracted from data fitting at 0.46 V vs. SHE for different electrode geometries.

electrode geometry	surface area [cm^2]	$R_{ct} \times A$ [$\Omega \text{ cm}^2$]	$\sigma_{ct} \times A$ [$\Omega \text{ cm}^2 \text{ s}^{-0.5}$]
250 μm disk	4.91×10^{-4}	1.1	36.7
25 μm disk	4.91×10^{-6}	1.7	35.1
multibarrel	2.95×10^{-5}	2.6	42.6

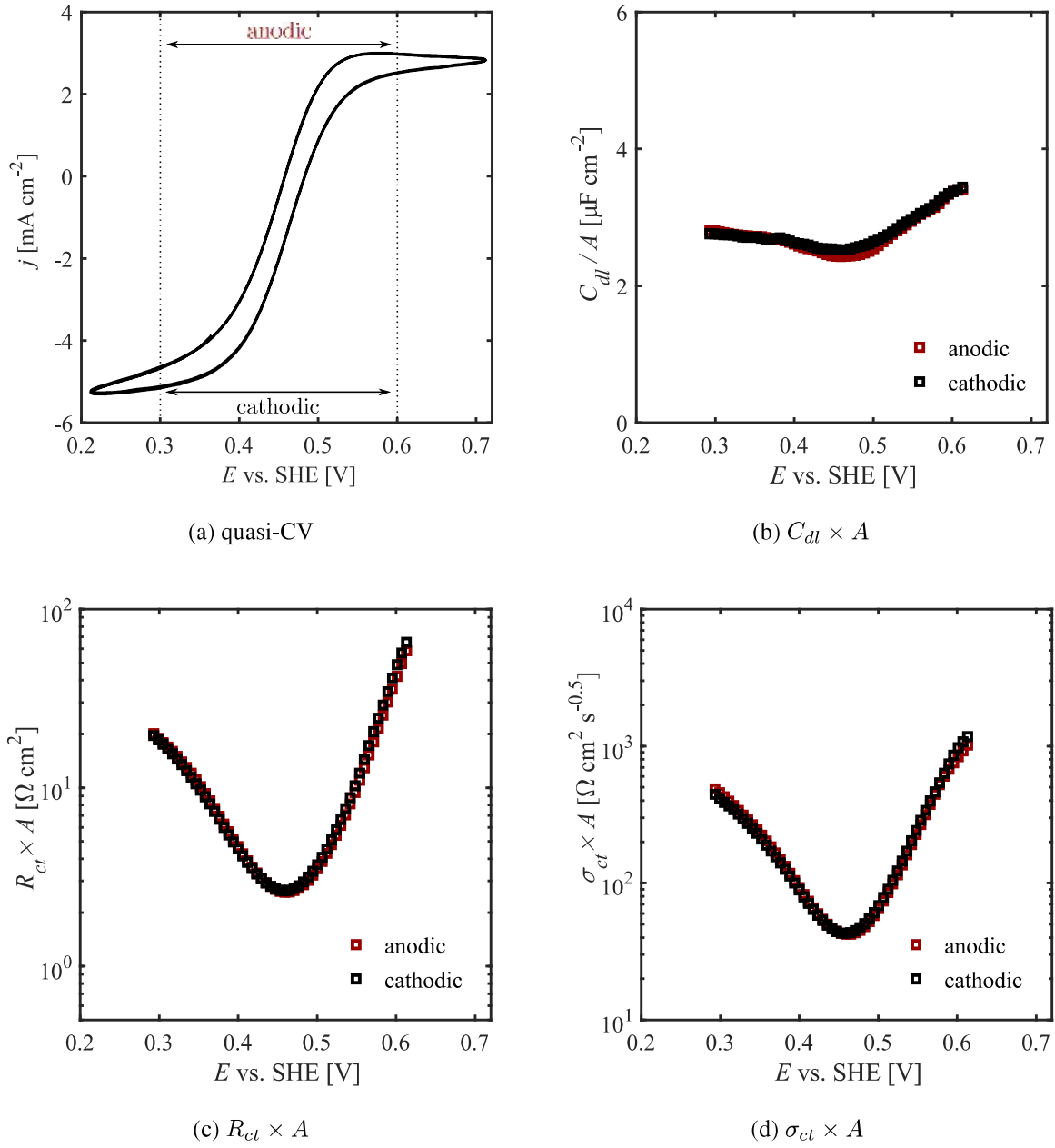


Figure 3.30.: Temporal evolution of fitting parameters extracted from data fitting of the dynamic impedance spectra recorded at a multibarrel electrode with the EEC presented in Figure 3.19.

Table 3.7.: Charge transfer resistance and Warburg coefficient per unit surface area extracted from data fitting at 0.55 V vs. SHE for different electrode geometries.

electrode geometry	surface area [cm ²]	$R_{ct} \times A$ [Ω cm ²]	$\sigma_{ct} \times A$ [Ω cm ² s ^{-0.5}]
250 μm disk	4.91×10^{-4}	5.3	281.4
25 μm disk	4.91×10^{-6}	5.3	298.5
multibarrel	2.95×10^{-5}	12.1	288.4

Table 3.8.: Diffusion resistance per unit surface area calculated from (3.9) for different electrode geometries.

electrode geometry	surface area [cm ²]	$R_{d(0.46\text{ V})} \times A$ [Ω cm ²]	$R_{d(0.55\text{ V})} \times A$ [k Ω cm ²]
250 μm disk	4.91×10^{-4}	153.4	1.17
25 μm disk	4.91×10^{-6}	14.9	0.15
multibarrel	2.95×10^{-5}	17.8	0.12

results confirm that the reaction kinetics remain basically unaffected by the change in electrode dimension. The minima of $R_{ct} \times A$ and $\sigma_{ct} \times A$ slightly exceed those extracted for the 250 μm and 25 μm electrodes, however, the parameters are still in a similar range, see Table 3.6. Also the values extracted at a potential of 0.55 V vs. SHE follow the trend observed in the previous investigations, as reported in Table 3.7.

The diffusion resistance calculated for the multibarrel electrode is in the same range as that obtained for the microelectrode, see Table 3.8. Therefore, it is confirmed that the diffusion profile established at multibarrel electrodes is similar to that observed at single microelectrodes when the spacing between the individual electrodes is large. Also in this case, mass transport is the rate-determining step.

The absolute R_s value of 750 Ω is slightly higher than its theoretical value of 476 Ω , where the deviation can be attributed to the fact that the radii of the individual electrodes were smaller than their theoretically expected values of 12.5 μm , as outlined above. However, the solution resistance is still significantly smaller than that recorded at single microelectrodes, which is one of the major advantages of multibarrel electrodes.

4. Studies on the Kinetics of the HER

After having studied the dynamic impedance behavior of a simple redox process, the optimized strategies of data recording and processing developed in the previous Chapter are employed for the kinetic investigation of a more complex system involving inner-sphere reactions, namely the cathodic HER.

The HER is of fundamental importance for a variety of electrochemical processes and represents one of the most studied reactions in the field of electro-catalysis. Mechanistic studies on the HER aim to extract kinetic variables that give an adequate physical description of the different processes involved in this reaction. As the HER is highly affected by a number of parameters, among them the choice of the electrode material and the composition of the electrolyte, the different experimental conditions under which the kinetics of the HER have been investigated in the studies presented in literature have lead to discrepancies in the formulation of a general reaction mechanism. Therefore, DMFA was employed to investigate the HER in dynamic conditions to obtain more insight into the kinetics governing this reaction. This Chapter is divided into two main Sections. First, Section 4.1 provides a comprehensive introduction into the topic, pointing out the relevance of the HER with respect to the development of a hydrogen economy. What is more, a detailed description of the reaction steps that are involved in the cathodic HER is given. Finally, an overview of various electrochemical techniques that may be employed for the investigation of the reaction kinetics of the HER is provided. The different methods are compared with respect to their challenges and prospects. The second part of this Chapter is concerned with the investigation of the HER by means of DMFA. The measurements presented in Section 4.2 were carried out in order to obtain a concatenated picture of the temporal development of the kinetic variables that underlie this multi-step reaction. Parts of the results presented in this Chapter were published in Koster (2019).

4.1. Movement Towards an Environmentally Friendly Energy Economy

Since the beginning of the industrialization, an alarming phenomenon has been observed, which may be described as ‘efficiency paradox’. This phenomenon suggests that an increase in energy efficiency of a technology is coupled with an increase in overall energy consumption. According to Saunders (1992), this effect can be explained by the relation between an increased energy efficiency, enabling energy provision at low costs and an excessive energy consumption. At the

same time, an increase in energy efficiency allows for rapid industrial evolution, which is again coupled with an elevated usage of energy. The efficiency paradox had a considerable impact on the energy economy in the course of the 20th century, in which the world's energy consumption increased by a factor of 80, while human population expanded by a factor of 6 (Züttel, 2010). The International Energy Outlook 2017 of the U.S. Energy Information Administration reported that at the end of 2015 the total world's energy consumption was at a level of 575 quadrillion British thermal units (Btu) and is expected to reach 736 Btu by 2040 (U.S. EIA, 2017). Today, more than 90% of the primary energy consumed worldwide is still linked to fossil energy carriers, such as coal, petroleum, and natural gas, whose common characteristic is the presence of carbon inside their molecules (Beccari and Romano, 2007). Thus, the combustion of fossil fuels involves the formation and emission of greenhouse gases, which is believed to be the main cause of global warming, as already predicted by Arrhenius (1896), who stated that doubling the CO₂ concentration in the atmosphere would result in an average temperature rise of 5–6 °C.

4.1.1. A Hydrogen Economy

In the United Nations Framework Convention on Climate Change (UNFCCC) representatives of 196 parties responded to climate change with an agreement aiming to keep the global temperature rise in this century at a level below 2°C as compared to the pre-industrial era. Facing this goal, taking into account an ever increasing energy demand due to a continuous growth in world's population and the associated depletion of fossil fuels, makes the development of new technologies based on renewable and emission free sources the main objective (Bennaceur, 2005).

The solution to this challenge might be found in the establishment of an energy economy based on hydrogen. The phrase 'hydrogen economy' was first introduced in 1970 by General Motors engineers, stating that hydrogen could be used as a fuel in the transport section (Dunn, 2003). Actually, the idea of a hydrogen economy was already established by Jules Verne in the 19th century, who foresaw the depleatability of resources and envisioned the application of hydrogen generated by water electrolysis as an energy carrier: "Water will be the coal of the future" (Verne, 1874). The interest in this topic increased due to the desire of an energy self-sufficiency after the first World War. The basic concept leading to a hydrogen economy was developed by Lawaceck in 1968 (Bockris, 2013). A few years later, Bockris (1972) pointed out the fundamental aspects that govern this concept in his research article 'A Hydrogen Economy'. An economy based on hydrogen considers hydrogen as the major energy carrier, exploiting its outstanding ability to store and transport energy in large amounts and over long distances. The mass energy density of this non-toxic substance is about three times higher compared to that of hydrocarbon based fuels, and its combustion only generates water and heat. The main idea is that hydrogen carries energy produced from different sources to locations where it is needed

to fuel e.g. turbines, internal combustion engines, or fuel cells (Mazloomi, 2012). Although the idea of a hydrogen economy has been promoted for almost 50 years, significant progress in the integration of H_2 into our present energy economy is still pending, thus indicating the complexity of the task. HYPOGEN and HYCOM are the leading projects in the European Union, working on the development of an emission free power plant based on fossil fuels and on the expansion of the hydrogen network, respectively. The FutureGen project is an analogue to the european HYPOGEN project, funded by the U.S. government (Bennaceur, 2005). Clearly, the difficulty of implementing a hydrogen economy is caused by various aspects, some of which are discussed in what follows.

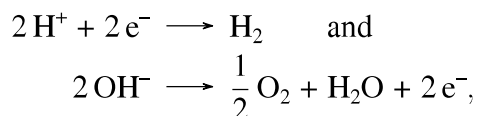
Gaseous hydrogen is commonly stored in gas tanks in its compressed form. As the energy density and content of hydrogen gas is low compared to its liquefied form, efficient storage can only be achieved when the gas is highly pressurized. Construction of suitable gas tanks is therefore limited by compression, cost of production, and, more importantly, by safety throughout operation (Mazloomi, 2012). Different technologies for safe transport of hydrogen have already been developed, where H_2 can be transported in its gaseous or liquid form, by road, by rail, by sea, or through pipelines. However, the enormous costs of hydrogen transport are the main reason why an adequate hydrogen infrastructure does not yet exist (Beccari and Romano, 2007). In addition to the difficulties in transportation and storage of hydrogen, the major limitation that has to be overcome is the availability of H_2 . At first glance, this limitation may seem confusing, as hydrogen is the most abundant element in the universe. However, it needs to be considered that hydrogen does not naturally occur in its molecular form but needs to be generated from hydrogen binding sources, i.e. water or hydrocarbons. Thus, one of the major goals is the development of an environmentally benign hydrogen production method, ideally based on renewable sources, guaranteeing a sustainable supply of hydrogen.

Nowadays, steam reforming of natural gas and gasification of coal still represent the leading hydrogen production technologies (Dincer, 2012). These methods provide large quantities of H_2 that mostly serve as reaction agent in a variety of chemical processes, including cryogenics and methanol production among others (Beccari and Romano, 2007), while only a very small fraction of H_2 produced is used as fuel. Electrolysis of water represents the cleanest method of producing ultrapure hydrogen and could be the key to the development of a sustainable and environmentally friendly energy supply. Nonetheless, currently its contribution to the overall generation of hydrogen worldwide is vanishingly low.

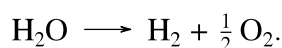
4.1.2. Generation of Molecular Hydrogen by Electrolysis

In water electrolysis the application of an electrical current forces water to decompose into its constituents, hydrogen and oxygen, where the reactions occurring at the cathode and anode can

be expressed as



respectively, while the total reaction is given by



The concept of hydrogen production by electrically induced water splitting has already been developed by Nicholson more than 200 years ago (Zeng, 2010). At the beginning of the 20th century, water electrolysis was already widely applied for the production of hydrogen (Kreuter, 1998). The low costs of hydroelectricity at the beginning of the 20th century enabled further progress in the development of this technique. However, the efficiency of water electrolysis was rather low and it was only applicable for small scale production of hydrogen (Santos, 2013).

In the course of the era of the industrial revolution the Haber process, representing the major industrial procedure for ammonia production, required the consumption of substantial amounts of hydrogen (Zeng, 2010). Simultaneously, the discovery of fossil fuels as primary energy sources lead to the establishment of a carbon based energy economy. At that time, new hydrogen production technologies based on raw materials containing carbon were developed. Hydrogen generation through gasification of coal and steam reforming of natural gas became economically favored over water electrolysis, as these methods enabled large scale production of hydrogen at low cost (Turner, 2004). Besides the tremendous environmental impact of production technologies related to raw materials containing carbon, fossil resources are not abundant. The ‘biogenic theory’ states that fossil fuels were formed by sedimentation of prehistoric organic material and are thus not regenerative. This theory is supported by much scientific evidence. However, this topic is controversially discussed in the geological community, as some geologists believe that crude oil originates from non-biological processes, which is referred to as ‘adiabatic theory’. Irrespective of which of the two theories holds true, accessible crude oil reservoirs are almost exhausted and its extraction becomes more and more economically unfavorable due to ever increasing costs (Höök, 2010). The Hubbert-peak theory, according to which the production of crude oil will reach a total maximum and then gradually decline due to its inevitable exploitation, has been developed by Hubbert (1956) in the 1950s and sought to determine what is nowadays referred to as ‘peak oil’, i.e. the instant of time at which the above described scenario occurs. Although Hubbert’s predictions were not correct, it is a matter of fact that fossil resources are diminishing, and that such a thing as peak oil exists. A foretaste of what to expect has already been experienced in the oil crisis in the 1970s. At that time, the vision of the hydrogen economy was brought to life and with it the worldwide interest in the optimization of the efficiency of water electrolysis (Santos, 2013).

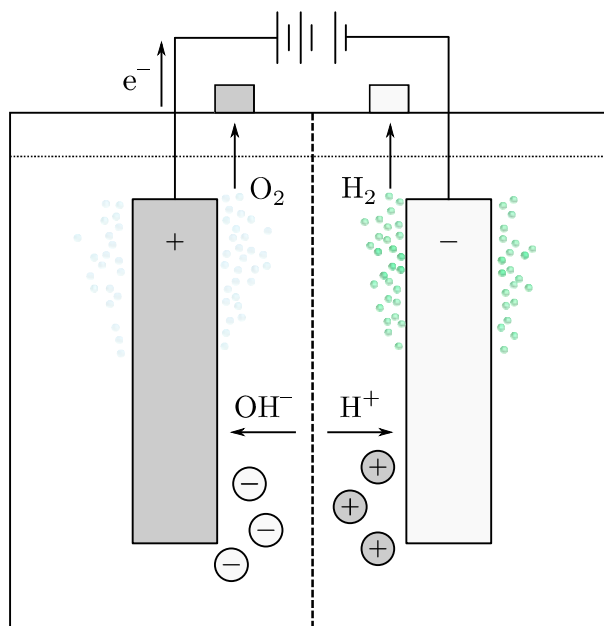


Figure 4.1.: Schematic representation of an electrolyzer, adapted from Santos (2013).

The working principle of an electrolyzer is rather simple: a *dc* is applied to an anode and a cathode, both immersed in an aqueous electrolyte solution and externally connected via a power supply, as illustrated in the above Figure 4.1. Inside the solution the two electrodes are separated by a diaphragm. Upon current flow, hydronium ions in solution move towards the cathode where they are reduced by electrons flowing from the power source to the electrode. Simultaneously, hydroxide ions are oxidized at the anode, which acts as an electron sink. Even though the concept of water electrolysis has been thoroughly studied in the last decades, in 2002 only 4% of the hydrogen produced worldwide was generated by electrolysis (Dunn, 2003), and most of the techniques currently used for hydrogen production by water electrolysis still stem from the period between 1920 and 1970 (Bowen, 1984). A poor energy efficiency, safety issues as well as high installation and operation costs still constitute the major drawbacks of this technique (Santos, 2013). Nevertheless, electrolysis of water or acidic solutions yields an alternative and clean approach to produce ultrapure hydrogen. Brine, river water, rain, or well water represent naturally accessible water sources from which hydrogen can be extracted by solar, wind, or water power (Dincer, 2012).

In recent years, as a consequence of the political agreements mentioned earlier and due to its outstanding advantages, water electrolysis has become one of the most relevant research topics. Optimization of the overall process with respect to efficiency and costs requires a detailed mechanistic understanding of the single electrode processes, where the focus of this Chapter is on the investigation of the kinetics of the cathodic HER.

4.1.3. The Cathodic Hydrogen Evolution Reaction

Due to its fundamental importance in electrocatalysis and corrosion science, the HER has thoroughly been examined in the last decades and presents one of the most discussed topics in electrochemistry (Jerkiewicz, 1998). Early studies in this field go back to Bowden and Rideal (1928), who investigated the HER on thin metallic films. Since that time, the HER has been in the focus of a multitude of scientific publications, among them the contributions of Conway and Bockris (1957), Trasatti (1972), Jerkiewicz (1998), and Lasia (2003), just to name a few. According to Conway and Tilak (2002), the generally accepted mechanism of the HER in acidic solutions involves the electro-sorption of atomic H_{ad} on the electrode surface



which is referred to as *Volmer reaction* and its subsequent transformation into H_2 . The second step can occur via two alternative pathways, given by



respectively. In his studies on the kinetics of the electrolytic generation of hydrogen, Tafel (1905) has identified (4.2) as rate-determining step. Therefore, this process is known as *Tafel reaction*. Reaction (4.3) is referred to as *Heyrovsky reaction*, describing an electrochemical desorption process. The below Figure 4.2 shows a schematic representation of the different reaction steps.

The electrode surface strongly interacts with the adsorbed atomic H intermediate, involving the formation of a chemical bond, while its interaction with the reactant and product species is only due to weak electrostatic attraction forces (Gerischer, 1958). Thus, the electro-sorption step plays a fundamental role in the HER and acts as a prerequisite for the generation of H_2 , indicating that the rate at which hydrogen is produced is strongly related to the rate of the electro-sorption process.

It is important to point out the fundamental difference between the formation of adsorbed hydrogen species induced by voltage changes in an electrochemical environment and due to hydrogen physisorption and chemisorption, respectively, which occur under low-pressure gas-phase conditions. According to Jerkiewicz (1998), the physisorption process



takes place at low temperatures and involves the adsorption of the H_2 molecule on the electrode surface by means of weak van der Waals interactions. Here, the covalent bond between the

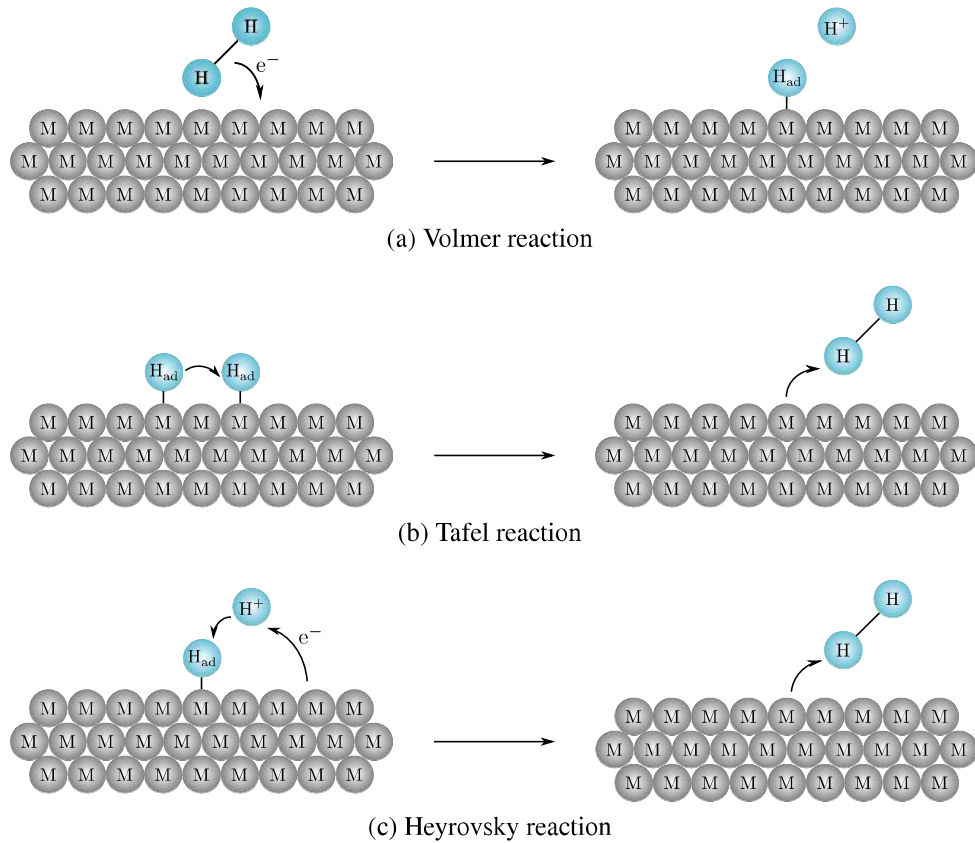
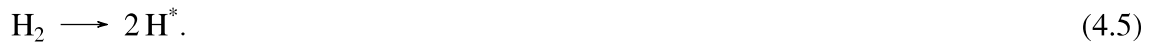


Figure 4.2.: Schematic representation of the reaction steps involved in the cathodic HER.

two hydrogen atoms remains intact, since its dissociation is thermodynamically unfavored, as the dissociation energy needed to break this bond is higher than the energy released during the adsorption process.

Chemisorption is observed at higher temperatures. In this case, the hydrogen molecule undergoes initial dissociation, given by



Subsequently, the 1s orbitals of the single hydrogen atoms overlap with the delocalized orbitals of the metal, resulting in a strong chemical interaction, such that



The dissociation step can occur via an activated path, in which the hydrogen molecule has to overcome an activation barrier. Alternatively, the reaction can proceed through an inactivated path, where H_2 dissociates spontaneously.

In contrast, the electrochemically induced electro-sorption of atomic H is characterized by an electron transfer reaction, where the discharge of a hydronium ion results in the formation of an adsorbed atomic H species, following (4.1). According to literature, there are two distinct

electro-sorbed hydrogen species, under-potential adsorbed hydrogen (H_{UPD}) and over-potential adsorbed hydrogen (H_{OPD}) (Jerkiewicz, 2010). H_{UPD} is formed at potentials larger than the hydrogen reversible potential, while the electro-sorption of H_{OPD} takes place at potentials negative to it (Conway and Tilak, 2002). The formation of H_{UPD} is a feature that is exclusively observed at Pt group metals, whereas H_{OPD} is generated at all surfaces that are active towards the HER. The presence of H_{UPD} can be easily demonstrated by means of cyclic voltammetry. In contrast, the surface coverage of H_{OPD} is not directly accessible and must be determined from an analysis of potential-decay gradients (Jerkiewicz, 2010). Due to the comparatively low $M-H_{OPD}$ bond strength, this species acts as the intermediate in the HER and thus determines the kinetics of the HER (Conway and Jerkiewicz, 2000). In contrast, H_{UPD} forms a strong bond with the metal and does not directly contribute to the generation of H_2 . However, it was assumed by Markovic et al. (1996) that at Pt group metals the HER takes place on a layer of H_{UPD} , which is embedded in the metal substrate, forming a sub-surface state. The modification of the electrode surface affects its interfacial properties with respect to hydrophobicity and hydrophilicity, resulting in an enhanced interaction with electroactive species and solvent molecules (Jerkiewicz, 1998).

Kinetic studies of the HER are concerned with the characterization of the rate-determining step of the reaction. Here, it is of particular interest which of the two possible pathways, (4.2) or (4.3), dominates the overall reaction kinetics. Tafel (1905) was the first to report the dependence of the HER kinetics on the electrode material, which was later found to be caused by the chemisorption properties of the metal. Although platinum group metals (Pt, Re, Rh, Ir) show the highest activity towards the HER (Lasia, 2003), their industrial application is unfavorable due to high costs. Therefore, various research publications focus on the optimization of electro-catalysts for the HER, where Ni and Ni-alloys are treated as promising electrode materials (Lasia and Rami, 1990; Chen and Lasia, 1991; Los, 1993; Lasia, 2003). The kinetics of the HER were found to be sensitive to changes in temperature, as stated by Birry (2004). Another important aspect that needs to be considered when investigating the kinetics of the HER is the poisoning of the active material by metal impurities or other catalyst poisons, such as CO_2 . The following Section 4.1.4 gives an overview of the different experimental approaches that have been proposed to determine the kinetics governing the HER.

4.1.4. Kinetics of the HER

The HER was found to be strongly dependent on the electrode material and properties, i.e. crystal size and orientation as well as on the electrolyte composition and temperature. Mechanistic studies aim to relate these factors by comparison of kinetic data, where electrode materials are commonly characterized according to their activity towards the HER. The activity of electrodes is usually determined by their Tafel parameters (Lasia, 2003). Although Tafel was not a corrosion scientist himself, his research on the reduction of organic compounds on metal electrodes

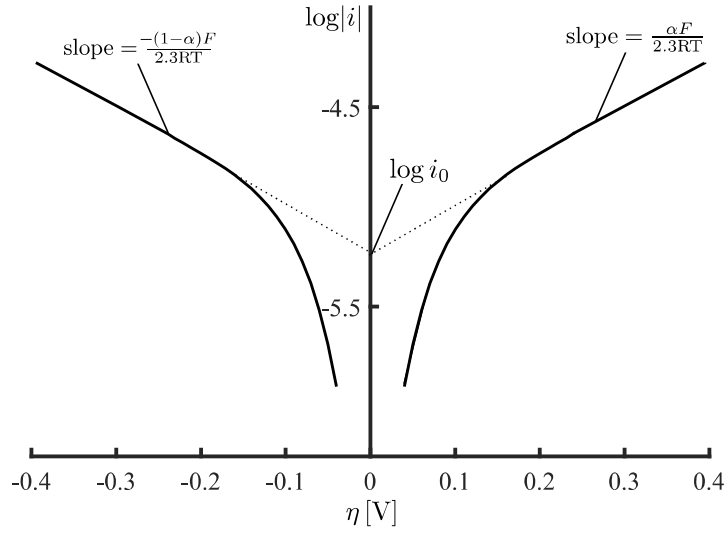


Figure 4.3.: Tafel plot, adapted from Bard (2001).

had a significant impact on the field of corrosion, as it indirectly lead to important insights into the catalytic behavior of metals towards the HER (Burstein, 2005). The Tafel equation (4.7) developed by Tafel (1905) more than a century ago, is of crucial importance in electrochemistry, as it relates the overpotential η to the current i , such that

$$\eta = a + b \log i. \quad (4.7)$$

The empirical constants a and b can be expressed as

$$a = \frac{-2.303 RT}{\alpha n F} \log i_0$$

and

$$b = \frac{2.303 RT}{\alpha n F},$$

respectively, with α representing the transfer coefficient, i_0 being referred to as the exchange current, and n describing the number of electrons involved in the reaction (Bard, 2001). The overpotential, which strongly depends on the electrode material, determines the rate at which hydrogen is produced at the electrode surface. According to Zeng (2010), the cathodic hydrogen generation overpotential is given by

$$\eta_{cat} = 2.303 \frac{RT}{\alpha n F} \log \frac{i}{i_0}. \quad (4.8)$$

The above Figure 4.3 shows a Tafel plot, representing $\log i$ as a function of η , where the linear segments of the function in the cathodic and anodic region have a characteristic Tafel

slope. The extrapolation of both branches gives an intercept with the y -axis, which refers to the logarithmic value of the exchange current $\log i_0$. Here, i_0 can be understood as the spontaneous reaction rate between H^+ and H_2 in equilibrium (Vesborg, 2015). The Tafel relationship is only valid at high overpotentials, where the kinetics of the faradaic reaction are totally irreversible. At low overpotentials this condition does not hold, since the reaction occurs in both directions resulting in a nonlinear behavior in the Tafel plot (Bard, 2001). The parameter i_0 as well as the Tafel slope can be used to extract mechanistic information on electrode processes (Lasia, 2003). Tafel slopes can be experimentally obtained from polarization curves and are usually expressed in Volts per decade of current. Bowden and Rideal (1928) were among the first who used the Tafel parameters in order to characterize the HER when investigating the electrodeposition of thin metal layers, involving the simultaneous formation of H_2 on the substrate surface. Since then, the determination of the HER reaction kinetics by means of Tafel slopes has become a widely accepted method. As a general rule one can say that the activity of the electrode towards the HER increases with decreasing Tafel slope. Conway and Tilak (2002) observed a decrease in Tafel slope with increasing porosity of the electrode material. However, according to Lasia (2003), Tafel parameters derived from voltammetric measurements usually lack accuracy, since the exchange current density is related to the unit surface area, which can most often not be precisely determined. In addition to that, complex reaction mechanisms involving multiple electron transfer steps may appear as nonlinear Tafel slopes, which can result in an erroneous extrapolation of i_0 , thus preventing a reliable comparison of electrode activities.

Another approach that has been reported in literature in order to explore the HER kinetics is based on volcano curves, relating the exchange current density to the $M-H_{ad}$ bond strength (Parsons, 1958; Gerischer, 1958). Trasatti (1972) was the first to develop a model based on the volcano relationship in order to predict the kinetics of the HER, concluding that the binding strength between platinum group metals (Pt, Re, Rh, Ir) and the adsorbed H intermediate slightly exceeds the optimum value, while a medium $M-H_{ad}$ bond strength results in maximum exchange current densities. The corresponding volcano plot is shown in Figure 4.4. As pointed out in a critical review by Zeradjanin (2016), the values used for the bond strengths correspond to strongly bounded H_{UPD} . However, the nature of the intermediate adsorbed species cannot be accurately classified. Later, Trasatti retracted this statement and presented a linear relation between the exchange current density and the adsorption strength. Here, the highest activity towards the HER is attributed to the strongest binding (Zeradjanin, 2016). In addition to that, computational approaches associated with DFT-based volcano relationships have been developed (Schmickler et al., 2012), where the major drawback of these models is that they require accurate experimental data in order to provide a reliable kinetic analysis of the HER. However, adsorption energies of the adsorbed species are not directly accessible in an electrochemical environment (Zeradjanin, 2016).

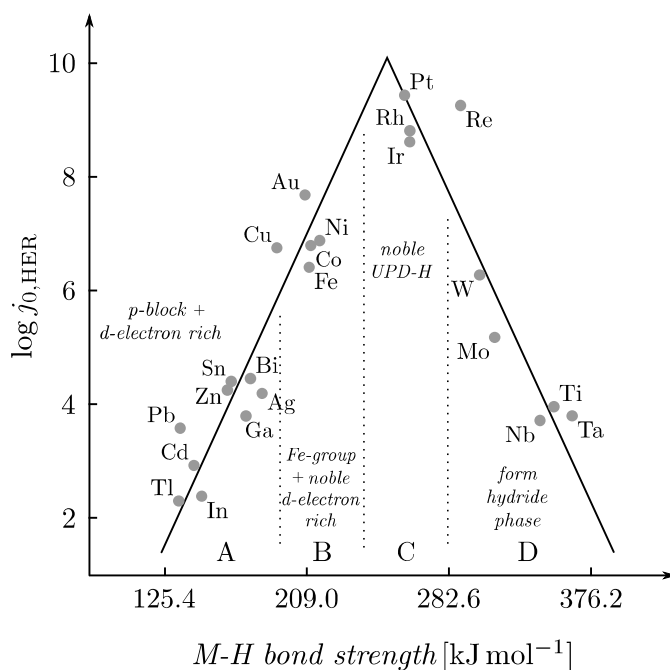


Figure 4.4.: Volcano plot of standard exchange current density vs. M-H bond energy, adapted from Lasia (2003).

EIS is considered the most powerful tool when studying reaction kinetics. However, classic EIS requires that the surface state of the electrode does not undergo changes during the experiment. When investigating the HER, steady-state conditions may be readily attained at potentials positive with respect to the hydrogen reversible potential, thus enabling the investigation of the reaction kinetics of the formation of H_{UPD} . Breiter (1963) employed EIS to analyze how the adsorption of hydrogen is affected by the presence of halide ions in the electrolyte. Vrubel (2013) presented an alternative approach of deriving Tafel plots from EIS data reflecting purely the charge transfer kinetics. Moreover, Barber et al. (1998) used EIS to study the reaction kinetics of the process of under-potential deposition (UPD) at different single-crystal surfaces of Pt, concluding that the reaction strongly depends on the surface lattice geometry. Reliable impedance data were also recorded at low cathodic overpotentials, where Conway (1998) investigated the over-potential deposition (OPD) process at Pt single-crystal surfaces. In contrast, the quality of impedance data acquired at higher cathodic overpotentials was very poor. In this case, the resulting impedance spectra showed severe distortions over the full range of frequencies (Birry, 2004; Los, 1993).

In summary, the HER is one of the most studied electrochemical processes. Reaction kinetics are usually investigated by electrochemical methods: steady-state polarization, potential-step coulometry, potential-relaxation, EIS (Barber et al., 1998). Steady-state polarization methods enable the observation of changes in the reaction kinetics, however, a quantitative analysis can only be accomplished by EIS or potential relaxation techniques (Barber et al., 1998). Tafel analysis may indicate a slow electron transfer reaction, but a change in Tafel slope can also be related

to mechanistic changes (Vrubel, 2013). In the field of electrocatalysis volcano relationships are still commonly applied in order to estimate activity trends, although adsorption energies of H_{ad} are not experimentally accessible (Zeradjanin, 2016), and some results presented in literature lead to contradictory conclusions. Therefore, the reliability of volcano curves remains doubtful.

Commonly, EIS provides an insight into reaction mechanisms and kinetic processes. However, it must be emphasized that the HER can only be investigated by means of classic EIS at potentials more positive than the hydrogen reversible potential or at very low overpotentials where steady-state conditions are readily established. At high overpotentials, instead, it is assumed that the nucleation of hydrogen gas bubbles creates an instability of the system and causes temporal variations in the surface state of the electrode, such that steady-state conditions cannot be reached. Under these conditions, the investigation of the HER by means of classic EIS is not possible. Moreover, the presence of nucleated gas bubbles partially blocks the active electrode surface area, thus making kinetic studies unfeasible.

4.2. Dynamic Impedance Studies on the HER by means of DMFA

This Section is concerned with the investigation of the HER in dynamic conditions to gain more insight into electrode surface properties that cannot be attained in static conditions. Dynamic impedance spectra were recorded by means of DMFA in order to extract reliable kinetic variables over a wide range of different potentials. In contrast to classic impedance measurements, the acquisition of accurate dynamic impedance spectra is not limited to potentials larger than the hydrogen reversible potential.

4.2.1. Voltammetric Characterization of the System

Due to its outstanding catalytic properties regarding the cathodic evolution of H_2 , mechanistic studies on this process have mostly been performed at Pt. Alkaline solutions, even when pre-electrolyzed, usually contain trace amounts of metal contaminants (mostly Fe in amounts less than 1 ppm), which strongly affect the kinetics of the HER, as they lower the electrode activity (Huot, 1987). The measurements presented in this Section were thus performed at a polychrystalline Pt-WE electrode, immersed in acidic solutions of $HClO_4$. Although the use of the multibarrel electrode presented in Section 3.2.3 was desired, its application was prevented by the strong formation of gas bubbles that caused blockage of the individual microelectrode surfaces. Therefore, an electrode having a diameter of 250 μm was employed. As an alternating oxidation-reduction pre-treatment of Pt electrodes was found to enhance the reversibility and reproducibility of subsequently performed electrochemical measurements (James, 1967), the Pt-WE was activated through voltammetric cycling in 100 mM solution of $HClO_4$ at the

beginning of each measurement. The below Figure 4.5 shows the voltammetric activation profile, revealing well-defined features that can be attributed to electro-sorption and -desorption processes as well as to the formation and reduction of PtO. According to Jerkiewicz (2010), the cathodic current peaks emerging at potentials below 0.3 V vs. reversible hydrogen electrode (RHE) are related to the electro-sorption of H_{UPD} . Upon reversal of the scan, similar anodic current patterns can be observed due to the process of H_{UPD} -desorption. At potentials larger than 1 V vs. RHE, the formation of PtO occurs, which is reduced in the backward scan at potentials lower than 1 V vs. RHE.

Subsequent to the electrochemical activation process, the WE was characterized by means of cyclic voltammetry in diluted solutions of $HClO_4$. The voltammograms displayed in Figure 4.6 were recorded at a scan rate of 100 mV s^{-1} in a potential range between -0.55 V and 0.45 V vs. RHE. The CVs can be divided into two different regions, corresponding to the two reaction steps that are involved in the HER. Region 1 refers to the electro-sorption reaction that precedes the cathodic evolution of H_2 . Starting at a potential of 0.45 V vs. RHE and sweeping the potential towards cathodic direction, hydronium ions are discharged at the electrode surface, resulting in the formation of adsorbed atomic hydrogen. This process is referred to reaction (4.1). In addition to that, in this potential region the oxidation of residual H_2 that was produced in previous cycles takes place, thus corresponding to the hydrogen oxidation reaction (HOR), which can be understood as the backward reaction of (4.3). The evolution of H_2 is observed in region 2. The latter may again be divided into two different areas in which cathodic and anodic currents are recorded, respectively. At potentials more negative than 0.0 V vs. RHE H_2 starts to evolve at the Pt surface. As already pointed out in Section 4.1.4, the generation of hydrogen

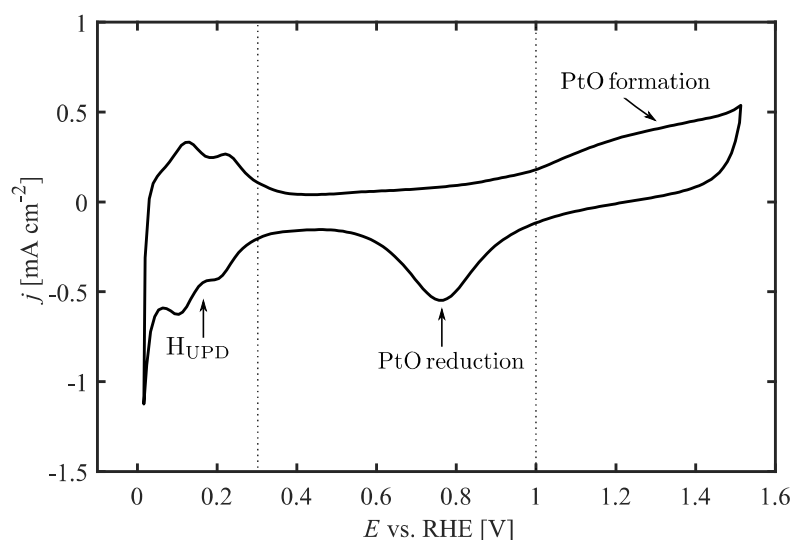


Figure 4.5.: CV recorded throughout the electrochemical activation of a $250 \mu\text{m}$ Pt-WE at a scan rate of 100 mV s^{-1} in 100 mM HClO_4 .

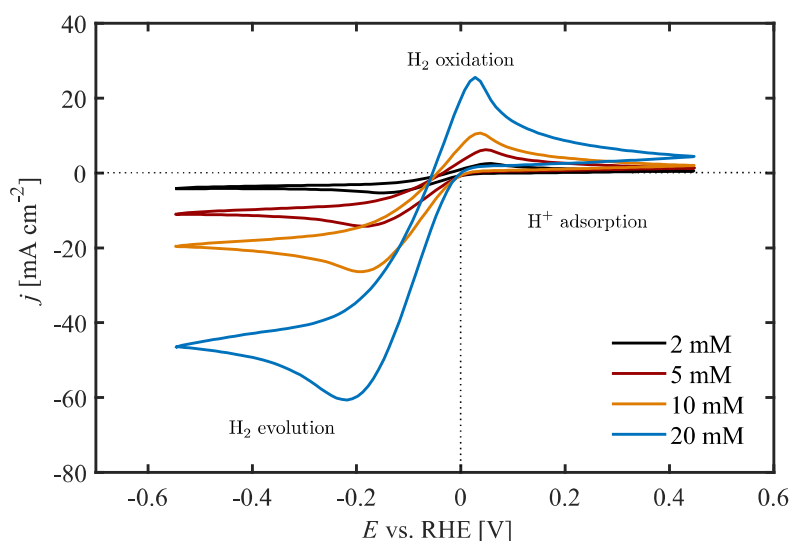


Figure 4.6.: CVs recorded at a 250 μm Pt-WE at a scan rate of 100 mV s^{-1} in 2 mM, 5 mM, 10 mM, and 20 mM HClO_4 .

gas is strongly related to the cathodic hydrogen generation overpotential (4.8). The higher the overpotential towards the cathodic hydrogen generation the more H_2 is generated, thus resulting in an increase in cathodic current. The cathodic current reaches a maximum and then declines, where in 2 mM and 5 mM electrolyte solutions a limiting current is reached. In contrast, in higher concentrated solutions no current plateau can be established in the potential range under investigation. Depending on the concentration of the electrolyte, the maximum cathodic current densities recorded throughout the evolution of H_2 vary between -5.32 mA cm^{-2} in 2 mM solution and $-60.61 \text{ mA cm}^{-2}$ in 20 mM HClO_4 and are thus much higher as compared to the current densities detected for the adsorption and desorption processes of H_{UDP} . Therefore, the specific features associated with these phenomena are no longer visible. Due to the formation of an H^+ depletion layer, the reaction is limited by mass transport of reactive species to the electrode surface. Upon reversal of the scan, ever lower amounts of hydrogen are produced at the metal surface, as the thickness of the H^+ depletion layer increases. Moreover, active surface sites may be blocked due to the formation of gas bubbles. At potentials more positive than -0.05 V vs. RHE anodic currents were recorded. In this potential region both the formation of H_2 as well as the HOR would take place at equal rates if the system was under equilibrium conditions. However, due to the fast triangular potential perturbation which was imposed on the WE, the system did not attain an equilibrium state. In this region of the scan large amounts of H_2 are accumulated at the electrode surface. Simultaneously, the electrolyte adjacent to the electrode surface is depleted by H^+ -ions, revealing that the HOR is favored over the HER. The anodic peak reaches a maximum at 0.03 V vs. RHE . Due to the comparatively larger amounts of accumulated H_2 present at the electrode surface, the maximum anodic current density increases with the electrolyte concentration. As a consequence of the fast potential sweep, molecular H_2 cannot fully be oxidized in the anodic scan. Therefore, the electro-oxidation process still

proceeds upon reversal of the potential towards cathodic direction. Due to net positive currents, the simultaneously occurring electro-sorption reaction is no longer visible. In the following, the dynamic impedance response obtained throughout the different steps of the HER process is discussed. The measurements were performed in solutions of HClO_4 of different concentrations in order to study in which way the electrolyte concentration affects the kinetics of the respective processes.

4.2.2. Impedance Spectroscopy in Forced Dynamic Conditions

DMFA was performed on the system by applying a constant potential of 0.45 V vs. RHE, which was superimposed by a quasi-triangular potential perturbation and the multi-sine signal with $d = 7$ that was presented in Section 3.1.2. The quasi-CVs were recorded in the same potential range as the CVs depicted in Figure 4.6. In contrast to the measurements presented in Chapter 3, the quasi-triangular potential perturbation was not applied symmetrically about the

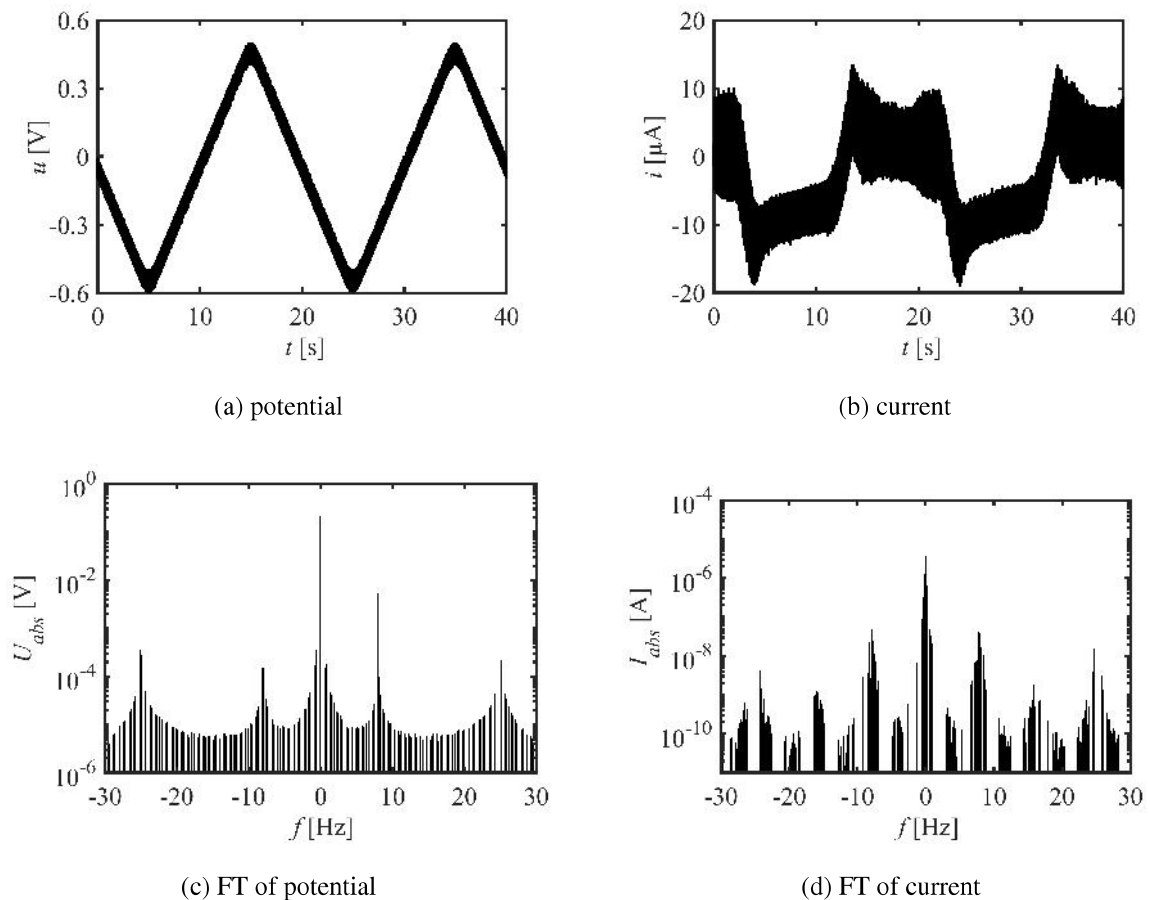


Figure 4.7.: Potential perturbation and current response recorded in 10 mM HClO_4 at a 250 μm Pt electrode for a multi-sine signal with $d = 7$ in the time and in the Fourier domain. In Fourier space, only a small fraction of the overall spectrum is displayed.
 $\Delta u_{dc} = 1$ V, $f_{dc} = 0.05$ Hz, $\Delta u_{ac} = 50$ mV, $f_b = 1$ Hz.

time-invariant potential. Instead, the potential was swept by 1 V towards negative potentials and then back to the initial value, while the multi-sine amplitude Δu_{ac} was set to a value of 50 mV. The scan was performed at a scan rate of 100 mV s^{-1} . Thus, according to (3.1), the fundamental frequency of the quasi-CV was 50 mHz. Based on the results presented in Section 3.2, stating that the time-scales of the two waveforms must not overlap, the base frequency of the multi-sine waveform was chosen to be 1 Hz. In doing so, it was possible to record a full impedance spectrum at each point of the scan, thus allowing for the investigation of the reaction kinetics of the processes of electro-sorption, hydrogen evolution, and hydrogen oxidation in a single measurement. The above Figure 4.7a shows the total voltage perturbation signal in the time domain, whereas the corresponding current response recorded in 10 mM solution of HClO_4 is depicted in Figure 4.7b. The voltage and current signals are investigated in Fourier space to determine the appropriate bandwidth of the filter function, which significantly affects the precision of the dynamic impedance spectra, as outlined in Section 3.1.2. As expected, FT of the voltage signal yields a similar spectrum as compared to that presented in Figure 3.6b. However, due to the higher scan rate, the skirts centered on the fundamental frequencies of the multi-sine wave that can be observed in the current response signal are wider than those detected in Figure 3.6d. Due to the close proximity of the different peaks, a bandwidth of 2 Hz is chosen to not collect unwanted perturbation signals related to the nonlinear response of the system. However, from Figure 4.7d it is clear that a bandwidth of 2 Hz rejects the utmost harmonic signals of the quasi-triangular wave. In order to guarantee that the loss of information does not affect the precision of the spectra, the quasi-triangular waveform reconstructed from the filtered data sets is compared to the quasi-CV that was recorded without the multi-sine perturbation. As illustrated in Figure 4.8, the shape of the two CVs is practically identical, thus demonstrating that the applied filter bandwidth is sufficiently large.

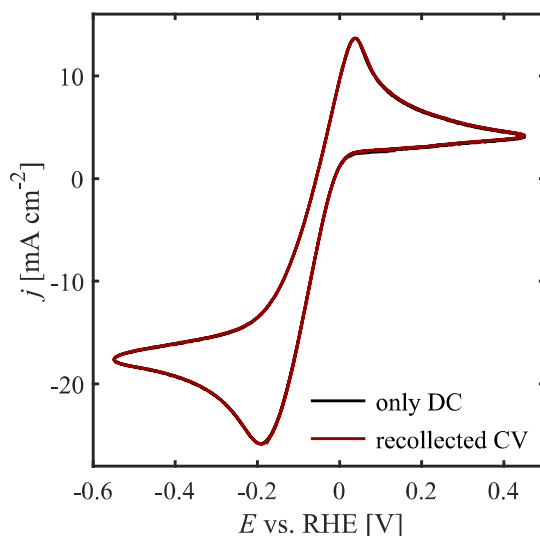


Figure 4.8.: Comparison of the original quasi-CV (without multi-sine perturbation) and the quasi-CV recollected from DMFA measurements in 10 mM HClO_4 .

4.2.3. The Electro-Sorption Reaction

As outlined in Section 4.1.3, the HER proceeds via two reaction steps, the electro-sorption of atomic H and the subsequent formation of gaseous hydrogen, where the reaction kinetics of the electro-sorption reaction strongly affect the overall process. In this Section, the dynamic impedance response obtained in the adsorption region is evaluated.

The below Figure 4.9 shows the dynamic impedance spectra recorded in diluted solutions of HClO_4 at a potential of 0.15 V vs. RHE on the cathodic branch of the quasi-CV. According to Figure 4.6, at this potential the adsorption of atomic hydrogen takes place via the discharge of hydronium ions at the electrified electrode surface, thus referring to reaction (4.1). Simultaneously, molecular H_2 is oxidized via the HOR. In 2 mM electrolyte the impedance spectrum is composed of a fraction of a bigger semicircle in the high-frequency region, which partially overlaps with a smaller semicircle at intermediate frequencies followed by a straight line with an angle of $67\text{--}86^\circ$. With increasing electrolyte concentration, the fraction of the semicircle in the high-frequency range decreases in size until it almost fully disappears in 20 mM solution of HClO_4 . At the same time, the radius of the second semicircle decreases, and the straight line becomes steeper in slope. The second semicircle is probably due to the electron transfer of the adsorption reaction, whereas the straight line shows almost pure capacitive behavior and can thus be affiliated with the accumulation of adsorbed H atoms on the electrode surface. In contrast, the origin of the first semicircle is not directly obvious. The intercept of the curve with the real axis in the high-frequency region usually gives an estimate for the solution resistance. In this case, the intercept obtained from graphical extrapolation of the first semicircle in Figure 4.9a falls into the $0\ \Omega$ region and cannot be attributed to the electrolyte resistance. Therefore, the feature observed in the high-frequency region is assumed to be related to a measurement artefact rather than to a physical process. Artefacts in the high-frequency domain might originate from input stray capacitances, which can e.g. be caused by a poor reference electrode with a non-negligible impedance, extended cables, or potentiostat input stray capacitances. As the measurements were performed with a fast RE (see Section 7.1.2) and extended cables were avoided, the first two sources can be ruled out. The high-frequency distortions are thus attributed to potentiostat stray capacitances, which, according to the manufacturer of the device, are in the order of 5 pF.

To extract the kinetic parameters that govern the adsorption process as well as to confirm the above made hypothesis, data fitting was performed by taking into account the potentiostat input impedance. An analytical model describing the chemico-physical properties of the processes of electro-sorption, H_2 evolution, and H_2 oxidation was developed by Dr. Alberto Battistel, Department of Molecular Sciences and Nanosystems, University of Venice. Based on that model, an EEC was constructed that was applied as electrical analogue for the HER process. Here, it is assumed that H_2 generation exclusively follows the Tafel path (4.2). The corresponding EEC,

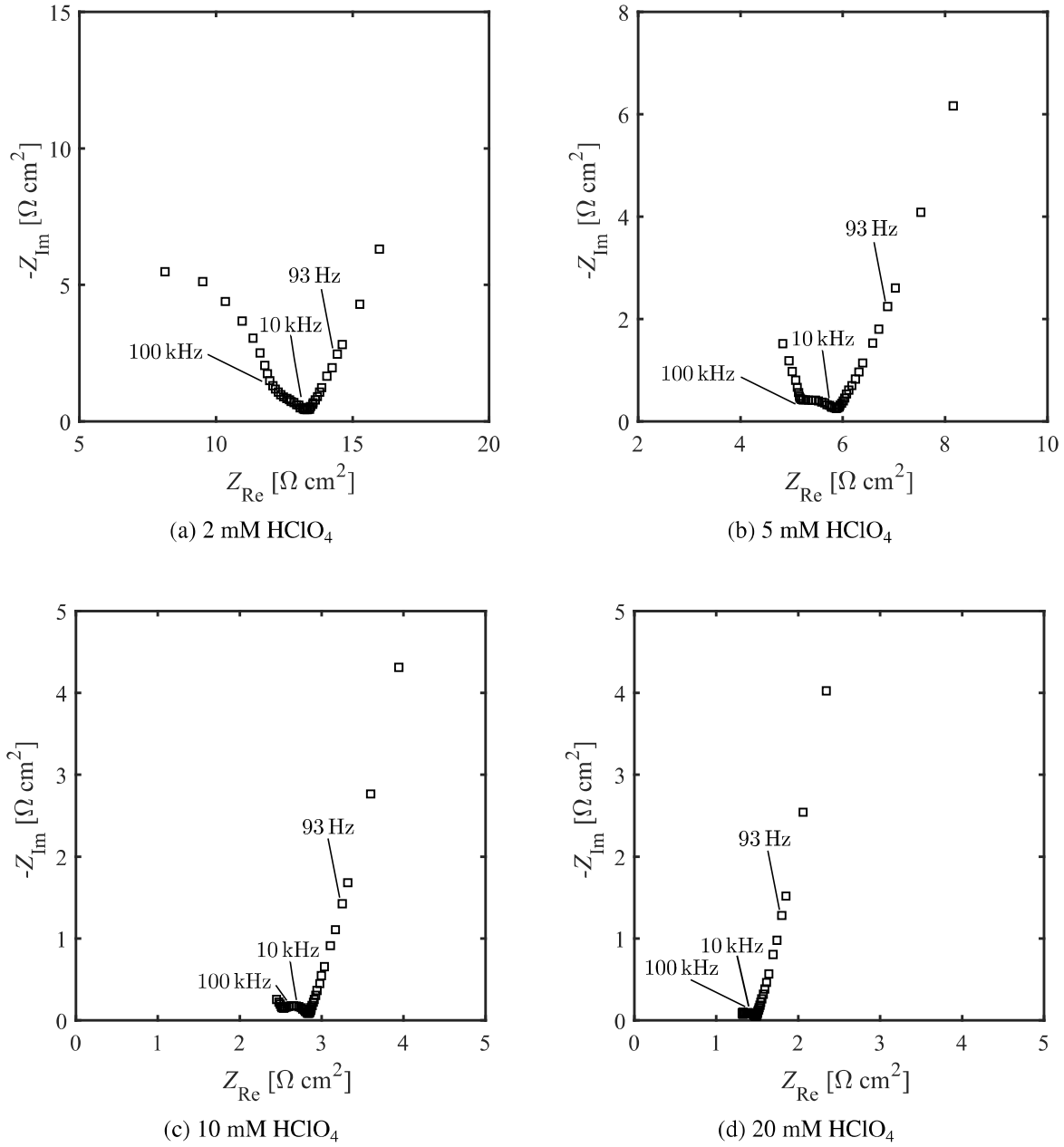


Figure 4.9.: Comparison of dynamic impedance spectra recorded at 0.15 mV vs. RHE in 2 mM, 5 mM, 10 mM, and 20 mM HClO₄ at a 250 μm Pt electrode. $\Delta u_{dc} = 1$ V, $f_{dc} = 0.05$ Hz, $\Delta u_{ac} = 50$ mV, $f_b = 1$ Hz, $d = 7$, $bw = 2$ Hz.

being composed of circuit elements that can be associated with the processes of adsorption, H₂ evolution, and mass transport, is shown in Figure 4.10a.

The quantity R_s represents the ohmic electrolyte resistance caused by the mobility of ions in the solution, whereas C_{dl} refers to the accumulation of charged species at the electrode/electrolyte interface due to the establishment of an electric field. R_{ad} represents the electrokinetic limitation of the reduction of H⁺ to form an adsorbed atomic H species and Z_{Wad} denotes the limitation imposed by the transport of charged H⁺ ions to the electrode surface. C_{ad} is related to the ac-

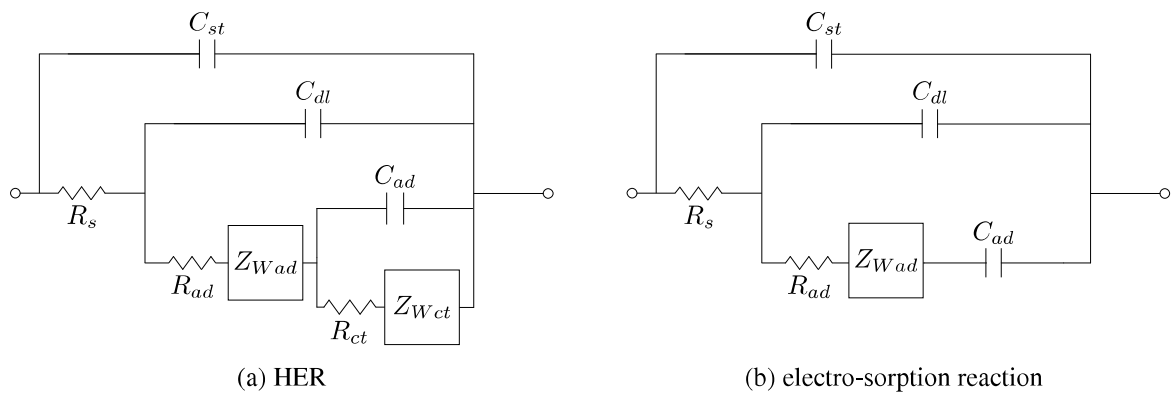


Figure 4.10.: EECs representing the physico-chemical processes governing the HER, applied for data fitting in the (a) hydrogen evolution and (b) electro-sorption region.

cumulation of adsorbed H on the electrode surface, while R_{ct} is related to the recombination of two electro-sorbed H atoms in terms of (4.2). Z_{Wct} may be regarded as the diffusion process of H^+ to the electrode surface or of H_2 away from the surface, respectively. The parameter C_{st} was inserted into the circuit in order to mimic the stray capacitance of the potentiostat. During data fitting, C_{st} was held at a fixed value of 5 pF. The remaining variables were set to initial input values, which were permitted to flexibly change until the minimum χ^2 -value was reached. The EEC composed of the above listed parameters provides an accurate physical description of the Volmer-Tafel reaction sequence in the potential region where H_2 evolution is observed (between -0.5 V and 0.05 V). In contrast, in the electro-sorption region (between 0.05 V and 0.45 V), the regression procedure did not lead to physically meaningful values of the parameters R_{ct} and Z_{Wct} . Therefore, in this potential region these parameters were discarded. Dynamic impedance spectra recorded in a range between 0.05 V and 0.25 V vs. RHE were fitted to the EEC presented in Figure 4.10b, following the procedure described in Section 2.4.4. The good quality of the experimental data enabled data fitting with an error of less than 3% ($\chi^2 \leq 6.77 \times 10^{-4}$). The impedance results obtained in the adsorption region are governed by similar features, irrespective of the electrolyte concentration. Moreover, the spectra obtained for the respective electrolyte concentrations do not significantly change within the potential range under investigation (see Figure D.1). Therefore, this discussion focuses on the dynamic impedance spectra recorded in 10 mM solution of $HClO_4$.

The subsequent Figure 4.11 shows the Nyquist plots of the experimental impedance data and their corresponding fitted spectra at different points in potential, ranging from 0.05 V to 0.25 V vs. RHE on the cathodic branch of the scan. In agreement with the results presented in Figure 4.9, all spectra are composed of a small semicircle representing the charge transfer reaction that leads to the formation of the adsorbed species. The radius of the semicircle decreases with decreasing potentials. This feature is followed by the characteristic straight line. Due to an increase in accumulated atomic H on the electrode surface, the line becomes steeper in slope when the potential is shifted towards cathodic values, thus indicating an almost pure capacitive

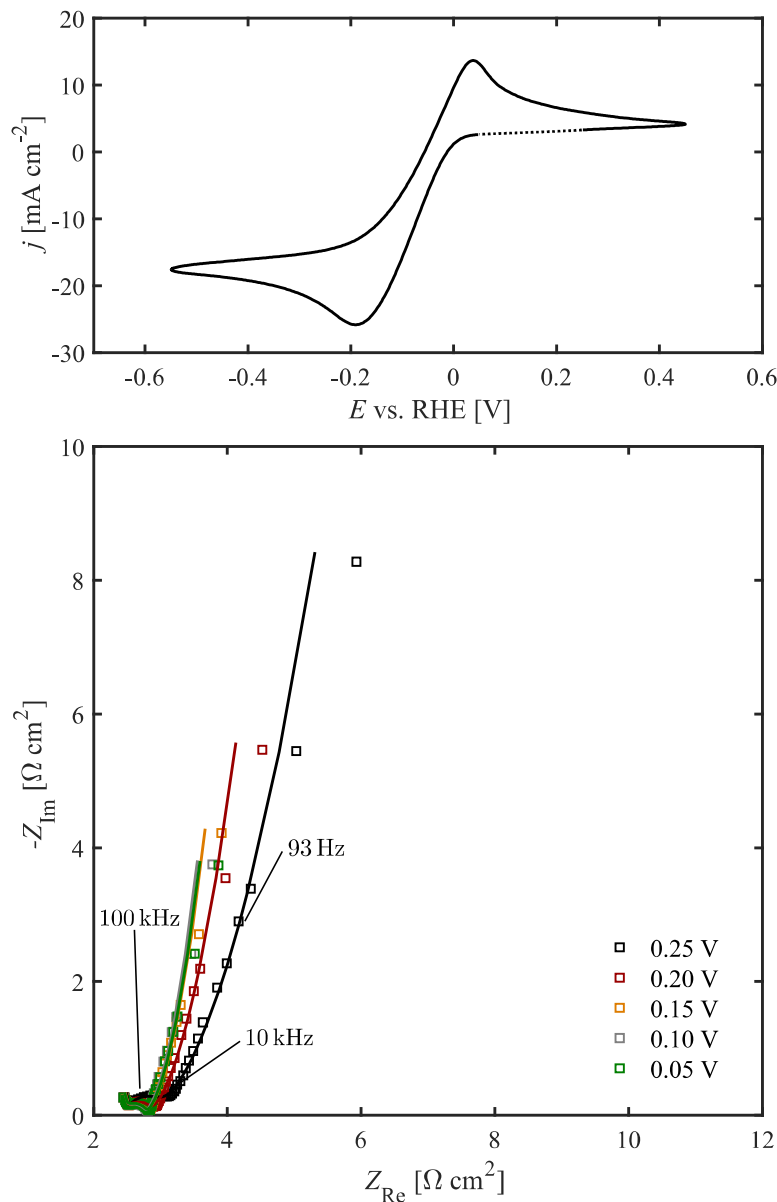


Figure 4.11.: Comparison of experimental (squares) and fitted (lines) dynamic impedance spectra in the adsorption region in 10 mM HClO_4 at a $250\text{ }\mu\text{m}$ Pt electrode. $\Delta u_{dc} = 1\text{ V}$, $f_{dc} = 0.05\text{ Hz}$, $\Delta u_{ac} = 50\text{ mV}$, $f_b = 1\text{ Hz}$, $d = 7$, $\text{bw} = 2\text{ Hz}$.

behavior. As aforementioned, the loop in the high-frequency region can be attributed to the stray capacitance of the electrolyte.

The potential variation of the kinetic quantities, extracted from data fitting in the adsorption region, is displayed in Figure 4.12. When allowing for a variation of 2%, the solution resistance does not change for the respective solutions within the potential region of interest. At a potential of 0.15 V vs. RHE R_s values ranging from $2.39\text{ k}\Omega$ up to $23.98\text{ k}\Omega$ are extracted, where R_s increases with decreasing electrolyte concentration. In order to confirm the validity of these values, the solution resistance was calculated according to expression (3.8). The follow-

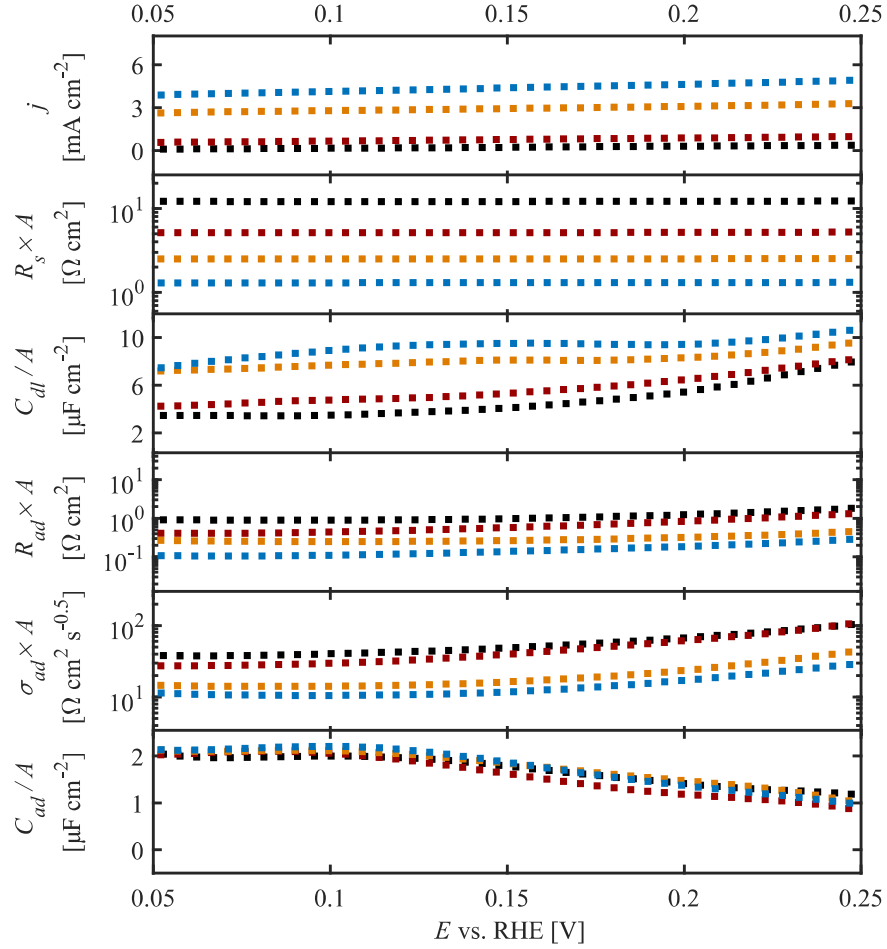


Figure 4.12.: Comparison of fitting parameters extracted from data fitting with the EEC presented in Figure 4.10b in the electro-sorption region in 2 mM (black), 5 mM (red), 10 mM (orange), and 20 mM HClO₄ (blue).

ing Table 4.1 gives a comparison of the solution resistances $R_{s(\text{cal})}$ calculated for the different electrolytes at a 250 μm disk electrode and those obtained from data fitting $R_{s(\text{fit})}$. The calculated values are consistent with the fitting results. Thus, confirming that even in the presence of high-frequency distortions reliable kinetic variables can be extracted.

The time constants of the processes occurring in the adsorption region as well as their characteristic frequencies are shown in Table 4.2. τ_{st} was calculated for the different electrolytes from $R_{s(\text{fit})}$ and C_{st} and refers to the time scale at which stray capacitance effects can be observed. In contrast, τ_{ad} , calculated from R_{ad} and C_{dl} , corresponds to the instant of time that is needed for the electro-sorption reaction to take place. The spectra presented in Figure 4.11 cover a frequency range between 794.3 kHz and 25 Hz, indicating that the characteristic frequencies f_{st} , arising from potentiostat stray capacitance effects, exceed the highest frequency contained in the multi-sine signal. Therefore, this feature should not interfere with that due to the electro-

Table 4.1.: Comparison of electrolyte resistances extracted from data fitting at 0.15 V vs. RHE and resistance values calculated from (3.8).

c_{HClO_4} [mM]	$R_{s(\text{cal})}$ [k Ω]	$R_{s(\text{fit})}$ [k Ω]
2	23.9	24.6
5	9.5	10.4
10	4.7	5.1
20	2.3	2.6

sorption process. However, it must be considered that even at frequencies corresponding to small fractions of f_{st} non-negligible impedance values are recorded. To illustrate this effect, a paradigm spectrum related to the parallel arrangement of a 100 Ω resistor and a 1.59 μF capacitor in a frequency range between 1 MHz and 1 Hz is shown in Figure 4.13. The characteristic frequency f_c of a process refers to the minimum value of the imaginary part of the impedance, which is indicated by a maximum in the Nyquist plot. In the specific case presented here, f_c has a value of 1 kHz. Although the impedance response detected at frequencies up to $0.02 \times f_c$ is negligibly small, it distinctly increases at higher frequencies. Based on that, a general expression was defined to describe the smallest frequency f_s that leads to a non-negligible impedance response, such that

$$f_s = 0.02 \times f_c. \quad (4.9)$$

Equation (4.9) reveals that the impedance response due to the potentiostat stray capacitance is visible in the Nyquist plot at all frequencies above $0.02 \times f_{st}$ and thus considerably affects the recorded spectra. Therefore, with decreasing electrolyte concentrations the high-frequency

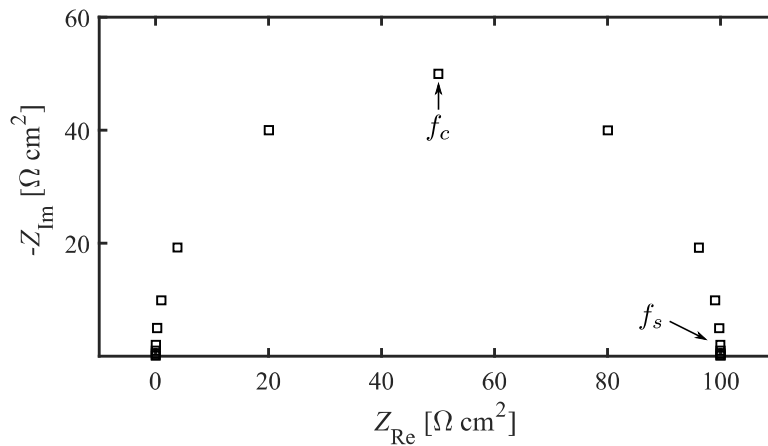


Figure 4.13.: Representation of the characteristic frequency. The spectrum was obtained from the parallel arrangement of a 100 Ω resistor and a 1.59 μF capacitor in a frequency range between 1 MHz and 1 Hz.

Table 4.2.: Time constants and characteristic frequencies calculated for different processes at a potential of 0.15 V vs. RHE.

c_{HClO_4}	τ_{st} [μs]	f_{st} [MHz]	τ_{ad} [μs]	f_{ad} [kHz]
2	0.12	1.29	4.08	39.0
5	0.05	3.03	3.09	51.4
10	0.03	6.21	2.16	73.8
20	0.01	11.94	1.33	120.0

distortion appears at ever lower values due to the increase in solution resistance. According to (4.9), in 2 mM solution of HClO_4 potentiostat stray capacitance effects dominate the Nyquist plot at frequencies higher than 26.8 kHz. In contrast, in 20 mM electrolyte solution stray capacitances lead to a non-negligible impedance response at frequencies exceeding 267.4 kHz. From the values reported in Table 4.2 it can be concluded that the impedance response due to potentiostat stray capacitances partially falls into the same frequency range as the signal originating from the electro-sorption reaction, thus confirming the hypothesis that the high-frequency arc is due to an instrumental artefact.

In the potential region under investigation the overall current density j_{tot} is composed of a cathodic current contribution j_{ad} due to the reduction of H^+ as well as of a positive current signal j_{HOR} , which is associated with the oxidation of residual molecular hydrogen at the electrode surface. Furthermore, charging of the double layer results in a negative current contribution j_{dl} when the potential is swept towards cathodic direction. According to Bard (2001), the current density related to the accumulation of charged species at the electrode surface can be linked directly to the double layer capacitance C_{dl} and the scan rate of the quasi-CV through the relationship

$$j_{dl} = C_{dl}\nu. \quad (4.10)$$

In the same way, the current flowing during the adsorption process can be described as a function of C_{ad} and ν , such that

$$j_{ad} = C_{ad}\nu. \quad (4.11)$$

From the above values, j_{HOR} may be deduced as follows

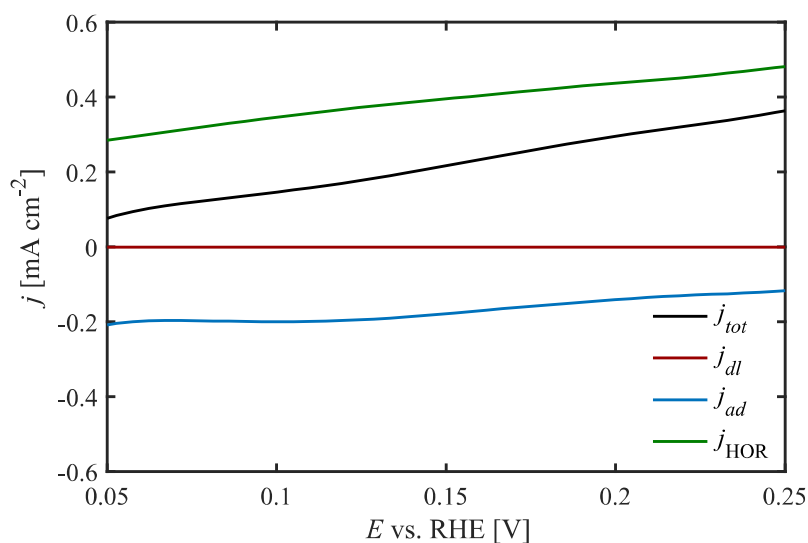
$$j_{\text{HOR}} = j_{tot} - j_{dl} - j_{ad}. \quad (4.12)$$

The values related to the different quantities at a potential of 0.15 V vs. RHE are listed in Table 4.3. Total anodic currents ranging from 0.21 mA cm^{-2} to 4.36 mA cm^{-2} are given. These values are almost fully determined by the anodic current density due to the HOR, which is partially compensated by j_{dl} and j_{ad} . Although at this point of the scan the Volmer reaction is

Table 4.3.: Overall current densities recorded at a potential of 0.15 V vs. RHE and different current contributions.

c_{HClO_4} [mM]	j_{tot} [mA cm^{-2}]	j_{dl} [$\mu\text{A cm}^{-2}$]	j_{ad} [mA cm^{-2}]	j_{HOR} [mA cm^{-2}]
2	0.21	−0.41	−0.18	0.39
5	0.75	−0.53	−0.17	0.92
10	2.92	−0.81	−0.19	3.11
20	4.36	−0.95	−0.19	4.55

assumed to be the guiding step, it becomes obvious that the HOR governs the overall process. Due to the fast scan rate of the quasi-CV (100 mV s^{-1}), molecular hydrogen that was formed in the cathodic branch of the preceding cycle cannot be fully oxidized in the backward scan. The higher the concentration of the electrolyte, i.e. the higher the amount of H_2 generated at the surface, the more dominant this effect becomes. As indicated in Figure 4.14, showing the potential variation of the overall current density and its respective current contributions in 2 mM solution of HClO_4 , the overall current slightly drops when sweeping the potential towards cathodic direction. This behavior can be attributed to a decrease in oxidation current due to ever lower amounts of H_2 evolved at the electrode surface. Simultaneously, the formation of adsorbed species results in the occupation of active surface sites and therefore slows down the adsorption reaction when moving towards cathodic potentials. The contribution of the charging current to the overall current is negligible, irrespective of the electrolyte concentration or the potential value. Interestingly, the variation in adsorption current densities in a potential range between 0.05 V and 0.25 V vs. RHE is in a similar range and follows the same path in all electrolyte solutions, as shown in Figure 4.15. In agreement with that, the values extracted for

Figure 4.14.: Variation of the overall current density and its respective current contributions in a potential range between 0.05 V and 0.25 V vs. RHE in 2 mM HClO_4 .

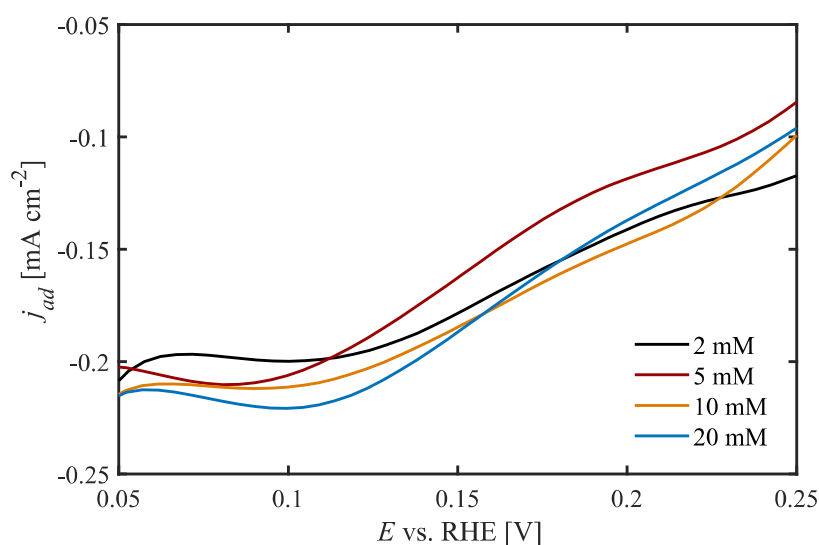


Figure 4.15.: Variation of the adsorption current density in a potential range between 0.05 V and 0.25 V vs. RHE in 2 mM, 5 mM, 10 mM, and 20 mM HClO_4 .

the adsorption capacitance of the different electrolyte solutions behave almost identically upon potential variation, see Figure 4.12. Therefore, it is concluded that the adsorption process leads to the same state of surface coverage, irrespective of the initial concentration of the reactive species.

As indicated in Figure 4.12, the adsorption resistance decreases in cathodic direction until a minimum $R_{ad} \times A$ value is attained at approximately 0.15 V vs. RHE. When sweeping the potential towards lower values, the parameter slightly increases again, an effect that may be attributed to the blockage of active surface sites by atomic H species. In consistence with that, the adsorption capacitance is in an anti-symmetric relation with the adsorption resistance. The potential variation of $R_{ad} \times A$ complies with that of the diffusion coefficient $\sigma_{ad} \times A$, indicating that the adsorption resistance is affected by mass transport of reactive species to the electrode surface.

4.2.4. The Hydrogen Evolution Region

After having discussed the kinetics of the electro-sorption reaction, this Section focuses on the potential region in which the formation of molecular H_2 is the dominating process. Dynamic impedance spectra recorded in diluted solutions of HClO_4 and their corresponding fitted spectra are shown in Figure 4.16. High quality data fitting with an error of less than 0.49% was performed with the EEC presented in Figure 4.10a. The impedance response was investigated in a range between -0.2 V and 0.0 V vs. RHE. As expected, the high-frequency region is perturbed by the potentiostat stray capacitance. Due to a decrease in solution resistance, this effect

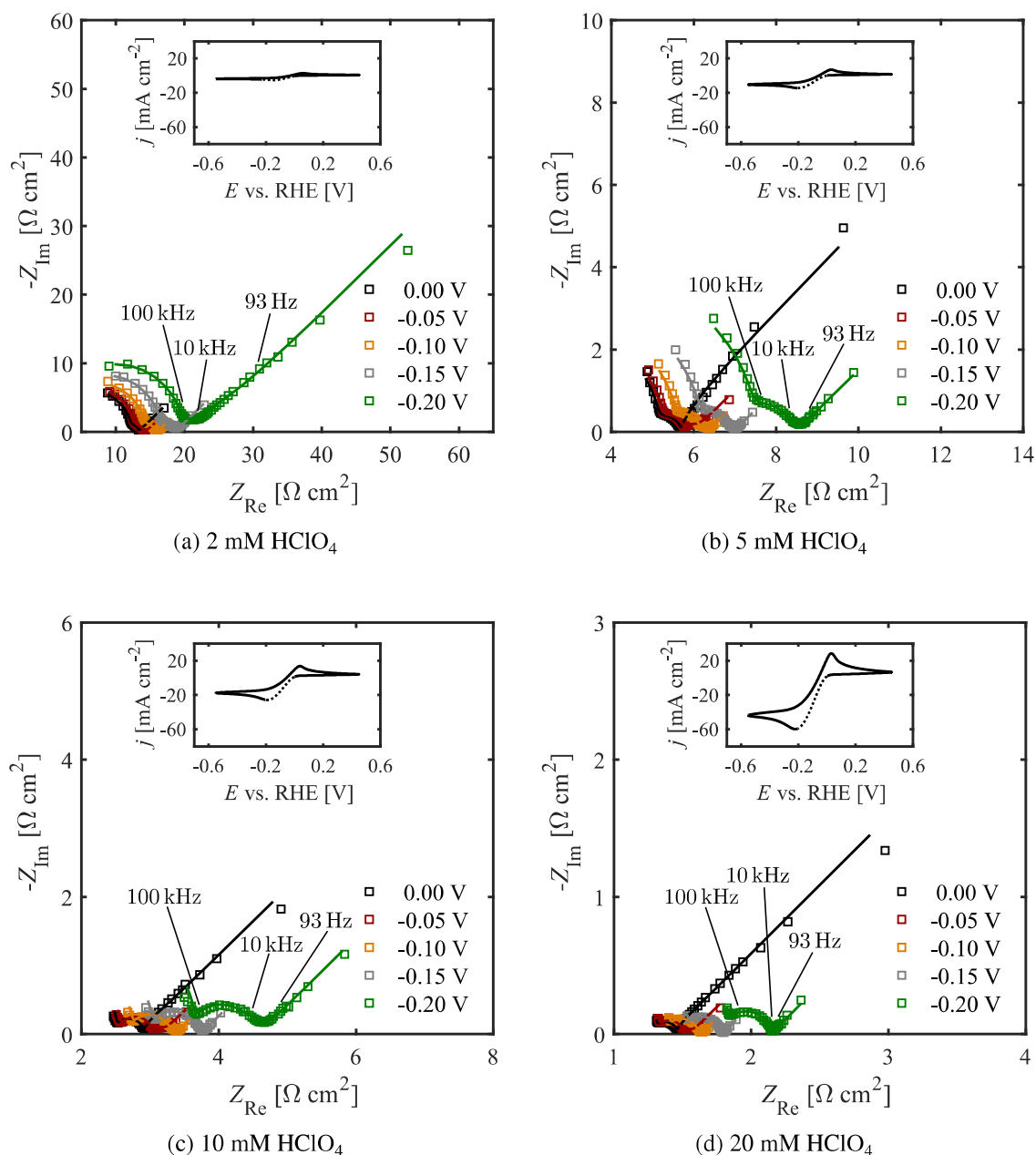


Figure 4.16.: Comparison of experimental (squares) and fitted (lines) dynamic impedance spectra recorded in the hydrogen evolution region in 2 mM, 5 mM, 10 mM, 20 mM HClO_4 at a $250 \mu\text{m}$ Pt electrode. $\Delta u_{dc} = 1 \text{ V}$, $f_{dc} = 0.05 \text{ Hz}$, $\Delta u_{ac} = 50 \text{ mV}$, $f_b = 1 \text{ Hz}$, $d = 7$, $\text{bw} = 2 \text{ Hz}$.

becomes less significant when increasing the concentration of the electrolyte. At intermediate frequencies the impedances related to the processes of electro-sorption and H_2 evolution fall into a single distorted semicircle. The low-frequency region is governed by a diffusion process, indicated by a straight line forming an angle of 45° with the real axis. In agreement with the results presented in Figure 4.9, the overall impedance decreases with decreasing electrolyte resistances, i.e. with higher concentrations. In contrast to what is observed in the adsorption region, the second semicircle increases when shifting the potential towards negative values. This

Table 4.4.: Comparison of electrolyte resistances extracted from data fitting at -0.1 V vs. RHE and resistance values calculated from (3.8).

c_{HClO_4} [mM]	$R_{s(\text{cal})}$ [k Ω]	$R_{s(\text{fit})}$ [k Ω]
2	23.9	29.1
5	9.6	11.4
10	4.8	5.6
20	2.4	2.9

behavior is attributed to the consumption of reactant during the generation of molecular H_2 , which causes depletion of H^+ in the vicinity of the electrode surface and leads to higher impedance values. In accordance with that, the curves are shifted to higher values along the real axis as the potential is swept towards cathodic directions, which is indicative of an increase in R_s , R_{ad} , and R_{ct} . In the hydrogen evolution region (-0.1 V vs. RHE) the fitted values $R_{s(\text{fit})}$ are larger than the calculated ones, since the electrolyte is depleted of reactive species. The lower the initial electrolyte concentration the more pronounced is the change in solution resistance. The corresponding values are reported in the above Table 4.4.

As can be seen in Table 4.5, at a potential of -0.1 V vs. RHE τ_{st} and f_{st} are very similar to the values presented in Table 4.2. The fact that the time constant does not significantly change upon variation in potential is in line with the assumption that this feature is related to an instrumental artefact. The parameters τ_{ad} and f_{ad} are in the same order of magnitude as their respective values observed in the electro-sorption region. The values of f_{ad} are about ten to twenty times larger than those of f_{ct} . Due to the design of the multi-sine signal, the two processes are separated by only 10 to 13 points in the spectrum, thus leading to the difficulty of distinguishing the different phenomena in the Nyquist plot.

The below Figure 4.17 depicts the potential variation of the kinetic quantities that were extracted from data fitting. Here, the formation of gaseous H_2 results in the flow of large reduction currents. The values in Table 4.6 reveal that at a potential of -0.1 V vs. RHE the overall current flow is almost completely due to the evolution of hydrogen gas. In contrast, the current contributions related to the processes of double layer charging j_{dl} and electro-sorption j_{ad} that were calculated according to (4.10) and (4.11) are practically negligible. Although the current

Table 4.5.: Time constants and characteristic frequencies calculated for different processes at a potential of -0.1 V vs. RHE.

c_{HClO_4}	τ_{st} [μs]	f_{st} [MHz]	τ_{ad} [μs]	f_{ad} [kHz]	τ_{ct} [μs]	f_{ct} [kHz]
2	0.14	1.09	5.5	28.9	88.1	1.8
5	0.05	2.79	2.7	58.7	59.9	2.6
10	0.03	5.65	3.7	42.1	44.8	3.5
20	0.01	11.07	1.7	93.5	18.7	8.5

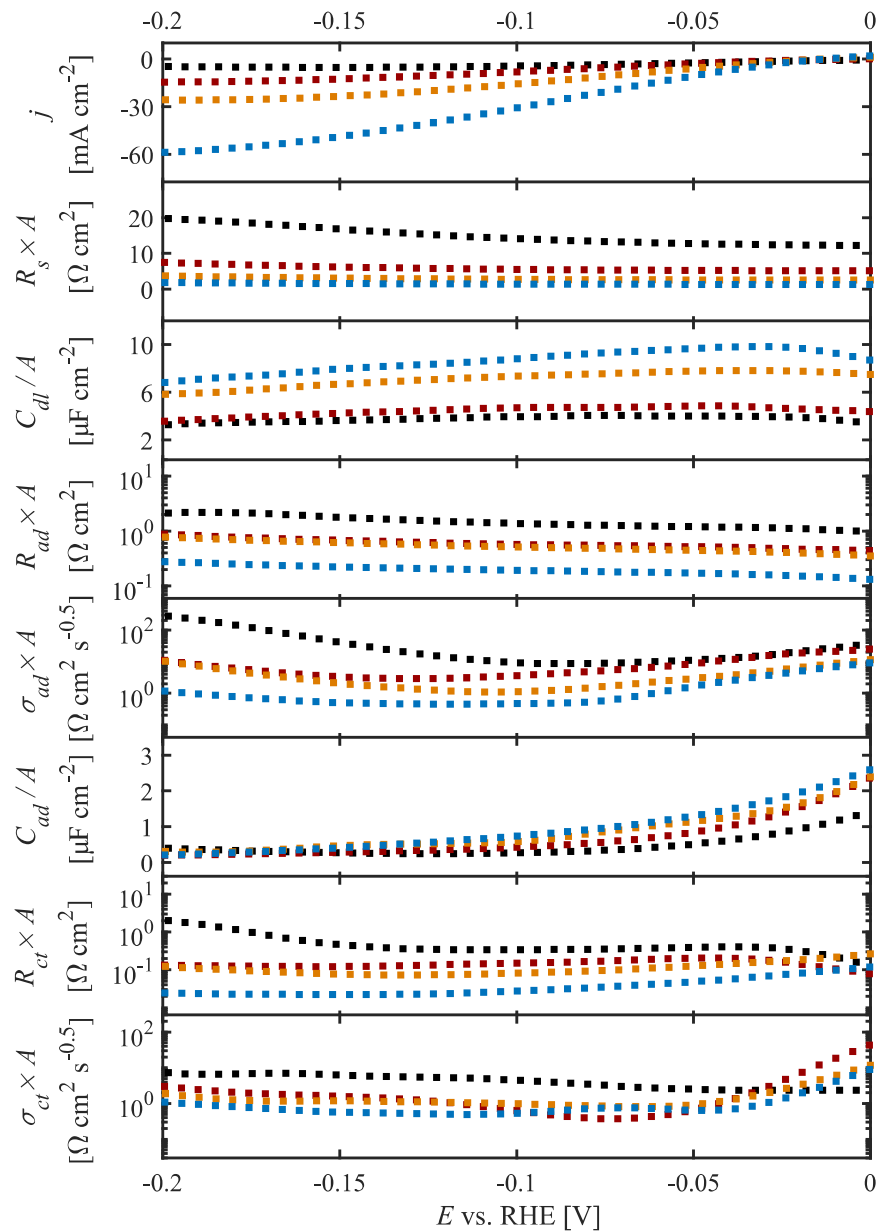


Figure 4.17.: Comparison of fitting parameters extracted from data fitting with the EEC presented in Figure 4.10a in the hydrogen evolution region in 2 mM (black), 5 mM (red), 10 mM (orange), and 20 mM HClO_4 (blue).

Table 4.6.: Overall current densities recorded at a potential of -0.1 V vs. RHE and different current contributions.

c_{HClO_4} [mM]	j_{tot} [mA cm^{-2}]	j_{dl} [$\mu\text{A cm}^{-2}$]	j_{ad} [$\mu\text{A cm}^{-2}$]	j_{HER} [mA cm^{-2}]
2	−4.56	−0.39	−25.82	−4.53
5	−8.61	−0.47	−40.58	−8.57
10	−16.58	−0.73	−56.10	−16.52
20	−32.74	−0.87	−70.31	−32.67

density j_{ad} related to the electro-sorption reaction increases with higher electrolyte concentration, the respective values are significantly smaller than those observed in the adsorption region, see Table 4.3. As expected, in this potential region the Tafel step is favored over the Volmer reaction, which is also indicated by the slightly lower values of $R_{ct} \times A$ compared to those of $R_{ad} \times A$. As shown in Figure 4.18, the cathodic adsorption current decreases when sweeping the potential towards cathodic direction. This behavior can be attributed to the decreasing amounts of reactive species in the vicinity of the electrode that can be discharged at the electrode surface. The lower the initial concentration the faster the depletion of the reactant. In addition to that, when shifting the potential towards negative values, the electro-sorption reaction becomes more and more kinetically unfavorable, which is indicated by a slight increase in $R_{ad} \times A$. In agreement with that, $C_{ad} \times A$ continuously declines in the direction of cathodic potentials, due to the consumption of adsorbed H species. The parameter $R_{ct} \times A$ initially increases and then drops until a minimum value is attained at a potential of approximately -0.15 V vs. RHE. In 5 mM, 10 mM, and 20 mM solution of HClO_4 the value slightly grows when the potential is decreased further. In contrast, in 2 mM HClO_4 $R_{ct} \times A$ strongly increases again at potentials lower than -0.15 V vs. RHE. The Warburg coefficients $\sigma_{ad} \times A$, extracted for the different electrolyte solutions, show a minimum at a potential of -0.15 V vs. RHE and are in the same order of magnitude as the corresponding values observed in the electro-sorption region. In this case, σ_{ad} seems to be linked to the parameter R_{ct} rather than to R_{ad} , thus revealing that the Tafel step is influenced by mass transport of H^+ to the electrode surface. In contrast, the evolution of $\sigma_{ct} \times A$ does not follow a clear trend. As aforementioned, the Tafel reaction is kinetically favored over the Volmer reaction in the potential region under investigation. However, the variation in potential of the different fitting parameters leads to the conclusion that the overall

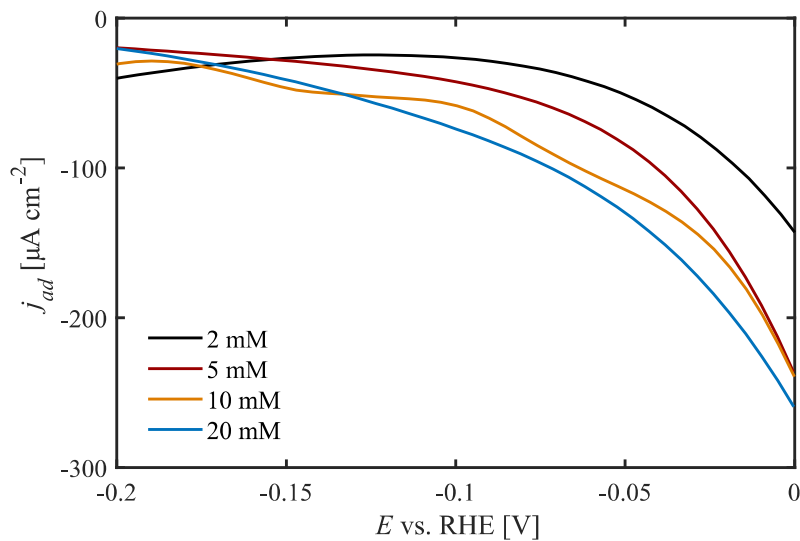


Figure 4.18.: Variation of the adsorption current density in a potential range between -0.2 V and 0.0 V vs. RHE in 2 mM, 5 mM, 10 mM, and 20 mM HClO_4 .

reaction is controlled by the change in electrolyte resistance, which strongly increases with the consumption of reactive species. Moreover, due to the formation of an H^+ depletion layer, mass transport effects limit the rate at which the HER takes place, whereas faradaic limitations have a minor effect on the overall reaction rate.

4.3. Effect of Perchlorates on the HER Kinetics

The kinetics of the HER in diluted acidic solutions of HClO_4 are mainly governed by the electrolyte resistance rather than by the resistances related to the charge transfer processes. In order to determine in which way the parameters R_{ad} and R_{ct} affect the rate of the HER, the experiments presented in Section 4.2 were repeated in the presence of different perchlorate salts, namely KClO_4 , NaClO_4 , and LiClO_4 , acting as supporting electrolytes. In Figure 4.19 the CV recorded at a $250\ \mu\text{m}$ Pt electrode in 10 mM solution of HClO_4 is compared to the voltammograms obtained in solutions of 10 mM HClO_4 and 90 mM KClO_4 , 90 mM NaClO_4 , and 90 mM LiClO_4 , respectively. The CVs recorded in the different perchlorate solutions are almost identical and show the same features as the voltammogram that was performed in absence of supporting electrolytes. However, due to the change in transport processes, the maximum cathodic current density decreases by a factor of approximately 0.5 when perchlorate salts are added. In the presence of supporting electrolytes the current is primarily carried by diffusion. In contrast, in diluted acidic solution the application of an electric field causes the movement of charged species in terms of migrational fluxes, which results in an increased current density. Polarization of the electrodes causes positively charged species to follow the direction of the electric

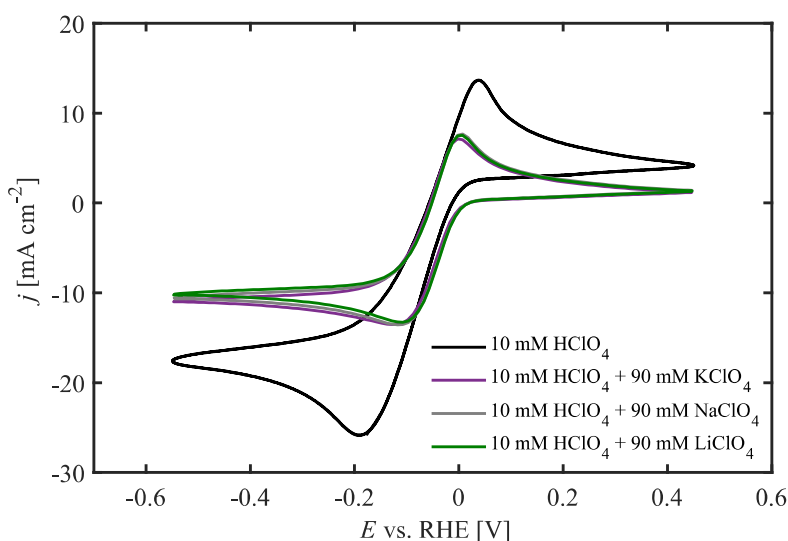


Figure 4.19.: CVs recorded at a $250\ \mu\text{m}$ Pt-WE at a scan rate of $100\ \text{mV s}^{-1}$ in 10 mM HClO_4 , 10 mM HClO_4 and 90 mM KClO_4 , 10 mM HClO_4 and 90 mM NaClO_4 , and 10 mM HClO_4 and 90 mM LiClO_4 .

Table 4.7.: Transport number of H^+ in different electrolyte solutions calculated from (7.7).

electrolyte composition	t_{H^+}
10 mM $HClO_4$	0.83
10 mM $HClO_4$ + 90 mM $KClO_4$	0.21
10 mM $HClO_4$ + 90 mM $NaClO_4$	0.24
10 mM $HClO_4$ + 90 mM $LiClO_4$	0.26

field, whereas ClO_4^- ions are moving towards the direction opposite to it. Since only H^+ participates in the HER, the consumption of reactive species leads to a diffusive flux that follows the direction of the migrational flux. Instead, diffusion of the non-reacting K^+ , Na^+ , Li^+ , and ClO_4^- species takes place in the direction opposite to that of migration in order to counterbalance the formation of concentration gradients according to the constraint of electroneutrality. As the transport number t_i can attain values between 0 and 1, the values of t_{H^+} , calculated according to (7.7) for different perchlorate solutions, are rather low, as can be seen in Table 4.7. Therefore, it is anticipated that in the presence of supporting electrolytes the current is mainly carried by diffusion, while the contribution of migration to the transport of current is negligible. In contrast, in 10 mM solution of $HClO_4$ t_{H^+} almost approaches unity, thus revealing that a large fraction of current is carried by migration of H^+ . Here, the contribution of both mass transport phenomena diffusion and migration results in a larger overall current density as compared to that detected in the presence of perchlorate salts. Moreover, upon addition of supporting electrolytes the peak separation becomes less. This may be attributed to a larger concentration gradient as the current is mainly carried by diffusion, so that the system rapidly reaches diffusion control.

DMFA was performed in different perchlorate solutions at a potential of 0.15 V vs. RHE in the adsorption region. The data were fitted with the EEC presented in Figure 4.10b. In this case, the element mimicking the stray capacitance was removed. Moreover, C_{dl} had to be replaced by a CPE in order to obtain satisfying fitting results ($\chi^2 \leq 3.54 \times 10^{-4}$), where an effective double layer capacitance was calculated according to (7.3). As shown in the below Figure 4.20, the Nyquist plots obtained for the solutions to which supporting electrolytes are added are very similar, independent of the type of cation of the perchlorate salt. Moreover, the spectra do not considerably differ from that recorded in 10 mM solution of $HClO_4$. Again, the governing feature is the accumulation of atomic H at the electrode surface, indicated by a straight line having a steep slope. Stray capacitance effects are no longer visible in the high-frequency region, as the spectra are shifted towards lower resistance values along the real axis as compared to the spectrum recorded in absence of supporting electrolytes.

The subsequent Figure 4.21 shows the evolution of the physical variables extracted from data fitting in a potential range between 0.05 and 0.25 on the cathodic branch of the scan. Interestingly, the change in the respective values is almost identical for the different electrolytes. Positive current densities were recorded for all electrolyte solutions, thus revealing that in the

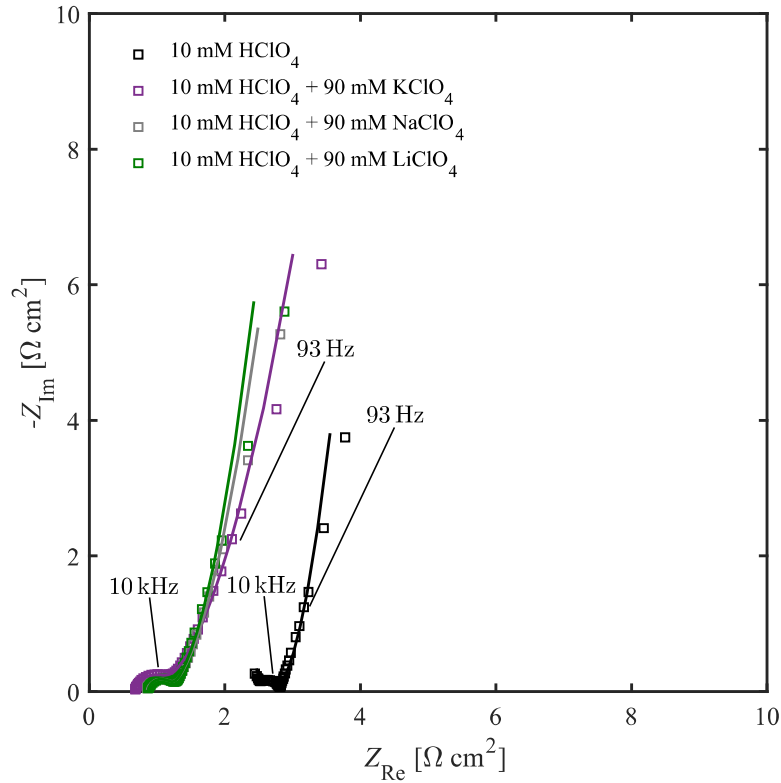


Figure 4.20.: Comparison of experimental (squares) and fitted (lines) dynamic impedance spectra at a potential of 0.15 V vs. RHE in different electrolyte solutions. $\Delta u_{dc} = 1$ V, $f_{dc} = 0.05$ Hz, $\Delta u_{ac} = 50$ mV, $f_b = 1$ Hz, $d = 7$, bw = 2 Hz.

presence of supporting electrolytes the HOR forms the major contribution to the overall current flow. This behavior is in good agreement with the results discussed in Section 4.2.3. As expected, the electrolyte resistance is higher in absence of perchlorate salts, where the respective solution resistances remain constant over the potential range under investigation. The solution resistances extracted at a potential of 0.15 V vs. RHE were employed to calculate theoretical time constants for the characterization of potentiostat stray capacitance effects, see Table 4.8. The values reveal that the time scale at which stray capacitance effects might affect the spectra is about three to four times smaller in the presence of supporting electrolytes. Therefore, high-frequency distortions are no longer visible when perchlorate salts are added.

Table 4.8.: Solution resistances of perchlorate solutions of different concentrations and corresponding time constants and characteristic frequencies related to stray capacitance effects at a potential of 0.15 V vs. RHE.

electrolyte composition	$R_{s(\text{fit})}$ [kΩ]	τ_{st} [ns]	f_{st} [MHz]
10 mM HClO ₄	5.1	26	6.21
10 mM HClO ₄ + 90 mM KClO ₄	1.4	7	23.02
10 mM HClO ₄ + 90 mM NaClO ₄	1.7	8	18.30
10 mM HClO ₄ + 90 mM LiClO ₄	1.8	8	18.01

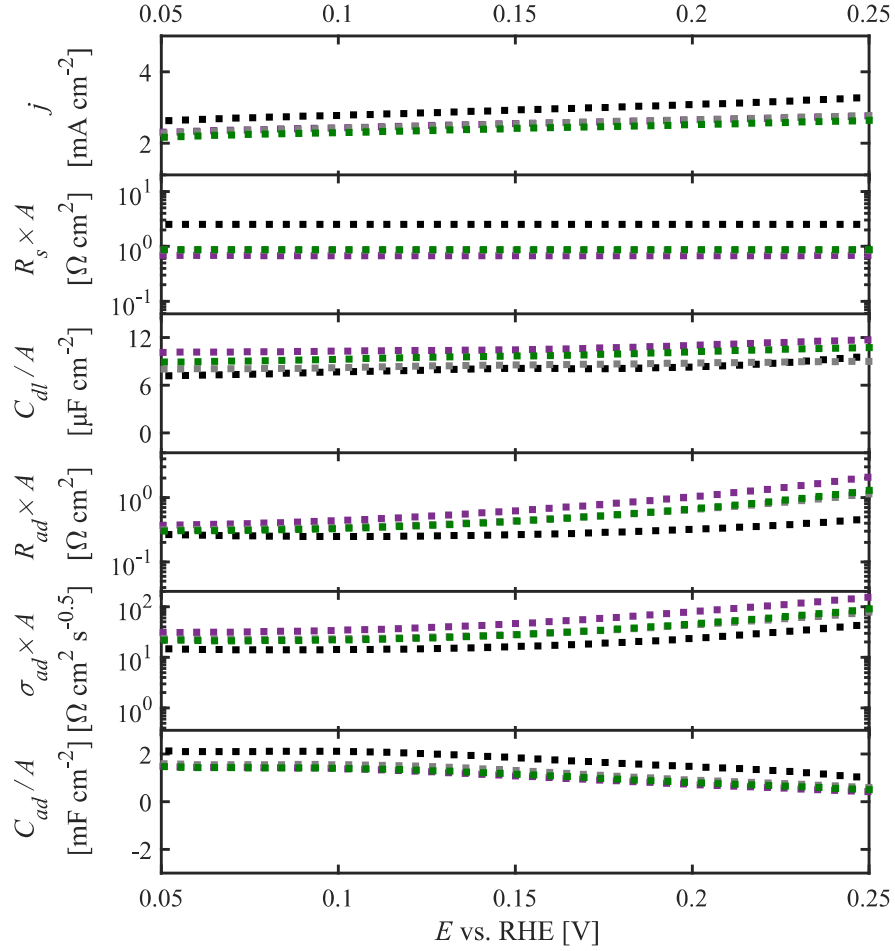


Figure 4.21.: Comparison of fitting parameters extracted from data fitting in the electro-sorption region in 10 mM HClO_4 (black) and solutions of 10 mM HClO_4 and 90 mM KClO_4 (purple), 10 mM HClO_4 and 90 mM LiClO_4 (gray), and 10 mM HClO_4 and 90 mM NaClO_4 (green).

As mentioned before, all physical variables follow the same trend, irrespective of the composition of the electrolyte. Therefore, it is concluded that the adsorption process is not only unaffected by the concentration of the electrolyte but also by the presence of different perchlorate salts.

The dynamic impedance spectra acquired in the hydrogen evolution region (-0.05 V vs. RHE) in the presence of perchlorate salts significantly differ from the spectrum recorded in 10 mM solution of HClO_4 , as illustrated in Figure 4.22. Due to the high-frequency distortion caused by potentiostat stray capacitances, the processes of adsorption and H_2 evolution cannot be clearly distinguished in the diluted electrolyte, see Figure 4.22b. In contrast, the features related to the different reaction steps can be nicely separated in the Nyquist plots acquired in the solutions containing supporting electrolytes. The spectra recorded in the electrolytes containing perchlorate salts are almost identical, showing two consecutive semicircles followed

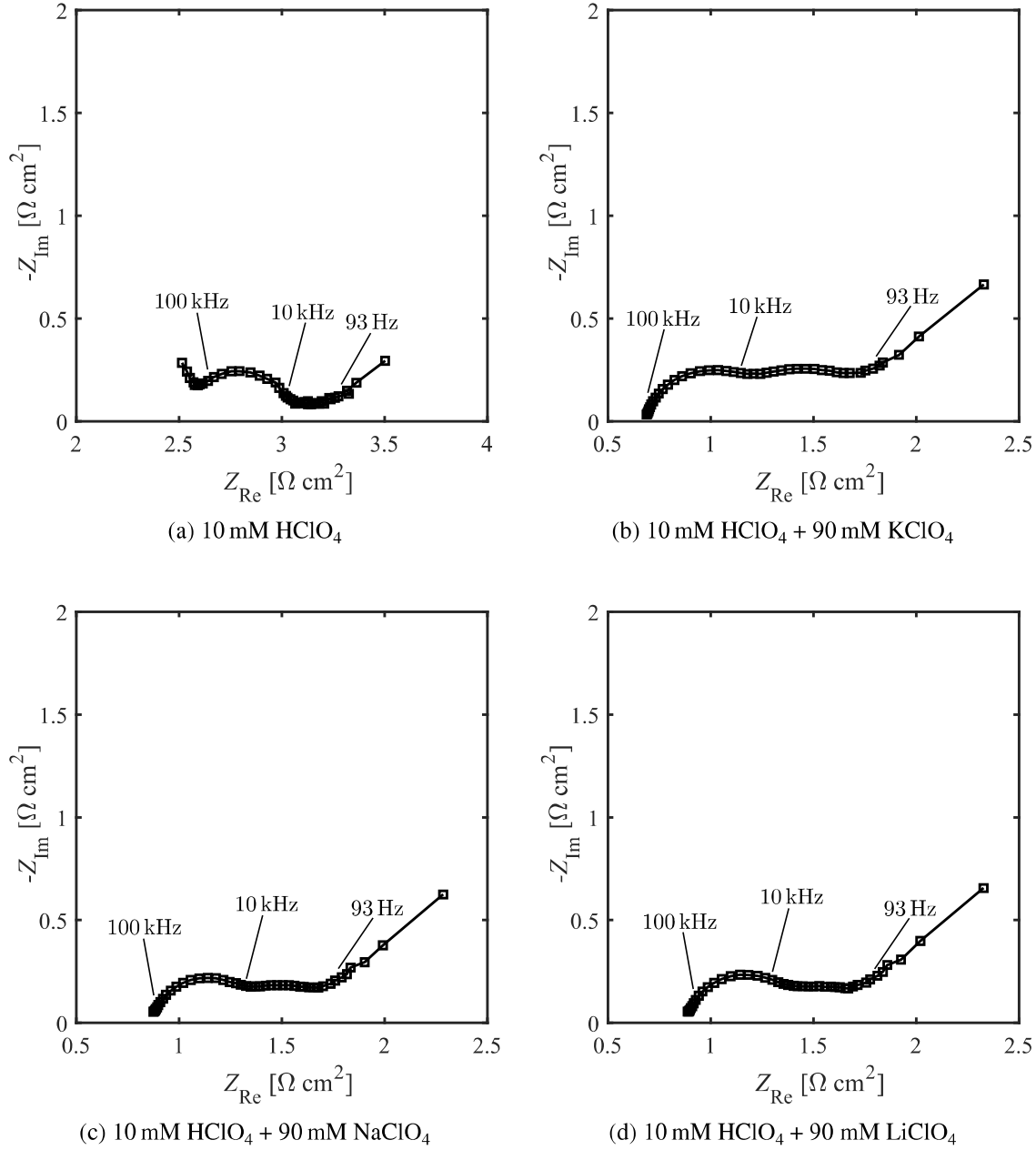


Figure 4.22.: Comparison of experimental (squares) and fitted (lines) dynamic impedance spectra at a potential of -0.05 V vs. RHE in different electrolytes. $\Delta u_{dc} = 1$ V, $f_{dc} = 0.05$ Hz, $\Delta u_{ac} = 50$ mV, $f_b = 1$ Hz, $d = 7$, $bw = 2$ Hz.

by a diffusion process. The curves are shifted towards lower values along the x -axis with respect to the spectrum acquired in 10 mM solution of HClO₄.

The physical variables governing the HER kinetics in the presence of supporting electrolytes were extracted by fitting the data to the EEC presented in Figure 4.10a, where C_{st} was again neglected and C_{dl} was replaced by a CPE. The below Figure 4.23 shows the potential variation of the different circuit components in a range between -0.2 V and 0.0 V vs. RHE. Upon addition of supporting electrolytes, the solution resistance is low with respect to the R_s values extracted for

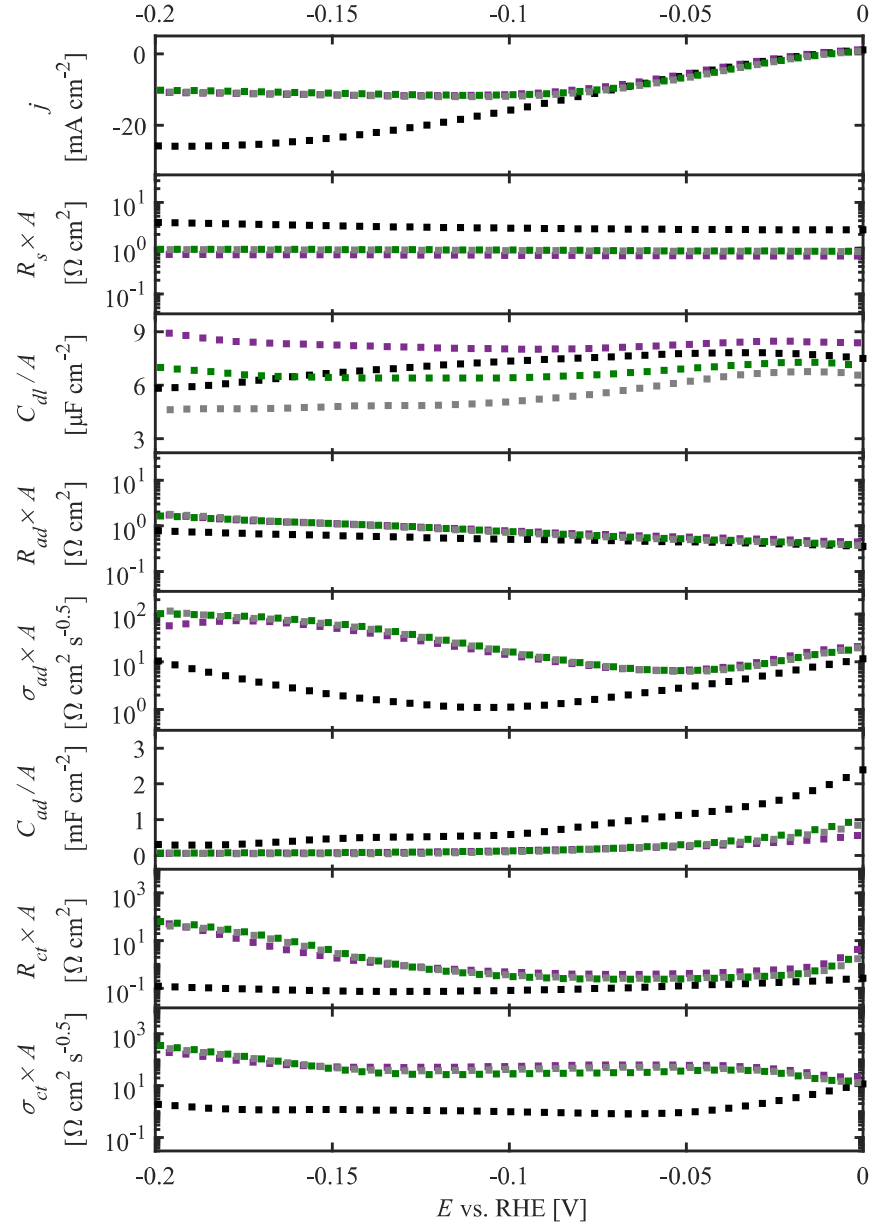


Figure 4.23.: Comparison of fitting parameters extracted from data fitting in the hydrogen evolution region in 10 mM HClO_4 (black) and solutions of 10 mM HClO_4 and 90 mM KClO_4 (purple), 10 mM HClO_4 and 90 mM LiClO_4 (gray), and 10 mM HClO_4 and 90 mM NaClO_4 (green).

the diluted solution and does not significantly change within the potential region under investigation. Table 4.9 compares the electrolyte resistances extracted for the different electrolytes at varying potentials. In 10 mM solution of HClO_4 the solution resistance is constant in the electro-sorption region (between 0.15 V and 0 V vs. RHE), thus revealing that the depletion of reactive species due to the formation of adsorbed H is compensated by the oxidation of residual H_2 . However, in the hydrogen evolution region, the electrolyte resistance increases by around 60% when sweeping the potential from 0.0 V to -0.2 V vs. RHE, indicating that the solution

Table 4.9.: Electrolyte resistances extracted from data fitting in different electrolyte solutions at varying potentials.

electrolyte composition	$R_{s(0.15\text{ V})}$ [k Ω]	$R_{s(0\text{ V})}$ [k Ω]	$R_{s(-0.2\text{ V})}$ [k Ω]
10 mM HClO ₄	5.1	5.1	8.3
10 mM HClO ₄ + 90 mM KClO ₄	1.4	1.4	1.5
10 mM HClO ₄ + 90 mM NaClO ₄	1.7	1.7	1.9
10 mM HClO ₄ + 90 mM LiClO ₄	1.8	1.7	1.9

is depleted by H⁺. In the presence of perchlorate salts the solution resistance remains virtually constant in the electro-sorption region and increases only slightly in the hydrogen evolution region, where $R_{s(-0.2\text{ V})}$ is about 10% larger than $R_{s(0\text{ V})}$. Due to the excess concentration of perchlorate salts, the consumption of H⁺ does not lead to appreciable changes in R_s . However, in absence of supporting electrolytes the depletion of reactive species causes R_s to increase and thus limits the overall reaction rate, as discussed in the previous Section.

In the presence of supporting electrolytes the charge transfer resistance presents the limiting value. Under these conditions, $R_{ct} \times A$ has a minimum at about -0.1 V vs. RHE and grows significantly when the potential is swept towards cathodic direction. At a potential of -0.2 V vs. RHE the $R_{ct} \times A$ values obtained for the different electrolytes exceed the corresponding values of $R_s \times A$ and $R_{ad} \times A$. The parameters $C_{dl} \times A$ and $R_{ad} \times A$ follow the same trend, irrespective of the composition of the electrolyte, indicating that the electro-sorption process remains unaffected by the presence of perchlorate salts. Also, the potential variation of the Warburg coefficients $\sigma_{ad} \times A$ and $\sigma_{ct} \times A$ is similar for the different electrolyte solutions. However, these variables increase upon addition of supporting electrolytes. This behavior can be attributed to the change in transport mechanisms, as outlined before.

5. Reaction Dynamics of the Oscillatory Electrodeposition of p-Type Silicon

The previous Chapters of this thesis were dedicated to the examination of electrochemical systems in forced dynamic conditions, allowing for the investigation of electrode surface properties that cannot be accessed by means of conventional EIS. Here, the reaction kinetics of naturally occurring dynamic phenomena are explored.

This Chapter is concerned with the investigation of the anodic electrodeposition of p-type silicon in fluoride containing electrolytes, exhibiting oscillatory reaction dynamics when an external resistance is connected in series with the WE. Although self-sustained current oscillations at p-type Si have extensively been studied under different conditions, the origin of their oscillatory instabilities has not yet been identified. To develop a framework for understanding the mechanism governing this process, the system was investigated by means of DMFA. The first part of this Chapter provides a brief introduction into dynamical systems theory, with the focus being on oscillatory dynamics. In the second part dynamic impedance measurements carried out on p-type Si are discussed. First, the system is characterized in dynamic equilibrium conditions. Later, the reaction is investigated in the oscillatory regime to determine the cause of spontaneously occurring current oscillations far from thermodynamic equilibrium. Two fundamentally different types of current oscillations can be identified, where the corresponding dynamic impedance spectra are qualitatively analyzed by a set of non-mechanistic fitting parameters. The measurements presented in this Chapter were performed in collaboration with the group of Nonequilibrium Chemical Physics, Technical University of Munich (TUM). A part of the results presented in this Chapter was published in Koster (2018) and Salman (2019).

5.1. Nonlinear Dynamics

Within certain conditions, dynamic instabilities may arise in any kind of chemical, biological, physical, or electrochemical system. These systems display fascinating phenomena such as periodic or chaotic temporal oscillations or spatial pattern formation (Epstein and Showalter, 1996). The interdisciplinary field of nonlinear dynamics provides a framework for the analysis of naturally occurring dynamic processes. The first attempt of solving dynamic problems goes back to the 17th century, where Newton derived differential equations, combining the laws of motion and gravitation to describe two-body problems. His analytical method allowed for a

quantitative description of the motion of the earth about the moon, however, dynamic problems containing more than two bodies could not be solved at that point (Strogatz, 2015). No significant breakthrough in this field was achieved until the development of a geometric approach by Poincaré at the end of the 19th century. His work on celestial mechanics provided the foundation for the modern theory of nonlinear dynamics (Holmes, 1990).

5.1.1. Oscillatory Dynamics

In nature a vast amount of dynamic systems, i.e. systems that evolve with time, can be found (Strogatz, 2015). Biological systems are generally classified as nonlinear and exhibit exceptional features that control the generation of mechanisms of highly complex processes, where a large variety of cellular and intercellular reactions are governed by oscillatory dynamics (Janson, 2012). Due to their applicability in a wide range of physical and mechanical systems, the investigation of these nonlinear oscillators gained particular interest in the course of the 20th century. In the last decades the development of high-speed computers provided entirely new possibilities for handling the differential equations needed to describe oscillatory systems (Strasser, 1999).

Chemical or electrochemical dynamic systems, exhibiting nonlinear reaction kinetics, can serve as simpler analogues for the dynamic behavior of biological systems. Therefore, they may be employed as model systems in order to study new theories in the field of oscillatory dynamics (Krischer, 2001). When discovered first, chemical oscillations caused skepticism among a large group of scientists, who interpreted these observations as a violation of the second law of thermodynamics (Epstein and Showalter, 1996). Therefore, the work of Belousov (1959), who detected spontaneous chemical oscillations when studying metabolic processes did not gain any attention until the existence of chemical self-organizing instabilities far from equilibrium conditions could finally be proved by Field and coworkers (1972). Nowadays, the reaction reported by Belousov (1959) represents one of the most studied processes in the field of chemical oscillators, which has become a well-established branch of science. A multitude of oscillating chemical systems was reported in literature (Nicolis and Portnow, 1973; Frerichs, 2001; Orbán, 2015). The mechanisms governing these reactions are usually highly complex and can involve large numbers of reaction steps. However, the reaction kinetics may often be described by few differential equations, since most of the underlying processes are rapidly equilibrated (Strogatz, 2015).

Also in electrochemistry, spontaneous oscillations of current or potential are widespread phenomena that were manifoldly observed in electrodisolution reactions (Koper, 1998). Electrochemical systems are usually investigated in non-equilibrium conditions, where the rate of reaction is controlled by a variety of processes related to different time constants, thus creating a perfect environment for the formation of spatio-temporal patterns (Strasser, 1999). In elec-

trochemical systems oscillations are linked to interfacial kinetics. Therefore, it is of particular interest to determine the experimental conditions in which oscillatory dynamics are observed.

5.1.2. Bifurcation Theory

In this Section some basic concepts of nonlinear dynamics are introduced that are crucial to gain an understanding of the formation of spontaneous electrochemical oscillations, occurring when a system is maintained far from thermodynamic equilibrium (Koper, 1998). Usually, upon perturbation of an electrochemical system by an abrupt change in experimental parameters, the time-dependent variables of the system undergo transient states until they settle in a steady-state. Stationary conditions may only be attained if the steady-state is stable, i.e. it is not affected by small perturbations. In this case, the system will always return to its steady-state when fluctuations decay. Instead, when the state is not stable, even smallest perturbations will cause the system to deviate from its steady-state (Strasser, 1999).

In dynamic conditions the instability of the steady-state is a prerequisite for spontaneous oscillations to form. Although unstable states cannot be observed experimentally, it is clear that their existence significantly affects the dynamic properties of electrochemical systems. Therefore, when investigating oscillatory dynamics, the main focus must be on the origin of the instability of the steady-state. According to Thompson and Stewart (2002), the behavior of a dynamic system may be described in terms of trajectories in an abstract phase space, where the coordinates of the trajectory provide the state of the system at each point in time, see Figure 5.1a. In contrast to LTI systems, which can be solved by linear combinations of responses due to basic input signals (see Section 2.2), a straightforward solution to nonlinear problems does not exist. Linear stability analysis may be employed to determine whether or not a steady-state is stable. This technique has widely been applied to investigate if a system recovers from small fluctuations by linearization of its differential equations about the steady-state. Often, the transition from a stable to an unstable state involves a bifurcation. In simple terms, a bifurcation in non-equilibrium conditions may be figured as a phase transition in equilibrated systems. The latter is related to transitions between solid and liquid phases, whereas dynamic systems switch between stable fixed points and oscillatory states (Koper, 1998). Bifurcations involve the destabilization of a stable fixed point and its transformation into a stable oscillatory state. In the phase space this behavior may be represented in terms of closed trajectories, which are referred to as stable limit cycles, as illustrated in Figure 5.1b.

As stated by Koper (1998), electrical quantities play a crucial role in the emergence of temporal periodic behavior. Due to the fact that the electrode surface cannot be considered perfectly homogeneous, the events occurring at it must be synchronized by long-range coupling. This can be done by applying an Ohmic resistance in series with the working electrode.

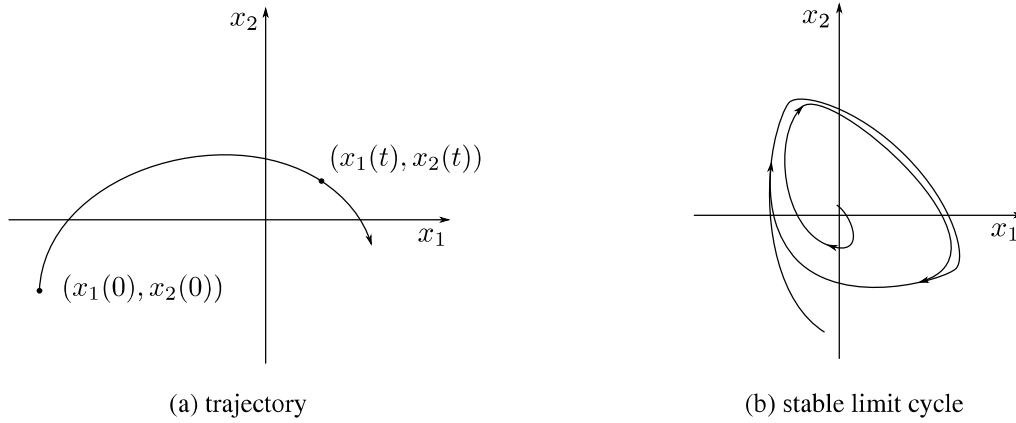
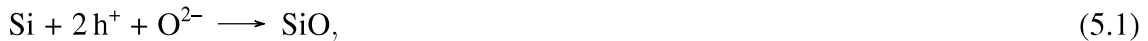


Figure 5.1.: Trajectory and stable limit cycle in the phase space, adapted from Thompson and Stewart (2002).

5.1.3. The Silicon Electrodeposition Reaction in Fluoride Containing Media

Among the vast amount of electrochemical systems exhibiting oscillatory reaction dynamics, the anodic electrodeposition of p-type Si has gained particular attention in the last decades. This process represents a model system for nonlinear reaction diffusion systems (Patzauer, 2016), where sustained pattern formation arises due to the interplay between reaction dynamics and transport processes (Krischer, 2001). The transport process allows for spatial communication of the system, where the connection of different locations allows for the transfer of information about the state of the system at different points (Krischer, 2001). In the presence of an external global coupling sustained current oscillations are observed during the anodization of p-type Si in fluoride containing electrolytes. Under these conditions, the formation of an oxide layer is accompanied by its chemical dissolution (Lehmann, 1995).

According to Salman (2019), the anodic oxidation of Si proceeds via different reaction steps, in which silicon reacts with O^{2-} ions in solution to form a silicon oxide layer. The reaction may involve the formation of partial oxide species SiO



which are subsequently oxidized to the final oxide SiO_2



where α corresponds to the amount of charge carriers (captured holes or injected electrons). This transformation may include different sub-steps. Alternatively, the final oxide can be formed in a single-step, as given below



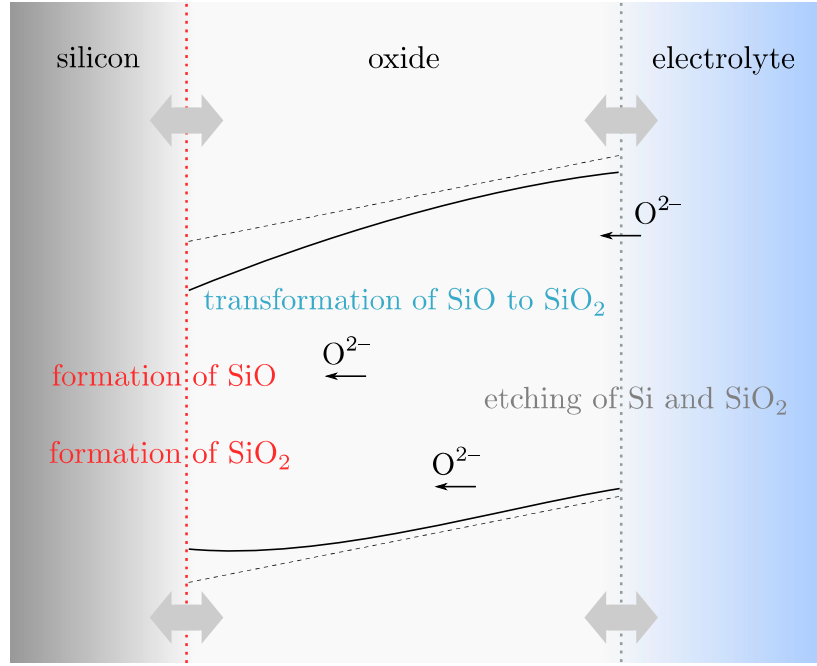
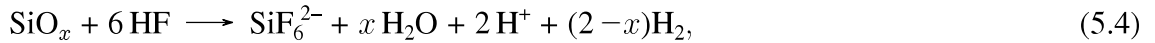


Figure 5.2.: Schematic representation of the anodic electrodisolution reaction at p-type Si, adapted from Salman (2019).

Here, it is assumed that (5.1) and (5.3) occur at the silicon/silicon oxide interface, whereas (5.2) takes place inside the oxide layer (Salman, 2019). Simultaneously, at the silicon oxide/electrolyte interface the oxide layer is chemically dissolved by the fluoride species in solution, such that



with $1 < x < 2$. The etching process depends on the total concentration of fluoride species in the electrolyte (Patzauer, 2016). The above Figure 5.2 provides a graphical representation of the anodic dissolution of silicon in fluoride containing media. Although the above reaction sequence must be understood as a simplified mechanistic representation of the overall process, it provides the most important aspects of the silicon electrodisolution reaction.

In his pioneering work on the electropolishing reaction of silicon in hydrofluoric acid solutions Turner (2004) was the first to observe self-sustained current oscillations, emerging at potentials above 3 V. Since then, the oscillatory reaction dynamics of the anodic Si electrodisolution reaction have intensely been studied under various experimental conditions in order to determine the origin of the instabilities governing this process. Its complexity is given by the fact that two interfaces are involved in the reaction, the silicon/silicon oxide interface where silicon defects are created and the silicon oxide/electrolyte interface where the dissolution of the oxide species occurs. According to Chazalviel (1992), the coupling between the dissolution rate at the outer interface and the defect creation rate at the inner interface plays a signifi-

cant role during the electrodeposition reaction. Lehmann (1995) studied the properties of the oxide film by means of x-ray reflectometry, atomic force microscopy (AFM), and ellipsometry, stating that the formation of current oscillations throughout the anodic electrodeposition of p-type Si can be attributed to a stress-induced transition of oxide morphology. Chazalviel (1998) suggested that the origin of the oscillation mechanism lies in a periodic breakdown of the blocking properties of the oxide, caused by ion permeation. The common assumption of the above attempts is that they assume periodic variations in oxide morphology to be the main cause of the existence of stable oscillations. However, high-resolution transmission electron microscopy (TEM) and AFM studies performed by Proost (2014) revealed that the occurrence of current oscillations does not involve variations in surface roughness or stress-induced cracks. In contrast, the oscillatory instabilities were attributed to a periodic charge dissipation within the oxide.

5.2. The Anodic Electrodeposition of p-Type Si in Quasi-Stationary Conditions

To gain further insight into the reaction dynamics governing the anodic electrodeposition of p-type silicon in fluoride containing electrolytes, the system was investigated by means of DMFA. The aim was to develop a framework for understanding the kinetics of the mechanism of this highly dynamic process. This Section is concerned with the examination of the Si electrodeposition reaction in quasi-stationary conditions. In the following Section 5.3 the system is studied in the oscillatory regime.

5.2.1. Voltammetric Characterization of the Si Electrodeposition Reaction

First, the p-type Si (111) sample was characterized by means of standard cyclic voltammetry in a solution of 0.06 M NH_4F in 142 mM H_2SO_4 (pH = 1). The below Figure 5.3 shows the CV recorded at a scan rate of 20 mV s^{-1} , which may be divided into three different regions. The first region extends from the starting point of the scan (0.64 V vs. SHE) to a potential of 2.1 V vs. SHE where the current is at a maximum. According to literature, this region is referred to as electropolishing region (Eddowes, 1990). In this potential range, the etching process is the dominating step. Therefore, no stable oxide can be formed (Patzauer, 2016). In contrast, at voltages higher than 2.1 V vs. SHE the growth of a stable oxide layer leads to a decrease in current, which can be attributed to the passivation of the electrode surface (region 2). This region is characterized by a negative slope of the current/voltage curve (Salman, 2019). This feature is due to the establishment of an equilibrium between the oxide layer growth and the dissolution reaction. The current drops until a current plateau is attained in the third region of the scan that starts to establish at potentials more positive than 4 V vs. SHE. Here, the growth of

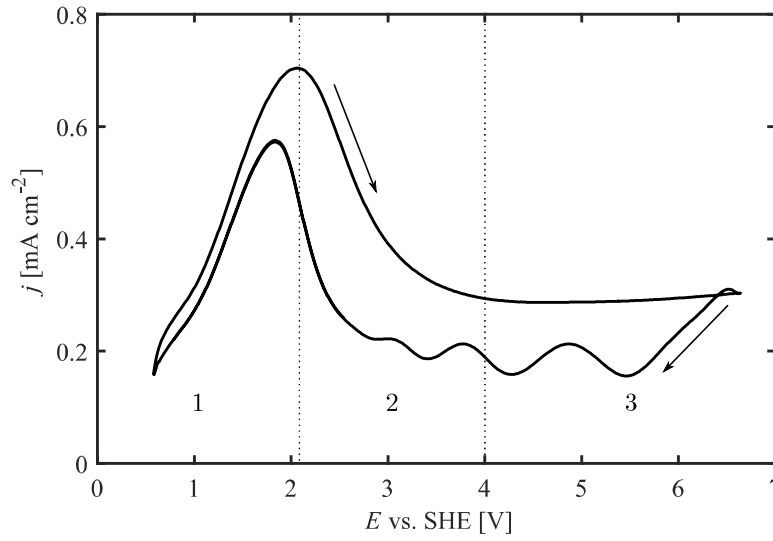


Figure 5.3.: CV recorded at p-type Si(111) in 0.06 M NH_4F in 142 mM H_2SO_4 (pH = 1) at a scan rate of 20 mV s^{-1} .

the oxide layer into the silicon electrode is the governing process. There is a hysteresis between the anodic and the cathodic scan, which can be attributed to a difference in mass of the oxide layer. Due to the scan rate of 20 mV s^{-1} , the formation of the oxide layer does not reach steady-state conditions. Therefore, its thickness still increases upon reversal of the scan, resulting in lower currents.

In region 3 spatially uniform oscillations can be observed when an external resistor is introduced in series with the WE. The external resistance creates a voltage drop u_{el} between the WE and the RE, which can be expressed as

$$u_{el} = u_{app} - R_{ext} i = u_{app} - R_{ext} A j, \quad (5.5)$$

where u_{app} is the initially applied voltage, R_{ext} is the external resistance, and i is the current flowing through the WE (Patzauer, 2016). From (5.5) it follows that the external resistance causes local destabilizations in each point of the electrode. However, due to the fact that the current response is investigated in terms of an averaged current density j per surface area A , the external resistance may be understood as a global coupling.

5.2.2. Impedance Studies in the Regime of Negative Differential Resistance

Before investigating the oscillatory regime of the Si electrodeposition process, the second region of the CV presented in Figure 5.3 is studied in more detail. In this potential range the electro-oxidation reaction and the etching of the oxide layer proceed at the same reaction rate.

The region governed by the negative slope of the current-potential curve was investigated by means of DMFA in dynamic equilibrium conditions. The measurements were carried out in a solution of 0.05 M NH_4F in 25 mM H_2SO_4 ($\text{pH} = 2.3$). In order to attain quasi-stationary conditions, the scan rate was set to a value of 1 mV s^{-1} . Dynamic impedance spectra were acquired by superposition of the quasi-triangular waveform with a multi-sine signal covering a frequency range between 3 kHz and 12 mHz.

The dynamic impedance spectra recorded at different points in potential are shown in Figure 5.4a. In the high-frequency range the spectra are governed by a small semicircle, which increases with increasing potentials. The semicircle is followed by a fraction of a loop, which is terminated by a kink at intermediate frequencies and evolves into a large semicircle that tends towards negative resistance values in the low-frequency region.

Salman (2019) developed a physical model in order to reproduce the impedance behavior that is observed during the electro-oxidation of Si in fluoride containing electrolytes in the potential region under investigation. The model is based on the assumption that the anodic electrodis-solution of Si follows reaction sequence (5.1)–(5.4). It is generally accepted that the etching process is purely chemical in nature, hence, it is not affected by variations in potential. However, the central idea of the model is that the etch rate depends on the composition of the oxide layer. The latter is strongly related to the applied potential. Therefore, the etch rate is assumed to exhibit an indirect potential dependence. Due to its consumption inside the oxide layer, the amount of partial oxide decreases with increasing distance from the silicon/silicon oxide inter-face. The concentration of the partial oxide species at the silicon oxide/electrolyte interface, which is directly linked to the rate of reaction (5.2), determines the etch rate of the oxide. It is assumed that the etch rate increases with increasing amounts of partial oxide, whereas the reaction rates of (5.1) and (5.3) are exclusively limited by the transport of O^{2-} inside the oxide layer.

The below Figure 5.4b shows a comparison of a dynamic impedance spectrum recorded at a potential of 2.2 V vs. SHE by means of DMFA and a simulated spectrum computed at a potential of 0.4 V. According to Salman (2019), the offset between the simulated and the exper-imental voltage can be related to the space charge layer and the Helmholtz layer, which were not considered in the model. The close similarity between the two spectra does not only reveal the high quality of the experimental data but also confirms the accuracy of the model. In the high-frequency region the spectra are almost identical. In the low-frequency region the characteristic big semicircle starts to evolve at positive real values and tends towards the direction of negative resistances. The simulated curve forms an intercept with the x -axis at real and negative values when $\omega \rightarrow 0$. In contrast to the experimental spectrum, the simulated spectrum does not exhibit the kink at intermediate frequencies. With the aid of the model it was possible to ascribe a phys-ical meaning to some of the features observed in the measured spectra. The high-frequency loop can clearly be attributed to the accumulation of charged species across the silicon/silicon oxide

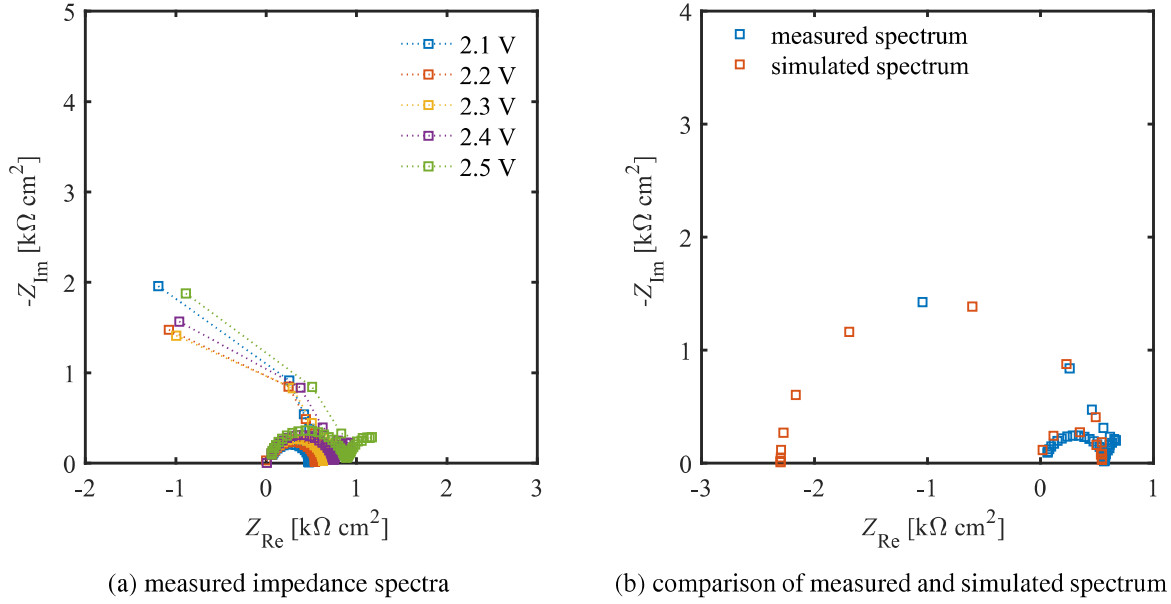


Figure 5.4.: Dynamic impedance spectra recorded at p-type Si in 0.05 M NH_4F and 0.025 M H_2SO_4 at different potentials and comparison of a simulated spectrum at a potential of 0.4 V and a measured spectrum at a potential of 2.2 V vs. SHE, adapted from Salman (2019). $\Delta u_{dc} = 2$ V, $f_{dc} = 0.25$ mHz, $\Delta u_{ac} = 300$ mV, $f_b = 3$ mHz, $d = 3$.

and the silicon oxide/electrolyte interface, respectively, since this feature disappears when the charging term in the model is neglected. As stated by Salman (2019), the amount of reactive O^{2-} species that enters the oxide layer increases with higher anodic potentials. An increase in O^{2-} concentration can be associated with a thickening of the oxide layer, as the reaction rates of (5.1) and (5.3) increase. At the same time, the rates of (5.1) and (5.3) are lowered by the oxide layer growth as the distance that needs to be covered by the O^{2-} species in order to reach the silicon/silicon oxide interface increases. In contrast, reaction (5.2) is even enhanced by the growth of the oxide layer. Consequently, the proportion of SiO_2 in the oxide layer increases at higher voltages. Under these conditions the etch rate is assumed to decrease, thus resulting in further thickening of the oxide layer. Therefore, the presence of the negative differential resistance might be attributed to the relation between the transformation of the partial oxide species and the etch rate dependence on the oxide composition.

The results show that high quality impedance spectra were obtained during the Si electro-oxidation process in steady-state conditions. The physical model provided by Salman (2019) allows for the reconstruction and interpretation of the impedance spectra recorded in the region of negative differential resistance. Although the model cannot fully mimic all the features observed in the measured spectrum, it exhibits the most dominant impedance characteristics. The ideas presented in this Section provide the foundation for the investigation of the oscillatory reaction dynamics of the silicon electrodisolution process that is dealt with in Section 5.3.

5.3. Reaction Dynamics in the Oscillatory Regime

After having identified the most significant physical processes governing the anodic electrodeposition of p-type silicon in dynamic equilibrium conditions, the system is studied in the oscillatory regime. In the presence of an external resistance sustained current oscillations can be observed at p-type silicon in wide parameter ranges and under different experimental conditions. Recently, Schönleber (2012) reported the existence of two fundamentally different types of current oscillations that emerge upon variation of the serial external resistance. At lower resistance values so-called low-amplitude oscillations can be observed that are characterized by an almost sinusoidal shape and a relatively small current amplitude. In contrast, when a higher external resistance is connected in series with the WE, the current oscillations exhibit a different shape and are higher in amplitude. Schönleber (2012) stated that low-amplitude oscillations are not associated with changes in oxide quality or etch rate, whereas high-amplitude oscillations undergo variations in oxide quality. This observation lead to the assumption that the transition between the two types of oscillations involves a change in mechanism. As classic impedance spectroscopy cannot be applied to investigate the reaction dynamics governing the Si electrodeposition in the oscillatory regime, the reaction is studied by means of DMFA in order to analyze the temporal evolution of the reaction kinetics that underlie the two fundamentally different types of oscillations. The measurements were performed at p-type Si(111) in a solution of 0.06 M NH_4F in 142 mM H_2SO_4 ($\text{pH} = 1$).

For the system under investigation, a variation in external resistance in a range between 10 k Ω and 30 k Ω leads to sustained oscillations when the WE is polarized at a potential of 8.64 V vs. SHE, as illustrated in Figure 5.5. When applying an external resistance of 10 k Ω , low-amplitude sinusoidal oscillations emerge, which oscillate at a frequency of 20 mHz, see Figure 5.5b. In contrast, when the external resistance is increased to 30 k Ω , the oscillations are more peak-shaped. In this case, the frequency and amplitude are increased by a factor of 1.5 with respect to low-amplitude oscillations, as shown in Figure 5.5d. Interestingly, when applying an external resistance of 17.5 k Ω , a special type of shoulder oscillation is observed, see Figure 5.5c. Shoulder oscillations have the same period as low-amplitude oscillations and are similar in amplitude. In literature it was proposed that high-amplitude oscillations emerge from low-amplitude oscillations, where shoulder oscillations form a stable intermediate state. Accordingly, their oscillatory instability may be caused by the same feedback-loops (Schönleber, 2012). In what follows, the oscillatory reaction dynamics governing the different types of oscillations are studied using DMFA.

The measurements presented in the previous Chapters of this thesis dealt with the investigation of systems that were subjected to forced dynamic conditions, where the potential was perturbed by a quasi-triangular waveform superimposed by a multi-sine signal. As already discussed in Section 3.2, the base frequency of the multi-sine wave must be about 10 times higher

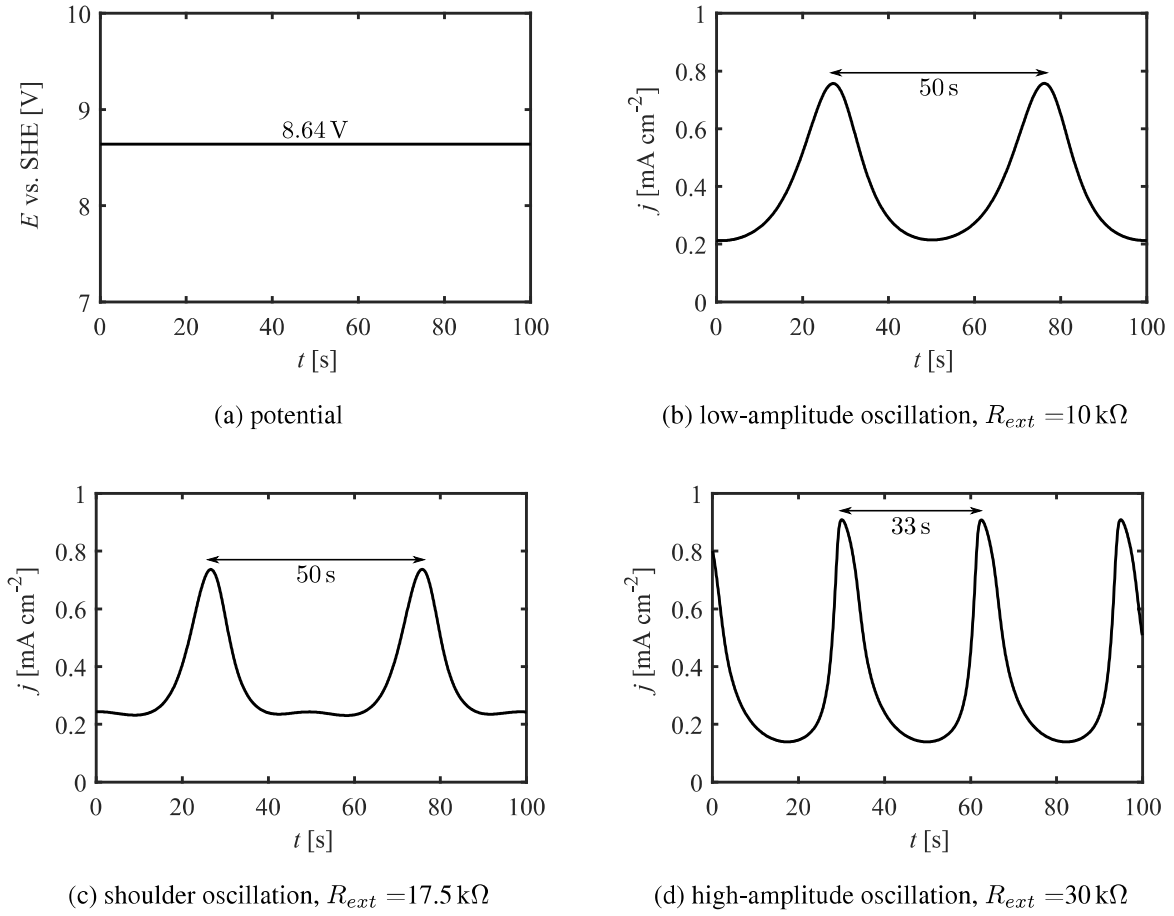


Figure 5.5.: Different types of current oscillations observed at p-type Si in 0.06 M NH_4F in 142 mM H_2SO_4 at 8.64 V vs. SHE. The external resistance R_{ext} was varied between 10 k Ω and 30 k Ω .

than the fundamental frequency of the quasi-CV to allow for reliable dynamic impedance spectra acquisition. In contrast, the system presented in this Chapter exhibits self-sustained current oscillations under the conditions outlined above. Due to the highly dynamic behavior of the anodic Si electrodisolution reaction, DMFA was performed by superposition of the constant *dc* signal with the multi-sine waveform. In this case, the design of the multi-sine waveform is strongly dependent on the natural current oscillation. For an accurate choice of multi-sine frequencies the different types of self-sustained oscillations have to be investigated in Fourier space. To do so, the signals presented in Figure 5.5 were transformed into the frequency domain by means of FT, where the corresponding spectra are shown in Figure 5.6. In Fourier space the time-invariant potential at which the different kinds of oscillations emerge appears as a sharp signal at 0 Hz. The current spectra are composed of the fundamental frequency f_{osc} of the respective type of oscillation and its higher order harmonics. The amount of higher order harmonics strongly varies for the different types of oscillations. The skirt about the fundamental frequency related to the low-amplitude oscillation has a bandwidth bw_{dc} of 340 mHz, whereas the bandwidth observed for shoulder oscillations is equal to 400 mHz. Here, it is assumed that

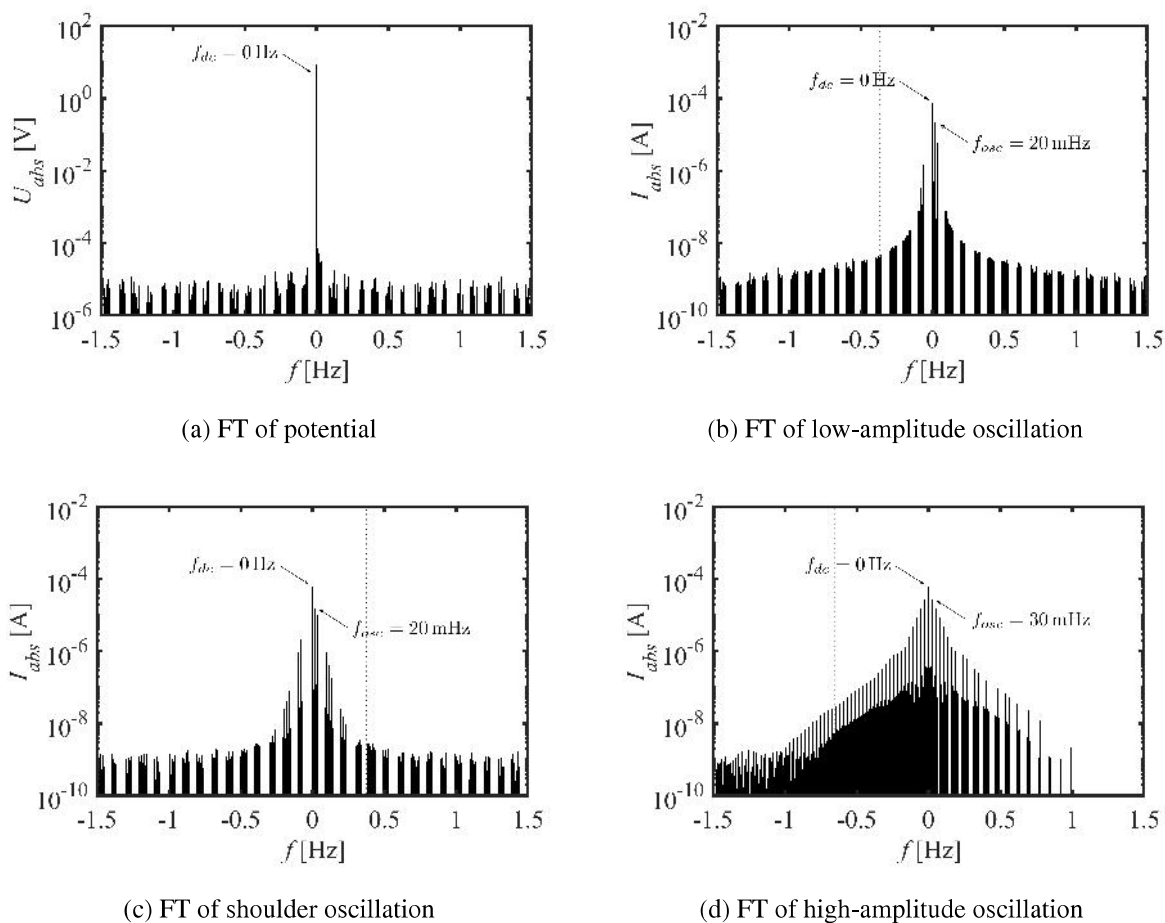


Figure 5.6.: Current signals observed for different types of oscillations at p-type Si in 0.06 M NH_4F in 142 mM H_2SO_4 at 8.64 V vs. SHE in the low-frequency range.

all peaks exhibiting a minimum amplitude of 5×10^{-9} A contribute to the signal. This value represents an estimate for the background noise level of the signal. In both cases, the intensity of the higher harmonic signals drops very fast. In contrast, for high-amplitude oscillations the decrease in amplitude of the higher harmonics occurs less abruptly. This behavior can be attributed to the shape of the different signals in the time domain. The representation of the more sinusoidal low-amplitude and shoulder oscillations in Fourier space requires only few harmonic signals, whereas the more peak-shaped high-amplitude oscillations are composed of a higher amount of harmonic signals. However, it was assumed that the higher harmonic signals contained within a bandwidth of 0.6 Hz about the fundamental frequency were sufficient to fully reconstruct the high-amplitude current oscillations in the time domain.

The reaction dynamics of the oscillatory electrodissolution seem to be highly affected by solid-state transport processes inside the silicon oxide layer. Consequently, the investigation of the low-frequency region is particularly desirable in order to gain information about the origin of the instabilities governing this reaction. Therefore, a new multi-sine waveform with $d = 3$ was designed, allowing for the first fundamental frequency of the multi-sine signal to be located

in close proximity to the natural current peaks. Considering the fact that the intermodulations of the dc signal with the fundamental harmonics of the multi-sine wave create a skirt centered on the respective fundamental frequency having a bandwidth similar to that of the dc component the lowest possible frequency of the first fundamental harmonic contained in the multi-sinusoid must be equal to $2 \times bw_{dc}$. Therefore, the base frequency of the multi-sine wave was individually adjusted for the different types of oscillations, such that the above condition was fulfilled. In the case of high-amplitude oscillations, the value of $2 \times bw_{dc}$ was still in a range where higher harmonics of the natural oscillation were observed. However, it was assumed that the intensity of these signals was negligibly small compared with that of the first frequency of the multi-sine wave.

5.3.1. Low-Amplitude Oscillations

Focusing on low-amplitude oscillations, the bandwidth of the dc signal was equal to 340 mHz, see Figure 5.6b. Therefore, the lowest fundamental frequency of the multi-sine signal was set to 680 mHz, corresponding to a base frequency of 170 mHz. Under these conditions, the time scale of the multi-sine wave did not coincide with that of the natural current oscillation ($f_b = 8.5 f_{osc}$). The amplitude of the multi-sine signal was set to $u_{ac} = 300$ mV. The below Figure 5.7a shows the potential perturbation related to the superposition of the constant dc signal and the multi-sine wave in Fourier space. The low-frequency region of the spectrum contains the 0 Hz signal related to the dc offset and the first two fundamental harmonics of the multi-sine signal, which oscillate at frequencies of 680 mHz and 2.38 Hz, respectively. In the corresponding current spectrum, shown in Figure 5.7b, the peaks are surrounded by small skirts. As aforementioned, the skirts stem from the intermodulation of the harmonics of the natural oscillation and the fundamental frequencies of the multi-sinusoid. Although the amplitude of the multi-sine signal

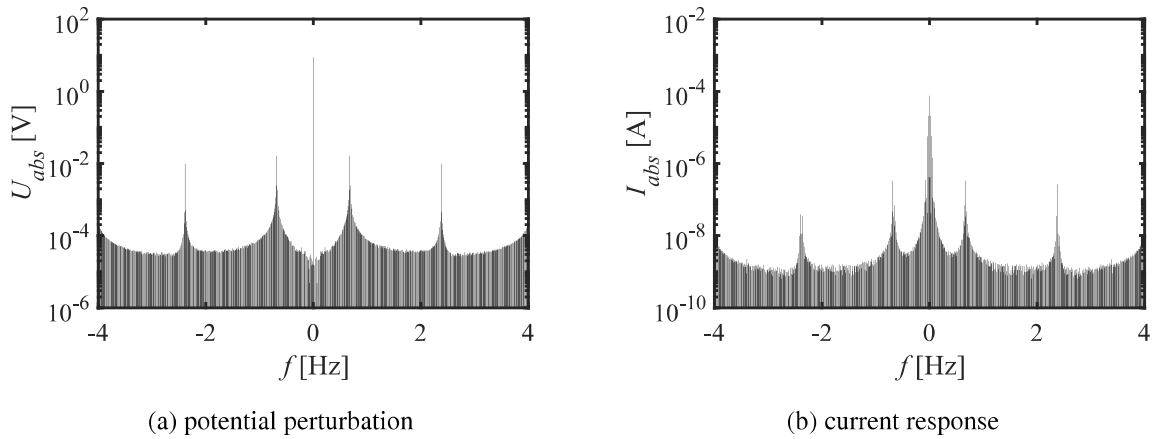


Figure 5.7.: Potential and current signals observed for low-amplitude oscillations at p-type Si in 0.06 M NH_4F in 142 mM H_2SO_4 at 8.64 V vs. SHE in the low-frequency range ($R_{ext} = 10 \text{ k}\Omega$).

was rather high, the spectra do not show any unwanted signals related to the nonlinear response of the system. Therefore, the system was considered quasi-linear. According to (3.5), which was derived in Section 3.2.1, the quadrature filter bandwidth bw may be varied in a range between $1 \times f_b$ and $2 \times f_b$. However, the Fourier spectra reveal that a filter bandwidth of $bw = 170$ mHz is sufficiently large to collect the partial current and voltage signals.

Dynamic impedance spectra were recorded at different points in time, see Figure 5.8. The close similarity between the natural low-amplitude oscillation and the current signal recollected from DMFA measurements indicates the correct choice of filter bandwidth. Due to the fact that the shape of the oscillation was not affected by the multi-sine perturbation, it was assumed that the system underwent a bifurcation and was transformed into a stable oscillatory state. The impedance response recorded at different points is highly reproducible for subsequent oscillations, thus demonstrating that sustained oscillations have formed. The spectra are composed of a high-frequency loop followed by a straight line of varying angles. At the current maxima low impedances were detected, whereas high impedances were recorded at the minimum current between two peaks. The impedance does not evolve perfectly symmetrically about the extrema of the peak but shows a slightly asymmetric behavior, where the high-frequency loop recorded at the descending slope of the oscillation is slightly bigger than that recorded at the same position of the ascending part.

The subsequent Figure 5.9 provides a 3-D representation of the temporal evolution of the dynamic impedance spectra. The periodic repetition of the impedance patterns reveals that the

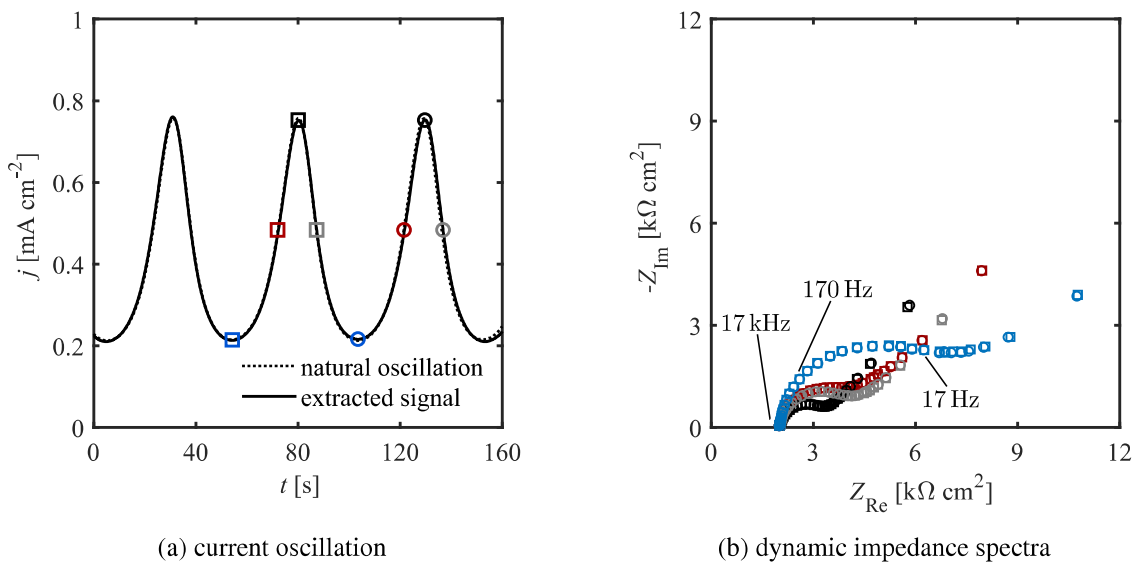


Figure 5.8.: Comparison of the natural and reconstructed current signal obtained for low-amplitude oscillations and dynamic impedance spectra recorded during two subsequent low-amplitude oscillations. $f_{osc} = 0.02$ Hz, $\Delta u_{ac} = 300$ mV, $f_b = 0.17$ Hz, $d = 3$, $bw = 170$ mHz, $R_{ext} = 10$ kΩ.

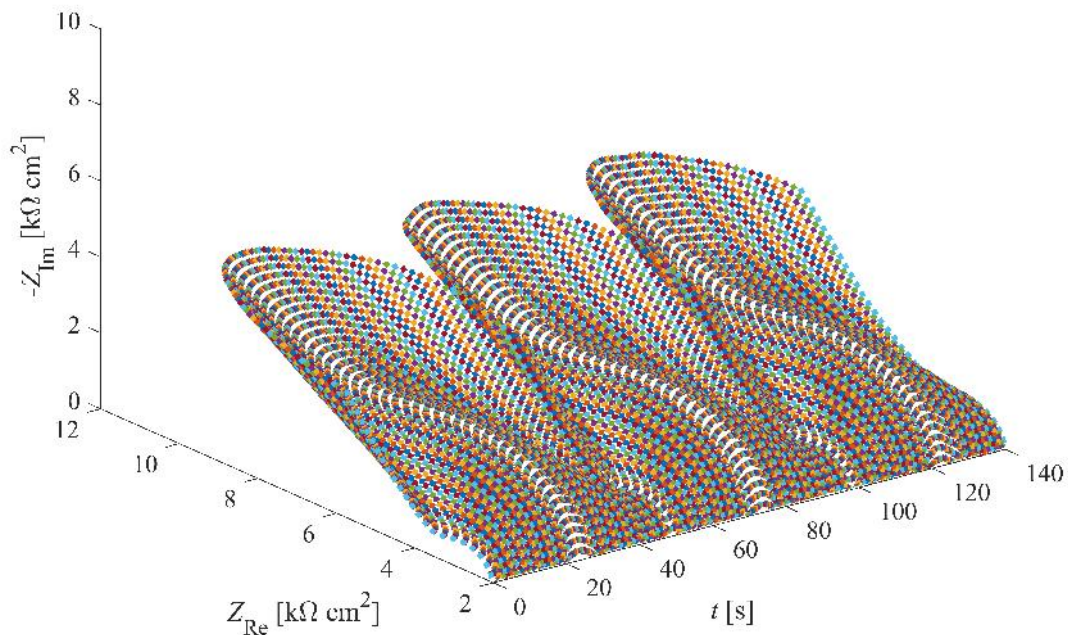


Figure 5.9.: 3-D representation of the dynamic impedance spectra recorded during low-amplitude oscillations. Impedance is given as a function of time, illustrated using Nyquist plots. $f_{osc} = 0.02$ Hz, $\Delta u_{ac} = 300$ mV, $f_b = 0.17$ Hz, $d = 3$, $bw = 170$ mHz, $R_{ext} = 10$ k Ω .

process is governed by oscillatory reaction dynamics. In the 3-D plot, the asymmetric evolution of the dynamic impedance spectra is particularly obvious. The shape of the spectra resembles that of a diffusion-limited single-step reaction. Therefore, data fitting was performed using a simple Randles circuit. Due to an inhomogeneous disk current density distribution, the use of a CPE instead of a classic capacitance was required. It must be stressed that this circuit does not reflect the real physico-electrochemical properties of the system. Instead, it was employed to observe specific trends in the temporal development of the circuit parameters. Based on that, the goal was to assign a physical meaning to the respective variables in order to make a guess on the origin of the oscillatory behavior of the system.

The below Figure 5.10 shows the dynamic impedance spectra recorded at different times during one oscillation period and their corresponding fitted spectra. The latter were obtained from CNLS regression, using the EEC presented in the inset of Figure 5.10. The fitted data match very well the experimental results, where the χ^2 value of 2.31×10^{-4} confirms that the quality of the fitting is very good. Here, the parameter R_s is to be understood as the sum of the solution resistance and the external global coupling of 10 k Ω , which was assumed to be constant. The $R_s \times A$ value of 1.98 k Ω cm² obtained from data fitting is practically identical to

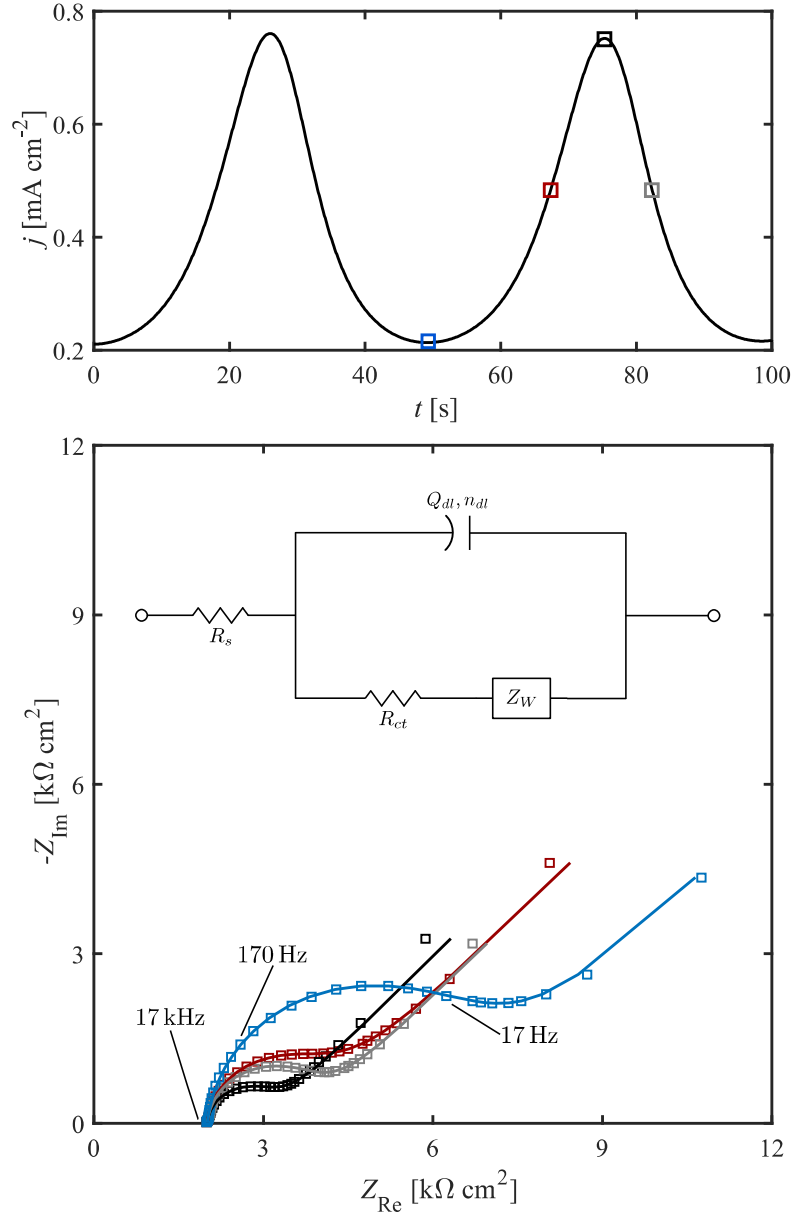


Figure 5.10.: Comparison of experimental (squares) and fitted (lines) dynamic impedance spectra at different points along one low-amplitude oscillation period. $\Delta u_{ac} = 300$ mV, $f_b = 0.3$ Hz, $d = 3$, $\text{bw} = 170$ mHz, $R_{ext} = 10$ k Ω .

that of the external resistance ($1.96 \text{ k}\Omega \text{ cm}^2$), thus demonstrating that this parameter is mainly governed by the global coupling. The phase angle n_{dl} of the CPE varies in a range between 0.88 and 0.91, showing almost pure capacitive behavior. In Figure 5.11, the temporal evolution of the fitting parameters is illustrated with respect to the natural current oscillation. In addition to that, the parameters are related to the change in effective potential, which was calculated according to (5.5) and to the variation in oxide layer thickness Δd_{ox} . The latter was deduced from integration of the current density, following

$$\Delta d_{ox} = \frac{M}{F\nu\rho} \int_0^T (j - \tilde{j})(t) dt, \quad (5.6)$$

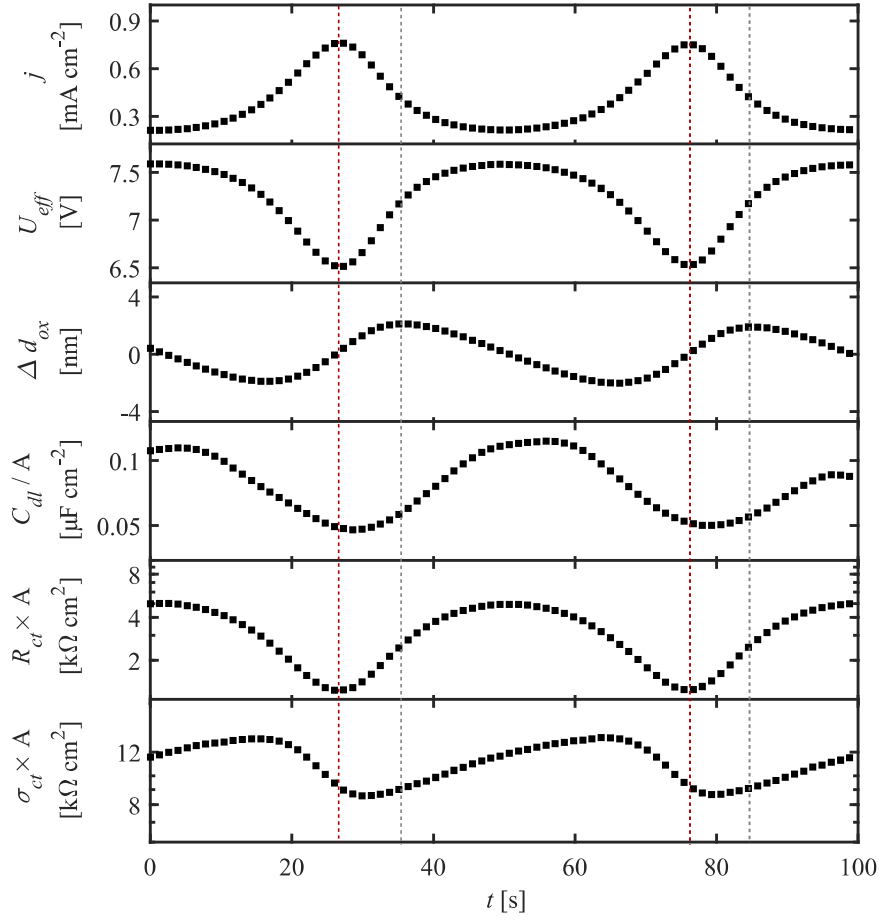


Figure 5.11.: Temporal evolution of the fitting variables extracted from dynamic impedance spectra recorded during low-amplitude oscillations. The vertical red and grey lines indicate the positions of the maxima of j and Δd_{ox} , respectively.

where M is the molar mass of SiO_2 ($M = 60.2 \text{ g mol}^{-1}$), F is the Faraday constant, ν is the number of charges contributing to the oxidation of one silicon atom ($\nu = 3.6$), and ρ is the density of the oxide layer ($\rho = 1.69 \text{ g cm}^{-3}$). The values of ν and ρ were taken from Miethe (2012). The parameter j is the overall current density, whereas \tilde{j} corresponds to the average current density recorded during one period of oscillation.

The variable C_{dl} corresponds to an effective capacitance calculated from Q_{dl} , n_{dl} , R_s , and R_{ct} , following the procedure described in Section 7.1.6. C_{dl} changes symmetrically and in anti-correlation with the current oscillation. The resistance R_{ct} shows the same symmetry as the effective potential. Due to its inverse correlation with the current oscillation, this quantity may be attributed to a charge transfer reaction. In contrast, the Warburg coefficient σ_{ct} does not evolve symmetrically about the natural current oscillation. Its temporal variation resembles that of an integrate-and-fire oscillation, where σ_{ct} starts to increase from a minimum value until a threshold is reached at which the variable is reset to its initial value. Due to the fact

that the impedance behavior of σ_{ct} did not change upon variation of the rotation speed of the rotating disk electrode (RDE), the Warburg element was assumed to be related to solid-state mass transport of reactive species inside the oxide layer (see Appendix E). This assumption is supported by the fact that σ_{ct} follows a similar trend as Δd_{ox} .

C_{dl} can be related to the dielectric behavior of the oxide layer. The mean value of the effective capacitance \check{C}_{dl} is linked to the average oxide layer thickness \check{d}_{ox} through the relationship

$$\check{C}_{dl} = \frac{\varepsilon_0 \kappa A}{\check{d}_{ox}}, \quad (5.7)$$

where A is the surface area of the electrode and ε_0 and κ are the vacuum permittivity and the dielectric constant of SiO_2 , respectively. With $\varepsilon_0 = 8.854 \times 10^{-12} \text{ F m}^{-1}$, $\kappa = 3.9$, and $\check{C}_{dl} = 0.08 \mu\text{F cm}^{-2}$, an average oxide layer thickness of 42.6 nm is obtained, which slightly exceeds the values reported in literature (Miethe, 2012). In contrast to what was expected, C_{dl} does not show the same pattern formation as observed for Δd_{ox} . Therefore, it is assumed that the behavior of C_{dl} is not only affected by the oscillations of the oxide layer thickness but also by changes in the electric properties of the oxide. Thus, it is concluded that the process may involve a change in oxide quality.

Even though the shape of the impedance spectra resembles that of a single step reaction, indicating that the formation of SiO_2 occurs exclusively via reaction (5.3), it is more likely that the oxidation of Si takes place via different sub-steps, following reactions (5.1) and (5.2). Here, it is assumed that the time constant corresponding to the partial oxide formation is either lower or almost identical to that of the transformation of SiO into SiO_2 . In the former case, reaction (5.1) occurs in a frequency range that is not visible in the spectrum. In the second case, the time scales of the different reaction steps coincide, such that the two processes cannot be distinguished in the Nyquist plot.

5.3.2. Shoulder Oscillations

For shoulder oscillations a bandwidth of $\text{bw}_{dc} = 400 \text{ mHz}$ was determined from Figure 5.6c. Therefore, the lowest fundamental harmonic of the multi-sine waveform was set to 800 mHz. Hence, the base frequency of the multi-sine signal was equal to 200 mHz. In this case, f_b was ten times higher than the fundamental frequency of the natural oscillation ($f_{osc} = 20 \text{ mHz}$). The potential perturbation and the current response signals in the Fourier domain are shown in Figure 5.12. Again, the applied constant potential of 8.64 V vs. SHE appears as a peak at 0 Hz, whereas the first two fundamental harmonics of the multi-sine signal can be observed at frequencies of 800 mHz and 2.8 Hz, respectively. For the extraction of the partial voltage and current signals, the bandwidth of the quadrature filter was set to 200 mHz.

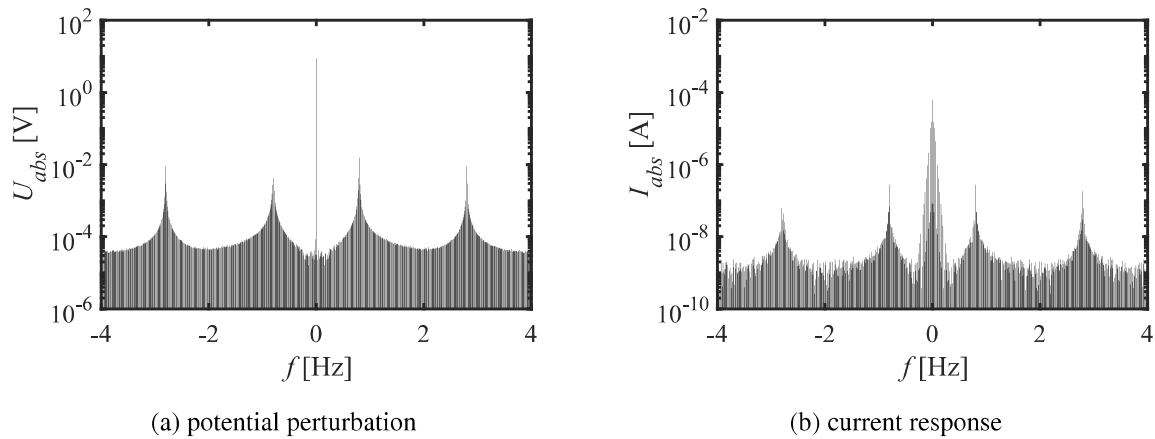


Figure 5.12.: Potential and current signals observed for shoulder oscillations at p-type Si in 0.06 M NH_4F in 142 mM H_2SO_4 at 8.64 V vs. SHE in the low-frequency range ($R_{ext} = 17.5 \text{ k}\Omega$).

In order to investigate if sustained current oscillations were established, dynamic impedance spectra were recorded during two subsequent periods of oscillations. In the below Figure 5.13 the impedance spectra obtained at characteristic points of the oscillation are compared. Similar to what was observed for low-amplitude oscillations, the current signal reconstructed from DMFA measurements perfectly matches the natural current oscillation, revealing that the filter bandwidth was sufficiently large. The spectra recorded during subsequent oscillations are highly reproducible, thus demonstrating that the oscillations were stable. The spectra exhibit

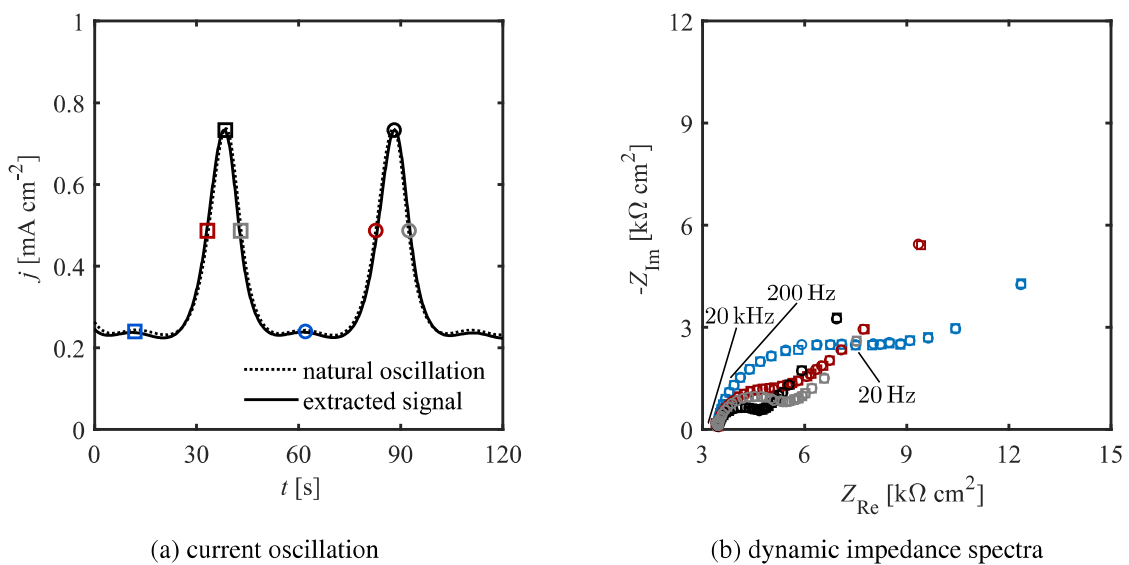


Figure 5.13.: Comparison of the natural and reconstructed current signal obtained for shoulder oscillations and dynamic impedance spectra recorded during two subsequent shoulder oscillations. $f_{osc} = 0.02 \text{ Hz}$, $\Delta u_{ac} = 300 \text{ mV}$, $f_b = 0.2 \text{ Hz}$, $d = 3$, $\text{bw} = 200 \text{ mHz}$, $R_{ext} = 17.5 \text{ k}\Omega$.

almost the same features as those recorded at low-amplitude oscillations, showing a semicircle followed by a straight line of varying angles. Due to the larger external resistance of 17.5 k Ω , the spectra are shifted to higher values along the real axis. Again, the impedance is inversely correlated with the current oscillation and evolves asymmetrically with respect to the phase of the natural current.

In Figure 5.14 the temporal evolution of the dynamic impedance spectra recorded during shoulder oscillations is illustrated, showing similar patterns as observed for low-amplitude oscillations, indicating that the different types of oscillations are governed by similar processes. Interestingly, the plots show a different behavior in the low-frequency region, which is not directly obvious when investigating single spectra. Due to the fact that the spectra are governed by similar features as observed for low-amplitude oscillations, data fitting was performed using the same EEC. Again, the χ^2 value of 5.88×10^{-4} indicates that the fitting quality is very good.

The dynamic impedance spectra recorded at different times during one oscillation period and the corresponding fitted spectra are presented in Figure 5.15. As expected, the value of the solution resistance per unit surface area (3.49 k Ω cm 2) is almost completely controlled by the

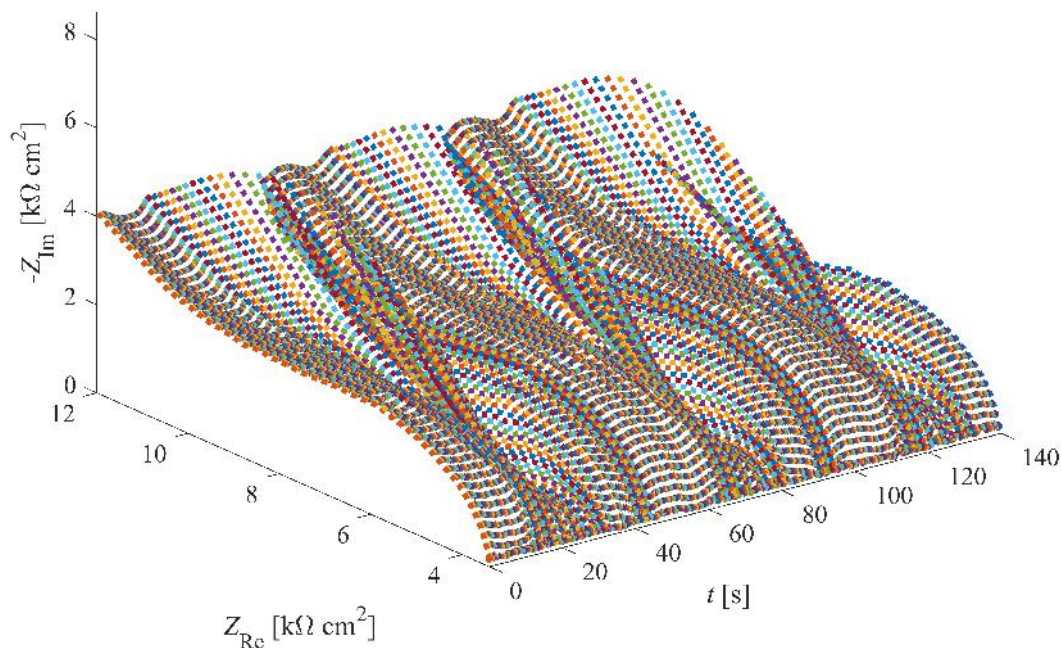


Figure 5.14.: 3-D representation of the dynamic impedance spectra recorded during shoulder oscillations. Impedance is given as a function of time, illustrated using Nyquist plots. $f_{osc} = 0.02$ Hz, $\Delta u_{ac} = 300$ mV, $f_b = 0.2$ Hz, $d = 3$, $bw = 200$ mHz, $R_{ext} = 17.5$ k Ω .

value of the external resistance ($3.34 \text{ k}\Omega \text{ cm}^2$). The phase angle of the constant phase element slightly varies within the time frame under investigation, exhibiting values between 0.91 and 0.93. These observations are in good agreement with the results observed for low-amplitude oscillations. The subsequent Figure 5.16 shows the temporal evolution of the reaction variables that were extracted from the fitting procedure. Although the external resistance is increased with respect to that applied during low-amplitude oscillations, the effective potential values are almost identical in both cases. Consequently, the charge transfer resistance shows a similar trend and is in the same range as that illustrated in Figure 5.11. Also the variation in oxide layer thickness is virtually identical to that observed during low-amplitude oscillations. However, the

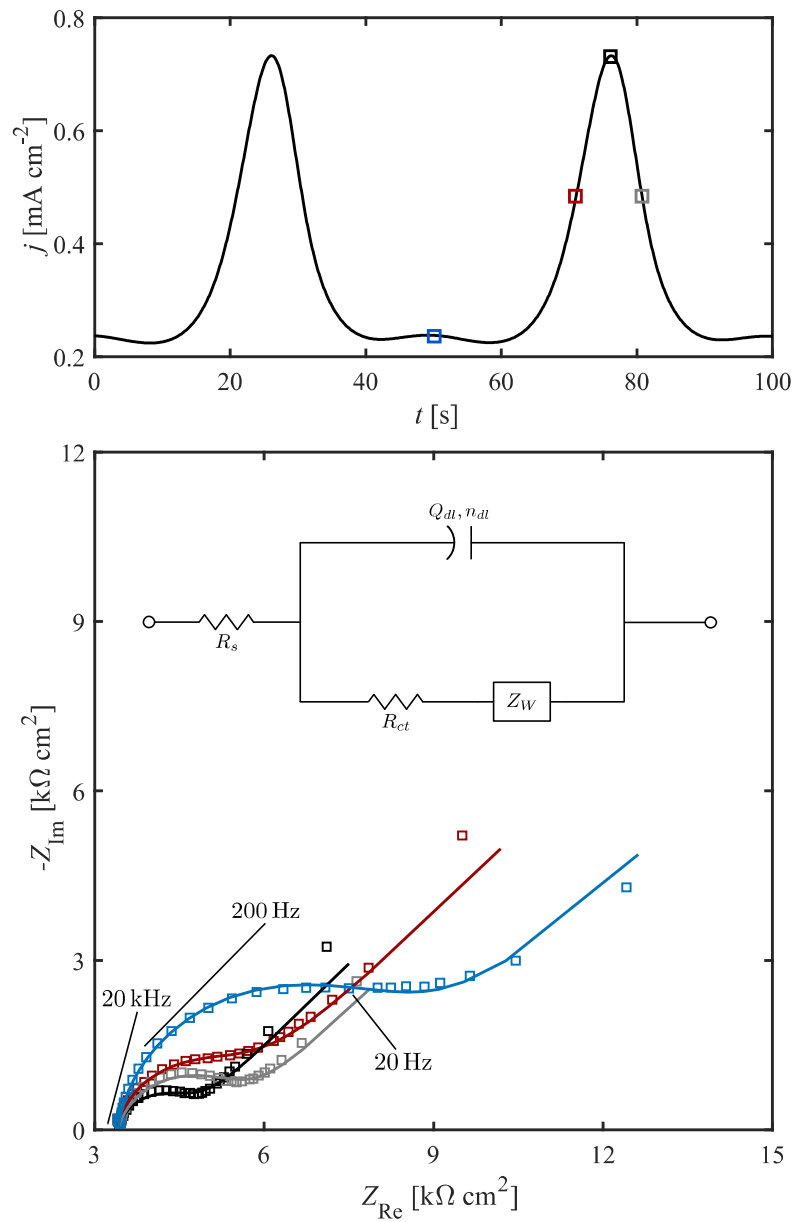


Figure 5.15.: Comparison of experimental (squares) and fitted (lines) dynamic impedance spectra at different points along one shoulder oscillation period. $\Delta u_{ac} = 300 \text{ mV}$, $f_b = 0.3 \text{ Hz}$, $d = 3$, $\text{bw} = 200 \text{ mHz}$, $R_{ext} = 17.5 \text{ k}\Omega$.

average oxide layer thickness of 25.54 nm is smaller than that calculated for low-amplitude oscillations. The behavior of the effective double layer capacitance strongly differs from that given in Figure 5.11. During low-amplitude oscillations this variable changes symmetrically and is in anti-correlation with the current signal. In contrast, during shoulder oscillations C_{dl} does not evolve symmetrically with respect to the phase of the current but resembles the integrate-and-fire oscillation shape of the Warburg coefficient observed in Figure 5.11. During shoulder oscillations, the trend of σ_{ct} shows similar patterns. In this case, the variable increases and establishes some kind of plateau until it suddenly drops to its initial value. The close similarity between C_{dl} and σ_{ct} leads to the assumption that mass transport inside the oxide layer is linked to the electric properties of the oxide.

As in the case of low-amplitude oscillations, reaction (5.2) seems to occur very fast. Therefore, it is assumed that the amount of SiO_2 present in the oxide layer outweighs that of SiO . Again, the variation in Δd_{ox} and C_{dl} indicates that there is probably a change in oxide quality, which affects the electric properties and thus the etch rate of the oxide.

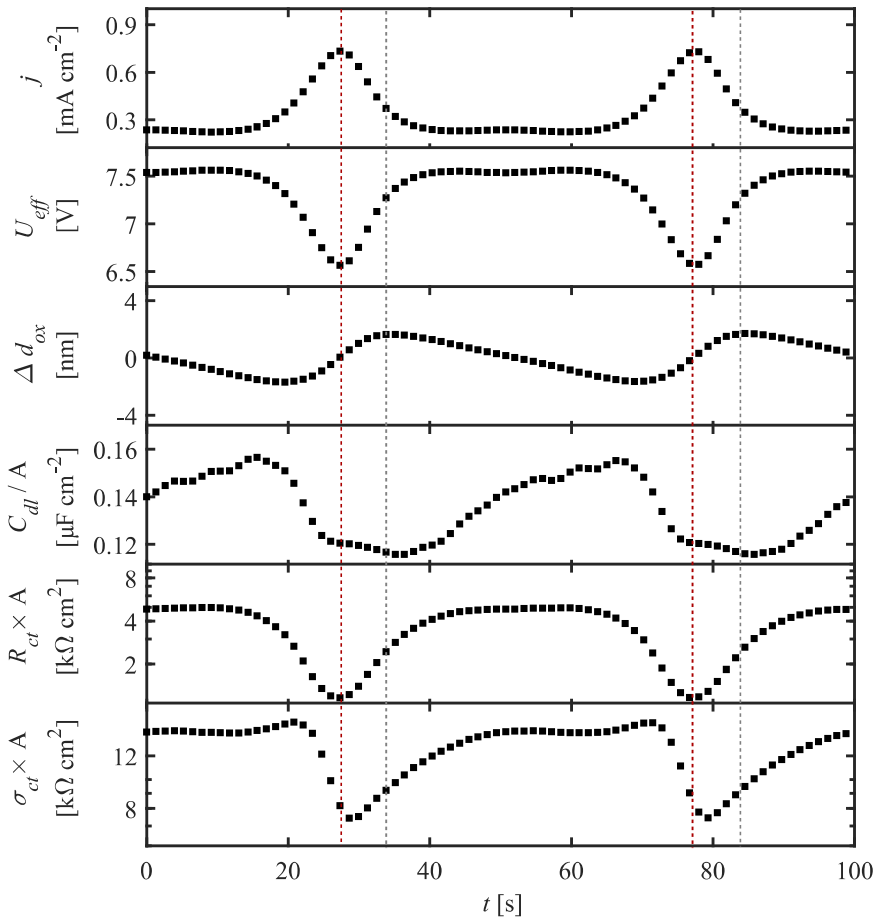


Figure 5.16.: Temporal evolution of the fitting variables extracted from dynamic impedance spectra recorded during shoulder oscillations. The vertical red and grey lines indicate the positions of the maxima of j and Δd_{ox} , respectively.

5.3.3. High-Amplitude Oscillations

Finally, DMFA was performed on high-amplitude oscillations. To do so, the lowest frequency contained in the multi-sine signal was set to 1.2 Hz, corresponding to a base frequency of 300 mHz. As before, the multi-sine amplitude was set to 300 mV.

The following Figure 5.17b shows that the smallest fundamental harmonic of the multi-sinusoid is in the same frequency range as the highest harmonic signals of the natural current oscillation. However, the intensity of the latter was considered very small compared to that of the first fundamental frequency contained in the multi-sine waveform. Although the skirts appearing about the respective multi-sine signals are broader than those detected for low-amplitude and shoulder oscillations, a filter bandwidth of $1 \times f_b$ was sufficient to extract the partial current and voltage signals.

The shape of the natural oscillation was perfectly reconstructed from the multi-sine data set, as illustrated in Figure 5.18a. Again, the high reproducibility of the impedance spectra recorded during subsequent oscillations reveals that the oscillations were stable, see Figure 5.18b.

The dynamic impedance behavior of high-amplitude oscillations differs from that of low-amplitude and shoulder oscillations. The spectra show a semicircle in the high-frequency region, where the size of the loop strongly varies between the different points along one oscillation period. In the low-frequency region the spectra do not follow a clear trend. In contrast to what was observed for the other types of oscillations, this part of the spectrum seems to be dominated by a second loop and does not exhibit mass transport-like behavior. However, due to the limitation of the lowest frequency to a value of 1.2 Hz, it is not possible to make a proper statement on the impedance phenomena occurring at lower frequencies. In this case, the

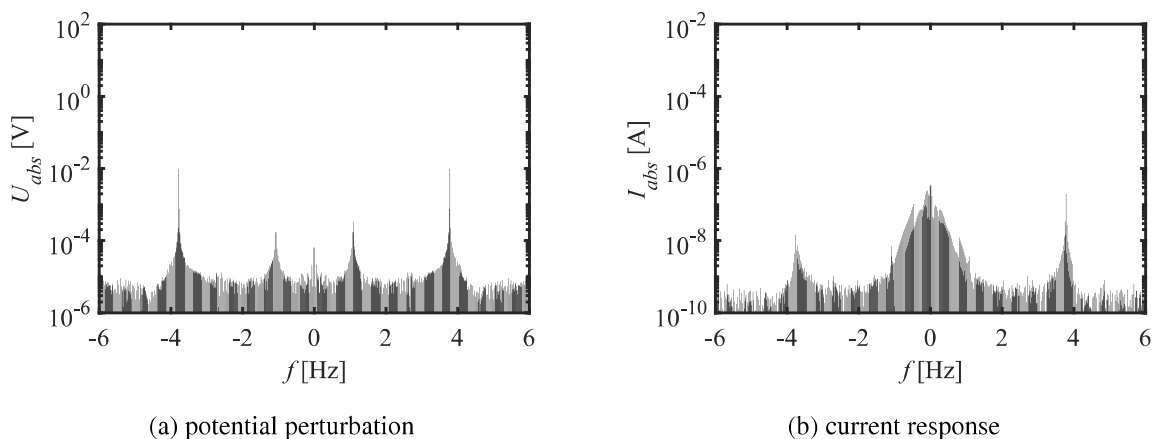


Figure 5.17.: Potential and current signals observed for high-amplitude oscillations at p-type Si in 0.06 M NH_4F in 142 mM H_2SO_4 at 8.64 V vs. SHE in the low-frequency range ($R_{ext} = 30 \text{ k}\Omega$).

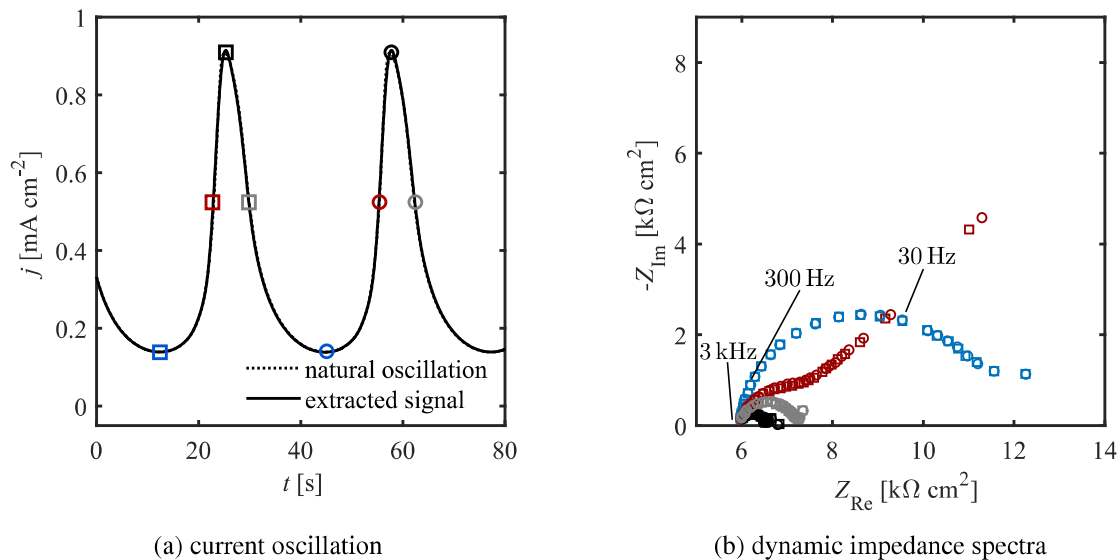


Figure 5.18.: Comparison of the natural and reconstructed current signal obtained for high-amplitude oscillations and dynamic impedance spectra recorded during two subsequent high-amplitude oscillations. $f_{\text{osc}} = 0.03 \text{ Hz}$, $\Delta u_{\text{ac}} = 300 \text{ mV}$, $f_b = 0.3 \text{ Hz}$, $d = 3$, $\text{bw} = 300 \text{ mHz}$, $R_{\text{ext}} = 30 \text{ k}\Omega$.

asymmetric behavior of the impedance spectra about the current peak is immediately apparent. The temporal evolution of the impedance spectra exhibits different patterns than that observed for low-amplitude and shoulder oscillations, as displayed in Figure 5.19. Again, it must be pointed out that the spectra recorded for the different types of current oscillations particularly differ in the low-frequency region, and thus stressing the assumption that the reaction dynamics are significantly affected by variations in mass transport in the oxide layer. However, in the case of high-amplitude oscillations, the process of mass transport is considered too slow to be observable in the frequency range under investigation.

Due to the difference in shape, the impedance spectra recorded during high-amplitude oscillations could no longer be fitted with the simple circuit that was employed for data fitting of low-amplitude and shoulder oscillations. As the spectra are composed of two semicircles a two-step mechanism was proposed in this case. Therefore, the spectra were fitted with the EEC shown in the inset of Figure 5.20, where a χ^2 value of 4.77×10^{-5} was obtained. As before, the fitting procedure followed a parametric approach and was not based on an analytical model. The measured and fitted spectra recorded at different points along the oscillation are shown in Figure 5.20. The fitted spectra match the experimental data very well when the lowest frequency is discarded. Due to the fact that different EECs had to be employed for data fitting of the different types of current oscillation, a direct comparison of their respective reaction variables is rather challenging. However, in what follows, the most dominant features of the temporal evolution of the variables governing high-amplitude oscillations, illustrated in Figure 5.21, are analyzed with respect to those observed for low-amplitude and shoulder oscillations.

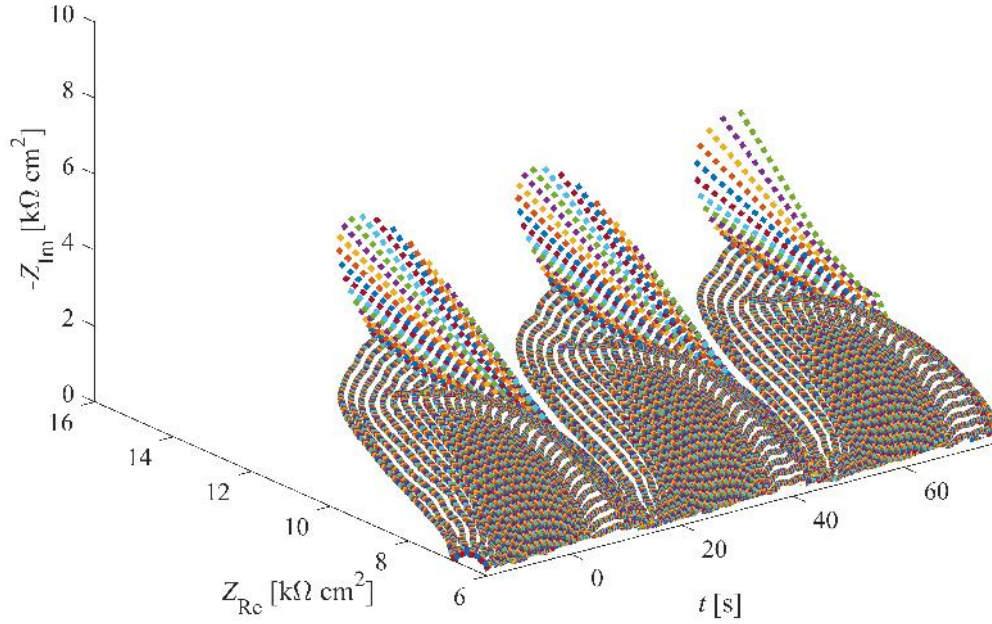


Figure 5.19.: 3-D representation of the dynamic impedance spectra recorded during high-amplitude oscillations. Impedance is given as a function of time, illustrated using Nyquist plots. $f_{osc} = 0.03$ Hz, $\Delta u_{ac} = 300$ mV, $f_b = 0.3$ Hz, $d = 3$, $bw = 300$ mHz, $R_{ext} = 30$ k Ω .

As in the case of low-amplitude and shoulder oscillations, the $R_s \times A$ value of 5.94 k Ω cm² is very similar to $R_{ext} \times A$ (5.89 k Ω). Both capacitances were replaced by CPEs, where the variables C_{dl} and C_{ad} were calculated according to the procedure described in Section 7.1.6. The phase angle n_{dl} , corresponding to Q_{dl} , is almost unity ($0.89 \leq n_{dl} \leq 0.93$), whereas n_{ad} shows less pronounced capacitive behavior and varies in a range between 0.5 and 0.74 . The average oxide layer thickness \check{d}_{ox} , calculated from (5.7), is equal to 25.1 nm, which is similar to the value obtained for shoulder oscillations. However, in the case of high-amplitude oscillations, there is a strong variation in oxide layer thickness. When the oscillations are at a maximum, the oxide layer is almost completely removed, thus resulting in higher current peaks as compared with those recorded during low-amplitude and shoulder oscillations.

Also, the variation in effective potential is larger than that observed during low-amplitude and shoulder oscillations. As outlined in Section 5.2.2, the interplay between the amount of reactive O^{2-} species entering the oxide and the oxide layer thickness controls the formation of partial oxide. It is assumed that due to higher effective voltages at the current maximum (approximately 6.5 V), larger amounts of O^{2-} enter the oxide layer during low-amplitude and shoulder oscillations, which leads to a fast increase in oxide layer thickness. Therefore, the formation of partial oxide is slowed down, while the transformation of SiO into SiO₂ is accelerated.

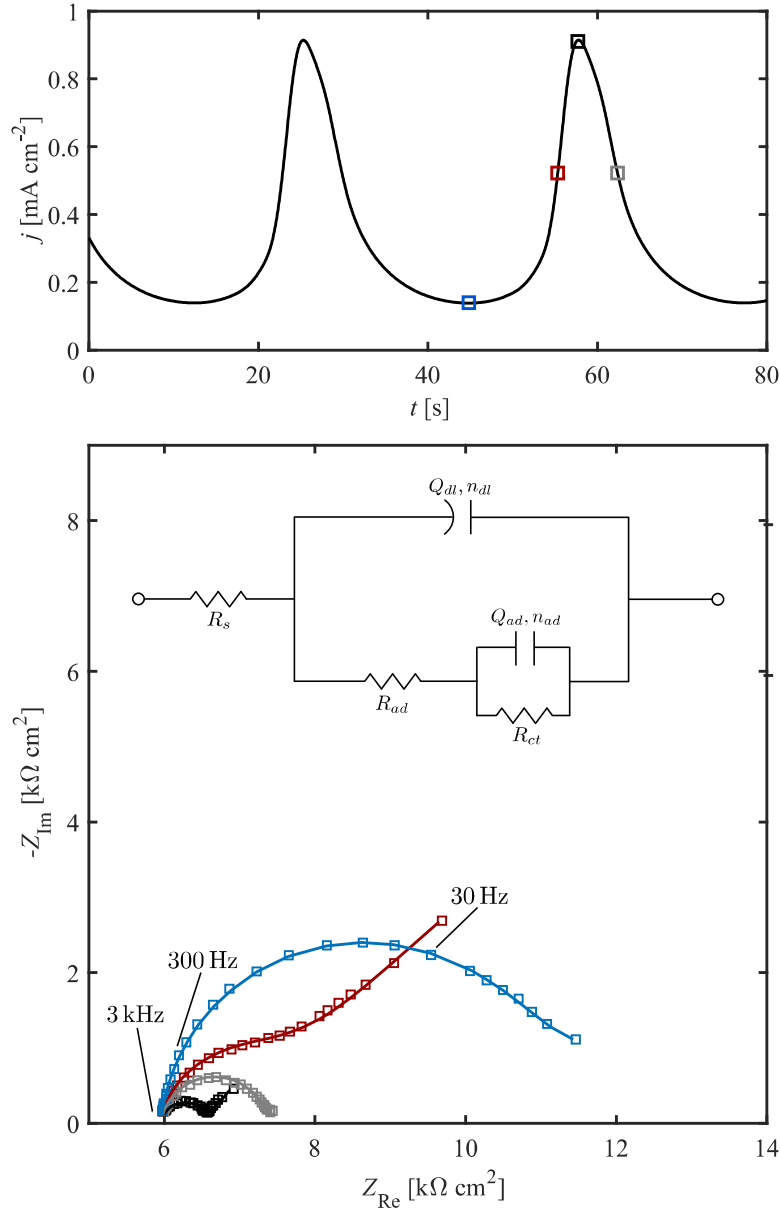


Figure 5.20.: Comparison of experimental (squares) and fitted (lines) dynamic impedance spectra at different points along one high-amplitude oscillation period.

$\Delta u_{ac} = 300 \text{ mV}$, $f_b = 0.3 \text{ Hz}$, $d = 3$, $\text{bw} = 300 \text{ mHz}$, $R_{ext} = 30 \text{ k}\Omega$.

In contrast, during high-amplitude oscillations, the effective potential takes values of approximately 6 V when the current is at a maximum. Here, it is assumed that lower amounts of O^{2-} penetrate the oxide. However, due to the smaller thickness of the oxide layer, the ions readily reach the silicon/silicon oxide interface and react under the formation of SiO or SiO_2 , respectively. At the same time, the transformation of SiO into SiO_2 proceeds rather sluggish. In this case, it is anticipated that the oxide layer is mostly composed of partial oxide species that seem to be more stable than in the case of low-amplitude and shoulder oscillations. Accordingly, the time constant $C_{dl} \times R_{ad}$ is attributed to reaction (5.1), whereas the time constant $C_{ad} \times R_{ct}$ is related to reaction (5.2). As expected, R_{ad} attains a minimum when the current is at a maximum,

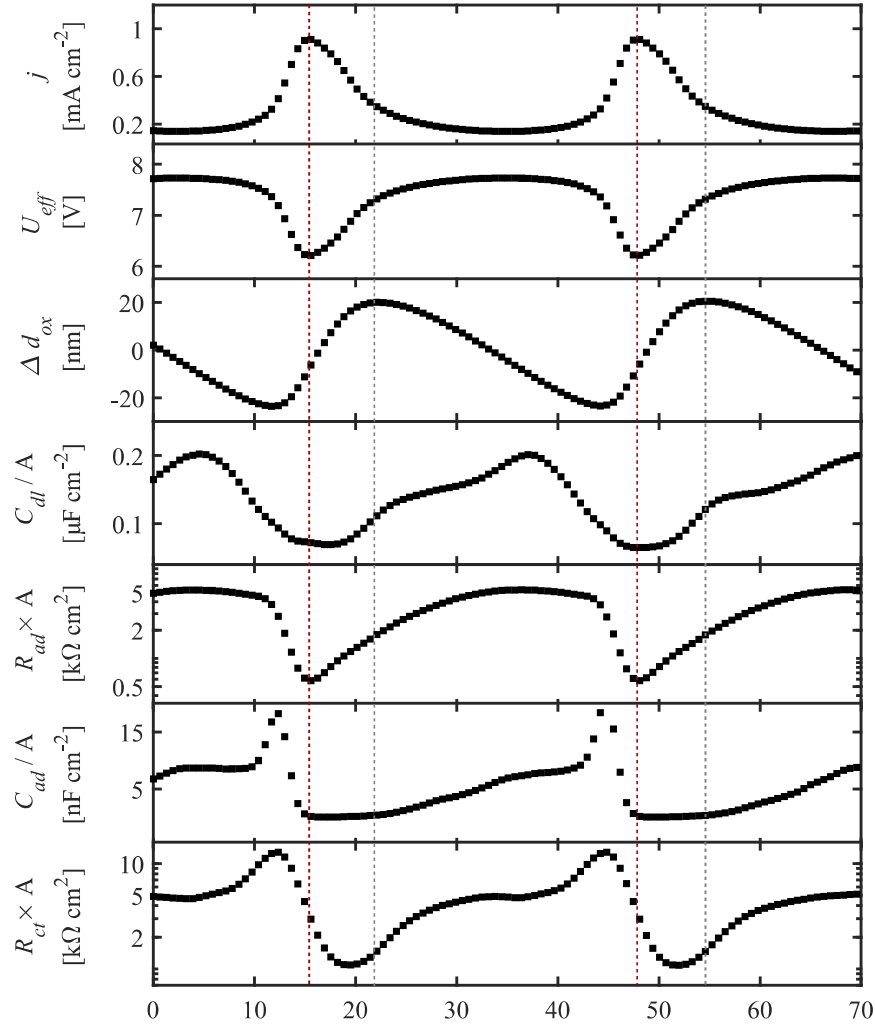


Figure 5.21.: Temporal evolution of the fitting variables extracted from dynamic impedance spectra recorded during high-amplitude oscillations. The vertical red and grey lines indicate the positions of the maxima of j and Δd_{ox} , respectively.

thus indicating that the rate of partial oxide formation is accelerated. When R_{ad} decreases, i.e. when the generation of SiO is facile, C_{ad} significantly increases due to the accumulation of partial oxide at the silicon/silicon oxide interface. With the transformation of SiO into SiO₂, C_{ad} suddenly drops as it is consumed in reaction (5.2). Therefore, R_{ct} is directly linked to C_{ad} . R_{ct} is slightly delayed with respect to R_{ad} and has to overcome a maximum before the transformation into SiO₂ can take place. This behavior indicates that the generation of SiO₂ only takes place when sufficient amounts of partial oxide have formed. Moreover, this leads to the assumption that the formation of SiO₂ occurs via different sub-steps rather than in a single step.

Interestingly, the shape of C_{dl} resembles that of R_{ct} , thus suggesting that the transformation of partial silicon oxide into final silicon oxide may be affected by the electric properties of the oxide. The variation in C_{dl} shows a similar trend as that observed during shoulder oscillations.

It must be noted that this variable is particularly influenced in the region where the current oscillations are at a minimum. Due to the fact that C_{dl} behaves in anti-correlation with the oxide layer thickness, there must be another parameter that influences the electric properties of the oxide. Here, the difference between Δd_{ox} and C_{dl} may be attributed to a variation in etch rate. As pointed out earlier, the electric behavior of the oxide layer may also be affected by changes in mass transport, which could result in a change in distribution of O^{2-} ions within the oxide.

Due to the fact that an analytical model describing the anodic silicon electrodisolution reaction in the oscillatory regime does not yet exist, the true origin of the dynamic instabilities governing this process cannot be identified. However, the above results reveal that it is likely that the origin of the current oscillations lies in the interplay between the electric properties of the oxide, the etch rate, and mass transport of reactive species in the oxide layer. The latter controls the rate at which partial or final oxide is formed at the silicon/silicon oxide interface. The oxide composition affects the electric properties of the oxide, and thus determines the etch rate. Another important parameter is the external resistance, which controls the voltage drop between the WE and the RE.

In contrast to what is found in literature, the results discussed in this Chapter give rise to the assumption that all types of current oscillations may involve variations in oxide quality or etch rate. Although the shape of the impedance spectra recorded during high-amplitude oscillations differs from that observed during low-amplitude and shoulder oscillations, the analysis of the circuit parameters leads to the conclusion that the different types of oscillations follow the same general mechanism. It is suggested that the transition between low-amplitude and high-amplitude oscillations involves a change in reaction kinetics. In the case of low-amplitude and shoulder oscillations, it is assumed that partial oxide species are only of transient nature and rapidly transform into SiO_2 . Therefore, the corresponding impedance spectra exhibit the shape of a single-step reaction. In contrast, during high-amplitude oscillations, partial oxide species appear to be more stable. It seems that SiO must be present in sufficient amounts before its transformation into SiO_2 can take place. In this case, the different reaction steps can be distinguished in the spectra and require the use of a more complex EEC.

6. Conclusion and Outlook

The aim of this thesis was to show that DMFA allows for the investigation of nonstationary electrochemical processes, exhibiting either forced or natural reaction dynamics. The concept of DMFA was first introduced by Battistel (2016), who tested the new method on simulated systems. In this work, the implementation of DMFA in real-world conditions was successfully completed.

First, DMFA was applied to a simple redox process. Qualitative studies were carried out on the system in order to determine suitable parameter settings that allow for an optimum performance of dynamic impedance spectra acquisition and analysis. In this context, the perturbation signals employed in DMFA were introduced. Here, the benefits of a quasi-triangular waveform over a classic triangular wave were highlighted. An algorithm for the design of a suitable multi-sine waveform was developed. The dynamic impedance was extracted for non-overlapping time-scales of the quasi-CV and the multi-sinusoid by applying a quadrature filter of suitable bandwidth to the voltage and current signals in Fourier space. It was found that the choice of bandwidth is strongly related to the base frequency of the multi-sine waveform and the parameter d , which influence the spacing between the fundamental frequencies in the multi-sine signal. Based on that, a general expression for the determination of the filter bandwidth was derived. Furthermore, the effect of the multi-sine intensity on the noise-level of the system was investigated by studying the influence of the nonlinear current contributions on the quality of the impedance spectra. It was demonstrated that the nonlinear noise increases quadratically with the multi-sine amplitude, whereas the intensity of the fundamental harmonics only increases linearly with it. However, the system can be regarded as quasi-linear if the partial current signals do not contain unwanted interferences due to intermodulations of fundamental frequencies and higher order harmonics. It has to be stressed that the effect of nonlinear noise on the accuracy of the dynamic impedance response had to be determined individually for each system under investigation. Finally, it was explained how to analyze dynamic impedance spectra by means of EECs in order to extract meaningful physical variables that provide an insight into the reaction kinetics. The temporal evolution of the physical variables revealed that the redox process was limited by mass-transport of the electro-active species to the electrode surface. It was demonstrated that DMFA measurements can be performed using electrodes of different dimensions, where similar kinetic variables were extracted, irrespective of the effective surface area of the electrode.

These results are promising for the kinetic investigation of processes that require the use of microelectrodes, e.g. when measuring in small volumes of solution. Multibarrel electrodes exhibit similar features as microelectrodes. In this case, the signal-to-noise ratio is greatly improved, which makes their application in dynamic impedance studies particularly amenable.

After having discussed the main principles of data recording and analysis by means of DMFA, the technique was employed for the investigation of different stages of the HER. The HER is of current relevance, as it builds the basis for the generation of H_2 by water electrolysis. To avoid bubble nucleation on the electrode surface, the system was subjected to forced dynamic conditions, thus enabling the investigation of surface properties that cannot be accessed in stationary conditions. The reaction was studied in diluted solutions of $HClO_4$. In absence of supporting electrolyte, the impedance spectra were distorted due to the influence of potentiostat stray capacitances. Even though the features observed in the high-frequency region of the spectra could not be readily interpreted, data fitting of the experimental impedance spectra to suitable EECs allowed for the extraction of the physico-electrochemical quantities governing the different stages of the HER. The evolution of the physical variables was investigated in different potential regions. When no supporting electrolyte was present in solution, the kinetics governing the hydrogen evolution region were limited by the solution resistance, since the formation of gaseous H_2 lead to the depletion of reactive species in the electrolyte. The lower the initial electrolyte concentration, the more dominant the depletion effects became. In contrast, in the presence of supporting electrolytes, the electrolyte resistance was low with respect to the values of R_{ad} and R_{ct} and remained practically constant in the potential region under investigation. In this case, the artefact due to potentiostat stray capacitances was not visible in the spectra, since the characteristic frequency related to this process was shifted to higher values. Therefore, it was possible to distinguish the processes of electro-sorption and H_2 evolution in the Nyquist plot. Under these conditions, the Tafel reaction was the limiting process in the hydrogen evolution region. In contrast, the electro-sorption reaction was not significantly affected by the reactant concentration or by the presence of supporting electrolytes.

A detailed kinetic analysis of the HER requires that there is no passivation of active surface sites due to the adsorption of anions originating from the electrolyte. Therefore, for future experiments, the effect of supporting electrolytes on the double layer and the hydronium adsorbate structure is proposed. In order to explore the processes governing the electrocatalytic activity for the HER, adsorption energies and rate constants of elementary steps must be deduced experimentally. This can be achieved by combining DMFA with Scanning-Kelvin-Probe technique. A detailed understanding of the mechanism governing the HER may allow for the optimization of the efficiency of water electrolysis, which could be the key to the development of a sustainable and environmentally friendly energy supply.

Finally, DMFA was employed to investigate the anodic electrodisolution of p-type Si in fluoride containing electrolytes exhibiting natural reaction dynamics. The silicon sample was char-

acterized by means of cyclic voltammetry, where the CV was broken into three parts, namely the electropolishing region, the region of negative current/voltage characteristics, and the oscillatory region. First, the system was explored in the potential range characterized by the negative slope of the current/voltage curve. To investigate the system in quasi-steady-state conditions, DMFA was performed on the silicon sample by superposition of a slow quasi-CV with a suitable multi-sine waveform. The corresponding dynamic impedance spectra exhibited some outstanding features. At intermediate frequencies the spectra showed a characteristic kink, while the low-frequency range was governed by a large negative resistance. Salman (2019) developed an analytical model that allows for the reconstruction of dynamic impedance spectra in the regime of negative differential resistance. The close similarity between the experimental and the simulated data revealed that reliable impedance spectra were recorded. Next, it was demonstrated that DMFA can be applied for the investigation of the reaction dynamics governing the anodic electrodisolution of p-type silicon in the oscillatory regime. In the presence of an external global coupling, different types of self-sustained current oscillations were identified when varying the value of the external resistance in a range between 10 k Ω and 30 k Ω . In the literature, the emerging low- and high-amplitude current oscillations are treated as two distinct phenomena, where it is assumed that the transition between the two types of oscillations involves a change in mechanism, with shoulder oscillations forming a stable intermediate state. In contrast, the dynamic impedance studies presented in this work lead to the conclusion that all types of oscillations follow the same general reaction mechanism. Although the impedance spectra recorded during high-amplitude oscillations did not exhibit the same features and required the use of a more complex EEC than those obtained for low-amplitude and shoulder oscillations, the differences were attributed to a change in reaction kinetics rather than to a change in mechanism. The shape of the dynamic impedance spectra acquired during low-amplitude and shoulder oscillations resembled that of a single-step reaction. Therefore, these spectra were analyzed using a classic Randles circuit. In contrast, for data fitting of the spectra related to high-amplitude oscillations an electrical analogue describing a two-step process was proposed. Even though the circuits did not represent the real physico-electrochemical properties of the highly complex system, a framework for the analysis of the mechanism of the silicon electrodisolution reaction by means of DMFA was developed. The investigation of the temporal evolution of the reaction variables allowed to make an educated assumption on the physical processes governing the reaction dynamics. Although the origin of the dynamic instabilities remains unclear, it is anticipated that the oscillatory behavior may be attributed to the interplay between the electric properties of the oxide, the etch rate, and mass transport of reactive species in the oxide layer.

Further experiments are needed to gain a detailed understanding of the mechanism governing the different types of current oscillations. In the future, coupling of DMFA with ellipsometry may be applied to directly relate the variation in oxide layer thickness to the change in reaction variables in order to determine the true origin of the instabilities causing the oscillatory reaction dynamics of the silicon electrodisolution process.

7. Experimental

This Chapter provides the experimental procedures that were applied to record and evaluate the data presented in this thesis. The first part of this Chapter describes the instrumental set-up and gives some general information on the acquisition and analysis of dynamic impedance spectra using DMFA (see Section 7.1). In Section 7.2 technical specifications on the materials and instrumentation used for the accomplishment of the measurements are provided. Next, the experimental protocols employed for data recording are presented in Section 7.3. Finally, ion specific properties that were used to calculate solution resistances and transport numbers are given in Section 7.4.

The measurements on the anodic silicon electrodisolution reaction presented in Chapter 5 were carried out in the laboratories of the group of Nonequilibrium Chemical Physics at TUM.

7.1. Dynamic Impedance Measurements

This Section is concerned with the performance and analysis of nonstationary impedance measurements by means of DMFA. First, the instrumental set-up and cell configurations employed for the acquisition of dynamic impedance spectra are presented. Subsequently, the procedures of data recording and processing are explained.

7.1.1. Instrumental Set-Up

The quasi-triangular and multi-sinusoidal perturbation signals were injected into the potentiostat through a 2-channel waveform generator. Home-made MATLAB scripts were used to create the desired potential perturbation, following the procedures described in Section 3.1.1 and 3.1.2, respectively. The experiments were carried out using a three-electrode set-up, where the WE was polarized at a desired constant potential on which the perturbation signal, created by the waveform generator, was imposed. In order to smooth the digital perturbation signal, the trueForm filter, included in the settings of the waveform generator, was activated. The equally sized time-domain data arrays related to the voltage and current output signals were recorded with a 2-channel oscilloscope. A schematic representation of the instrumental set-up used for dynamic impedance measurements by means of DMFA is illustrated in Figure 7.1.

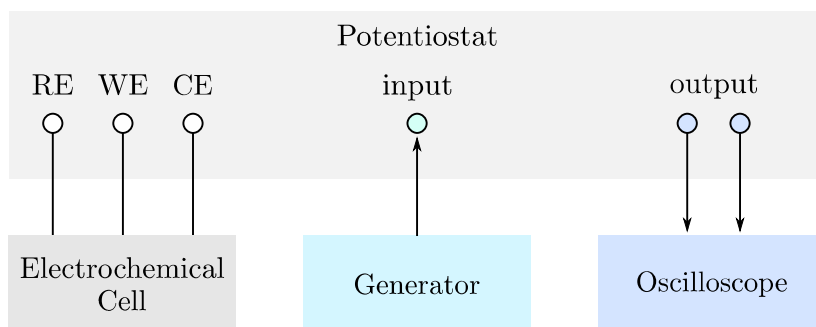


Figure 7.1.: Schematic representation of the instrumental set-up used in DMFA.

7.1.2. Cell Set-Up

All measurements presented in this thesis were performed using the instrumental set-up illustrated above. Two different types of cell configuration were employed, which are described below.

Coaxial Cell Geometry

The quality and precision of impedance measurements are affected by improper positioning of the electrodes, where current line distribution may cause severe distortions in the recorded spectra. Therefore, the measurements presented in Chapters 3 and 4 were carried out using the coaxial cell geometry shown in Figure 7.2, which was designed by Battistel (2014). Here, the WE is surrounded by a cylindrical Pt-mesh CE. The WE's tip is positioned in the upper third of the CE, while the RE is located outside the CE. As stated by Battistel (2014), in the aforementioned cell geometry the electric field is confined by the enclosure of the CE. The electrolyte solution outside the CE is to be understood as an equipotential region. Under these conditions, the RE may be positioned far from the WE without causing an increase in electrolyte resistance. Moreover, this cell geometry is insensitive to misalignment of the WE and allows for highly re-

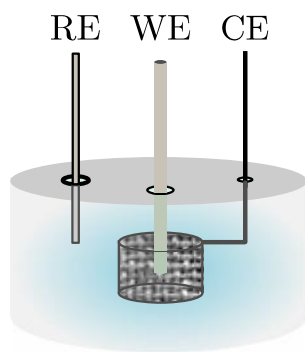


Figure 7.2.: Coaxial cell set-up employed for the measurements presented in Chapters 3 and 4.

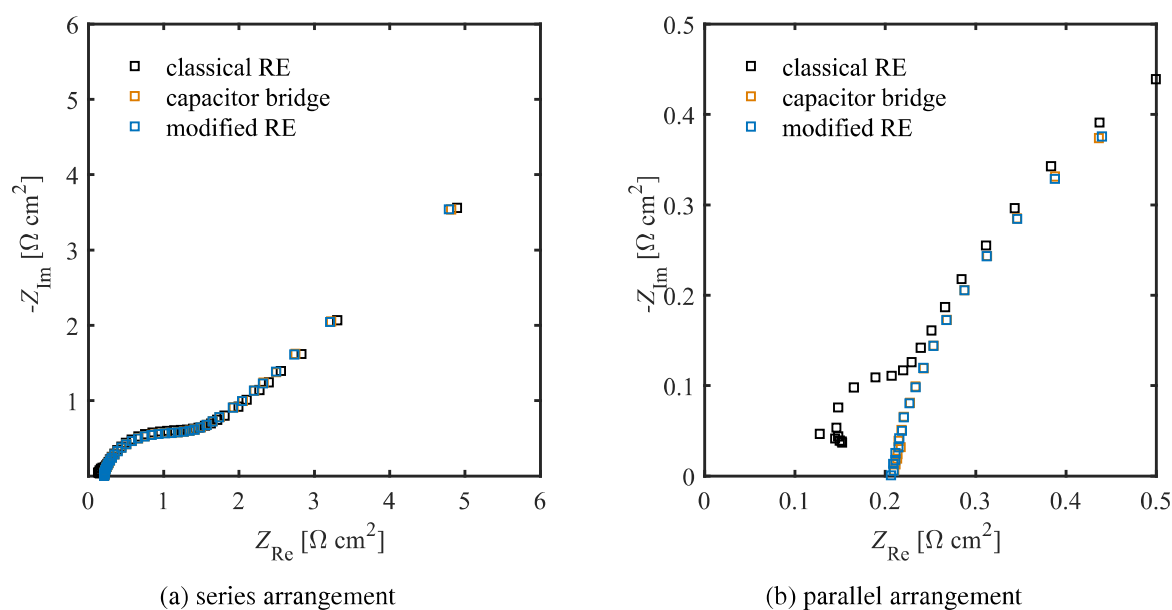


Figure 7.3.: Impedance spectra recorded at a 250 μm Pt-WE in 10 mM $\text{K}_3[\text{Fe}(\text{CN})_6]$ in 0.5 M KF. Spectra acquisition was performed using a Pt-mesh CE and a home-made Ag/AgCl (3 M KCl) RE with and without additional capacitive coupling.

producible impedance measurements, as it minimizes frequency dispersion (Battistel, 2014). Impedance measurements are very sensitive towards artefacts related to the measurement set-up, which can be caused by extended cables or instrumental limitations. The impedance of a single electrode can only be measured when a three-electrode configuration is employed. Ideally, there is no current flow between the WE and the RE. In real-world conditions, any RE is polarizable to a certain extent, and the current flowing through it causes high-frequency distortions that cannot be neglected (La Mantia, 2009). As proposed by Battistel (2014), this artefact can be removed by introducing a capacitor bridge, which increases the capacitive coupling between the RE and the WE. An alternative solution is the use of a so called ‘fast RE’, where a Pt-coil surrounding the tip of the RE is coupled with a capacitor. The above Figure 7.3 shows dynamic impedance spectra measured for a redox couple. Here, the unstable reference voltage leads to a high-frequency arc when no additional capacitive coupling is employed. In contrast, when a 100 nF capacitor bridge is introduced into the set-up, the artefact disappears. Similar results are obtained upon modification of the RE with a 100 μm Pt wire and a parallel bypass 100 nF capacitor. In order to reduce high-frequency distortions, the impedance data presented in Chapters 3 and 4 were acquired using a fast RE.

Rotating Disk Electrode Configuration

The experiments presented in Chapter 5 were performed in a home-made polymethylmethacrylate (PMMA) cell, using a three-electrode set-up with an RDE configuration, as shown in Figure 7.4. The measurements were carried out at a p-type silicon WE, having a diameter of 5 mm and a resistivity of 5-25 Ω . The potential was measured versus a Hg/Hg₂SO₄-RE, and a Pt wire was employed as CE. Additionally, an external resistance was connected in series with the WE, which was varied in a range between 0 Ω and 30 k Ω . The PMMA cell and the p-type Si sample were provided by the group of Nonequilibrium Chemical Physics, TUM.

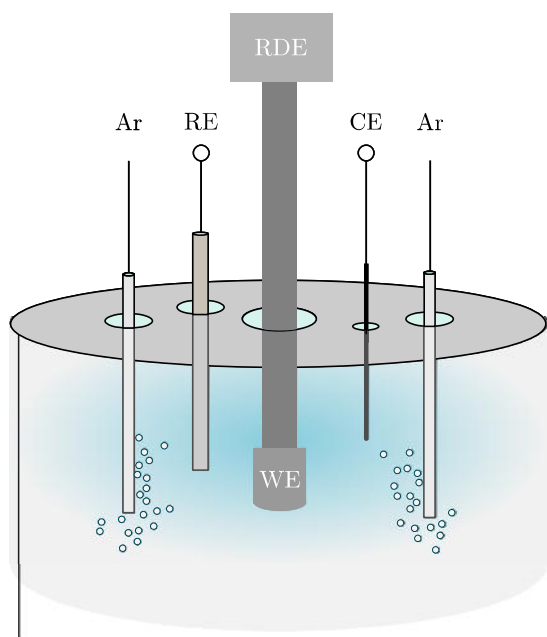


Figure 7.4.: RDE set-up used for the measurements presented in Chapter 5.

7.1.3. Perturbation Signals

DMFA combines multi-sine impedance spectroscopy and quasi-*dc* voltammetry. Section 3.1.2 was concerned with the generation of the multi-sine signal. In Section 3.1.1 the advantages of a quasi-triangular waveform over a classic triangular waveform were discussed. The mathematical definition of the quasi-triangular waveform that was employed for dynamic impedance spectra acquisition is given by the following equation:

$$QT(t) = \begin{cases} 4t & 0 \leq t \leq 0.2 \\ 0.8 + \frac{0.4}{\pi} \sin \left[\frac{(t-0.2)}{0.1} \pi \right] & 0.2 < t < 0.3 \\ 2 - 4t & 0.3 \leq t \leq 0.7 \\ -0.8 + \frac{0.4}{\pi} \sin \left[\frac{(t-0.8)}{0.1} \pi \right] & 0.7 < t < 0.8 \\ -4 + 4t & 0.8 \leq t \leq 1, \end{cases}$$

where $QT(t)$ was normalized with respect to t .

7.1.4. Data Acquisition

According to the Nyquist-Shannon sampling theorem, the sampling rate determines the highest frequency at which a digitally generated signal can be evaluated, such that

$$f_{sa} = 2 f_{max}, \quad (7.1)$$

where f_{sa} corresponds to the sampling frequency, and f_{max} refers to the maximum possible frequency (Lüke, 1999). In order to fully capture the characteristic features of the continuous-time voltage and current signals, the value of the sampling frequency must be at least twice as big as that of the highest frequency contained in the multi-sine signal. Therefore, in each measurement up to 220 million data points were recorded, where the sampling time was ranging from hundreds of nanoseconds to few microseconds. Spectral leakage was avoided by using a multi-sine perturbation with a base frequency oscillating at an integer multiple of the fundamental frequency of the quasi-CV and recording an integer number of multi-sine oscillations. In Section 3.2 it was discussed how to correctly choose the base frequency of the multi-sine wave with respect to the fundamental frequency of the quasi-CV.

7.1.5. Data Processing

Data processing of the perturbation and response signals was performed simultaneously, using home-made MATLAB scripts. When a data set contains a non-integer number of periods of the quasi-triangular waveform, the dynamic impedance values calculated for the data points located at the beginning and at the end of the data array are highly distorted (Battistel and La Mantia, 2019). In the experiments presented in this work a pseudo-periodicity was attained by mirroring of the original data sets, thus enabling the evaluation of aperiodic signals. In doing so, impedance distortions were highly reduced. However, due to mirroring, the impedance spectra recorded up to a distance of $\frac{1}{bw}$ from the time boundaries had to be discarded. After mirroring,

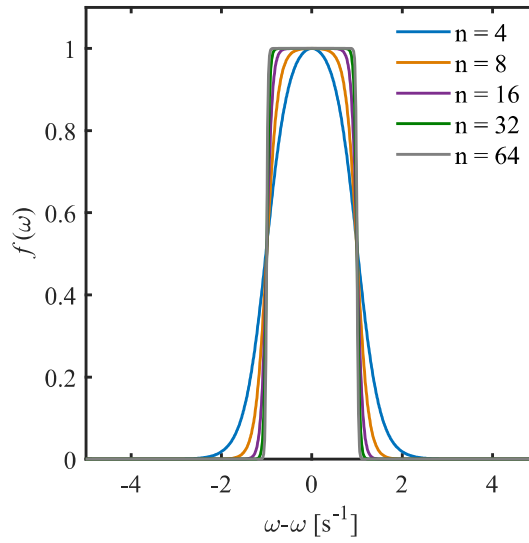


Figure 7.5.: Representation of the quadrature filter function defined in (7.2) for different values of n in the Fourier domain. The amplitude of the filter was normalized to 1 and the bandwidth bw was equal to 1 s^{-1} .

the full data sets were transformed from the time domain into Fourier space by means of discrete Fourier transform (DFT). A quadrature filter function of finite bandwidth was applied to extract the partial voltage and current signals about the fundamental frequencies of the multi-sine wave and the fundamental *dc* signal, respectively, as discussed in Section 3.2.1. The mathematical expression of the quadrature filter function g was derived from multiplication of two Fermi-Dirac functions. The amplitude of g was normalized to 1 at the central frequency ω , yielding

$$g(\omega - \omega_0, bw) = \frac{[1 + \exp(-n)]^2}{[1 + \exp(-n \frac{\omega - \omega_0 + bw}{bw})][1 + \exp(n \frac{\omega - \omega_0 + bw}{bw})]}. \quad (7.2)$$

Depending on the value of n , the filter can have an ideal rectangular shape or a quasi-rectangular shape with rounded borders, see Figure 7.5. In the experiments presented in this thesis, the parameter n was set to a value of 8. As pointed out in Section 2.4.1, the dynamic impedance was calculated from (2.25) by applying iFT to the partial current and voltage signals. The amount of theoretically accessible impedance spectra was equal to the number of sampling points contained in the original data sets. However, the number of spectra was reduced to a maximum of 2000, using an integration term. Following the procedure reported by Battistel (2014), an additional calibration file was employed for the correction of the nonideal behavior of the potentiostat observed at high-frequencies.

7.1.6. Fitting of Dynamic Impedance Spectra

The dynamic impedance spectra recorded by means of DMFA were fitted to EECs using home-made MATLAB scripts. Suitable equivalent circuits and the cost function were implemented as MATLAB functions. The passive elements used to construct the EECs presented in this work and their respective impedance expressions are reported in Table 7.1. Due to a non-uniform disk current density distribution, some fitting attempts required the use of a CPE instead of an ideal capacitor. A CPE is composed of the parameter Q and its corresponding phase angle n . Using Brug's formula it is possible to translate CPE values into capacitances, where the two quantities are linked through the relationship

$$C = \frac{Q}{(R_1^{-1} + R_2^{-1})^{\frac{1-n}{n}}}. \quad (7.3)$$

In the measurements presented in this thesis C refers to C_{dl} when using Q_{dl} and n_{dl} . In this case, R_1 and R_2 refer to R_s and R_{ct} , respectively. In contrast, C corresponds to C_{ad} when inserting Q_{ad} and n_{ad} . Consequently, R_1 and R_2 refer to R_{ad} and R_{ct} , respectively (Brug, 1984). Data fitting was performed using the modified CNLS regression approach introduced in Section 2.4.4. The procedure was based on the *fminunc* algorithm incorporated in the MATLAB software, which aims to minimize an unconstrained multivariable function. The amount of impedance spectra included in the fitting procedure and the number of iterations (attempts on minimization of the cost function) strongly influence the duration of the fitting. In the work presented here, a maximum of 108 impedance spectra was fitted simultaneously, where the number of iterations was set to 500. In doing so, high quality fitting results were obtained in a reasonable time scale. Due to the fact that the impedance recorded at high frequencies is very sensitive to instrumental artefacts, the highest frequency value was discarded during data fitting of the spectra presented in Chapters 3 and 4. Moreover, when performing CNLS regression on the impedance spectra shown in Chapter 3 and in Sections 4.2.3 and 4.3 (only in the electro-sorption region), the data points recorded at 8 Hz and 59 Hz were rejected.

Table 7.1.: Passive elements used for the construction of EECs.

acronym	circuit element	physical process	impedance expression
C_{st}	stray capacitance	stray capacitance of the potentiostat	$(j \omega C_{st})^{-1}$
C_{dl}	double layer capacitance	accumulation of charge at the interface	$(j \omega C_{dl})^{-1}$
C_{ad}	adsorption capacitance	accumulation of adsorbed species at the interface	$(j \omega C_{ad})^{-1}$
$Q(n)$	constant phase element	inhomogeneous charge distribution	$(j \omega Q)^{-n}$
R_{ad}	adsorption resistance	electrokinetic limitation imposed by electro-sorption	R_{ad}
R_{ct}	charge transfer resistance	electrokinetic limitation imposed by faradaic reaction	R_{ct}
R_s	solution resistance	ohmic drop in the electrolyte	R_s
R_w	mathematical correction term	—	R_w
Z_W	Warburg impedance	limitation due to mass-transport	$\frac{\sigma}{\sqrt{2\pi f}}$

7.2. Materials and Instruments

This Section provides technical specifications on the materials and instrumentation used to perform the experiments presented in this work.

List of Chemicals

component	chemical formula	specification	supplier
acetone	$\text{C}_3\text{H}_6\text{O}$	p.a.	Merck
ammonium fluoride	NH_4F	p.a.	Merck
ethanol	$\text{C}_2\text{H}_6\text{O}$	p.a.	Merck
isopropanol	$\text{C}_3\text{H}_8\text{O}$	purity $\geq 99.999\%$	VWR
isopropanol	$\text{C}_3\text{H}_8\text{O}$	p.a.	Merck
lithium perchlorate	LiClO_4	purity $\geq 99.99\%$	Sigma Aldrich
methanol	CH_4O	p.a.	Merck
potassium fluoride	KF	purity $\geq 99.5\%$	Sigma Aldrich
potassium hexacyanoferrate(III)	$\text{K}_3[\text{Fe}(\text{CN})_6]$	purity $\geq 99.0\%$	Sigma Aldrich
potassium perchlorate	KClO_4	purity $\geq 99.99\%$	Sigma Aldrich
perchloric acid	HClO_4	70%, purity $\geq 99.999\%$	Sigma Aldrich
sodium perchlorate	NaClO_4	purity $\geq 99.99\%$	Sigma Aldrich
sulphuric acid	H_2SO_4	10%, purity $\geq 99.999\%$	Sigma Aldrich
sulphuric acid	H_2SO_4	96%, Suprapur	Merck
ultrapure water	H_2O	Type 1, conductivity = $0.055 \mu\text{S cm}^{-1}$	Sartorius

List of Materials

component	specification	supplier
abrasive paper	Grade = 12.6 μm , 18.3 μm , 21.8 μm	Matador
borosilicate glass capillaries	L = 100.0 mm, OD = 1.0 mm, ID = 0.58 mm	Science Products
7-barreld borosilicate glass capillaries	L = 100.0 mm, OD = 1.0 mm, ID = 0.56 mm	Hilgenberg
platinum wire	0.025 mm, purity $\geq 99,99\%$	Goodfellow
copper wire	0.1 mm, purity $\geq 99,9\%$	Goodfellow
copper wire	0.5 mm, purity $\geq 99,9\%$	Goodfellow
polishing paper	Grain size = 1 μm / 3 μm	3 M
silver epoxy adhesive	Polytec EC 244	Polytec PT

List of Instruments

component	specification	supplier
micropipette puller	PE-22	Narishige
2-channel oscilloscope	4262	Pico technology
2-channel potentiostat	SP-300	Bio-Logic
RDE set-up	AFM-SRCE	Pine Research Instrumentation
sonication bath	Elmasonic P	Elma-ultrasonic
2-channel waveform generator	33512b	Keysight

List of Electrodes

component	diameter	supplier
Ag/AgCl (3 M KCl)	-	produced in our lab
Hg/Hg ₂ SO ₄ (3 M KCl)	-	produced in our lab
platinum disk	25 μ m	self-made
platinum disk	250 μ m	produced in our lab
platinum multibarrel	6 \times 25 μ m	self-made
platinum mesh	L = 12.0 mm, OD = 10.0 mm	Labor Platina
platinum wire	OD = 5 mm, purity \geq 99.99%	Chempur
silicon disk	5 mm, ρ = 5-25 Ω cm	provided from TUM

Software

The measurements were controlled using MATLAB 9.4 (R2018a, Mathworks) and EC-Lab[®] V5.56 Express (Bio-Logic) software. Data analysis and plotting were performed with MATLAB 9.4 (R2018a, Mathworks) software. For manual graphing, Inkscape 0.48 (Inkscape Community) was employed.

7.3. Experimental Protocols

In the following, the experimental procedures employed in this work are reported. First, the fabrication of micro- and multibarrel electrodes is described. Next, the measurement protocols are detailed.

7.3.1. Fabrication of Micro- and Multibarrel Electrodes

Fabrication of microelectrodes was performed by vertically inserting a single circular borosilicate glass capillary with an outer diameter of 1 mm into a micropipette puller. The ends of the capillary were held by a topside and a downside drill chuck, respectively. The intermediate

part of the capillary was placed in the center of a Kanthal wire heating element with an inner diameter of 5 mm. The capillary was vertically stretched by heating the element and using the gravitational force of the weight of the downside chuck. The pulling force was adjusted by activation of an electromagnet attracting the downside chuck. First, a gradual gentle force was applied by a sub-magnet. Subsequently, the upper and lower part of the capillary were pulled apart by the strong force of the main magnet. The heater and magnet output of the micropipette puller can be varied in a range between 0 and 100. The heater was set to a value of 40, whereas the sub-and main magnet were set to 30. In doing so, a microelectrode body was produced, whose upper end was held by the topside drill chuck. The downwards pointing end formed a conically tapered tube with a closed sharp tip. In contrast, the residual part of the capillary that was attached to the downside chuck was deformed and had to be disposed. The microelectrode body was removed from the micropipette puller. A Pt wire with a diameter of $25\text{ }\mu\text{m}$ and a length of approximately 15 mm was inserted carefully into the capillary through the hole on the opposite side of the tapered tip. The wire was pushed gently towards the conical end of the capillary, using a Cu wire with a diameter of 0.5 mm. When the Pt wire was in the desired position, the Cu wire was removed from the glass body. The capillary was again fixed into the topside chuck of the micropipette puller, with the tapered tip pointing downwards. The other end of the capillary was connected to a peristaltic pump through a flexible polymer tube. The external part of the tapered tip was brought to the center of the heating element, and the Pt wire was sealed into the capillary by applying moderate heat for the duration of 30 s. Subsequently, the filament was heated for the duration of 90 s. In order to avoid the incorporation of gas bubbles in the glass mantle during the sealing process, a vacuum was created inside the capillary. The capillary was moved vertically and the last step was repeated, until two-thirds of the Pt wire were sealed into the glass body. The capillary was disconnected from the pump and removed from the micropipette puller. The part of the Pt wire that was not sealed into the glass was con-

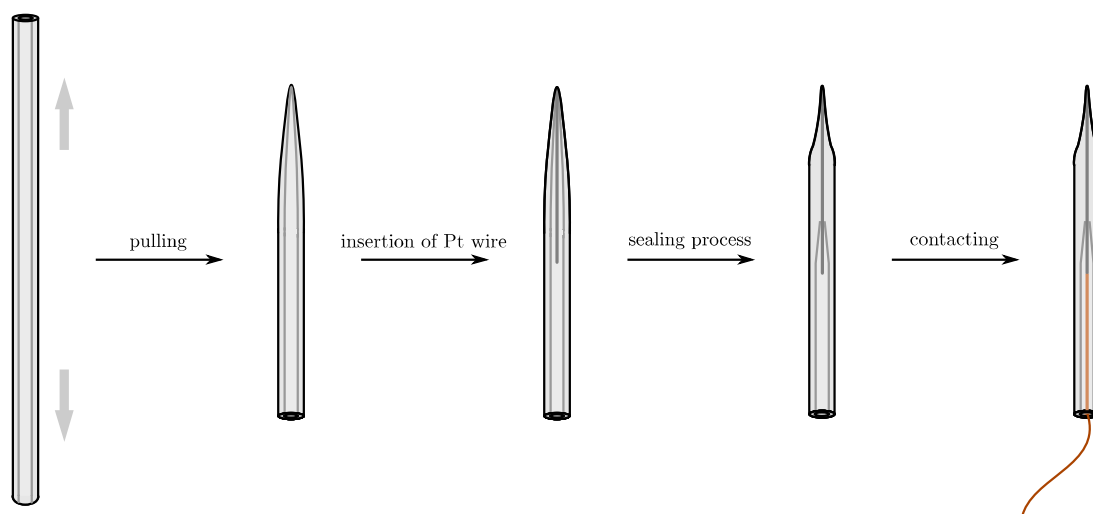


Figure 7.6.: Schematic representation of the fabrication process of microelectrodes.

tacted with a Cu wire with a diameter of 0.1 mm, using two-component silver epoxy adhesive. The tapered tip of the microelectrode was smoothened with abrasive paper of grade 12.6 μm and thoroughly rinsed with ultrapure water. The fabrication of microelectrodes is schematically displayed in the above Figure 7.6.

Multibarrel electrodes were produced using a commercially available sevenfold bundle of borosilicate glass capillaries. In order to protect the fragile assembly from stress-induced cracks during the pulling process, its both ends were covered with shrinking tube. Then, the bundle was inserted into the micropipette puller. It was fixed by the drill chuck method, where its intermediate section was positioned in the center of a heating element with an inside diameter of 7 mm. The filament was heated using an output value of 60. After 40 s, the topside chuck was rotated around its vertical axis by 360°. In doing so, the different capillaries got twisted together at their intermediate section, enclosed by the heating element. Simultaneously, the gravitational force of the weight of the downside chuck pulled the upper and lower fraction of the bundle apart. In this case, the magnets were not activated during the pulling process. The multibarrel electrode body was removed from the micropipette puller, and a Pt wire of 25 μm diameter was inserted into each of the 6 outer capillaries, while the capillary located in the center of the bundle was left empty. The wires were sealed into the glass body, following a similar procedure as mentioned above. In each sealing step the capillary was heated for 60 s by applying an output value of 95. Each Pt wire was contacted separately to a Cu wire, as it was done in the fabrication process of microelectrodes. Finally, the shrinking tube was removed. The multibarrel electrode was polished intensely, using abrasive paper of grade 21.8 μm , 18.3 μm , and 12.6 μm , successively. The below Figure 7.7 shows a schematic representation of a multibarrel electrode.

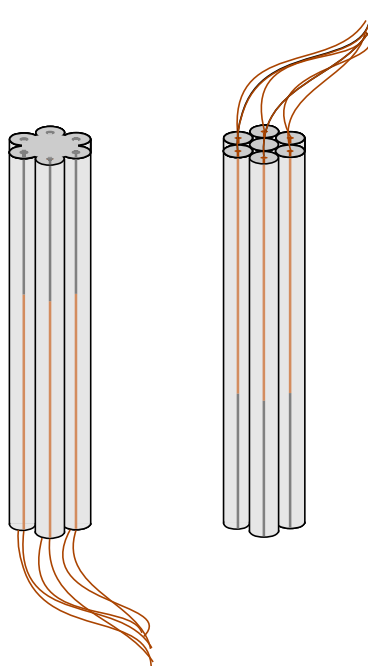


Figure 7.7.: Schematic representation of a multibarrel electrode.

Before each set of experiments, the WE was cleaned using abrasive paper of grade 12.6 μm . Subsequently, the electrode was smoothened by polishing the surface with lapping film of grade 3 μm and 1 μm , respectively. After each step, the electrode was rinsed thoroughly with isopropanol and ultrapure water.

7.3.2. Measurements on the Reaction Dynamics of a Redox Couple

The measurements presented in Chapter 3 were performed in 10 mM $\text{K}_3[\text{Fe}(\text{CN})_6]$ in 0.5 M KF using the coaxial cell set-up presented in Section 7.1.2 and a Bio-Logic SP-300 potentiostat. All measurements were carried out at room temperature (RT) in argon saturated solutions.

Pre-Treatment of the WE

CVs were performed in a potential range between 0.21 and 0.71 V vs. SHE at a scan rate of 50 mV s^{-1} . In addition to that, a potentiostatic impedance spectrum was recorded in a frequency range between 1 MHz and 1 Hz by applying a time-invariant potential of 0.46 V vs. SHE and a perturbation amplitude of 15 mV.

DMFA Measurements

After pre-characterization of the system by means of CV and potentiodynamic EIS, DMFA measurements were performed. To do so, the WE was polarized at 0.46 V vs. SHE, using the chronoamperometry technique embedded in the EC-Lab[®] software of the potentiostat. The current range was set to 10 μA when using the 25 μm WE. In contrast, a current range of 100 μA was applied when the 250 μm or the multibarrel electrode was employed. In a first measurement, a quasi-CV was recorded by imposing only the quasi-triangular waveform on the constant potential. The potential was changed symmetrically about the time-invariant potential, where the total amplitude of the triangular waveform was set to 500 mV. Consequently, a full cycle was equal to 1 V. The scan rate of the quasi-CV was chosen to be 50 mV s^{-1} , thus corresponding to a frequency of 0.05 Hz. Spectral leakage was avoided by setting the total duration of the experiment to 40 s, which equals 2 full periods of the quasi-triangular wave. To not violate the sampling theorem, the data were recorded at a time interval of 40 μs .

Subsequently, the multi-sine signal was added to the quasi-triangular waveform, and the total perturbation signal was superimposed onto the time-invariant potential. The measurements were performed using two different arbitrary waveforms, one with $d = 1$, containing 51 frequencies in a range between 1 MHz and 7 Hz and the other one with $d = 7$, including 45 frequencies ranging from 1 MHz to 8 Hz. The base frequency was set to 1 Hz. The settings of the

quasi-triangular waveform and the constant potential remained the same as outlined above. The amplitude of the multi-sine signal was varied in a range between 10 mV and 50 mV. Data were acquired for 44 s, where the time interval was set to 200 ns. The data recorded within the first and last 2 s of the data array were discarded.

7.3.3. Measurements on the Reaction Dynamics of the HER

The measurements presented in Chapter 4 were performed using the coaxial cell set-up presented in Section 7.1.2 and a Bio-Logic SP-300 potentiostat. The measurements were carried out at RT in argon saturated solutions.

Pre-Treatment of the WE

The WE was investigated by means of cyclic voltammetry in 5 mM solution of $K_3[Fe(CN)_6]$ in 0.5 M KF in order to assure that the electrode surface was clean and that its roughness was not too high. The CVs were recorded in a potential range between 0.735 V and 0.085 V vs. SHE.

In a subsequent step, the electrode surface was activated by voltammetric cycling in a solution of 100 mM solution of $HClO_4$, as described in Section 4.2.1. To do so, 100 CVs were recorded in a potential range between 0.012 V and 1.512 V vs. RHE at a scan rate of 100 mV s^{-1} .

The HER was investigated in 2, 5, 10, and 20 mM solution of $HClO_4$ and in electrolytes containing 90 mM $KClO_4$ in 10 mM $HClO_4$, 90 mM $NaClO_4$ in 10 mM $HClO_4$, and 90 mM $LiClO_4$ in 10 mM $HClO_4$. Before each set of dynamic impedance measurements, the system was pre-characterized in the respective electrolyte solution, using *dc* voltammetry and potentiostatic EIS. CVs were performed in a potential range between -0.55 V and 0.45 V vs. RHE at a scan rate of 100 mV s^{-1} . The potential values were calculated from

$$E_{\text{RHE}} = E_{\text{Ag/AgCl (3 M KCl)}} + 0.059 \text{ pH} + E_{\text{Ag/AgCl (3 M KCl)}}^0,$$

Table 7.2.: pH values of different electrolyte solutions.

electrolyte	pH
2 mM $HClO_4$	2.7
5 mM $HClO_4$	2.3
10 mM $HClO_4$	2.0
20 mM $HClO_4$	1.7
100 mM $HClO_4$	1.0
10 mM $HClO_4$ + 90 mM $KClO_4$	2.0
10 mM $HClO_4$ + 90 mM $NaClO_4$	2.0
10 mM $HClO_4$ + 90 mM $LiClO_4$	2.0

where $E_{\text{Ag/AgCl (3 M KCl)}}^0$ corresponds to the standard potential of the Ag/AgCl (3 M KCl)-RE (Wang, 2013). The pH values of the different solutions are reported in Table 7.2. Potentiostatic impedance spectra were recorded in a range between 1 MHz and 10 Hz at a potential of 0.45 V vs. RHE, where the perturbation amplitude was set to 15 mV.

DMFA Measurements

DMFA measurements were performed in the different electrolyte solutions by applying a time-invariant potential of 0.45 V vs. RHE to the WE. In 2 mM and 5 mM solution of HClO_4 the current range of the potentiostat was set to 100 μA . In contrast, in 10 mM and 20 mM solution of HClO_4 it was set to 1 mA. A quasi-CV was acquired by perturbation of the constant potential with the quasi-triangular waveform. The amplitude of the quasi-CV was set to 1 V. Starting from a potential of 0.45 V vs. RHE, the potential was changed towards cathodic potentials. The scan rate of the quasi-CV was chosen to be 100 mV s^{-1} . Thus, according to (3.1), the frequency of the quasi-CV was equal to 0.05 Hz. Two full cycles were recorded at a sampling time of 40 μs , thus corresponding to a total duration of 40 s.

Dynamic impedance spectra were recorded using the arbitrary waveform presented in Section 3.1.2. The multi-sine signal contained 45 frequencies with $d = 7$. The amplitude of the multi-sine signal was set to 50 mV. The multi-sine base frequency was chosen to be 1 Hz, thus resulting in fundamental harmonics ranging from 1 MHz to 8 Hz. The settings of the quasi-CV and the constant potential remained the same as aforementioned. The total time of the experiment was 44 s, where data points were recorded every 200 ns. The data points collected within the first and last 2 s of the data array were discarded.

7.3.4. Measurements on the Anodic Electro-Dissolution of p-Type Si

The measurements presented in Chapter 5 were performed using the RDE set-up presented in Section 7.1.2 and a 2-channel Bio-Logic SP-300 potentiostat. All experiments were carried out at RT. Throughout the measurement the electrolyte was purged with argon.

Pre-Treatment of the WE

Before mounting the silicon wafer to the sample holder of the RDE set-up, the surface was rinsed with acetone, ethanol, methanol, and ultra-pure water. The electrode was characterized by means of cyclic voltammetry in a solution of 0.06 M NH_4F in 142 mM H_2SO_4 (pH = 1). CVs were recorded in a potential range between 0.64 V and 6.64 V vs. SHE at a scan rate of 20 mV s^{-1} .

DMFA Measurements in the Steady-State

The steady-state studies presented in Section 5.2 were carried out in a solution of 0.05 M NH_4F in 25 mM H_2SO_4 (pH = 2.3). DMFA measurements were performed by applying a time-invariant potential of 1.64 V vs. SHE. The potential was perturbed by an arbitrary waveform with $d = 3$, containing 49 frequencies covering 5 decades, which was superimposed on a slow quasi-triangular scan. The amplitude and phase spectra corresponding to the multi-sine signal are illustrated in Figure 7.8. The scan rate of the quasi-CV was set to 1 mV s^{-1} . Therefore, the fundamental frequency of the quasi-CV was equal to 0.25 mHz. Its amplitude was set to 2 V, so that the potential was swept in a range between 1.64 V and 3.64 V vs. SHE. The base frequency and amplitude of the multi-sine wave were chosen to be 3 mHz and 300 mV, respectively. In each measurement, 2.5 cycles were recorded, thus corresponding to a total duration of 10000 s, where the sampling time was 0.1 ms. The current range was set to 1 mA. The data were extracted using a filter bandwidth bw of $1 \times f_b$.

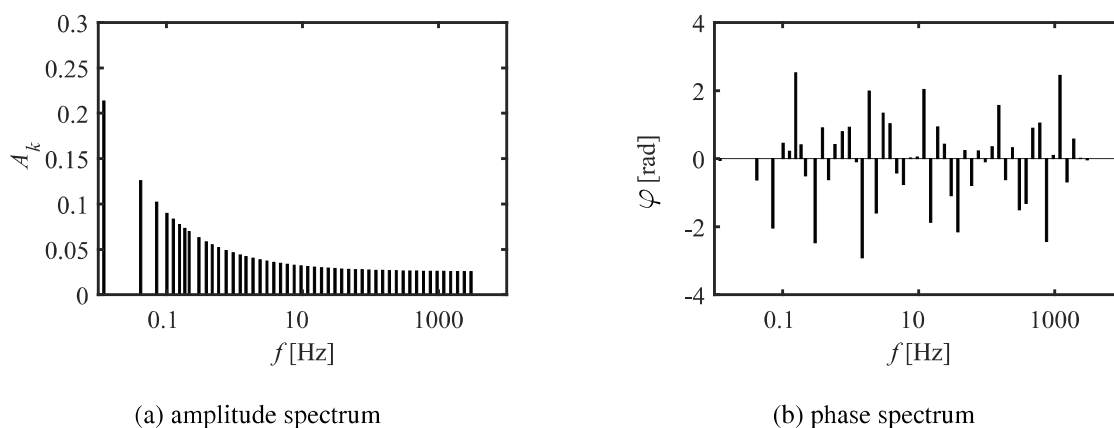


Figure 7.8.: Amplitude and phase spectra of the multi-sine signal used for the investigation of the Si electrodisolution reaction in dynamic equilibrium conditions. The signal contains 49 frequencies, covering a range between 3 kHz and 12 mHz with $d = 3$.

DMFA Measurements in the Oscillatory Regime

In order to investigate the Si electrodisolution process in the oscillatory regime (Section 5.3), DMFA measurements were performed in an electrolyte solution of 0.06 M NH_4F in 142 mM H_2SO_4 (pH = 1). The WE was polarized at a constant potential of 8.64 V vs. SHE by means of standard chronoamperometry. The current range was set to 1 mA. Additionally, an external resistance was connected in series with the WE. Dynamic impedance spectra were recorded by superposition of the constant potential with the multi-sine signal. The measurements were performed using two arbitrary waveforms with $d = 3$, one containing 29 frequencies covering 3 decades and the other one containing 39 frequencies over 4 decades. The latter contained

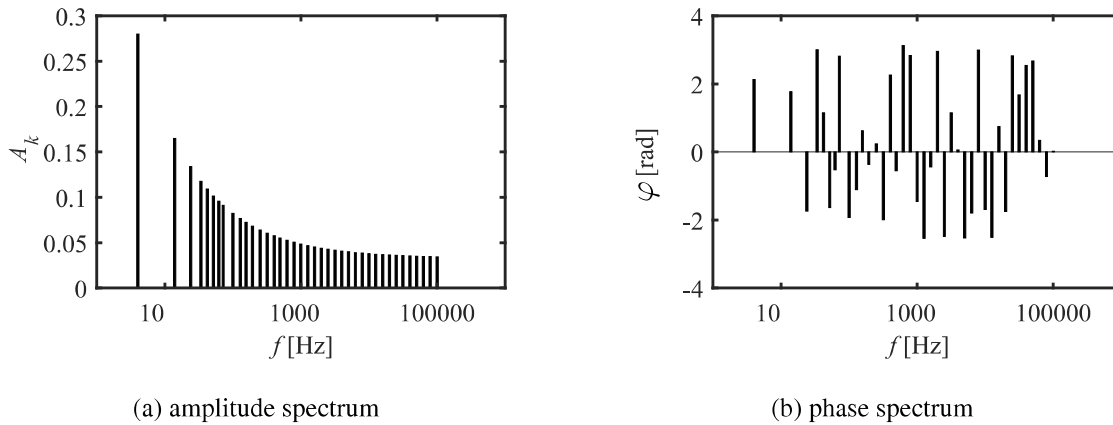


Figure 7.9.: Amplitude and phase spectra of the multi-sine signals used for the investigation of the Si electrodisolution reaction in the oscillatory regime. Low-amplitude and shoulder oscillations were investigated with a multi-sine signal containing 39 frequencies covering 4 decades, whereas high-amplitude oscillations were studied with a signal containing 29 frequencies over 3 decades ($d = 3$). Only the 4 decade signal is shown here, as it contains the same m_k values as the first waveform and ten additional signals in the high-frequency region. The m_k values must be multiplied with the base frequency of the respective waveform to obtain the frequencies applied during the measurement.

the same frequencies as the first waveform and ten additional signals in the high-frequency region, see Figure 7.9. The experimental settings that were chosen for the investigation of different types of current oscillations are summarized in Table 7.3. Here, f_{osc} corresponds to the frequency of the natural current oscillation and f_b is the base frequency of the multi-sine signal. f_{min} is related to the smallest frequency applied during the measurement, f_{max} is the largest fundamental harmonic in the multi-sine wave, and R_{ext} corresponds to the external resistance that was connected in series with the WE.

Table 7.3.: Experimental settings employed for the investigation of different types of current oscillations by means of DMFA.

oscillation	waveform	f_{osc} [mHz]	f_b [Hz]	f_{min} [Hz]	f_{max} [kHz]	R_{ext} [k Ω]
low-amplitude	4 decades	20	0.17	0.68	17	10
shoulder	4 decades	20	0.2	0.8	20	17.5
high-amplitude	3 decades	30	0.3	1.2	3.0	30

7.4. Conductivity and Mobility

This Section provides the equations employed for the calculation of the transport number. The electrolyte resistance arises from the transport of ions in the bulk solution. An exact determination of the solution resistance is rather complex, as this parameter is affected by a number of parameters, among them the type and concentration of ions in the electrolyte, temperature, the distance between CE and WE, and the geometry of the WE. An analytical approach cannot provide an adequate formulation of the solution resistance, unless the system is subjected to specific restrictions. As outlined in Section 3.2.3, the solution resistance R_s can be expressed as

$$R_s = \frac{1}{4\kappa r}$$

when the solution adjacent to the electrode is regarded as a surface with uniform potential. The ionic conductivity κ of an electrolyte is given by

$$\kappa = \lambda^\circ c, \quad (7.4)$$

where λ° is its molar conductivity. The molar conductivity is the sum of the molar conductivities of the single ions

$$\lambda^\circ = \nu_+ \lambda_+ + \nu_- \lambda_-, \quad (7.5)$$

where ν_+ and ν_- represent the stoichiometric coefficients of the cations and anions, respectively.

The below Table 7.4 contains the molar conductivities of various ions from which the ionic conductivities κ of different electrolytes were calculated, see Table 7.5.

In infinitely diluted solutions the mobility u_i of an ion i is given by

$$u_i = \frac{\lambda_i}{(z_i F)^2}. \quad (7.6)$$

The values of u_i calculated for certain ionic species investigated in this work are reported in Table 7.6. The transport number t_i of the reactive ion is a measure of the fraction of current that is carried through migration of this species. It may be expressed in terms of the ratio between the ionic conductivity of the ionic reactant and the sum of the conductivities of all ionic species in the electrolyte, such that

$$t_i = \frac{\kappa_i}{\sum_k \kappa_k} = \frac{z_i^2 c_i u_i}{\sum_k z_k^2 c_k u_k}. \quad (7.7)$$

Table 7.4.: Molar conductivities and diffusion coefficients of various ions (Lide, 2005).

ion	λ_i [10^{-4} S m ² mol ⁻¹]	D_i [10^{-5} cm ² s ⁻¹]
H ⁺	349.65	9.311
K ⁺	73.48	1.957
Li ⁺	38.66	1.029
Na ⁺	50.08	1.334
ClO ₄ ⁻	67.3	1.792
F ⁻	55.4	1.475
$\frac{1}{3}$ [Fe(CN) ₆] ³⁻	100.9	0.896
$\frac{1}{4}$ [Fe(CN) ₆] ⁴⁻	110.4	0.735

Table 7.5.: Ionic conductivities of different electrolytes.

electrolyte composition	κ [S m ⁻¹]
2 mM HClO ₄	0.08
5 mM HClO ₄	0.21
10 mM HClO ₄	0.42
20 mM HClO ₄	0.84
10 mM HClO ₄ + 90 mM KClO ₄	1.68
10 mM HClO ₄ + 90 mM NaClO ₄	1.47
10 mM HClO ₄ + 90 mM LiClO ₄	1.37

Table 7.6.: Ion mobilities of various ions in infinitely diluted solutions.

ion	u_i [cm ² mol J ⁻¹ s ⁻¹]
H ⁺	3.76×10^{-8}
K ⁺	7.89×10^{-9}
Li ⁺	4.15×10^{-9}
Na ⁺	5.38×10^{-9}
ClO ₄ ⁻	7.23×10^{-9}

A. Complex Impedance Expression

According to (2.7), a small amplitude *ac* perturbation can be expressed as

$$u(t) = u_{dc} + |\Delta u| \sin(\omega t + \phi_u).$$

With (2.10) and $\frac{|\Delta u|}{2j} = \tilde{u}_{ac}$, the potential perturbation may be written as

$$u(t) = u_{dc} + \tilde{u}_{ac} (e^{j(\omega t + \phi_u)} - e^{-j(\omega t + \phi_u)}). \quad (\text{A.1})$$

FT of (A.1) for positive values of ω yields:

$$\begin{aligned} \text{FT}[u(t)](\omega) &= \int_0^T \tilde{u}_{ac} (e^{j(\omega t + \phi_u)} - e^{-j(\omega t + \phi_u)}) \cdot e^{-j\omega t} dt = \\ &= \tilde{u}_{ac} \left(e^{j\phi_u} t + \frac{1}{2j\omega} e^{-j(2\omega t + \phi_u)} \right) \Big|_0^T = \\ &= \tilde{u}_{ac} \left(e^{j\phi_u} T + \frac{1}{2j\omega} e^{-2j\omega T} e^{-j\phi_u} - \frac{1}{2j\omega} e^{-j\phi_u} \right) = \\ &= \tilde{u}_{ac} \left(e^{j\phi_u} T + \frac{1}{2j\omega} e^{-j\phi_u} (e^{-2j\omega T} - 1) \right). \end{aligned} \quad (\text{A.2})$$

It must be noted that the total duration of the measurement T is equal to an integer number n of the period of the applied frequency f . Therefore, ω can be expressed in terms of $\omega = 2\pi f = \frac{2\pi n}{T}$. Thus, the term $(e^{-2j\omega T} - 1)$ becomes $(e^{-4j\pi n} - 1) = 0$, since $\sin(4\pi n) = 0$. Therefore, (A.2) can be rewritten as

$$\text{FT}[u(t)](\omega) = \tilde{u}_{ac} e^{j\phi_u} T.$$

The derivation of the FT of the corresponding current response (2.8) is analogous to the above procedure. Therefore, the complex impedance can be expressed as

$$Z(\omega) = \frac{U(\omega)}{I(\omega)} = \frac{\tilde{u}_{ac}}{\tilde{i}_{ac}} e^{j(\phi_u - \phi_i)}.$$

In contrast, the FT of (2.7) for negative values of ω is performed according to

$$\begin{aligned}
 \text{FT}[u(t)](-\omega) &= \int_0^T \tilde{u}_{ac} (e^{j(\omega t + \phi_u)} - e^{-j(\omega t + \phi_u)}) \cdot e^{-j(-\omega t)} dt = \\
 &\quad \tilde{u}_{ac} \left(-e^{-j\phi_u} t + \frac{1}{2j\omega} e^{j(2\omega t + \phi_u)} \right) \Big|_0^T = \\
 &\quad \tilde{u}_{ac} \left(-e^{-j\phi_u} T + \frac{1}{2j\omega} e^{2j\omega T} e^{j\phi_u} - \frac{1}{2j\omega} e^{j\phi_u} \right) = \\
 &\quad \tilde{u}_{ac} \left(-e^{-j\phi_u} T + \frac{1}{2j\omega} e^{j\phi_u} (e^{2j\omega T} - 1) \right) = \\
 &\quad -\tilde{u}_{ac} e^{-j\phi_u} T.
 \end{aligned}$$

Thus, the corresponding impedance expression is given by

$$Z(-\omega) = \frac{U(\omega)}{I(\omega)} = \frac{\tilde{u}_{ac}}{\tilde{i}_{ac}} e^{-j(\phi_u - \phi_i)} = \overline{Z}(\omega).$$

B. Comparison of EIS and DMFA

Impedance measurements were carried out in a solution of 10 mM $\text{K}_3[\text{Fe}(\text{CN})_6]$ in 0.5 M KF at a 250 μm Pt electrode by means of DMFA and EIS, respectively. DMFA was performed by superposition of a constant dc potential of 0.46 V vs. SHE with a quasi-triangular potential perturbation and a multi-sine signal with $d = 7$. The potential was changed symmetrically about the dc potential. In doing so, dynamic impedance spectra covering a frequency range between 1 MHz and 8 Hz were recorded. In contrast, classic EIS was carried out in a frequency range between 1 MHz and 1 Hz by applying a constant dc potential of 0.46 V vs. SHE and a perturbation amplitude of 15 mV to the WE. Under these conditions, the stationary and the dynamic impedance spectra are almost identical, as illustrated in Figure B.1.

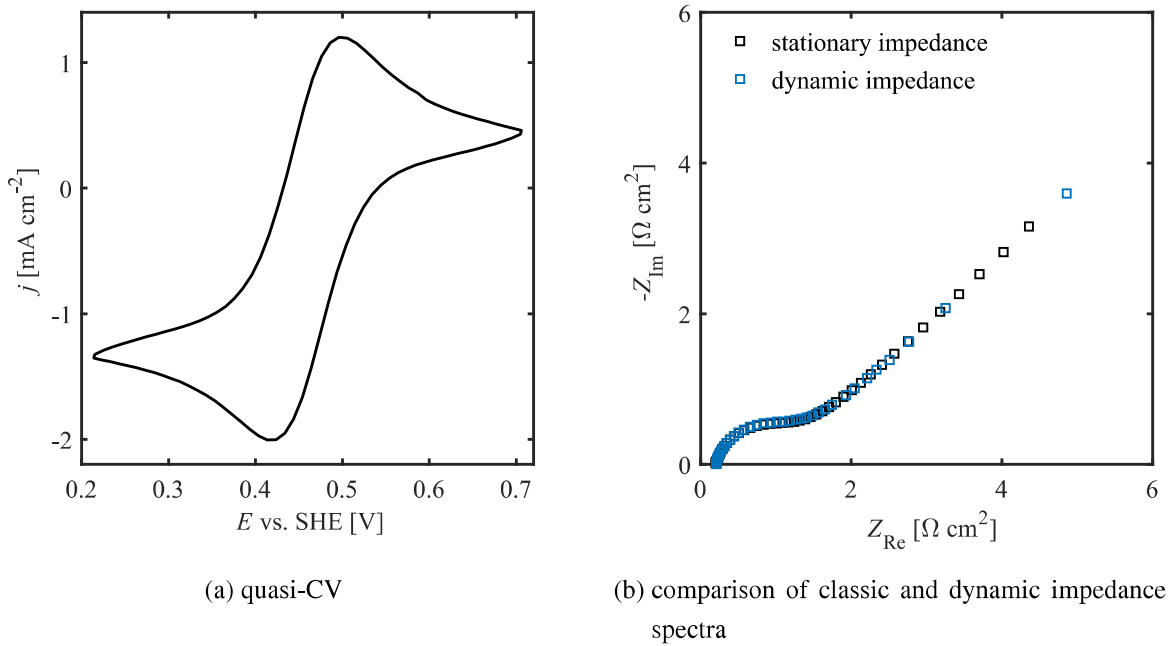


Figure B.1.: Quasi-CV recollected from DMFA measurements and comparison of a classic and a dynamic impedance spectrum. The measurements were recorded at a potential of 0.46 V vs. SHE in 10 mM $\text{K}_3[\text{Fe}(\text{CN})_6]$ in 0.5 M KF at a 250 μm Pt electrode. $\Delta u_{dc} = 500$ mV, $f_{dc} = 0.05$ Hz, $\Delta u_{ac} = 10$ mV, $f_b = 1$ Hz, $d = 7$, bw = 2 Hz.

C. Multi-Sine Amplitude at Micro- and Multibarrel Electrodes

The below Figures show that a multi-sine amplitude of 50 mV does not lead to distortions in the fundamental harmonics of the quasi-CV and the multi-sine signal when employing micro- or multibarrel electrodes. The second order harmonic signals are excluded by proper choice of the filter bandwidth.

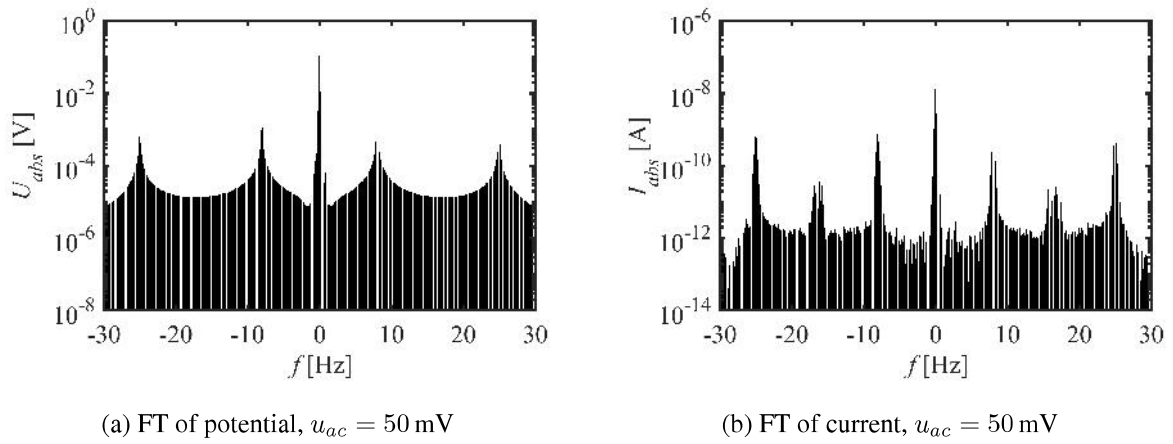


Figure C.1.: Potential perturbation and current response recorded in 10 mM $\text{K}_3[\text{Fe}(\text{CN})_6]$ in 0.5 M KF at a 25 μm Pt electrode for a multi-sine signal with $d = 7$ in the Fourier domain. $u_{dc} = 500$ mV, $f_{dc} = 0.05$ Hz, $u_{ac} = 50$ mV, $f_b = 1$ Hz.

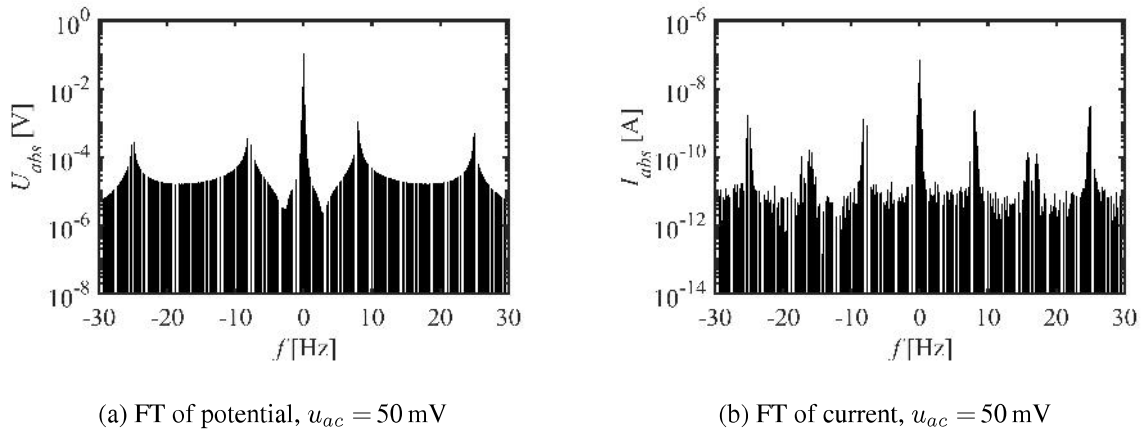


Figure C.2.: Potential perturbation and current response recorded in 10 mM $\text{K}_3[\text{Fe}(\text{CN})_6]$ in 0.5 M KF at a Pt multibarrel electrode for a multi-sine signal with $d = 7$ in the Fourier domain. $u_{dc} = 500$ mV, $f_{dc} = 0.05$ Hz, $u_{ac} = 50$ mV, $f_b = 1$ Hz.

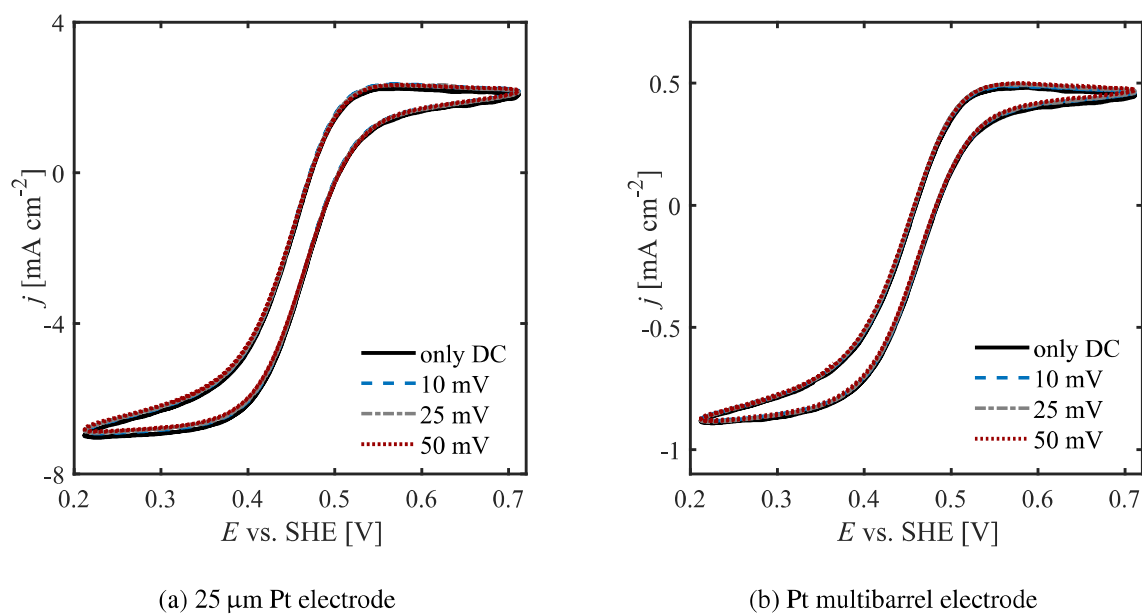


Figure C.3.: Comparison of quasi-CVs recollected from DMFA measurements in 10 mM $\text{K}_3[\text{Fe}(\text{CN})_6]$ in 0.5 M KF at a 25 μm Pt and a Pt multibarrel electrode using different values of multi-sine amplitude. The shape of the quasi-CVs are practically identical, irrespective of the choice of multi-sine amplitude. $\Delta u_{dc} = 500$ mV, $f_{dc} = 0.05$ Hz, $f_b = 1$ Hz, $d = 7$, $\text{bw} = 2$ Hz.

D. Dynamic Impedance Spectra in the Adsorption Region

The dynamic impedance spectra recorded in the electro-sorption region in diluted solutions of HClO_4 exhibit similar characteristics, irrespective of the potential under investigation.

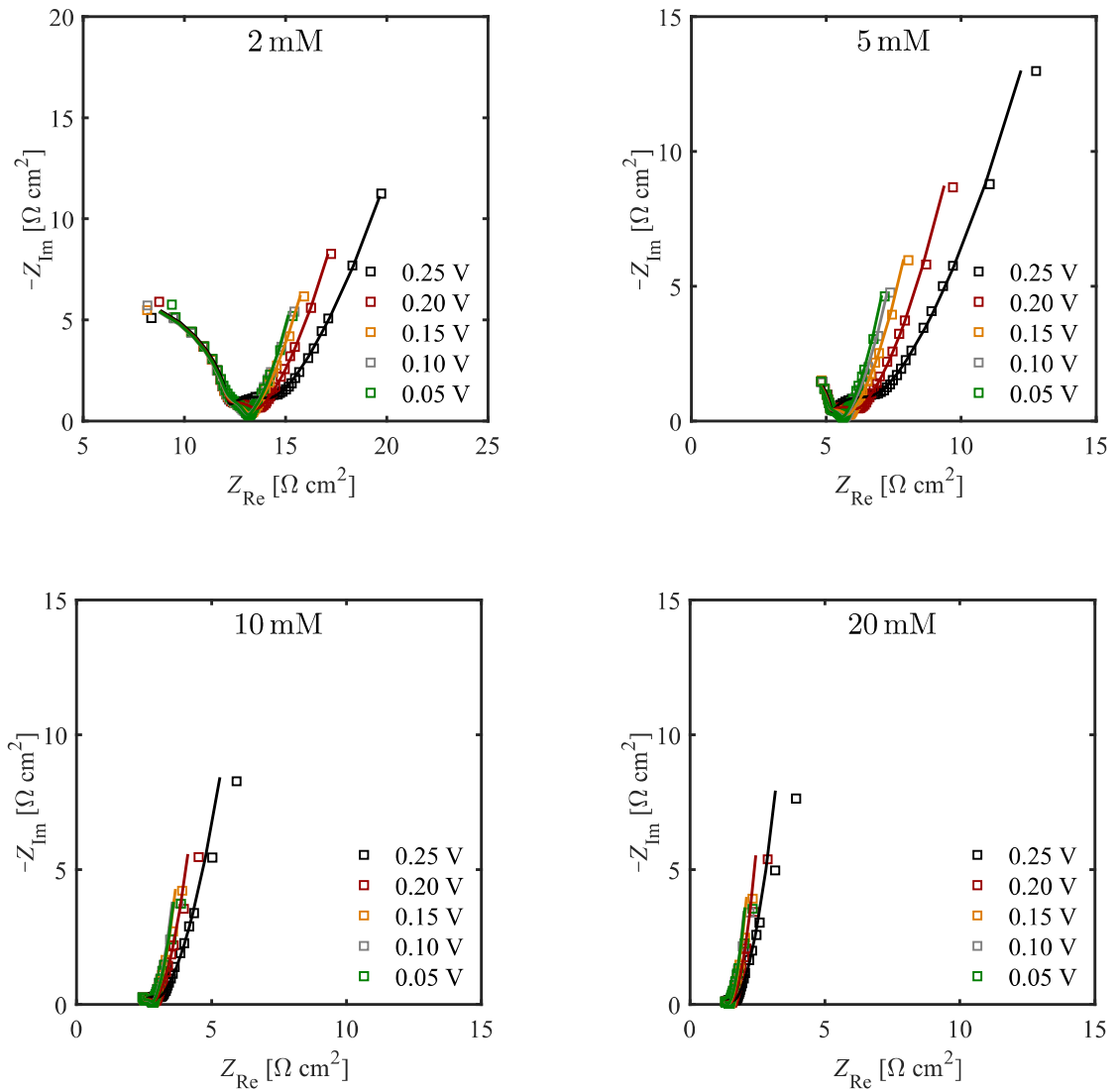


Figure D.1.: Comparison of experimental (squares) and fitted (lines) dynamic impedance spectra recorded in the electro-sorption region in 2 mM, 5 mM, 10 mM, 20 mM HClO_4 at a 250 μm Pt electrode. $\Delta u_{dc} = 1$ V, $f_{dc} = 0.05$ Hz, $\Delta u_{ac} = 50$ mV, $f_b = 1$ Hz, $d = 7$.

E. Effect of the Rotation Speed on the Dynamic Impedance Response

The dynamic impedance behavior of low-amplitude current oscillations, emerging during the anodic electrodisolution of p-type silicon, was investigated at different rotation speeds of the RDE. The impedance spectra are virtually not affected when changing the rotation speed in a range between 250 rpm and 2500 rpm, thus indicating that the feature observed in the low-frequency range can be attributed to solid-state mass transport phenomena.

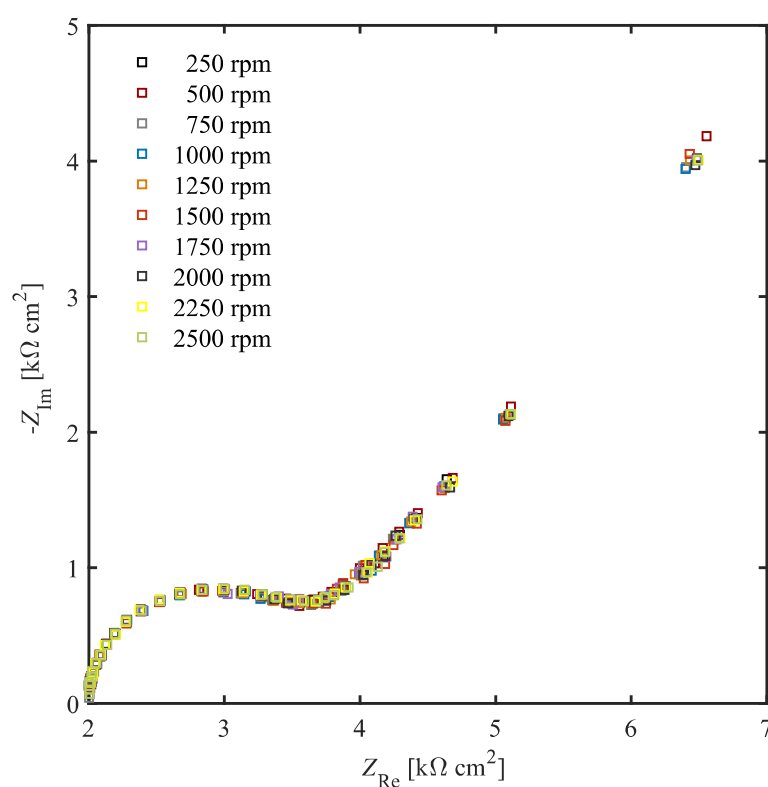


Figure E.1.: Dynamic impedance spectra recorded during low-amplitude current oscillations emerging at p-type Si in 0.06 M NH_4F in 142 mM H_2SO_4 at 8.64 V vs. SHE. The spectra were recorded at different rotation speeds of the RDE at the maximum of the current oscillation. $f_{osc} = 0.02$ Hz, $\Delta u_{ac} = 300$ mV, $f_b = 0.17$ Hz, $d = 3$, $R_{ext} = 10$ kΩ.

Bibliography

- Arrhenius, S. 1896. On the Influence of Carbonic Acid in the Air upon the Temperature of the Ground. *Philosophical Magazine and Journal of Science*. 41, 237-276.
- Bandarenka, A. S. 2013. Exploring the Interfaces between Metal Electrodes and Aqueous Electrolytes with Electrochemical Impedance Spectroscopy. *Analyst*. 138, 5540-5554.
- Barber, J., Morin, S., Conway, B. E. 1998. Specificity of the Kinetics of H₂ Evolution to the Structure of Single-Crystal Pt Surfaces, and the Relation between OPD and UPD H. *Journal of Electroanalytical Chemistry*. 446, 125-138.
- Bard, A. J., Faulkner, L. R. 2001. *Electrochemical Methods. Fundamentals and Applications*. John Wiley & Sons, New York, 2nd edition.
- Battistel, A., La Mantia, F. 2013. Nonlinear Analysis: The Intermodulated Differential Immitance Spectroscopy. *Analytical Chemistry*. 85, 6799-6805.
- Battistel, A. 2014. Development of the Intermodulated Differential Immitance Spectroscopy for Electrochemical Analysis. Dissertation. Ruhr-Universität Bochum, Germany.
- Battistel, A., Fan, M., Stojadinovic, J., La Mantia, F. 2014. Analysis and Mitigation of the Artefacts in Electrochemical Impedance Spectroscopy due to Three-Electrode Geometry. *Electrochimica Acta*. 135, 133-138.
- Battistel, A., Du, G., La Mantia, F. 2016. On the Analysis of Non-Stationary Impedance Spectra. *Electroanalysis*. 28, 2346-2353.
- Battistel, A., La Mantia, F. 2019. On the Physical Definition of Dynamic Impedance: How to Design an Optimal Strategy for Data Extraction. *Electrochimica Acta*. 304, 513-520.
- Beccari, M., Romano, U. 2007. *Encyclopedia of Hydrocarbons. Volume III/ New Developments: Energy, Transport, Sustainability*. Istituto dell'Enciclopedia Italiana, Rome.
- Belousov, B. P. 1959. Oscillation Reaction and its Mechanism (in Russian). *Sbornik Referatov po Radiacioni Medicine*, p. 145.

- Bennaceur, K., Clark, B., Orr, Jr. F. M., Ramakrishnan, T. S., Roulet, C., Stout, E. 2005. Hydrogen: A Future Energy Carrier?. *Oilfield Review*. 17, 30-41.
- Birry, L., Lasia, A. 2004. Studies of the Hydrogen Evolution Reaction on Raney Nickel-Molybdenum Electrodes. *Journal of Applied Electrochemistry*. 34, 735-749.
- Bockris, J. O'M. 1972. A Hydrogen Economy. *Science*. 176, 1323-1323.
- Bockris, J. O'M., Reddy, A. K. N. 1998. *Modern Electrochemistry 1. Ionics*. 1970 Plenum Press, New York, 2nd edition.
- Bockris, J. O'M., Reddy, A. K. N. 2000. *Modern Electrochemistry 2A. Fundamentals of Electrode Processes*. Kluwer Academic/ Plenum Publishers, New York, 2nd edition.
- Bockris, J. O'M. 2013. The Hydrogen Economy: Its History. *International Journal of Hydrogen Energy*. 38, 2579-2588.
- Bond, A. M., Schwall, R. J., Smith, D. E. 1977. On-Line FFT Faradaic Admittance Measurements. Application to A.C. Cyclic Voltammetry. *Journal of Electroanalytical Chemistry*. 85, 231-247.
- Bowden, F. P., Rideal, E. K. 1928. The Electrolytic Behaviour of Thin Films. Part I.—Hydrogen. *Proceedings of The Royal Society A, Mathematical, Physical and Engineering Sciences*. 120, 59-79.
- Bowen, C. T., Davis, H. J., Henshaw, B. F., Lachance, R., LeRoy, R. L., Renaud, R. 1984. Developments in Advanced Alkaline Water Electrolysis. *International Journal of Hydrogen Energy*. 9, 59-66.
- Breiter, M. W. 1963. Voltammetric Study of Halide Ion Adsorption on Platinum in Perchloric Acid Solutions. *Electrochimica Acta*. 8, 925-935.
- Brug, G. J., van den Eeden, A. L. G., Sluyters-Rehbach, M., Sluyters, J. H. 1984. The Analysis of Electrode Impedances Complicated by the Presence of a Constant Phase Element. *Electroanalytical Chemistry*. 176, 275-295.
- Buchberger, D. 1998. *Elektrochemische Analyseverfahren*. Spektrum, Heidelberg.
- Burstein, G. T. 2005. A Hundred Years of Tafel's Equation. *Corrosion Science*. 47, 2858-2870.
- Chan, C. K., Tüysüz, H., Braun, A., Ranjan, C., La Mantia, F., Miller, B. K., Zhang, L., Crozier, P. A., Haber, J. A., Gregoire, J. M., Park, H. S., Batchellor, A. S., Trotochaud, L., Boettcher,

- S. W. 2015. Advanced and In Situ Analytical Methods for Solar Fuel Materials. Topics in Current Chemistry, vol 371. Springer, Cham.
- Chazalviel, J. N., da Fonseca, C., Ozanam, F. 1992. Resonant and Nonresonant Behavior of the Anodic Dissolution of Silicon in Fluoride Media: An Impedance Study. Journal of The Electrochemical Society. 139, 2491-2501.
- Chazalviel, J. N., da Fonseca, C., Ozanam, F. 1998. In Situ Infrared Study of the Oscillating Anodic Dissolution of Silicon in Fluoride Electrolytes. Journal of The Electrochemical Society. 145, 964-973.
- Chen, L., Lasia, A. 1991. Study of the Kinetics of Hydrogen Evolution Reaction on Nickel-Zinc Alloy Electrodes. Journal of The Electrochemical Society. 11, 3321-3328.
- Conway, B. E., Bockris, J. O'M. 1957. Electrolytic Hydrogen Evolution Kinetics and Its Relation to the Electronic and Adsorptive Properties of the Metal. The Journal of Chemical Physics. 26, 532-541.
- Conway, B. E., Barber, J., Morin, S. 1998. Comparative Evaluation of Surface Structure Specificity of Kinetics of UPD and OPD of H at Single-Crystal Pt Electrodes. Journal of Electroanalytical Chemistry. 44, 1109-1125.
- Conway, B. E., Jerkiewicz, G. 2000. Relation of Energies and Coverages of Underpotential and Overpotential Deposited H and Pt and Other Metals to the 'Volcano Curve' for Cathodic H₂ Evolution Kinetics. Electrochimica Acta. 45, 4075-4083.
- Conway, B. E., Tilak, B. V. 2002. Interfacial Processes Involving Electrocatalytic Evolution and Oxidation of H₂, and the Role of Chemisorbed H. Electrochimica Acta. 47, 3571-3594.
- Creason, S. C., Smith, D. E. 1972. Fourier Transform Faradaic Admittance Measurements. I. Demonstration of the Applicability of Random and Pseudo-Random Noise as Applied Potential Signals. Journal of Electroanalytical Chemistry. 36, A1-A7.
- Creason, S. C., Smith, D. E. 1972. Fourier Transform Faradaic Admittance Measurements. II. Ultra-Rapid, High Precision Acquisition of the Frequency Response Profile. Journal of Electroanalytical Chemistry. 40, 1-5.
- Creason, S. C., Hayes, J. W., Smith, D. E. 1972. Fourier Transform Faradaic Admittance Measurements. III. Comparison of Measurement Efficiency for Various Test Signal Waveforms. Journal of Electroanalytical Chemistry. 47, 9-46.

- Darowicki, K. 2000. Theoretical Description of the Measuring Method of Instantaneous Impedance Spectra. *Journal of Electroanalytical Chemistry*. 486, 101-105.
- Darowicki, K., Orlikowski, J., Arutunow, A. 2003. Investigations of the Passive Layer Cracking by means of Dynamic Impedance Spectroscopy. *Electrochimica Acta*. 48, 4189-4196.
- Dincer, I. 2012. Green Methods for Hydrogen Production. *International Journal of Hydrogen Energy*. 37, 1954-1971.
- Dunn, S. 2003. Hydrogen Futures: Toward a Sustainable Energy System. *International Journal of Hydrogen Energy*. 27, 235-264.
- Eddowes, M. J. 1990. Anodic Dissolution of p- and n-type Silicon: Kinetic Study of the Chemical Mechanism. *Journal of Electroanalytical Chemistry*. 280, 297-311.
- Epstein, I. R., Showalter, K. 1996. Nonlinear Chemical Dynamics: Oscillations, Patterns, and Chaos. *Journal of Physical Chemistry*. 100, 13132-13147.
- Field, R. J., Koros, E., Noyes, R. M. 1972. Oscillations in Chemical Systems. II. Thorough Analysis of Temporal Oscillation in the Bromate-Cerium-Malonic Acid System. *Journal of the American Chemical Society*. 94, 8649-8664.
- Fleischmann, M. 1991. The AC Impedance of Spherical, Cylindrical, Disk, and Ring Microelectrodes. *Journal of Electroanalytical Chemistry and Interfacial Electrochemistry*. 317, 1-26.
- Frerichs, G. A., Mlnarik, T. M., Grun, R. J. 2001. A New pH Oscillator: The Chlorite-Sulfite-Sulfuric Acid System in a CSTR. *Journal of Physical Chemistry*. 105, 829-837.
- Gabrielli, C., Keddam, M., Portail, N., Rousseau, P., Takenouti, H., Vivier, V. 2006. Electrochemical Impedance Spectroscopy Investigations of a Microelectrode Behavior in a Thin-Layer Cell: Experimental and Theoretical Studies. *Journal of Physical Chemistry*. 110, 20478-20485.
- Gerischer, H. 1958. Mechanismus der Elektrolytischen Wasserstoffabscheidung und Adsorptionsenergie von Atomarem Wasserstoff. *Bulletin des Sociétés Chimiques Belges*. 67, 506-527.
- Guo, S., Bond, A. M., Zhang, J. 2015. Fourier Transformed Large Amplitude Alternating Current Voltammetry: Principles and Applications. *Review of Polarography*. 61, 21-32.
- Hardt, D. Department of Mechanical Engineering, Massachusetts Institute of Technology. 2004.

- Analysis and Design of Feedback Control Systems. The Dirac Delta Function and Convolution. URL <http://web.mit.edu/2.14/www/Handouts/Handouts.html>. Last accessed: 4/4/2019
- Harrington, D. A. 1993. Ac Voltammetry for Measurement of Surface Kinetics. *Journal of Electroanalytical Chemistry*. 355, 21-35.
- Hazi, J., Elton, D. M., Czerwinski, W. A., Schiewe, J., Vicente-Backett, V. A., Bond, A. M. 1997. Microcomputer-Based Instrumentation for Multi-Frequency Fourier Transform Alternating Current (Admittance and Impedance) Voltammetry. *Journal of Electroanalytical Chemistry*. 437, 1-15.
- Holmes, P. 1990. Poincaré, Celestial Mechanics, Dynamical -Systems Theory and "Chaos". *Physics Reports*. 193, 137-163.
- Höök, M., Bardi, U., Feng, L., Pang, X. 2010. Development of Oil Formation Theories and their Importance for Peak Oil. *Marine and Petroleum Geology*. 27, 1995-2004.
- Hubbert, M. K. 1956. Nuclear Energy and the Fossil Fuels. *Drilling and Production Practice*, Publication No. 95. Washington, DC: American Petroleum Institute & Shell Development Co.
- Huot, J. Y. 1987. Time Dependence of the Hydrogen Discharge at 70°C on nickel cathodes. *International Journal of Hydrogen Energy*. 12, 821-830.
- James, S. D. 1967. The Electrochemical Activation of Platinum Electrodes. *Journal of The Electrochemical Society*. 114, 1113-1119.
- Janson, N. B. 2012. Non-Linear Dynamics of Biological Systems. *Contemporary Physics*. 53, 137-168.
- Jerkiewicz, G. 1998. Hydrogen Sorption at/in Electrodes. *Progress in Surface Science*. 57, 137-186.
- Jerkiewicz, G. 2010. Electrochemical Hydrogen Adsorption and Absorption. Part 1: Underpotential Deposition of Hydrogen. *Electrocatalysis*. 1, 179-199.
- Koper, M. T. M. 1998. Non-Linear Phenomena in Electrochemical Systems. *Journal of the Chemical Society*. 94, 1369-1378.
- Koster, D., Du, G., Battistel, A., La Mantia, F. 2017. Dynamic Impedance Spectroscopy using Dynamic Multi-Frequency Analysis: A Theoretical and Experimental Investigation. *Electrochimica Acta*. 246, 553-563.

- Koster, D., Patzauer, M., Salman, M., Battistel, A., Krischer, K., La Mantia, F. 2018. Measurement and Analysis of Dynamic Impedance Spectra Acquired During the Oscillatory Electrodeposition of p-Type Silicon in Fluoride-Containing Electrolytes. *ChemElectroChem*. 5, 1548-1551.
- Koster, D., Zeradjanin, A. R., Battistel, A., La Mantia, F. 2019. Extracting the Kinetic Parameters of the Hydrogen Evolution Reaction at Pt in Acidic Media by means of Dynamic Multi-Frequency Analysis. *Electrochimica Acta*. 308, 328-336.
- Kreuter, W., Hofmann, H. 1988. Electrolysis: The Important Energy Transformer in a World of Sustainable Energy. *International Journal of Hydrogen Energy*. 23, 661-666.
- Krischer, K. 2001. Spontaneous Formation of Spatiotemporal Patterns at the Electrode/Electrolyte Interface. *Journal of Electroanalytical Chemistry*. 501, 1-21.
- La Mantia, F. 2008. Characterization of Electrodes for Lithium-Ion Batteries through Electrochemical Impedance Spectroscopy and Mass Spectrometry. Dissertation. ETH Zürich, Switzerland.
- Lasia, A., Rami, A. 1990. Kinetics of Hydrogen Evolution on Nickel Electrodes. *Journal of Electroanalytical Chemistry*. 294, 123-141.
- Lasia, A. 2003. *Handbook of Fuel Cells - Fundamentals, Technology and Applications, Volume 2: Electrocatalysis*. John Wiley & Sons, New Jersey.
- Lehmann, V. 1995. On the Origin of Electrochemical Oscillations at Silicon Electrodes. *Journal of the Electrochemical Society*. 143, 1313-1318.
- LeVeque, R. J. 2007. *Finite Difference Methods for Ordinary and Partial Differential Equations. Steady-State and Time-Dependent Problems*. Siam, Philadelphia.
- Lide, D. R. 2005. *Handbook of Electrochemistry and Physics*. CRC Press, Boca Raton, 85th edition.
- Los, P., Rami, A., Lasia, A. 1993. Hydrogen Evolution Reaction on Ni-Al Electrodes. *Journal of Applied Electrochemistry*. 23, 135-140.
- Losiewicz, B., Jurczakowski, R., Lasia, A. 2012. Kinetics of the Hydrogen Underpotential Deposition at Polychrystalline Platinum in Acidic Solutions. *Electrochimica Acta*. 80, 292-301.
- Lüke, H. D. 1999. The Origins of the Sampling Theorem. *IEEE Communications Magazine*. 106-108.

- Macdonald, J. R., Garber, J. A. 1977. Analysis of Impedance and Admittance Data for Solids and Liquids. *Journal of Electrochemical Society*. 124, 1022-1030.
- Macdonald, J. R., Potter, Jr. L. D. 1987. A Flexible Procedure for Analyzing Impedance Spectroscopy Results: Description and Illustrations. *Solid State Ionics*. 24, 61-79.
- Macdonald, D. D. 2006. Reflections on the History of Electrochemical Impedance Spectroscopy. *Electrochimica Acta*. 51, 1376-1388.
- Markovic, N. M., Sarraf, S. T., Gasteiger, H. A., Ross, P. N. 1996. Hydrogen Electrochemistry on Platinum Low-Index Single-Crystal Surfaces in Alkaline Solution. *Journal of the Chemical Society, Faraday Transactions*. 92, 3719-3725.
- Mazloomi, K., Gomes, C. 2012. Hydrogen as an Energy Carrier: Prospects and Challenges. *Renewable and Sustainable Energy Reviews*. 16, 3024-3033.
- Miethe, I., Krischer, K. 2012. Ellipsomicroscopic Studies of the Anodic Oxidation of p-Type Silicon in Fluoride Containing Electrolytes During Current Oscillations. *Journal of Electroanalytical Chemistry*. 666, 1-10.
- Morin, S., Dumont, H., Conway, B. E. 1996. Evaluation of the Effect of Two-Dimensional Geometry of Pt Single-Crystal Faces on the Kinetics of UPD of H Using Impedance Spectroscopy. *Journal of Electroanalytical Chemistry*. 412, 39-52.
- Nernst, W. 1894. Methode zur Bestimmung von Dielektrizitätskonstanten. *Zeitschrift für Elektrochemie*. 14, 622-663.
- Newman, J., Thomas-Alea, K. A. 2004. *Electrochemical Systems*. John Wiley & Sons, New Jersey, 3rd edition.
- Nicholis, G., Portnow, J. 1973. Chemical Oscillations. *Chemical reviews*. 73, 365-384.
- Oppenheim, A. V., Willsky, A. S. 1983. *Signals and Systems*. Prentice Hall, New Jersey, 2nd edition.
- Orazem, Mark. E., Tribollet, B. 2017. *Electrochemical Impedance Spectroscopy*. John Wiley & Sons, New Jersey, 2nd edition.
- Orbán, M., Kurin-Csörgei, K., Epstein, I. R. 2015. pH-Regulated Chemical Oscillators. *Accounts of Chemical Research*. 48, 593-601.

- Parsons, R. 1958. The Rate of Electrolytic Hydrogen Evolution and the Heat of Adsorption of Hydrogen. *Transactions of the Faraday Society*. 54, 1053-1063.
- Patzauer, M. 2016. Multistability in the Oscillatory Electrodeposition of Silicon. Master thesis. KTH Stockholm, Sweden.
- Pons, S., Fleischmann, M. 1987. The Behavior of Microelectrodes. *Analytical Chemistry*. 59, 1391A-1399A.
- Popkurov, G. S. 1996. Fast Time-Resolved Electrochemical Impedance Spectroscopy for Investigation Under Nonstationary Conditions. *Electrochimica Acta*. 41, 1023-1027.
- Proost, J., Blaffart, F., Turner, S., Idrissi, H. 2014. On the Origin of Damped Electrochemical Oscillations at Silicon Anodes (Revisited). *ChemPhysChem*. 15, 3116-3124.
- Ragoisha, G. A. 2004. Potentiodynamic Electrochemical Impedance Spectroscopy: Lead Underpotential Deposition on Tellurium. *Journal of Electroanalytical Chemistry*. 565, 227-234.
- Ragoisha, G. A., Bondarenko, A. S. 2005. Potentiodynamic Electrochemical Impedance Spectroscopy. *Electrochimica Acta*. 50, 1553-1563.
- Randles, J. E. B. 1947. Kinetics of Rapid Electrode Reactions. *Discussions of the Faraday Society*. 1, 11-19.
- Riley, K. F., Hobson, M. P., Bence, S. J. 2004. *Mathematical Methods for Physics and Engineering*. Cambridge University Press, Cambridge, 3rd edition.
- Sacci, R. L., Seland, F., Harrington, D. A. 2014. Dynamic Electrochemical Impedance Spectroscopy for Electrocatalytic Reactions. *Electrochimica Acta*. 131, 13-19.
- Salman, M., Patzauer, M., Koster, D., La Mantia, F., Krischer, K. 2019. Electro-Oxidation of p-Silicon in Fluoride-Containing Electrolyte: A Physical Model for the Regime of Negative Differential Resistance. *European Physical Journal Special Topics*. 227, 2641-2658.
- Santos, D. M. F., Sequeira, C. A. C., Figueiredo, J. L. 2013. Hydrogen Production by Alkaline Water Electrolysis. *Quimica Nova*. 36, 1176-1193.
- Santos, E., Quaino, P., Schmickler, W. 2012. Theory of Electrocatalysis: Hydrogen Evolution and More. *Physical Chemistry Chemical Physics*. 14, 11224-11233.
- Saunders, H. D. 1992. The Khazzoom-Brookes Postulate and Neoclassical Growth. *Energy Journal*. 13, 131-148.

- Schönleber, K., Krischer, K. 2012. High-Amplitude versus Low-Amplitude Current Oscillations During the Anodic Oxidation of p-Type Silicon in Fluoride Containing Electrolytes. *ChemPhysChem*. 13, 2989-2996.
- Sharifi-Asl, S., Macdonald, D. D. 2013. Investigation of the Kinetics and Mechanism of the Hydrogen Evolution Reaction on Copper. *Journal of The Electrochemical Society*. 160, H382-H391.
- Sheng, W., Gasteiger, H. A., Shao-Horn, Y. 2010. Hydrogen Oxidation and Evolution Reaction Kinetics on Platinum: Acid vs Alkaline Electrolytes. *Journal of The Electrochemical Society*. 157, B1529-B1536.
- Sheppard, R. J., Jordan, B. P., Grant, E. H. 1970. Least Squares Analysis of Complex Data with Applications to Permittivity Measurements. *Journal of Physics D: Applied Physics*. 3, 1759-1764.
- Smith, D. E. 1976. The Acquisition of Electrochemical Response Spectra by On-Line Fast Fourier Transform. *Data Processing in Electrochemistry. Analytical Chemistry*. 48, 221 A-240.
- Stone, M., Goldbart, P. 2009. *Mathematics and Physics*. Cambridge University Press, Cambridge.
- Stoynov, Z. B., Savova-Stoynov, B. S. 1985. Impedance Study of Non-Stationary Systems: Four-Dimensional Analysis. *Journal of Electroanalytical Chemistry*. 183, 133-144.
- Stoynov, Z. B. 1993. Nonstationary Impedance Spectroscopy. *Electrochimica Acta*. 38, 1919-1922.
- Strasser, K. P. 1999. *Kinetic Oscillations and Spatiotemporal Self-Organization in Electrocatalytical Reactions*. Dissertation. Freie Universität Berlin, Germany.
- Strmcnik, D., Lopes, P. P., Genorio, B., Stamenkovic, V. R. 2016. Design Principles for Hydrogen Evolution Reaction Catalyst Materials. *Nano Energy*. 29, 29-36.
- Strogatz, S. H. 2015. *Nonlinear Dynamics and Chaos*. Westview Press, Boulder, 2nd edition.
- Stulik, K., Amatore, C., Holub, K., Marecek, V., Kutner, V. 2000. Microelectrodes. Definitions, Characterization, and Application. *International Union of Pure and Applied Chemistry*. 72, 1483-1492.

- Tafel, J. 1905. Über die Polarisation bei Kathodischer Wasserstoffentwicklung. *Zeitschrift für Physikalische Chemie*. 50A, 641-712.
- Thompson, J. M. T., Stewart, H. B. 2002. *Nonlinear Dynamics and Chaos*. John Wiley & Sons, Chichester, 2nd edition.
- Trasatti, S. 1972. Work Function, Electronegativity, and Electrochemical Behaviour of Metals. III. Electrolytic Hydrogen Evolution in Acid Solutions. *Electroanalytical Chemistry and Interfacial Electrochemistry*. 39, 163-184.
- Turner, J. A. 2004. Sustainable Hydrogen Production. *Science*. 305, 972-974.
- U.S. Energy Information Administration. 2017. *International Energy Outlook 2017*, Washington, D.C., USA.
- Verne, J. 1874. *The Mysterious Island*. URL http://www.online-literature.com/verne/mysterious_island/. Last accessed: 4/23/2019
- Vesborg, P. C. K., Seger, B., Chorkendorff, I. 2015. Recent Development in Hydrogen Evolution Reaction Catalysts and their Practical Implementation. *The Journal of Physical Chemistry Letters*. 6, 951-957.
- Vrubel, H., Moehl, T., Grätzel, M., Hu, X. 2013. Revealing and Accelerating Slow Electron Transport in Amorphous Molybdenum Sulphide Particles for Hydrogen Evolution Reaction. *Chemical Communications*. 49, 8985-8987.
- Wang, L., Lee, C.-Y., Schmuki, P. 2013. Solar Water Splitting: Preserving the Beneficial Smaller Feature Size in Porous α -Fe₂O₃ Photoelectrodes During Annealing. *Journal of Materials Chemistry A*. 1, 212-215.
- Warburg, E. 1899. Über das Verhalten sogenannter unpolarisierbarer Elektroden bei Wechselstrom. *Annalen der Physik und Chemie*. 67, 493-499.
- Wheatstone, C. 1843. An Account of Several New Instruments and Processes for Determining the Constants of a Voltaic Circuit. *Philosophical Transactions of the Royal Society of London*. 133, 303-327.
- Zeng, K., Zhang, D. 2010. Recent Progress in Alkaline Water Electrolysis for Hydrogen Production and Applications. *Progress in Energy and Combustion Science*. 36, 307-326.
- Zeradjanin, A. R., Grote, J. P., Polymeros, G., Mayrhofer, K. J. J. 2016. A Critical Review on

Hydrogen Evolution Electrocatalysis: Re-exploring the Volcano-relationship. *Electroanalysis*. 28, 2256-2269.

Züttel, A., Remhof, A., Borgschulte, A., Friedrichs, O. 2010. Hydrogen: the Future Energy Carrier. *Philosophical Transactions of the Royal Society A*. 368, 3329-3342.

Publications

Parts of this thesis have been published in the following peer-reviewed scientific journals:

- Koster, D., Zeradjanin, A. R., Battistel, A., La Mantia, F. 2019. Extracting the Kinetic Parameters of the Hydrogen Evolution Reaction at Pt in Acidic Media by means of Dynamic Multi-Frequency Analysis. *Electrochimica Acta*. 308, 328-336.
- Salman, M., Patzauer, M., Koster, D., La Mantia, F., Krischer, K. 2019. Electro-Oxidation of p-Silicon in Fluoride-Containing Electrolyte: A Physical Model for the Regime of Negative Differential Resistance. *European Physical Journal Special Topics*. 227, 2641-2658.
- Koster, D., Patzauer, M., Salman, M., Battistel, A., Krischer, K., La Mantia, F. 2018. Measurement and Analysis of Dynamic Impedance Spectra Acquired During the Oscillatory Electrodissolution of p-Type Silicon in Fluoride-Containing Electrolytes. *Chem-ElectroChem*. 5, 1548-1551.
- Koster, D., Du, G., Battistel, A., La Mantia, F. 2017. Dynamic Impedance Spectroscopy using Dynamic Multi-Frequency Analysis: A Theoretical and Experimental Investigation. *Electrochimica Acta*. 246, 553-563.